Journal "Light & Engineering" had been founded by Prof. Julian B. Aizenberg in 1993

MOSCOW, 2020

Light & Engineering" is an international scientific Journal subscribed to by readers in many different countries. It is the English edition of the journal "Svetotekhnika" the oldest scientific publication in Russia, established in 1932.

Establishing the English edition "Light and Engineering" in 1993 allowed Russian illumination science to be presented the colleagues abroad. It attracted the attention of experts and a new generation of scientists from different countries to Russian domestic achievements in light and engineering science. It also introduced the results of international research and their industrial application on the Russian lighting market.

The scope of our publication is to present the most current results of fundamental research in the field of illumination science. This includes theoretical bases of light source development, physiological optics, lighting technology, photometry, colorimetry, radiometry and metrology, visual perception, health and hazard, energy efficiency, semiconductor sources of light and many others related directions. The journal also aims to cover the application illumination science in technology of light sources, lighting devices, lighting installations, control systems, standards, lighting art and design, and so on.

"Light & Engineering" is well known by its brand and design in the field of light and illumination. Each annual volume has six issues, with about 80–120 pages per issue. Each paper is reviewed by recognized world experts.

CONTENTS

VOLUME 28 **NUMBER 6** **2020**

LIGHT & ENGINEERING

INSOLATION AND COVID-19: PROTECTION FROM THE AGGRESSOR

Yuri B. Popovskiy[1] and Nikolay I. Shchepetkov[2]

[1]INSOLYATSIYA LLC
[2]Moscow Institute of Architecture (State Academy)
E-mails: 01@insilation.pro; n _shchepetkov@inbox.ru

Places lacking the sunlight
are often visited by doctors

ABSTRACT

The article reviews the importance of insolation as a factor of prevention and containment of infectious diseases and epidemics. The authors consider insolation not as a mean of curing the Coronavirus Disease (WHO fairly calls such possibility "a myth") but as a means to lower the risks of dissemination of the infection, to reduce viability of the virus in the environment, to support human protective immune mechanisms affecting susceptibility of the population as a whole, severity and recovery time, i.e. both sanitary and hygienic and prevention factors of the COVID-19 epidemic containment. Apart from the germicidal and virucidal sanitising effects of solar rays, the article reviews anti-epidemic capabilities of insolation as a microclimate factor and a psychological and physiological regulator of human protective capabilities as well as the insolation standards as a mechanism of development density regulation. It is impossible to efficiently combat massive dissemination of highly contagious infections without concerted utilisation of all available means and measures: both medical and preventive and organisational. The unprecedented mobilisation of healthcare systems and large-scale restrictive quarantine measures are under special attention of the society. This article reviews the importance of insolation as a universal natural anti-epidemic factor which is undeservedly placed in the end of the list of effective infection combating measures.

Keywords: insolation, communal hygiene, insolation standards, sunlight, psychophysiology, anti-epidemic measures, prevention, health security, COVID-19

1. INTRODUCTION

It is impossible to efficiently combat massive dissemination of highly contagious infections without concerted utilisation of all available means and measures: both medical and preventive and organisational. The unprecedented mobilisation of healthcare systems and large-scale restrictive quarantine measures are under special attention of the society. This article reviews the importance of insolation as a universal natural anti-epidemic factor which is undeservedly placed in the end of the list of effective infection combating measures. The authors do not consider insolation as a remedy against the Coronavirus Disease (replying to Donald Trump's statement, WHO fairly called such possibility "a myth"), but as a means to lower the risks of dissemination of the infection, to reduce viability of the virus in the environment, to support human protective immune mechanisms affecting susceptibility of the population as a whole, severity and recovery time, i.e. both sanitary and hygienic and prevention factors of the COVID-19 epidemic containment.

Since the period of establishment of communal hygiene as a scientific discipline, the range of tools of doctors and hygienists has been largely enhanced by cheap and efficient antiseptics, hardware and pharmacologic means of diagnostics and treatment as well as artificial substitutes of solar radiation, UV emitters.

The shift of emphasis from natural means of protection to technical, disinfection, and pharmacological ones stems from the fact that, other than high efficiency of the latter, the natural factors are not goods as they are available everywhere and, not being commercially attractive, have no other ways of "promotion" apart from common sense, applicable standards, and self-sacrifice of a few specialists. On the contrary, many of recognised factors of hygienic security of the artificial human habitat, which are specified in standards, raise the prices of municipal infrastructure maintenance and reduce profitability of construction, and targeted pressure on sanitary and hygienic standards, which have allegedly lost their applicability in the new urban reality brought by concerned parties (construction investors and customers), including via government entities, is associated with it.

However, as we can see through the example of the COVID-19 epidemic, contemporary cities and contemporary people have not become less vulnerable to new infections, primarily those caused by viruses.

Lack of efficient means to be used for prevention and containment of the COVID-19 epidemic makes it necessary to solve the problem using restrictive and quarantine measures, which are the most damaging for economy and ultimately for the most of population. But if we say that all possible resources shall be used for combating the epidemic, it is fair to start with the least resource-intensive, available to everyone and essentially free natural factors, and especially with insolation.

Someone may doubt the efficiency of insolation as an anti-epidemic resource given that no country has avoided the pandemic irrespective of the degree of direct sunlight availability. Undoubtedly, the key factors of dissemination of COVID-19 included intensity of transport flows, population density and traditionally social forms of labour and leisure. However, since the moment the infection appeared, further development of the epidemic process has been regulated by the entire set of anti-epidemic factors, both targeted and natural or occasional ones. In terms of the subject matter of this article, the following significant features of the centres of the pandemic are obvious:

− Geography – currently, the morbidity of COVID-19 per 1,000 individuals is much higher in the countries located in the Northern hemisphere which are now leaving the period of seasonal deficiency of sunlight;

− Population density – COVID-19 mostly affects megalopolises with high density of development, a factor that determines insufficient availability of sunlight in urban areas, especially in conditions of its seasonal deficiency.

It is important to bear in mind that the hygienic importance of insolation is not only defined by direct sanitising effect of the short-wave region of sunlight spectrum. The climate-forming role of insolation is of the same importance for containment of the infection, including formation of microclimate of indoor spaces, buildings and territories, which had been specified as a "general health-improving effect" in Russian insolation standards before 2001. Let us consider each group of factors separately.

2. SANITISING EFFECT

The direct antivirus effect of solar radiation, especially of direct sunlight (insolation) specifically against the COVID-19 virus, is associated with damage of the RNA molecule of the virus, which makes it impossible to replicate it in a host cell. It is not possible to evaluate the degree of sunlight resistance of the COVID-19 virus based on the materials available as of now. However, even if the results of such studies had been available, their practicability would have been low since actual insolation is determined by constantly changing factors: cloud amount, state of atmosphere, the Sun angle, sunshine duration as well as the position of the exposed surface and its texture. Nevertheless, availability of the UV-B component in the sunlight spectrum [1] guarantees its virus-inactivating effect, and given the duration of sunshine on clear days (at least 2 hours in Moscow even in winter [2]), the virucidal potential of insolation may be comparable with that of short-time irradiations by means of germicidal UV emitters and even largely exceed it in summer months. With that, the virucidal potential of insolation manifests itself everywhere and dynamically: depending on the date and time which define the position of the Sun in the sky. Not only and not so much the indoor spaces and territories are insolating with the standardised insolation regime, but also all urban areas are, such as streets and roads, parks, urban air, facades of houses open to sunlight, and all indoor spaces where insolation is not required as per

standards but its sanitising effect is also efficient and necessary.

Insolation of urban areas and facades provides also efficiency of another hygienic factor, natural ventilation of indoor spaces.

3. CLIMATE AND MICROCLIMATE

Based on preliminary results of the publicly available studies [3], temperature of (5–9) °C and humidity of (35–50) % are the optimal conditions for dissemination of the COVID-19 virus, and its viability in the environment is reduced when temperature is increased and humidity is lowered, and virulence of the virus falls down to zero at 30 °C. Therefore, the infra-red region of the sunlight spectrum also has the same sanitising effect which the short-wave UV region has. Ingress of direct sunlight through double glazing rises the temperature of an irradiated wooden or plastic surface by (14–15) °C, which will be equal to (35–40) °C at room temperature of (20–25) °C, the conditions neutralising activity of the virus. In open urban areas, the heat effect of insolation has the same values ((13–15) °C depending on the Sun angle and the state of the atmosphere), and temperature of concrete and asphalt surfaces rises from (1–10) C° to 1(4–15) °C[1] during the inter-season periods most favourable for the infection, which makes them an unfavourable environment for survival of the COVID-19 virus and promotes its inactivation.

Simultaneously with increase in temperature of insolate surfaces, humidity also reduces during the inter-season periods, which is also a factor of infection containment.

4. PSYCHOPHYSIOLOGY AND IMMUNITY STATUS

Apart from the direct physical and biochemical virucidal effect, insolation directly and indirectly contributes to regulation of some physiological processes in human body, which also significantly affects the course of the entire epidemic process defining susceptibility to the infection of population as well as severity of the disease and recovery time. This set of factors is called psychophysiological ac-

tion. In this case, the entire visible part of sunshine spectrum is of importance, and direct and scattered sunlight affect retina simultaneously with further transmission of nerve impulses to endocrine control centres via the visual pathway. Illuminance within a light spot increases by more than 30 times under direct sunlight. With the size of a light spot of (2.5–3.5) % of the floor area, illuminance on the horizontal surface in the centre of an indoor space increases by (2–2.5) times at height of 0.8 m above the floor level and by (3–3.5) times at a floor level just by means of reflected light (beyond visual line of sight of the light spot). A light spot of 20 % of the floor area increases the same values by 4.5 and 9 times, respectively[2]. Given the fact that a physiological standard value of daylight factor in indoor spaces is (5–10)% (based on recommendations of WHO), and standard illuminance of, for instance, residential spaces is 0.5 %, contemporary residents of cities live in conditions of constant deficiency of environmentally friendly, free, and unexpendable daylight. Increase of illuminance by several times by means of direct sunlight on sunny days eliminates this deficiency partially or completely.

The subject 'light and health' has been repeatedly discussed in the Svetotekhnika Journal [4, 5, 6, 7]. Therefore, it is sufficient just to list the "light-dependent" psychological and physiological processes in the context of this article.

High levels of daytime illuminance promote proper work of circadian rhythms responsible for normal endocrine control of physiological processes in a body. Impairment of the sleep-wake cycle, including insomnia, diurnal somnolence, performance decrement, and apathy is the most well-known consequence of circadian rhythm deregulation. Low levels of illuminance, which do not provide necessary light contrast between day and night, is the cause of development of seasonal affective disorder (SAD) during autumn and winter, which causes development of depression and reduction of distress tolerance. The said negative consequences of insufficient daytime illumination (and sufficient natural illumination without direct sunlight is impossible in megalopolis environment) reduce the immunity status of body, which manifests itself in increased susceptibility to the infection, poor im-

---

[1] The data of changes in temperature of insolated surfaces is based on the authors' own reference measurements made on April 21, 2020 in Moscow

[2] The data of dynamics of illuminance in insolated indoor spaces is based on the authors' own reference measurements made on April 21, 2020 in Moscow

mune response and, subsequently, harder development of the disease. A number of studies conducted in the 20th century [8] confirmed the well-known fact that wound healing is much faster in well-insolate wards than in insufficiently insolate wards provided that disinfection and antiseptic regimes in both wards are the same.

Even short-time contribution of direct sunlight to formation of a lighting environment 'adjusts' the inner clock of a body by forming daytime light accents, which increases human psycho-emotional status, promotes distress tolerance and supports efficiency of all protective mechanisms including immune ones.

5. INSOLATION STANDARDS AS A REGULATOR OF DEVELOPMENT DENSITY AND POPULATION DENSITY

With all importance of the climatic factor, immune status of population and quality of healthcare systems, it must be admitted that the main factor of COVID-19 dissemination is population density and associated load of public transport and social centres such as cultural, trade and sports areas. It should be noted that one of the only factors preventing urban densification is standardisation of insolation and natural illumination, and the dynamics of modifications of such standards demonstrates a number of highly doubtful from the scientific point of view opportunistic compromises between requirements of sanitary and epidemiological security and interests of the urban development industry. Over the half-century history of insolation standardisation, the norms have been shortened from (3–4) hours to an hour and a half or two hours [9], the calculation dates for the central geographic zone, where most of Russia's population resides, were shortened by two months in 2017 without any reasons provided (now they are worse than those for the northern zone), summer insolation requirements and prohibition of all-year shading were cancelled. The above listed regulatory easements change the emphasis from the human health improving factor (as in the 1982 version) to the factor "causing health-improving effect on human habitat" (as in the 2001 version), which is essentially limited to the bactericidal effect. Apparently, the logic of social development implies that human species has changed sufficiently over the previous 50 years to cancel its mechanisms of self-protection and self-regulation that had

been forming for millions of years. However, it is not true. Vulnerability of a modern city to highly contagious infections is directly proportional to development density, i.e. the volume of non-insolate facades and territories, and population density, i.e. just the number of hand grasps per one door handle. In this context, construction of non-residential apartments, which are in most cases used for residence, but are not compliant with any regulatory requirements to residential premises, including sanitary and epidemiological requirements, and not providing any social infrastructure including medical institutions, is a very questionable trend.

The COVID-19 pandemic poses a question whether contemporary cities are safe enough to ignore the natural factors of human protection and its artificial habitat which are justified by evolution, life and science [10].

6. CONCLUSIONS

The role of sunlight transformed by the atmosphere is not less important in human life. The standards of its utilisation, which is more large-scale than utilisation of insolation, are also cut off by the two authorities issuing them, namely, the Ministry of Construction and the Ministry of Healthcare of the Russian Federation, from time to time although it does not attract attention of the society for some reasons. In the last editions of the natural illumination standards, the reference point for the most of indoor spaces is relocated from the depth to the centre with the same rather poor standard value daylight factor. It is obvious that illuminance in indoor spaces becomes much lower, which will require utilisation of additional artificial illumination being not capable to replace daylight neither in terms of quality nor in terms of quantity, over the most part of a year.

The basics of the Russian standards of natural lighting and insolation were established in the hard years after WWII when, nevertheless, the return to peaceful life could not be imagined without a comprehensive solution of the problems of safety and quality of life in cities being reconstructed. The government planned and subsidised comprehensive studies in the field of sanitary and hygienic safety of environment, in particular, determination of lighting and climatic parameters necessary for productive life. Dedicated organisations and high-level scientists engaged in different spheres such as light engineering, hygiene, architecture participated in the re-

search programmes. The first sanitary standards of natural lighting and insolation were developed and put into effect on the basis of the evidence base. Unfortunately, that generation of independently thinking scientists with high levels of professionalism and scientific potential has passed away, the institutes and laboratories engaged in always topical works in the field of public health have been either closed or assigned new functions, and the following generation of specialists responsible for the fate of hygiene as a scientific discipline is represented more by government officials than by well-known scientists, which made it possible to adopt legal and regulatory easements under pressure of the interests of the construction industry [9]. For instance, it is impossible to understand the motivation of decreasing the standard requirements of insolation for the central geographic zone of the Russian Federation adopted by the Chief Sanitary Inspector A. Yu. Popova without any scientific research, justifications, discussions in the professional community and more in disregard of its opinion, just 'supported by the Moscow Investors Club'. Anna Yurievna did not reply to the open letter [10] addressed to her.

It is to be added that the mankind has just two proven means of combating infections like COVID-19 before the start of industrial manufacturing of efficient vaccines and introduction of efficient treatment methods: restrictive quarantine measures and the sunlight. And the more a contemporary city has of the latter, the less strict and destructive can be the former.

REFERENCES

1. Obolensky, N.V. Architecture and the Sun [Arkhitektura i solntse]. Moscow: Stroyizdat, 1988.

2. Moscow Ecological and Climatic Characteristics Handbook (Based on Observations of the Meteorological Laboratory of Moscow State University) [Spravochnik ekologo-klimaticheskikh kharakteristik g. Moskvy (po nablyudeniyam meteorologicheskoy laboratorii MGU)]. Vol. 1. Moscow: Moscow State University Press. 2003, pp. 35–37.

3. URL: https://iz.ru/986191/anna-urmantceva-mariia-nediuk/minusy-pliusa-koronavirus-luchshe-vsego-rasprostraniaetsia-pri-8–9degc/ (date of reference: 22.04.2020).

4. Boyce P. Light and Health [Svet i zdorovye]. Svetotekhnika, 2006, # 2, pp. 43–48.

5. Anisimov Vladimir N. Light Desynchronosis and Health// Light & Engineering, 2019, Vol. 27, # 3, pp. 14–25.

6. Gašper Čož Senior Living – Lighting, Circadian Rhythm and Dementia II// Light & Engineering, 2019, Vol. 27, #5, pp. 9–14.

7. Light Engineering Handbook [Spravochnaya kniga po svetotekhnike] / Edited by Ju.B. Aizenberg. 4th Issue, Section Fifteen. Light and Health. Non-Visual Functions of Light [Svet i zdorovye. Nezritelnyie funktsii sveta]. Moscow: 2019, pp. 809–813.

8. Saatov Kh.I. On Wound Healing in Conditions of Body Exposure to Ionising Radiation and Insolation [K osobennostyam zazhivleniya ran v usloviyakh vozdeystviya na organizm ioniziruyushchey radiatsii i insolyatsii]: Thes. of Cand. of Med.: Vol. 1–2 / I.P. Pavlov Samara Medical Institute,1967.

9. Popovskiy Yu.B. The History of Sanitary and Epidemiological Standardisation of Insolation of Residential Premises in USSR and Russian Federation [Istoriya sanitarno-epidemiologicheskogo normirovaniya insolyatsii zhilykh pomeshcheniy v SSSR i Rossiyskoy Federatsii]. National Association of Scientists. 2015, Vol. 6–3 (11), pp. 27–30.

10. Shmarov I.A., Zemtsov V.A., Korkina E.V. Insolation: Standardisation and Calculation Practice [Insolyatsiya: praktika normirovaniya i raschyota] // Zhilishchnoye stroitelstvo, 2016, # 7, pp. 48–53.

11. Shchepetkov, N.I. Open Letter to Chief Sanitary Inspector of the Russian Federation A. Yu. Popova [Otrkytoye pismo Glavnomu sanitarnomu vrachu RF A. Yu. Popovoy]// Svetotekhnika, 2017, Vol. 6, pp. 100.
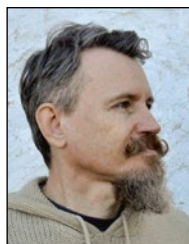
Yuri B. Popovskiy, Architect, graduated from MArkhI in 1983, and Doctor in the field of medical and preventative care, graduated from the I.M. Sechenov First Moscow State Medical University (Sechenov University) in 2012. At present, he is a Chief Specialist of INSOLYATSIYA LLC and Associate Professor of the Chair of Architectural Physics at the MArkhI

Nikolay I. Shchepetkov, Dr. of Architecture, Professor. At present, he is a head of the Architectural Physics Department of Moscow Architecture Institute, laureate of the State Prize of the Russian Federation (for architectural lighting of Moscow), editorial board member of the Light & Engineering Journal

PHYSICAL–MATHEMATICAL MODEL OF THE INTERNAL QUANTUM EFFICIENCY DEPENDENCE ON THE CURRENT OF LEDS WITH QUANTUM WELLS

Fedor I. Manyakhin and Lyudmila O. Mokretsova

National University of Science and Technology "MISIS"
E-mail: zaomisis@yandex.ru

ABSTRACT

A physical-mathematical model of dependence of internal quantum efficiency on current for LED structures with quantum wells has been developed. The volt-ampere characteristic is modelled with the involvement of Shockley, Noyce, Sah recombination theory, supplemented by the quantum wells distribution function. In order to obtain dependence of internal quantum efficiency of LEDs on current, model of rate of ABC recombination in quantum wells is used. The developed model was tested with variations of quantum wells parameters and external impact conditions.

Keywords: LED structures with quantum wells, internal quantum efficiency, Shockley, Noyce, Sah recombination model; ABC recombination model

1. INTRODUCTION

Light emitting diodes (LEDs) with quantum wells (QW) are promising sources of light for lighting devices, full-colour displays, optrons, etc.

Quantum efficiency (QE) is one of the main parameters of LEDs QW. After commencement of serial production of LEDs based on QW hetero-structures *AlGaN/InGaN/GaN* and *AlInGaP* [1, 2], intensive studies of dependence of QE on forward-current density *J* have begun.

In one of the first works analysing behaviour of efficiency of a blue and green LED by *Lumileds Lighting* [3], it was shown that it has a maximum at *J* = (1–10) A·cm⁻². It was noted that higher values of maximum efficiency correspond to higher barrier doping and explicit periodical changes of doping density in the QW region (the modulated and doped region of QW).

According to the data of [4], with strong light excitation, when charge carriers (CC) generation rate was equal to $1.7 \cdot 10^{26}$ cm⁻³·s⁻¹, with reduction of dislocation density from $5.7 \cdot 10^{9}$ down to $5.3 \cdot 10^{8}$ cm⁻², external QE (η_E) rose from 31 % up to 64 %. With that, the maximum of η_E reduces with reduction of quality of epilayers and shifts towards higher values of *J*.

Measurements of η_E at different temperatures [4, 5] have shown that, with increase of temperature of QW LED structures, the maximum of QE lowers and shifts to the range of higher *J*.

In the course of analyses of QW recombination processes, the *ABC* model [6–10] is widely used: it allows us to describe recombination rate of LED structures at different injection levels with consideration of radiative and non-radiative mechanisms:

$$R(n) = \frac{n}{\tau} = An + Bn^2 + Cn^3 + f(n), \qquad (1)$$

where *R* is the recombination rate, *n* is the excessive concentration of CC taking part in the recombination process; τ is the average CC life span; *A, B, C* are the coefficients defined experimentally for recombination rates of the Shockley-Read-Holl recombination mechanism (*A*), radiative mechanism (*B*) and the Auger mechanism (*C*). The other mechanisms of current formation are taken into account by an additional member $f(n)$.

The finer mechanisms affecting QE of QW LEDs are analysed in [11, 12] and other works, however, all the differences identified there correspond to the *ABC* model.

The analysis of literature allowed to identify that: 1) the η_E-current dependence curve of QW LED structures is bell-shaped with the maximum at $J = (1 \cdot 10^{-2}-1 \cdot 10)$ A $\cdot$ cm^{-2}; 2) the height of the maximum and its current position depends on perfection of a hetero-structure and its temperature; 3) there are still no mathematical models of the dependence of η_E and internal QE (η_I) on current and the Sah-Noyce-Shockley (SNS) model [13] (further developed in [14]) is used as the voltage-current relationship (VCR) model without taking non-uniformity of recombination rate in the space charge region (SCR) with a QW into account).

Based on the analysis, the common problem was identified: lack of the analytical model defining the relationship between VCR and lumen-voltage characteristics (LVC) for LED heterostructures based on wide-band-gap semiconductors with QW and allowing to satisfactorily describe and simulate behaviour of η_E and η_I with different external effects and distinctions of LED technological structure.

The goal of this work is to develop the analytical model of the dependence of η_I (η_E) on current on the basis of physical representation of recombination processes in QW hetero-structures.

The objectives of the work: to conduct experimental studies of VCR and η_E behaviour of QW LEDs at different temperatures and with introduction of point and continuous defects (dislocations, disordering areas); to create the physical and mathematical model of the dependence of η_E (η_I) on current; to check validity of this model with different external effects and variations of technological parameters of LED hetero-structures.

For the purpose of clarity and to prevent complication of the model, it is assumed in the work that there is a proportional relation between η_E and η_I expressed through the constant coefficient: $\eta_E = \alpha \cdot \eta_I$, $\alpha < 1$. Therefore, when modelling of QE depending on current, η_I will be meant and η_E may be derived from it by means of the coefficient α.

In the course of the model development, it is assumed that distribution of CC in quazi-neutral regions and in SCR corresponds to the Boltzmann distribution.

2. EXPERIMENT

The green, yellow and red LED's based on *AlGaN/InGaN/GaN* and *AlInGaP* hetero-structures manufactured in PCR by *Lumileds* and *Epistar* were studied. VCR, LVC and distribution of dopant over the QW region were measured at temperatures of 300 K and 373 K. Graphic representation of these characteristics is given in [15].

The blue experimental samples manufactured by *Lumileds* were marked with letter *B*, the greed samples were marked with *G* (the *InGaN/GaN* structure) and the red ones were marked with letter *R* (the *AlInGaP* structure).

VCR were measured by means of a computerised unit. The current measurement range was $(1 \cdot 10^{-7}-1 \cdot 10^{-1})$ A or $J = (1 \cdot 10^{-4}-1 \cdot 10^2)$ A $\cdot$ cm^{-2} up to maximum voltage of 5.12 V. Forward-bias potential increment was equal to $\Delta U = (0.02 \pm 1 \cdot 10^{-4})$ V.

Dopant distribution over the QW region was measured by means of an original computerised unit [16] using the dynamic capacity method. Resolution of the dopant concentration profile depth was up to 1 nm.

Radiation was registered by the PhD 7K silicon photodiode operating in the light-to-photoelectric-current conversion mode.

In order to identify the effect of point and continuous microdefects on η_I, all LEDs were affected by reactor neutron fluxes (Φ) of 10^6, 10^7, 10^8 and 10^{15} cm^{-2} by means of the IRT 2000 installation. In the course of it, the energy spectrum and the neutron-flux density (equal to $5 \cdot 10^{10}$ cm^{-2} $\cdot$ s^{-1}) were measured.

Processing of the experimental data and simulation of LED characteristics were conducted by means of *Origin 8* and *MathCad 14*.

The experimental dependences of η_E on current *I* are presented in the Figs. 1a and 2a. With temperature rising from 300 K to 373 K, the maximum of η_E reduces by $(8-12)\%$ and shifts to the range of higher values of current by more than one order of magnitude (not shown in the Figure).

More significant reduction of η_E was observed in LEDs after they being irradiated by neutrons at $\Phi = 1 \cdot 10^{15}$ cm^{-2}. The maximum of η_E reduces differently in *AlGaN/InGaN/GaN* and *AlUnGaP* structures and shifts towards higher values of current. At Φ of up to $1 \cdot 10^8$ cm^{-2}, no significant changes of the dependence $\eta_E(I)$ were observed at ambient temperature.
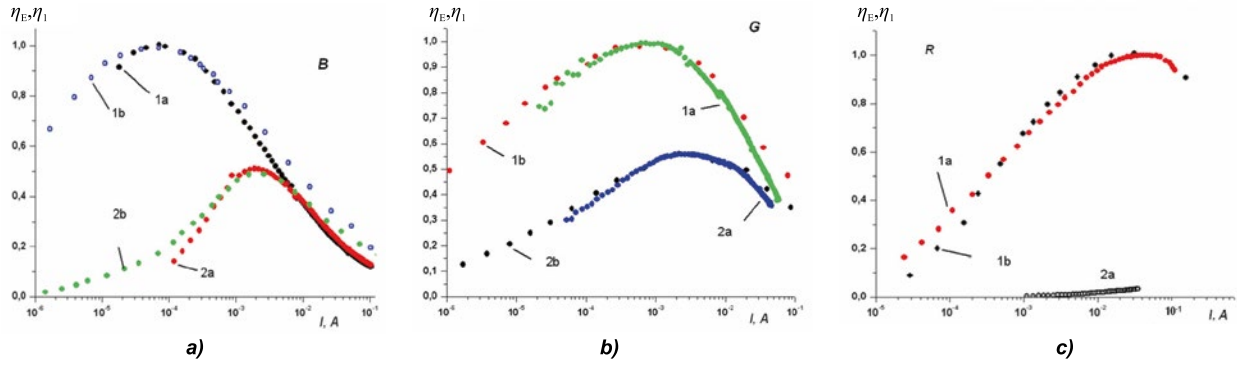
Figure. The dependences of η_E (experimental, graphs 1a, 2a) and η_I (simulated, graphs 1b, 2b) on current I for blue (*a*), green (*b*) and red (*c*) LEDs, graphs 1a and 1b are for the initial structures and are normalised to one, graph 2a is for neutron-irradiated structures, graph 2b is for model structures with concentration of radiation defects introduced in the model

The effect of neutron irradiation on lens transparency was not studied, however, no visible changes in lens transparency occurred.

The changes in distribution of charge centres of dopant in the QW region after neutron irradiation at Φ of up to 10^{15} cm^{-2} for LEDs with different quantum energy occurred in different ways. For instance, in blue and green LEDs, dopant compensation was observed only in the small region near the border of the edge of SCR of the lightly doped layer. Significant reduction of concentration of active dopant within the range of SCR changes occurred in yellow and red LEDs.

After neutron irradiation, the non ideality factor of the exponential region of VCR increased by (20–30)% and the saturation current increased by (5–6) orders of magnitude.

3. DISCUSSION

Let us assume an asymmetrical $p-n^+$ LED structure with uniformly doped p and n^+ layers as the model. QWs are located in the relatively slightly doped p layer within SCR without bias voltage. The QW coordinates are measured starting from the metallurgical border.

It is assumed that no tunnelling, leak currents, and other mechanisms of current formations are available other than the Shockley-Read-Holl (SRH), radiative and Auger recombination mechanisms; the Shockley diffusion mechanism [17] and SNS [13] are the main mechanisms of current formation of LED structures. With that, QWs are represented as single recombination centres with trap cross-section of σ.

CCs trapped in QWs form current, which is divided into two components: the zone-zone radiative one and the nonradiative local centre and Auger recombination component. Also, if there are point defects in the forbidden band of local levels, formation of recombination current over the entire SCR by means of the SNS mechanism is possible. Therefore, density of total recombination current J with forward bias in such structure is a particular sum:

$$J = J_{QW} + J_{rec} + j_{dif},$$

where J_{QW} is the density of quantum-well recombination current, J_{rec} is the density of recombination current through local levels of point defects in SCR, J_{dif} is the density of diffusion current of CCs that crossed the $p-n^+$ junction barrier and are trapped in QWs in the quasi-neutral part of the p region and within the range of operating currents of LED, J_{rec}, $J_{QW} >> J_{dif}$.

Therefore, η_E proportional to η_I is defined by the ratio between radiative and nonradiative recombination currents. The experimental results (see the Figure) witness that the coefficients of the *ABC* model vary significantly for different types of LEDs, which is pointed at by different positions of the maximums of $\eta_I(\eta_E)$ [7]. Simulation has shown that it mostly refers to the *A* and *C* coefficients.

In order to develop the model of the dependence of η_I on forward current, the SNS VCR theory was used, and it was assumed that the levels of recombination centres are located close to the centre of the forbidden band and the trap cross-sections of the electrons and holes are the same. However, as opposed to its classic description, where it is assumed that recombination centres are distributed uniformly over SCR of the symmetrical $p-n$ structure, here it was taken into account that QWs are discretely distributed in the asymmetrical structure, i.e.

11

$$F_{QW}(U) =$$

$$= \int_{-x_n}^{x_p} \frac{1}{W(U)} \cdot \frac{f_{QW}(x,U) \cdot \exp\left(-\frac{\varphi_k}{kT}\right)\left(\exp\left(\frac{qU}{kT}\right)-1\right)}{b \cdot \exp\left(-\frac{(\varphi_k - qU)}{W(U) \cdot kT}(x-x_n)\right) + \exp\left(-\left(\frac{(\varphi_k - qU)-\frac{(\varphi_k - qU)}{W(U)}(x-x_n)}{kT}\right)\right) + g} dx =$$

$$= \exp\left(\frac{-\varphi_k}{n^*(U)kT}\right) \cdot \exp\left[\frac{qU}{n^*(U)kT}-1\right]. \tag{3}$$

the recombination centres are distributed in accordance with some function $f_{QW}(x, U)$. In the general case, energy levels of point defects are distributed non-uniformly too [18], in accordance with the function $f_t(x, U)$.

With these assumptions made, the magnitude J_{QW} may be expressed as

$$J_{QW} = q\sigma N_{QWmd}(U)W(U)V_T N_d \cdot F_{QW}(U) =$$

$$= q\sigma N_{QWmd}(U)W(U)V_T N_d \times$$

$$\times \exp\left(-\frac{\varphi_k}{n^*(U)kT}\right)\left[\exp\left(\frac{qU}{n^*(U)kT}\right)-1\right] =$$

$$= J_{SQW}(U)\left[\exp\left(\frac{qU}{n^*(U)kT}\right)-1\right], \tag{2}$$

where, with the SNS model involved (Eq. 3),

Here $f_{QW}(x, U)$ is the function of QW distribution in the relatively slightly doped layer; $N_{QWmd}(U)$ is the average QW concentration in SCR depending on bias voltage U due to change in SCR width and the number of QWs in it; φ_k is the barrier potential;

$$N_{QWmd}(U) = \frac{1}{W(U)}\int_{-x_n}^{x_p} N_{QW}(x,U)dx; N_{QW}(x, U) \text{ is}$$

the QW distribution over SCR;

$$f_{QW}(x,U) = \frac{N_{QW}(x,U)}{N_{QWmd}(U)}; x_n = -\frac{W(U)\cdot N_a}{N_d + N_a};$$

$$x_p = \frac{W(U)\cdot N_d}{N_d + N_a};$$

$$W(U) = \sqrt{\frac{2\varepsilon\varepsilon_o(N_a + N_d)\cdot(\varphi_k - qU)}{qN_a N_d}} \text{ is SCR}$$

width; $b = N_d / N_a$; $g = 2n_i / N_a$; N_a and N_d are the concentrations of acceptor and donor dopants.

In the expression (3), it is assumed that the front of potential barrier at the side of the n^+ region grows linearly, therefore it is identified as $\frac{(\varphi_k - qU)}{W(U)}(x-x_n)$ in the formula; this assumption causes virtually no impact on the nature of the model.

The coefficient $n^*(U)$ is defined using the formula

$$n^*(U) = -\frac{(\varphi_k - qU)}{kT}\left[\ln(F_{QW}(U))\right]^{-1}.$$

Given the discrete nature of QW distribution, let us write the function $f_{QW}(x, U)$ as

$$f_{QW}(x,U) = \frac{N_{QW}(x,U)}{N_{QWmd}(U)} =$$

$$= \frac{\sum_i \left(\begin{array}{c} 0 \mapsto x < a_i \\ (\frac{1}{H} + \beta \cdot N_{rec}) \mapsto a_i \geq x \geq (a_i + H) \\ 0 \mapsto x > (a_i + H)\end{array}\right)}{N_{QWmd}(U)},$$

where a_i is the position of the edge of the *i-th* QW relative to the metallurgical border, H is the QW width, N_{rec} is the concentration of nonradiative centres in QW, $\beta = \sigma_{rec}/\sigma$ is the ratio of trap cross-section of nonradiative recombination centres to QW trap cross-section, $1/H$ is the coefficient from the condition $\frac{1}{H} \cdot \int_a^{a+H} dx = 1$ (for a single recombination centre).

The current of SNS non-radiative recombination in SCR depending on U is described by the expres-

sions identical to (2) and (3). Current density J_t is expressed as

$$J_t = q\sigma_t N_{\mathrm{tmd}}(U)W(U)V_T N_d F_t(U) =$$
$$= q\sigma_t N_{\mathrm{tmd}}(U)W(U)V_T N_d \times$$
$$\times \exp\left(-\frac{(\varphi_k)}{n_t^*(U)kT}\right)\left[\exp\left(\frac{qU}{n_t^*(U)kT}\right) - 1\right] =$$
$$= J_{st}\left[\exp\left(\frac{qU}{n_t^* kT}\right) - 1\right],$$

where $F_t(U)$ is the function identical to the function in (3), where the distribution function, $f_t(x, U)$, the sums of concentrations of initial, $N_{\mathrm{to}}(x, U)$, and generated (by running, radiation), $N_{\mathrm{tr}}(U)$, point defects, as well as CC trap cross-sections of defect recombination centres σ_t and σ_r therefore: $\sigma_r/\sigma_t = \gamma$, are introduced instead of QW distribution. As a result of it, $f_t(x, U) = [N_{\mathrm{to}}(x, U) + \gamma \cdot N_{\mathrm{tr}}(U)]/N_{\mathrm{tmd}}(U)$, where $N_{\mathrm{tmd}}(U)$ is the average concentration of point defects in SCR.

The exponent index coefficient $n_t^*(U)$ for $F_t(U)$ is written as

$$n_t^*(U) = -\frac{(\varphi_k - qU)}{kT}\left[\ln(F_t(U))\right]^{-1}.$$

Let us assume that radiative recombination occurs only in QW and is limited by the fraction of nonradiative flux. Therefore, it is acceptable to apply the *ABC* model for definition of η_I, and this for each *i*-th QW, since concentration of excessive CCs in QW is different at the same *U*:

$$n_{\mathrm{1QWi}} = \exp\left(\frac{\Delta E}{n_i^*(U)\cdot kT}\right)\cdot N_d \cdot \int_{-x_n}^{x_p} F_{\mathrm{1QWi}}(x,U)dx, \quad (4)$$

where $F_{\mathrm{1QW}}(x, U)$ is the (3)-type function for single QW, ΔE is energy difference of forbidden bands of barrier materials and QWs.

$$f_{\mathrm{1QW}}(x,U) = \frac{\left(\begin{array}{c} 0 \mapsto x < a_i \\ (\frac{1}{H} + \beta \cdot N_{\mathrm{rec}}) \mapsto a_i \geq x \geq (a_i + H) \\ 0 \mapsto x > (a_i + H) \end{array}\right)}{N_{\mathrm{1QWmd}}(U)},$$

and

$$N_{\mathrm{1QWmd}}(U) =$$
$$= \frac{1}{W(U)}\int_{-x_n}^{x_p}\left(\begin{array}{c} 0 \mapsto x < a_i \\ (\frac{1}{H} + \beta \cdot N_{\mathrm{rec}}) \mapsto a_i \geq x \geq (a_i + H) \\ 0 \mapsto x > (a_i + H) \end{array}\right)dx.$$

According to the three-dimensional *ABC* model, the recombination rates in the *i-th* QW are expressed by the formulae

$$R_{\mathrm{Si}}(U) = A \cdot n_{\mathrm{1QWi}}, \quad R_{\mathrm{Ri}}(U) = B \cdot n_{\mathrm{1QWi}}^2,$$
$$R_{\mathrm{Ai}}(U) = C \cdot n_{\mathrm{1QWi}}^3,$$

where $R_{\mathrm{Si}}(U)$, $R_{\mathrm{Ri}}(U)$ and $R_{\mathrm{Ai}}(U)$ are the recombination rates of SRH, zone-zone and Auger mechanisms in the same *i*-th QW respectively; *A, B* and *C* are the *ABC* model coefficients. With that, the principle of equality of recombination fluxes as per SNS and the *ABC* model shall be met.

The QW regions are essentially two-dimensional. Therefore, concentration of excessive CCs calculated using (4) and measured in cm^{-3} for QW shall be assumed equal to two-dimensional concentration of CC, i.e. (4) shall be multiplied by QW width *H* and the coefficients *A, B* and *C* shall be normalised to the two-dimensional *ABC* model [19]. Then η_I depending on concentration of excessive charge carriers in QWs may be expressed by the formula

$$\eta_I = \frac{B \cdot \sum_i \left(Hn_{\mathrm{1QWi}}\right)^2}{\left[A \cdot \sum_i \left(Hn_{\mathrm{1QWi}}\right) + J_t/q\right] + \\ + B \cdot \sum_i \left(Hn_{\mathrm{1QWi}}\right)^2 + C \cdot \sum_i \left(Hn_{\mathrm{1QWi}}\right)^3}, \quad (5)$$

where the *A, B, C* coefficients correspond to the two-dimensional model.

The dependence of η_I on current is defined by dependence of excessive concentration on current and the dependence of external quantum efficiency *L* on *J* is described as

$$L(J) = \alpha \cdot \frac{J}{q} \cdot \eta_I.$$

In (5), nonradiative recombination rate in barriers between QWs is expressed by the relation $J_t/q = A_t \cdot n_t$, where A_t is the *ABC*-model coefficient for the SRH recombination mechanisms in regions between QWs and n_t is effective concentration

Table 1. LED Model Parameters

Sample of LED	Donor concentration, N_d, cm^{-3}	Acceptor concentration, N_a, cm^{-3}	QW width, nm	Barrier width, nm	Position of the first QW, a_1, nm
B (5 QWs)	$2 \cdot 10^{19}$	$7 \cdot 10^{18}$	3.0	12	5.2
G (5 QWs)	$2 \cdot 10^{19}$	$8 \cdot 10^{17}$	3.0	12	4.5
R (8 QWs)	$2 \cdot 10^{18}$	$8 \cdot 10^{17}$	2.5	7.5	2.0

Table 2. Model Coefficients *A, B, C* and Parameters of the Dependences η_I for Initial LED Samples

Sample of LED	A, s^{-1}	B, cm$^2 \cdot$s^{-1}	C, cm$^4 \cdot$ s^{-1}	n_{max}, cm^{-2} at 300 K (model)	I_{max}, A		η_{Imax}	
					$T = 300$ K	$T = 373$ K	$T = 300$ K	$T = 373$ K
B (5 QWs)	$1 \cdot 10^4$	$8 \cdot 10^{-6}$	$1 \cdot 10^{-15}$	$1.5 \cdot 10^8$	$7.1 \cdot 10^{-5}$	$1.3 \cdot 10^{-3}$	1.0	0.93
G (5 QWs)	$3 \cdot 10^4$	$8 \cdot 10^{-6}$	$4 \cdot 10^{-19}$	$9 \cdot 10^{12}$	$7.2 \cdot 10^{-4}$	$1.0 \cdot 10^{-2}$	1.0	0.94
R (8 QWs)	$8 \cdot 10^6$	$4 \cdot 10^{-5}$	$8 \cdot 10^{-20}$	$1 \cdot 10^{13}$	$4.6 \cdot 10^{-2}$	$2.5 \cdot 10^{-1}$	1.0	0.90

of CCs at an energy level $(\varphi_k - qU)/(n_t^* k)$ (effective level of CC flow to the recombination region).

CONCLUSION

The presented model was tested by exposure to temperatures ranging between –200 K and 500 K and neutron Φ ranging between 10^6 and 10^{15} cm^{-2}, by degree of QW region doping ranging between $1 \cdot 10^{17}$ and $7 \cdot 10^{18}$ cm^{-3} as well as by QW coordinates and width. The model dependences η_I without consideration of the fourth member of $f(n)$ in (1) are presented in the Figs. 1b and 2b. The model parameters are summarised in Table 1. The parameters of semiconductors for the models were taken from [20].

The variations of the model parameters have shown that the dependence of η_I on current is primarily influenced by QW position relative to the metallurgical border, degree of doping of the *p* and *n* regions, initial width of SCR and depth of QWs. To the lesser extent the position of the maximum η_I and its values are influenced by QW width.

In order to obtain satisfactory fit of the results of modelling of η_I, the coefficients of the two-dimensional *ABC* model [19] were selected and the features of interaction between neutrons and semiconductors were taken into account: cross-section of neutron and atom interaction, formation of tracks, etc. Concentration of point defects formed by neutrons was calculated using the formula [21, p. 27].

$$N_{tr} = \Phi N_i \sigma_d \overline{v},$$

where Φ is the neutron fluence, N_i is the number of atoms in a unit of semiconductor volume, σ_d is the collision cross-section, $\overline{v}$ is the average number of shifted atoms per one primarily displaced atom.

$\overline{v}$ equals approximately to $3 \cdot 10^2$ per one incident neutron. Since neutron collides with the atom core, σ_d is taken approximately equal to $1 \cdot 10^{-24}$ cm^2. The disordering area after collision between a neutron and a primary atom is about (50–60) nm [21].

The model coefficients *A, B* and *C* for the two-dimensional *ABC* model are presented in Table 2. For the red LED (*R*), modelling was not conducted in the case of neutron irradiation at $\Phi = 1 \cdot 10^{15}$ cm^{-2} due to significant reduction of η_I which is apparently related to formation of tunneling current due to formation of large disordering areas comparable with QW repetition period.

In Table 2, n_{max} and I_{max} are the values of excessive concentration of CC and current at the maximum value of η_I (η_{Imax}) normalised to one.

The rate of nonradiative SRH recombination and, therefore, the coefficients *A* and A_t are largely influenced by degree of perfection of QW crystal structure [4].

The main conclusions are the next:

1. The physical and mathematical model of dependence of internal quantum efficiency of QW LED on current was developed using the SRH and *ABC* recombination models; the QW distribution function was introduced in the SNS model and the *ABC* model was applied for identification of rates of radiative and nonradiative recombination in QWs.

2. Due to low QW width, to calculated their recombination rate using the *ABC* model, it is necessary to use the numeric value of CC concentration as two-dimensional concentration of excessive charge carriers and the relevant coefficients *A, B* and *C* normalised to the two-dimensional model.

ACKNOWLEDGMENTS

REFERENCES

1. Nakamura, S., Iwasa, M.S. Method of manufacturing p-type compound semiconductors // Patent N5306662. Apr.1994. Japan.

2. Amano, H., Akasaki, I. et.al. Method for producing a luminous element of III-group nitride. Patent #5496766. Mar. 1996. Japan.

3. Mamakin, S.S., Yunovich, A.E., Vattana, A.B., Manyakhin, F.I. Electric Properties and Fluorescence Spectra of LED's Based on InGaN/GaN Heterojunctions with Modulated and Doped Quantum Wells [Elektricheskiye svoystva i spektry luminestsentsii svetodiodov na osnove geteroperekhodov InGaN/GaN s modulirovanno-legirovannymi kvantovymi yamami] // FTP, 2003, Vol. 37, # 9, pp. 1131–1137.

4. Voytsekhovsky, A.V., Nesmelov, S.N., Kulchitsky, N.A., Melnikov, A.A. The Influence of Dislocations on Internal Quantum Efficiency of Light-Emitting Structures Based on InGaN/GaN Quantum Wells [Vliyaniye dislokatsiy na vnutrennyuyu kvantovuyu effektivnost svetoizluchayushchikh struktur na osnove kvantovykh yam InGaN/GaN] // Nano i mikrosistemnaya tekhnika, 2011, Vol. 8η_I, pp. 27–35.

5. Shim, J.-I., Shin, D.-S. Measuring the internal quantum efficiency of light-emitting diodes towards accurate reliable room-temperature characterization // Nanophotonics, 2018, September, pp. 1–15.

6. Zang, M., Bhattacharya, P., Singh, J., Hinckley, J. Direct measurement of auger recombination in $In_{0.1}Ga_{0.9}N/$GaN quantum well and its impact on the efficiency in $In_{0.1}Ga_{0.9}N/$GaN multiply uantum well light emitting diodes // Appl. Phys. Letter, 2009, Vol. 95, # 20, pp. 1108.

7. Dai, Q., Shan, Q., Wang, J., Chhajed, S., Cho, J.M., Shubert, E.F., Crawford, M.H., Koleske, D. D., Kim, M.-H., Park, Y. Carrier recombination mechanisms and efficiency droop in GaInN/GaN light-emitting diodes // Appl. Phys. Letter, 2010, Vol. 97, # 13, pp. 3507.

8. David, A., Grundmann, M.J. Droop in InGaN light-emitting diodes: A differential carrier lifetime analysis // Appl. Phys. Letter, 2010, Vol. 96, # 10, pp. 3504.

9. David, A., Hurni, C.A., Young, N.G., Craven, M.D. Electrical properties of III-nitride LEDs recombination-based injection model and theoretical limits to electrical efficiency and electroluminescent cooling // Appl. Phys. Letter, 2016, Vol. 109, # 8, pp. 3501.

10. Hopkins, M.A., Allsopp, D.W.E., Kappers, M.J., Oliver, R.A., Humpreys, C.J. The ABC model of recombination reinterpreted: Impact on understanding carrier transport and efficiency droop in InGaN/GaN light emitting diodes // J. Appl. Phys. 2017, Vol. 122, # 23, pp. 4505.

11. Bochkaryova, N.I., Rebane, Yu.T. Shreter, Yu.G. Growth of Shockley-Reed-Hall Recombination Rate in InGaN/GaN Quantum Wells as the Major Mechanism of Loss of LED Efficiency at High Injection Levels [Rost skorosti rekombinatsii Shokli-Rida-Holla v kvantovykh yamakh InGaN/GaN kak osnovnoy mekhanizm padeniya effektivnosti svetodiodov pri vysokikh urovnyakh inzhektsii] // FTP, 2015, Vol. 49, # 12, pp. 1714–1719.

12. Prudaev, I.A., Skakunov, M.S., Lelekov, M.A., Ryaboshtan, Yu.L., Gorlachuk, P.V., Marmalyuk, A.A. Recombinant Currents in LEDs Based on Multiple Quantum Wells $(Al_xGa_{1-x})_{0.5}In_{0.5}P/(Al_yGa_{1-y})_{0.5}In_{0.5}P$ [Rekombinatsyonnyye toki v svetodiodakh na osnove mnozhestvennykh kvantovykh yam (AlxGa1-x)0.5In0.5P/(AlyGa1-y)0.5In0.5P] // Izvestiya vuzov. Fizika, 2013, Vol. 56, # 8, pp. 44–47.

13. Sah C.T., Noyce R.N., Shockley W. Carrier Generation and Recombination in P-N Junctions and P-N Junction Characteristics // Proc. IRE, 1957, Vol. 45, pp. 1228–1243.

14. Choo, S.C. Carrier generation-recombination in the space-charge region of an assymmetrical p-n junction // Solid State Electronics,1968, Vol. 11, pp. 1069–1077.

15. Fedor I. Manyakhin, Arthur B. Vattana, and Lyudmila O. Mokretsova Application of the Sah-Noyce-Shockley Recombination Mechanism to the Model of the Voltage-Current Relationship of LED Structures with Quantum Wells// Light & Engineering Journal, 2020, Vol. 28, #5, pp. 31–38.

16. Goryunov, N.N., Manyakhin, F.I., Klebanov, M.P., Lukashev, N.V. Impulse Three-Frequency Method of Measurement of Charged Centre Parameters in the Space Charge Region of Semiconductor Structures [Impulsnyy tryokhchastotnyy metod izmereniya parametrov zaryazhennykh tsentrov v oblasti prostranstvennogo zaryada

poluprovodnikovykh struktur] // Pribory i sistemy upravleniya, 1999, Vol. 10, pp. 46–49.

17. Shockley, W. The Theory of p – n Junctions in Semiconductors and p-n Junction Transistors // Bell Syst. Tec. J. 1949, Vol. 28, pp. 435–489.

18. Abdullaev, Zh.S., Gusev, M. Yu., Zyuganov, A.N., Torchinskaya, T.V. Parameters of Deep Centres in AlGaAs LEDs Evaluated by Capacity and Injection Spectroscopy Methods [Parametry glubokikh tsentrov v svetodiodakh AlGaAs otsenyonnyye metodami emkostnoy i inzhektsionnoy spektroskopii] // Ukr. Phys. Journal. 1989, Vol. 34, # 8, pp. 1220–1224.

19. Voytsekhovky, A.V., Gorn, D.I. Recombination Mechanisms in InGaN/GaN Structures with Quantum Wells at High Levels of Excitation [Mekhanizmy rekombinatsii v strukturakh InGaN/GaN s kvantovymi yamami pri vysokikh urovnyakh vozbuzhdeniya] // Izvestiya vuzov. Fizika, 2015, Vol. 58, # 8/2, pp. 171–173.

20. NSM Archive. Physical Properties of Semiconductors. URL: http://www.ioffe.rssi.ru/SVA/NSM/Semicond/ (reference date: 28.02.2020).

21. Ladygin, E.A. The Effect of Ionising Radiation on Electronic Equipment [Deystviye pronikayushchey radiatsii na izdeliya elektronnoy tekhniki]. Moscow: Sovetskoye radio, 1980, 224 p.

Fedor I. Manyakhin,
Doctor of Physical and Mathematical Sciences, Professor. In 1973, he graduated from the Moscow Institute of Electronic Engineering (MIEM). At present, he is a Professor of the Automatic Design sub-department of NITU MISIS, author and co-author of more than 150 publications, awarded with the diploma of the Ministry of Education and Science of Russia, prize winner of the Golden Names of Higher Education 2018 contest in nomination of Contribution to Science and Higher Education. His research interests: semiconductor electronics, physics of semiconductor devices

Lyudmila O. Mokretsova,
Associate Professor, Ph.D. in Technical Sciences. In 1978, she graduated from the Moscow Institute of Steel and Alloys (MISIS). At resent, she is Associate Professor of the Automatic Design sub-department of NITU MISIS, prize winner of the Golden Names of Higher Education 2018 contest in nomination of Introduction of Innovative Teaching Techniques. Her research interests: 3D modelling in light design

A STUDY ON THE SAFETY AND PARAMETERS OF POWER DIRECT LED LAMP
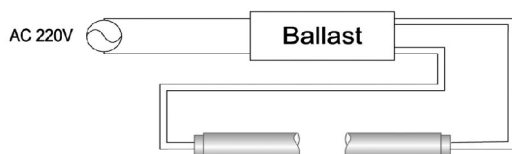
Jin-Tai Kim[1] and Chung-hyeok Kim[2]

[1]*Korea Testing and Research Institute*
[2]*Ingenium College of Engineering, Kwangwoon University*
E-mail: bighhs@naver.com

ABSTRACT

As energy problems emerge, high-efficiency lighting devices that can replace conventional lighting are required to save energy, and among them, LED (light emitting diode) lighting has begun to emerge as the next-generation lighting. Since LED has low power, high efficiency, long lifetime, and fast response speed, it is suitable to replace existing lighting such as incandescent lamps, fluorescent lamps, and halogen lamps. The present study proposes safety of household appliances to prevent a degraded replacement effect due to excessive luminous flux of an LED lamp that replaces a bending-type fluorescent lamp (FPL), to prevent excessive design investment for manufacturers by providing appropriate optical reference values, to identify safety issues during the installation of AC power direct LED lamps, and to standardize the optimal power supply method that can be fixed by using the LED lamp based on external converters and the LED lamp for fluorescent lamp replacement.

Fig. 1. Fluorescent lamp replacement type LED lamp – built-in converter type (the certified lamps and ballasts for fluorescent lamps can be used without modification)

Keywords: LED luminaire, LED lighting, safety standards for electrical appliances, electrical appliances safety standards in Korea, electrical safety management, safety certification, ballast, power direct, power supply, connection method

1. INTRODUCTION

1.1. Background of the Present Study

The LED lighting market has rapidly appeared due to the rapid growth of the green energy business since 2009. Furthermore, to meet the demand for energy saving, LED light sources are being replaced by traditional light sources with low energy efficiency. The light source has evolved from candles in the past, to incandescent lamps, fluorescent lamps, and LED lamps.

LED light sources have been replacing fluorescent lamps, and related luminaire are appearing in the market. In particular, the fluorescent replacement LED lamps have been actively developed to increase energy efficiency and reduce the use of mercury for environmentally friendly factors. Fluorescent lamps have been used most often in homes, offices, and industrial facilities, and recently, G13 cap's linear-type LED lamps are actively being used.

Furthermore, safety standards have been recently enacted (14.4.30) for LED lamps and linear-type LED lamps, which can replace the conventional FPL fluorescent lamps (FPL) used in homes in Korea, and certified to be distributed and commercialized.

Table 1. FPL LED Lamp Safety Standard (KC10025)

Item	Linear type (G13 cap)		FPL type (2G11 cap)	
Shape				
Power, W	20, 32, 40		36, 55	
Luminous flux standard	20 W	1100 lm → 858 lm	36 W	2590 lm → 2202 lm
	32 W	2300 lm (simulation)	55 W	4000 lm → 3400 lm
Note	The calculated luminous flux is 85 % of the luminous flux standard of KS C7601 (fluorescent lamp)			

There are different types of LED lamps. The first type is shown in Fig. 1 and it is the so-called G13/2G11 cap-shaped fluorescent lamp replacement LED lamp-built in converter, which only uses LED lamps. The second type is G13 linear type with an external converter, as shown in Fig. 2. The final type of LED lamp is shown in Fig. 3, where 220 V commercial power is supplied to the LED lamp caps of the linear type with a G13 cap and the FPL type with a 2G11 cap. [1]

Criteria for the optical characteristics of the linear type LED lamp can be found in the safety standards (KC) for the conventional fluorescent lamp replacement type LED lamp–built-in converter and the linear type LED lamp–external converter. Furthermore, the criteria for the linear type FPL LED lamps are only discussed in the safety standards of the conventional fluorescent lamp replacement type LED lamp–built-in converter (KC10025). However, as shown in Table 1, because the suggested value is defined as 85 % or higher of the standard value of the fluorescent lamp (KS C7601), rather than the actual measurement data, research needs to be conducted to determine whether fluorescent lamps can be replaced by those LED lamps or not. [2]

The fluorescent lamp replacement LED lamp can save time and money by using existing luminaires for fluorescent lamps without modification. Therefore, compared to the case where new LED luminaires need to be installed, the burden for the installation can be relatively reduced and the existing luminaires for fluorescent lamps can be recycled without discarding them. Therefore, these luminaires have three main advantages: high efficiency, long lifetime, and eco-friendliness.

The linear type lamps are classified as:

1. The fluorescent lamp (1200 mm 32 W, 36 W, 40 W);

2. The LED lamp-external converter;

3. The fluorescent lamps replacement type (ballast compatible);

4. The power direct-type LED lamp.

Among them, the first, second, and third can be certified through the KC certification by the National Institute of technology and standards, but the forth (the power direct-type LED lamp) has not been certified due to the lack of safety items to be tested, such as standardization of the power system when a LED lamp is used with conventional lamps and fluorescent light bulbs having the same shape as the LED lamp. As a result, due to the lack of certification standards, the demand for certification by Korean companies is increasing rapidly.

When direct-type LED lamps are supplied, it is expected that problems such as fire, electric shock, and burning accidents may arise due to misuse of lamps with different power supply methods. Therefore, this paper will study and analyse the problems

Converter: a device for operating LED (AC input–DC output)
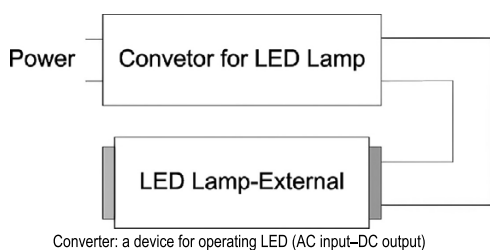
Fig. 2. Linear LED lamp – external converter type (an LED converter and an LED lamp with AC/DC50 V or lower)
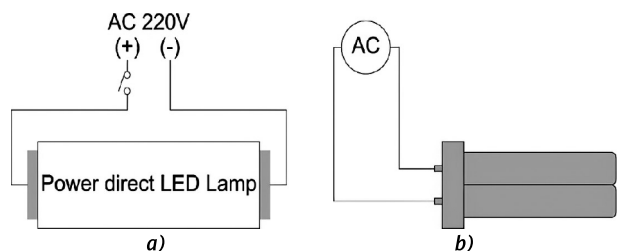

Fig 3. Power direct LED lamp (a) and FPL lamp (b) (this is a 220 V direct input method, where a converter and an LED lamp are integrated)
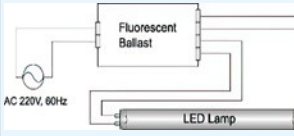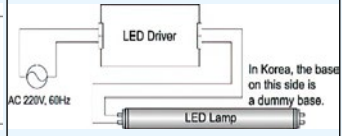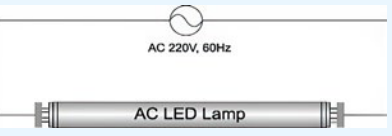
Table 2. Linear LED Lamp Certification Status

Method	Compatible ballast	External convertor	220 V power direct
Circuit			
Manufacturer	20 companies	300 companies	No certified companies exist *foreign manufacturing companies cannot sell in Korea
Standard trend	Established in 2/25/2013	Established in 12/21/2010	–
Standard number	KC10025 (G13 base)	KC20001 (G13 and D12 bases)	–
International standard	IEC62776 (G13 and G5 bases)	IEC62931 (GX16t-5 base)	–

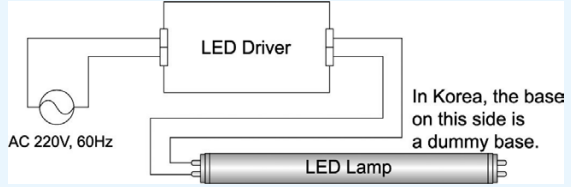**Table 3. Linear LED Lamp – External Converter Type**

Lamp type (date of notice on safety standards)	LED converter and LED lamp below AC/DC 50 V used ⇒ (Notice of Electrical Appliances Safety Standards: 2010.12.21)
Structure	

Table 4. Fluorescent Lamp Replacement Type LED Lamp – Built-in Converter Type

Lamp type (date of notice on safety standards)	Certified luminaires and ballasts for fluorescent lamps are used without modification ⇒ (Notice of Electrical Appliances Safety Standards: 2013.03.25)
Structure	
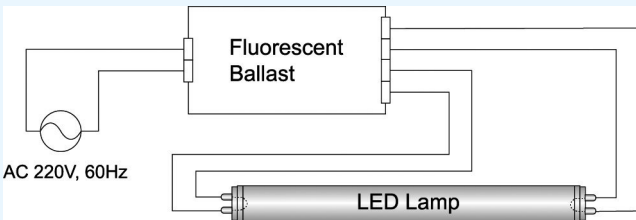
of the conventional fluorescent lamps and the expected problems in the actual use of those lamps, which are summarized in Tables 2, 3 and 4.

Furthermore, safety standards for electrical appliances (KC) will be established to ensure that safe and high-quality products are distributed, and consumers can use safe products.

Therefore, with this study, it is possible to derive the safety problems that can occur when the direct-type LED lamp, which is shown in Table 4, is attached to the conventional fluorescent lamp and the luminaires shown in Table 2 and Table 3, and

to ensure safety when using them together by standardizing the optimum power supply method. Furthermore, the conventional FPL fluorescent lamps are mounted on a luminaire, and the lamp power, luminous flux, and illuminance are measured and analysed to study optimized optical characteristics that can replace the conventional lamps, based on which the domestic electrical appliance safety standards (KC) will be proposed.

Table 5 shows the connection circuit for the power direct LED lamp, which will be analysed in this work.
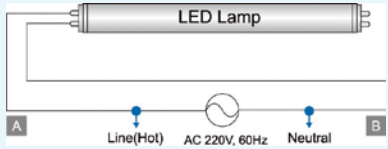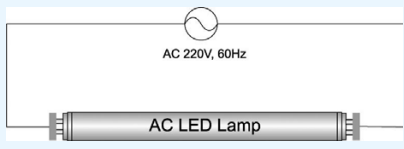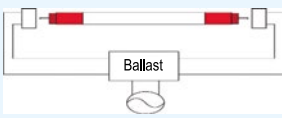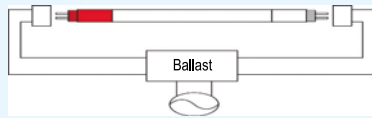
Table 5. Power Direct LED Lamp

Lamp type (date of notice on safety standards)	220 V direct input method is used and a converter and an LED lamp are integrated ⇒ Absence of safety standards	
Structure	Input in one side	Input in both sides

Table 6. Direct Power LED Lamp Cross Table

Item	Power direct LED lamp	
	Connection method 1	**Connection method 2**
Luminaires for fluorescent lamp / LED lamp for replacing a fluorescent lamp with a built-in converter		
LED Lamp-external converter type		
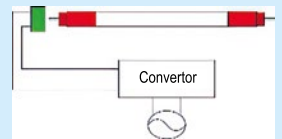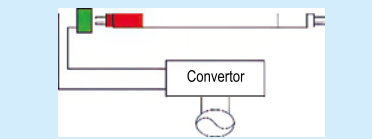
2. MATERIALS AND METHODS

This study analyses the risks when the power direct-type LED lamps are installed in the conventional luminaires for fluorescent lamps and LED lamp built-in converter type and LED lamp-external converter, which are shown in Table 6, for safety investigation. Furthermore, as shown in Table 7, the risks are analysed when the LED lamp-external converter is installed in the existing luminaires for fluorescent lamps and luminaires for power direct-type LED lamps, and as shown in Table 8, the risks are analysed when the fluorescent lamps and fluorescent lamp replacement LED lamps are installed in luminaires for the LED lamp-external converter and luminaires for the power direct-type LED lamps.

Based on the analyses, problems such as compatibility, electric shock, and fire risk were derived:

1. The products that were certified by KC10025 (fluorescent lamp replacement type LED lamp-built-in converter) were analysed and the suitability for the specified luminous flux was confirmed as shown in Table 1;

2. The revised proposal was made by comparing and analysing the luminaire parameters for three FPL 36 W lamps with fluorescent lamps and LED lamps respectively;

3. The revised proposal was made by comparing and analysing the luminaire parameters for three FPL 55 W lamps with fluorescent lamps and LED lamps respectively to propose safety standards.

In addition, the reason why a luminaire with three FPL lamps was used for testing is that this type of luminaire is most common in household applications.

The optical properties were measured in accordance with Annex B of IEC60901: Single-capped fluorescent lamps–Performance specifications and illuminance simulations were analysed with a Goniophotometer (LMT, Germany) in accordance with Annex A of KS C8000: General rules for lighting equipment. The lighting method of the luminaire was measured by connecting the test ballast specified in KS C7601 (fluorescent lamp) standard as shown in
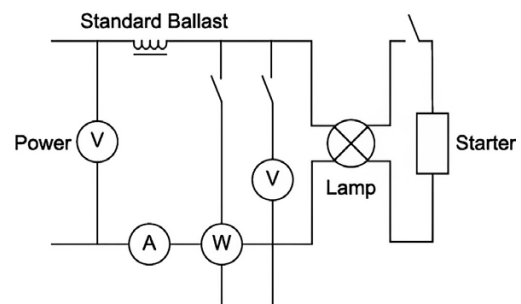

Fig. 4. Test circuit
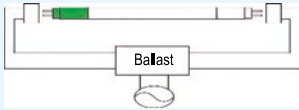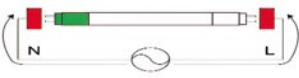
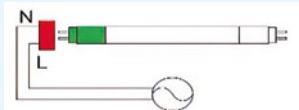**Table 7. Converter External LED Lamp Cross Table**

Item	LED lamp-external converter type	Note
Luminaire for fluo-rescent lamp		–
Luminaire for power direct LED lamp		Connection method 1
		Connection method 2

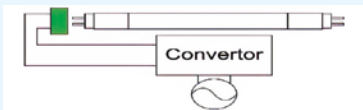**Table 8. Fluorescent Lamp and LED Lamp Built-In Converter Type Cross Table**

Item	Fluorescent lamp	LED lamp built-in converter	Note
Luminaire for LED lamp-external con-verter type			–
Luminaire for power direct LED lamp			Connection method 1
			Connection method 2
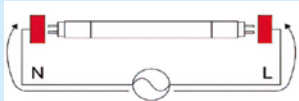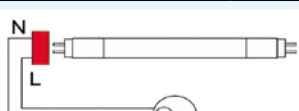
Table 9. Certified Product Analysis Results

Parameter	Unit	FPL 36 W			FPL 55 W	
		Fluorescent lamp		LED lamp	Fluorescent lamp	LED lamp
		A	B			
Luminous flux	lm	5410	5733	6558	8295	9948
Luminaire power	W	91	101	54	159	94
Luminous efficacy	lm/W	59.5	57.0	121.4	52.2	105.8
Floor surface average illuminance	lx	150	161	215	218	319

Table 10. Comparison Characteristics of FPL 36 W Fluorescent Lamp with LED Lamp

Parameter	Unit	Luminaire for three FPL 36 W lamps	
		Fluorescent Lamp	LED Lamp
Luminous flux	lm	5733	4967 (1902)
Luminaire power	W	101	42 (14)
Luminous efficacy	lm/W	57.0	117.9
Floor surface average illuminance	lx	161	160

Table 11. Comparison Luminaire Characteristics with FPL 36 W Fluorescent Lamp and LED Lamp

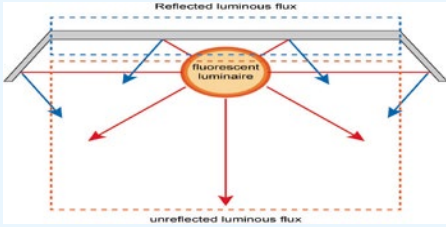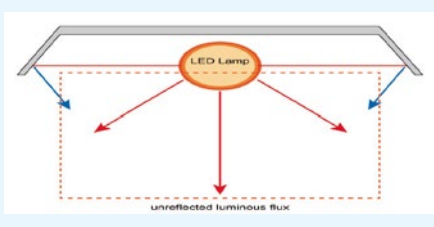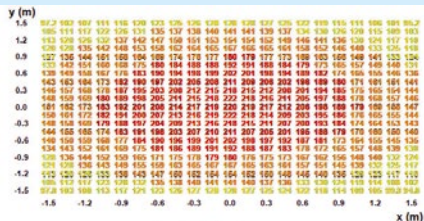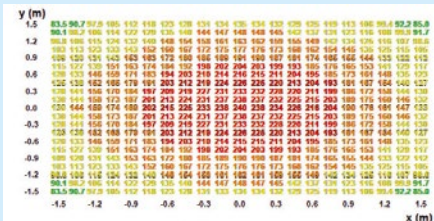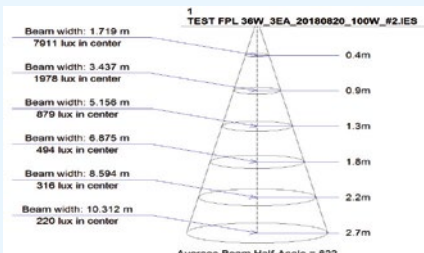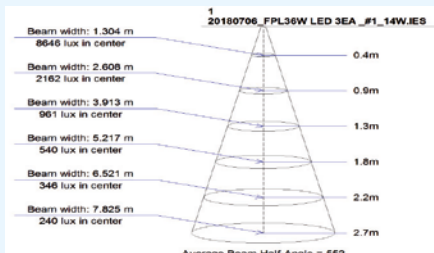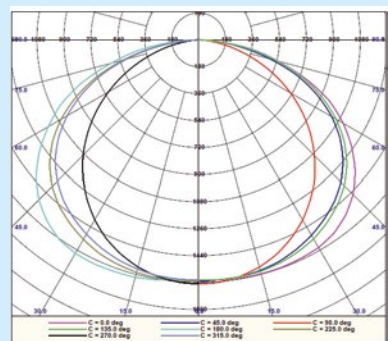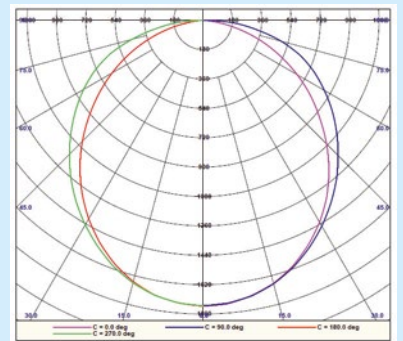| Type / Item	Luminaire for fluorescent lamp (FPL 36 W×luminaire for three lamps)	LED luminaire (FPL 14 W×luminaire for three lamps)
Luminaire Operation conceptual diagram	Reflected luminous flux / fluorescent luminaire / unreflected luminous flux	LED Lamp / unreflected luminous flux
Illuminance distribution	Horizontal Illuminance. All illuminance values in lux. Table Average: 161 Table Maximum: 222 Table Minimum: 94.8 Mounting Height = 2.7 m	Horizontal Illuminance. All illuminance values in lux. Table Average: 160 Table Maximum: 240 Table Minimum: 83.5 Mounting Height = 2.7 m
Illuminance	TEST FPL 36W_3EA_20180820_100W_#2.IES. Beam width: 1.719 m / 7911 lux in center (0.4m); Beam width: 3.437 m / 1978 lux in center (0.9m); Beam width: 5.156 m / 879 lux in center (1.3m); Beam width: 6.875 m / 494 lux in center (1.8m); Beam width: 8.594 m / 316 lux in center (2.2m); Beam width: 10.312 m / 220 lux in center (2.7m). Average Beam Half-Angle = 62°	20180706_FPL36W LED 3EA_#1_14W.IES. Beam width: 1.304 m / 8646 lux in center (0.4m); Beam width: 2.608 m / 2162 lux in center (0.9m); Beam width: 3.913 m / 961 lux in center (1.3m); Beam width: 5.217 m / 540 lux in center (1.8m); Beam width: 6.521 m / 346 lux in center (2.2m); Beam width: 7.825 m / 240 lux in center (2.7m). Average Beam Half-Angle = 55°
Distribution curve (of luminous intensity)	C = 0.0 deg; C = 45.0 deg; C = 90.0 deg; C = 135.0 deg; C = 180.0 deg; C = 225.0 deg; C = 270.0 deg; C = 315.0 deg	C = 0.0 deg; C = 90.0 deg; C = 180.0 deg; C = 270.0 deg

Fig. 4, and measurements were made in a darkroom at 25 °C ± 1 °C. [3]

3. TEST RESULTS

For cross-sectional analysis, safety studies were conducted for two connection methods (the first method and the second method), as shown in Table 8, and the measurement results according to IEC60901 and KS C8000 are as follows.

Product analysis showed that replacing the fluorescent lamp FPL 36 W with a KC10025 certified commercially produced LED lamp with a built-in current converter provides a higher illuminance value of 65 lx while reducing power consumption by 47 W, as shown in Table 9. In addition, if the fluorescent lamp FPL 55 W was replaced with an LED one, the illuminance level increased by 101 lx, and the power consumption decreased by 65 W. Based on this, it can be concluded that the luminous flux of LED lamps exceeds the regulated values specified in the standard, so they need to be modified. [2]

The result of a comparative analysis of an EX-D fluorescent lamp (daylight) and an LED lamp in a three-dome luminaire designed for FPL 36 W lamps is as follows: each light source was turned on at the

Table 12. Comparison Characteristics of FPL 55 W Fluorescent Lamp with LED Lamp

Parameter	Unit	Luminaire for three FPL 55 W lamps	
		Fluorescent lamp	LED lamp
Luminous flux	lm	8295	6898 (3217)
Luminaire power	W	159	70 (23)
Luminous efficacy	lm/W	52.2	98.8
Floor surface average illuminance	lx	218	219

Table 13. Comparison Luminaire Characteristics with FPL 55 W Fluorescent Lamp and LED Lamp
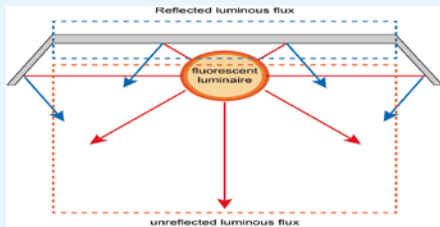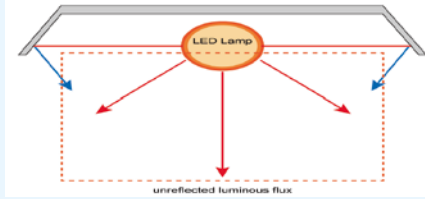

Type / Item	Luminaire for fluorescent lamp (FPL 55 W×luminaire for three lamps)	LED luminaire (FPL 23 W×luminaire for three lamps)
Luminaire Operation conceptual diagram		
Illuminance distribution		
Illuminance		
Distribution curve (of luminous intensity)		

Table 14. Connection Diagram Suggestion

Connection	Connection diagram
Connection method 1	Example power (1–3), dummy (2–4) or power (1–4), dummy (2–3) L N AC 220V, 60Hz
Connection method 2	Example power (1–2), dummy (3–4) N L AC 220V, 60Hz

Table 15. Safety Inspection of Luminaires for Fluorescent Lamp and Direct Power LED Lamp

Safety product combination	Luminaire for fluorescent lamp	
	Power direct LED lamp	
	Luminaire for fluorescent lamp + Power direct LED lamp	
	Test setup	

same area in a certain space, the illuminance from the fluorescent lamp and the average illuminance from the LED lamp were evaluated under the same conditions, and the luminous flux was calculated and analysed, as shown in Tables 10 and 11.

As a result of the analysis, the luminous flux of the LED lamp was 1902 lm, and the power was 14 W at the same average illuminance. Compared to the current standard of 2202 lm shown in Table 1, it should be reduced by about 300 lm. [4]

Below are the results of a comparative analysis of EX-D fluorescent lamps (daylight) and led lamps in a three-column lamp designed for 55 W FPL lamps.

After each light source was turned on under the same conditions in the same space as in the actual

test, the point at which the illuminance from the fluorescent lamp and the led lamp are identical was evaluated, and the appropriate luminous flux was calculated and analysed. The results are shown in Tables 12 and 13.

As a result of the analysis, it was found that the luminous flux of the LED lamp was 3217 lm at the same average illuminance, and the power was 23 W. In comparison with the current standard, the value of the luminous flux should be reduced to 183 lm. [4]

A detailed connection diagram is shown in Table 14.

As a result of the cross-analysis of the luminaire for fluorescent lamp and the power direct LED

**Table 16. Safety Inspection of Luminaires for Direct Power LED Lamp and Fluorescent Lamp
(LED Lamp Built-In Converter)**

Safety product combination	Fluorescent lamp, LED lamp built-in converter	
	Luminaire for power direct LED lamp	
	Fluorescent lamp, LED lamp built-in converter + Luminaire for power direct LED lamp	
	Test setup	
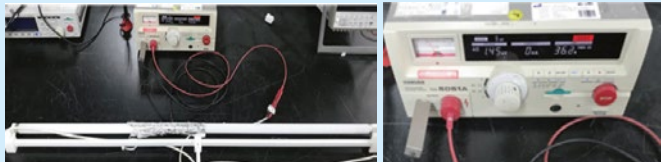
lamp, the connection method 1 was working well and no safety problem was found. However, in the case of connection method 2, the lamp was damaged and flickered, resulting in a risk of electric shock and fire. The results of safety inspection in this case are shown in Table 15.

In the case of the connection method 1, where the luminaire for the power direct LED lamp and the fluorescent lamp were used, the lamp did not turn on and there were no safety problems occurred, and after the testing, the safety can be ensured for fluorescent lamps, as shown in Table 16. However, in the case of connection method 2, all the fluorescent lamps were damaged, resulting in the safety and electric shock problems of the lamp.

As a result of the cross test of the combination of LED lamp built-in converter and luminaire for the power direct LED lamp, the connection method 1 did not turn on the lamp and there were no safety problems occurred on the lamp and luminaire, while in case of the connection method 2, some LED lamps built-in converter were damaged, there was a safety problem occurred, and electric shock and fire risk problems were identified.

As a result of the cross test of the combination of the luminaire for power direct LED lamp and the LED lamp-external converter, the connection method 1 did not turn on the lamp, and after the testing, the lamps were normally turned on and no de-

fects or safety problems were found, as shown in Table 17.

However, in case of connection method 2, the LED lamp- external converter was damaged, smoke was generated, and a safety problem was found.

The cross-analysis of the luminaire for LED lamp-external converter and the power direct LED lamp showed that the lamps did not turn on for both connection methods. As shown in Table 18, no damages or safety problems were found, and the lamps turned on properly after the test.

4. DISCUSSION

In this study, the comparative analysis of the LED lamps, which can potentially replace the FPL 36 W and 55 W fluorescent lamps using the 2G11 cap, was conducted. Since the level of technology at the time when the existing safety certification was carried out is very different from what is currently happening, since the efficiency of the LED chip and driving part is rapidly improving due to the technology development of related companies, there is a need to revise the relevant standards in accordance with the realistic standards.

As a result of the cross-analysis according to the connection method 2 using the power direct LED lamp, the LED lamp built-in converter, the LED lamp-external converter, and the fluorescent lamp

Table 17. Safety Inspection of Luminaire for Direct Power LED Lamp and Converter External LED Lamp

Safety product combination	Luminaire for direct power LED lamp	
	LED lamp – external converter	
	Luminaire for direct power LED lamp + LED lamp external converter	
	Test setup	
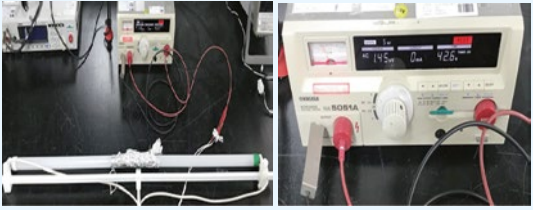
Table 18. Safety Inspection of Luminaire for Converter External LED and Direct Power LED Lamp

Safety product combination	Power direct LED lamp	
	Luminaire for LED lamp – external converter	
	Luminaire for LED lamp – external converter + Power direct LED lamp	
	Test Setup	
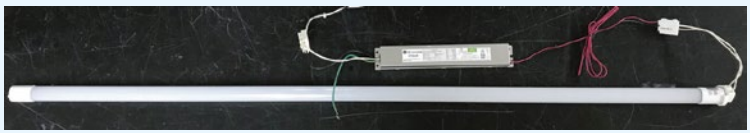
were damaged serious safety problems occurred, as shown in Table 19. On the other hand, the power direct-type LED lamp in connection method 1 can ensure safety without any problem such as fire, electric shock, burns even when used with different luminaires and lamps. Furthermore, to prevent a decrease in energy efficiency due to excessively luminous flux, it is necessary to revise the relevant standards to a suitable level. The standards are proposed in Table 20.

In other words, it is necessary to redefine relevant standards to use safe products, and the suggested connection method is shown in Table 21.

Further research will be required in the future to evaluate the safety and performance of the power direct type of luminaire and lamp.

Table 19. Cross-Risk Analysis Table

	Power direct LED lamp	LED lamp built-in converter	LED lamp-external convertor	Fluorescent lamp
Luminaire for power direct LED lamp		Risk ↑	Risk ↑	Risk ↑
Luminaire for fluorescent lamp	Risk ↓		Risk ↓	
Luminaire for LED lamp-external convertor	Risk ↓	Risk ↓		Risk ↓

Table 20. Proposed Safety Standards

Standard	Unit	FPL 36 W LED Lamp	FPL 55 W LED Lamp
KC10025	lm	2202 (85 % of KS standard)	3400 (85 % of KS standard)
Proposed standard	lm	1900 (74 % of KS standard)	3200 (80 % of KS standard)

Table 21. Direct Power LED Lamp Power Supply Connection Method

Double Cap LED Lamp		Cap
Power	Dummy	
1, 2 or 1, 4	2, 4 or 2, 3	G13, G5
2, 3 or 2, 4	1, 4 or 1, 3	

ACKNOWLEDGEMENT

REFERENCES

1. IEC60901: Single-capped fluorescent lamps – Performance specifications, 2011.

2. KC10025: LED Lamp for Fluorescent Lamp Retrofit – Internal converter type, 2014.

3. Go JJ, Kim CH. A Study on the Optical Characteristics of LED Lamp as Alternative Type of FPL Lamp. Journal of the Korean Institute of Illuminating and Electrical Installation Engineers. 2015, V29, #10, pp. 1–6.

4. KS C7601: Fluorescent lamps for general lighting service, 2009.

Jin-Tai Kim, is the Director of Institute of Electrical and Electronics Research, Korea Testing & Research Institute, Evaluator at Korea Laboratory Accreditation Scheme (KOLAS), IECEE Technical Assessor, and he is involved in doctoral course of plasma bio display at Kwangwoon University

Chung-hyeok Kim, Professor, Ingenium College of Engineering, Kwangwoon University, Council member, The Korean Institute of Electrical and Electronic Material Engineers

THERMAL ANALYSIS IN FIXED, FLOWED AND AIRLESS ENVIRONMENT FOR COOLING IN LED LUMINAIRES

Mehmet Sait Cengiz[1] and Seda Yetkin[2]

Department of Technical Vocational School, Bitlis Eren University, Turkey
E-mails: [1]msaitcengiz@gmail.com, [2]syetkin@beu.edu.tr

ABSTRACT

In this study, a simulation study was conducted for the loss of efficiency caused by the heat emitted by the LED chips. The temperature change of LED luminaire was analysed for three different scenarios using finite element method. Due to the increase in the internal temperature of the luminaire and due to the air effect inside the LED luminaires, failure of the LEDs has been tried to be prevented. For this purpose, a passive cooling method was proposed in the simulation environment. So, in high power LED luminaires, the high heat emitted by the LED chips is reduced to low heat by an air flow method. In this way, efficiency in LED outputs has been achieved.

Keywords: LED lighting, LED temperature, thermal analysis, energy efficiency

1. INTRODUCTION

LED (light emitting diode) technology, which makes efficient lighting with less energy consumption, is preferred because of its features such as high luminous efficacy, good colour rendering, different colour options and long lifetime. In addition, as semiconductor technology continues to evolve, the efficiency of LEDs is constantly increasing. However, values of luminous efficacy are valid for experimental studies of LED chips in the laboratory environments. It is known that the luminous fluxes and lifetimes of LEDs are affected by temperature changes more than that of conventional light sources. When the optimal operating temperatures are exceeded, the distortion rate of the LEDs in-

creases, the luminous fluxes decrease, and the colour properties worsen. As a result of this situation, high luminous efficacy, which are stated as advantages for LED light sources, suffer from loss of efficiency. Therefore, lighting installations using inefficient LED luminaires are seen in many applications [1–5].

According to ASSIST-2005, measuring LED chips requires a total of 6000 hours of LED operation. The first 1000 hours measurement lifetime are not included in the calculations, the last 5000 hours of the 6000 hours measurement are used. To be able to evaluate the LEDs as thermal, it recommends to measure temperature by connecting a temperature measuring device to the soldering point if possible. ASSIST specifies the soldering point temperatures as 45 °C, 65 °C, and 85 °C for high power LED chips with driving current of more than 100 mA. The luminous flux values obtained at the end of the first 1000 hours of measurement are normalized to 100 %. At 6000 hours, the luminous flux change is compared with the 1000-hour values. ASSIST publications provide an infrastructure for LED lifetime measurements, although some measurement and calculation methods are not fully recommended [6].

2. LED ARMATURE PARAMETERS

Today we live in a period when energy efficiency is very important. As the population grows, energy consumption increases at any time. For this reason, inefficient methods that cause energy consumption are abandoned and efficient methods are

Table 1. Heat Transfer Forms for Light Sources

Type of light source	Irradiance,%	Convection,%	Transmission,%
Incandescent	>90	<5	<5
Fluorescent	40	40	20
HID (discharge)	>90	<5	<5
LED	<5	<5	>90

sought. For this purpose, many methods of the energy efficient have been tested, both for improving the maintenance factors, as well as for automation and smart lighting. The main purpose here is to use energy more efficiently. For this reason, it has been searched for solutions to the problems of LEDs that provide energy efficiency in lighting [7–14].

Since the efficiency of the light source depends on the temperature in LED luminaires, thermal analysis is very important. Parameters that affect thermal design of the LED luminaire are luminaire body material, PCB elements, thermal intermediate filling materials, LED thermal powers, and ambient temperature.

Thermal analysis in LED luminaires is done for printed circuit board (PCB), on which the LED chip is mounted, and for the luminaire body. Because the heat produced by the LED chip is collected in the armature body due to the PCB. For the heat inside the armature body to pass outside, the thermal resistance must be minimal. Efficiency is directly related to thermal design, especially in luminaires that use high power LEDs. For thermal analysis, it is necessary to know the thermophysical properties of elements such as the LED chip, the housing material, PCB, thermal intermediate filling material that makes up the LED armature. As a result, in order for LED luminaires to work with optimal performance that will meet the necessary criteria for illuminance, it is necessary to perform optical analyses that corresponds to the type of luminaire and achieve the desired cooling solutions.

The heat transfer mechanisms of LEDs differ from other light sources. Conventional light sources generally transmit the generated heat to the environment through radiation. However, LEDs must transmit the heat they produce through transmission. This difference requires different solutions when designing systems for working with LEDs. A thermal path is required to exhaust the heat generated in the LEDs. Therefore, heat conduction problem must be solved in luminaire design. Disadvantages such as phosphor layer degradation, damage of

lenses, and degradation of solders are encountered with high temperature effect in LED armatures [15]. In his study on the cooling of LEDs in 2006, James Petroski compared conventional light sources with LED light sources according to their heat transfer properties [16].Table 1 shows the heat transfer patterns for light sources [17].

In this research, we studied changes in the properties of LED light sources with temperature. For this purpose, thermal changes in the simulation environment were analysed using the finite element method for an LED luminaire used in road lighting.

3. LED ARMATURE THERMAL DESIGN

The heat produced in the LEDs affects the LED efficiency. As the driving current passing through the LED chip increases, the electrical power and luminous flux it draws increases. However, as the electrical power increases, heat is also released. Therefore, for LEDs driven at high currents, wider cooling surfaces are required. In this way, the temperature can be reduced, because the LED efficiency decreases with increasing temperature. LEDs transmit most of the heat they produce to the PCB, the armature body, or the ambient air inside the armature, which they use as a transmission path. Especially in high power LED armatures, metal cooling elements are used to transfer the heat generated by the LEDs to the ambient air. In addition, to reduce the luminaire temperature, thermal intermediate filling materials (thermal paste or thermal gel) are used. Because the heat accumulated in the spaces increases the junction temperature. Each part combined in the LED armature needs to be filled with solder, gel or paste. The lower the heat transfer resistances of the thermal intermediate filling materials, the easier it is to remove the heat generated in the LEDs. The thermal parameters of the LEDs are given below [1–7].

• Ambient temperature: the heat produced in the LED chips passes to the armature body through the conduction way, and then transferred to the out-
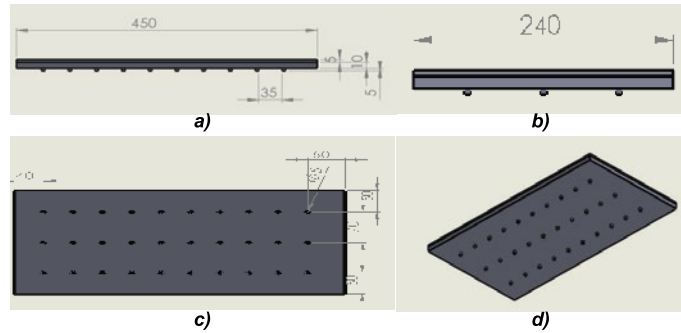
Fig. 1. The space between surfaces: 0 cm – without air flow (*A*1 – *P*1) scenario, front (a), left (b), bottom (c), and isometric (d) views

side air. Increasing the temperature in the luminaire leads to the fact that the lifetimes of the LEDs is reduced and they do not work. The heat accumulated in the armature body remains in the armature, increasing the junction temperature. For this study, the ambient temperature in the luminaire was selected as 22 °C.

• Thermal power of the LED chip: part of the electrical power in LED chips is emitted as optical power, the rest is produced as thermal power. For the LEDs to work efficiently, this thermal power produced must be removed from the LEDs. Increasing the thermal power of the LED chip increases the junction temperature. In particular, the junction temperatures of the LED chips driven above their rated currents become harmful with increasing thermal power. It is known that high temperature negatively affects luminaire efficiency and LED lifetime.

• Armature body material: different body materials effectively dissipate the heat produced in the LED chips and transport it to the external environment. In this way, the junction temperature values can be reduced. In this study, an aluminium body was chosen as body material for simulation.

• Printed circuit board: PCBs are the surface where LED chips or other elements are soldered. PCBs deliver the current from the LED driver to the LEDs. Therefore, heating occurs on PCBs.

• Thermal intermediate filling material: the main purpose of thermal intermediate filling material is to fill the gaps on the surfaces to be joined and prevent the high temperatures that will be created by the air gaps.

Therefore, important thermal parameters related to LEDs are the ambient temperature, the thermal power of the LED chip, the armature body material, PCB, and the thermal intermediate filling material. The thermal power of the LED chip is the factor that has the greatest impact on the junction temperature. *ANSYS* simulation was prepared in accordance with this approach.

4. SIMULATION AND PERFORMANCE ANALYSIS

The thermal efficiency depends on the junction temperature of the LEDs. It is known that luminous flux decreases with increasing temperature in LEDs. LED chip catalogues generally provide luminous flux at a junction temperature of 25 °C. These values (which are also referred to in the literature as cold luminous flux) are the luminous flux values obtained as a result of pulsed currents in the range of (10–20) ms in the LED production band [18]. In these measurements, the LEDs light for a very short time, and there is no increase in temperature at the junction. LEDs measured before reaching thermal equilibrium show lower performance under real operating conditions [19]. Luminaire designs usually 85 °C made with these luminous fluxes, which are called warm lumens, can give more realistic results. In this study, the initial temperature of the LED luminaire was simulated according to the junction temperature of 22 °C and the maximum temperature of 85 °C in *ANSYS* program. It is assumed that the simulated LED luminaire works ideally and operates in the temperature range of (22–85) °C. So, this LED luminaire is a quality error-free light source. While designing LED luminaire, luminaire and light source were evaluated as a single unit. Thanks to the simulation, it is easy to estimate the internal temperature of the LED armature or the LED junction temperature, which makes it easier to estimate the optical and colour characteristics of the LEDs used at that temperature. In this study, *ANSYS* program was used to predict LED junction temperatures. It is assumed that the heat discharged from the electronic element emerges from the junction point. It is assumed that part of the heat passes from the bottom to the printing circuit, and part from the top to the medium or the refrigerant block. The simulation was prepared in accordance with this principle.

Table 2. The Properties of Polyethylene and Aluminium Materials

Design-1 Materials	Density, kg/m³	Isotropic thermal conductivity, W/(m·°C)	Specific heat, J/(kg·°C)
Polyethylene	950	0.28	950
Aluminium	2689	237.5	951

Table 3. Material Properties for ($A2 – P2$) Scenario

Design-2 Materials	Density, kg/m³	Isotropic thermal conductivity, W/(m·°C)	Specific heat, J/(kg·°C)
Polyethylene	950	0.28	950
Aluminium	2689	237.5	951
Air	1.1614	0.026	1007

4.1. Simulation Scenarios

The structure, consisting of 2-layer polyethylene and aluminium, was made to represent an LED luminaire for outdoor lighting. There are 30 LED chips on the polyethylene surface. The thickness of the polyethylene surface is 10 mm (1 cm). The upper cooling surface is 0.5 cm thick (aluminium). If each LED chip emits a temperature of 85 °C, appropriate boundary conditions are simulated. According to the simulation designed by the finite element method, there is no air gap between these two surfaces. That is, the spaces are filled with thermal paste or thermal gel. In Fig. 1, representing the LED armature, the space between surfaces: 0 cm – without air flow ($A1 – P1$) scenario, front, left, bottom, and isometric views is seen.

Space between surfaces: 0 cm – without air flow ($A1 – P1$) scenario, as it consists of two parts, 2 different materials are defined. In Fig. 2, the first piece on the top is aluminium, and the second piece on the bottom is polyethylene. *ANSYS* form for the space between surfaces: 0 cm – without air flow ($A1 – P1$) scenario is shown in Fig. 2. The properties of polyethylene and aluminium material are given in Table 2 [15].

Space between surfaces: 0.5 cm – without air flow ($A2 – P2$) scenario, an air gap of 5 mm stays between the polyethylene plate and the aluminium plate. The circumference of the air gap between the two surfaces is closed. So, there is no air flow. In this design, the air showed an insulating effect, like double glass windows. Fig. 3 shows space between surfaces: 0.5 cm – without air flow ($A2 – P2$) scenario, front view, and left view.

Time-independent thermal analysis was performed in *ANSYS* program. In Fig. 4, an air gap of 0.5 cm is left between aluminium and polyeth-
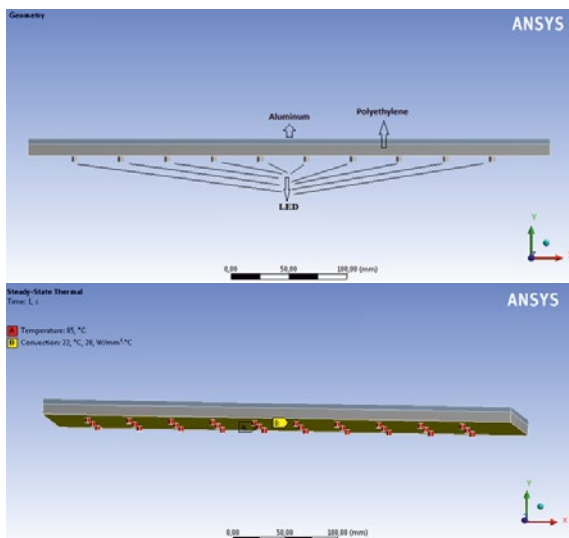
Fig. 2. *ANSYS* form for space between surfaces: 0 cm – without air flow ($A1 – P1$) scenario
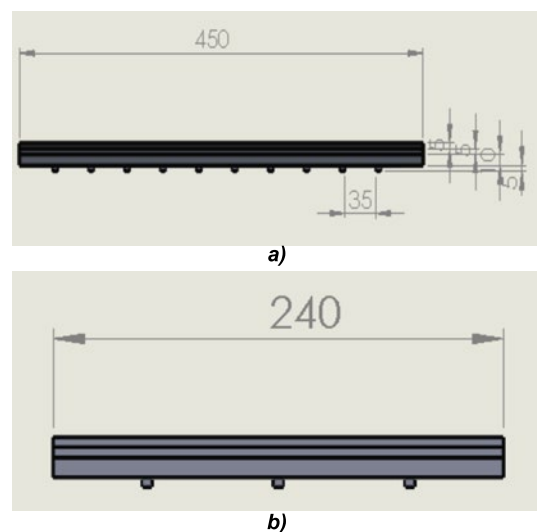
Fig. 3. Space between surfaces: 0.5 cm – without air flow ($A2 – P2$) scenario, front view (*a*), and left view (*b*)
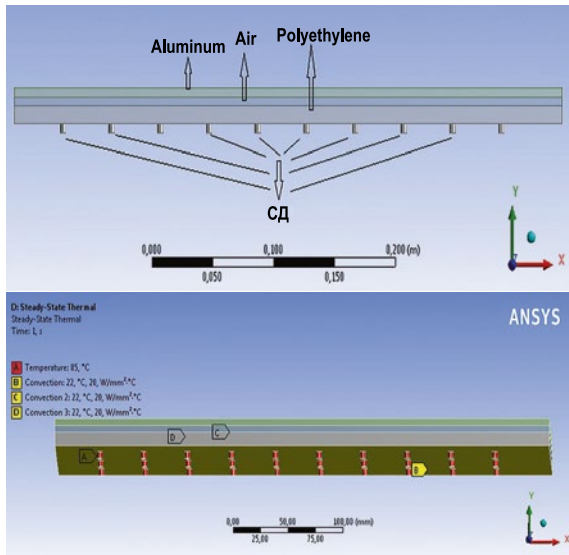
Fig. 4. *ANSYS* form for space between surfaces: 0.5 cm – without air flow (*A2* – *P2*) scenario

ylene. In this way, a 3-storey design was formed. There is no air flow in this design. This design is called "space between surfaces: 0.5 cm – without air flow (*A2* – *P2*) scenario". *ANSYS* form for space between surfaces: 0.5 cm – without air flow (*A2* – *P2*) scenario is shown in Fig. 4. In Table 3, material properties are given for the (*A2* – *P2*) scenario.

If all properties in Fig. 4 and Table 3 are equal, if there is air flow between the two plates, then the simulation used for this scenario is called "space between surfaces: 0.5 cm – air flow (*A3* – *P3*) scenario".

4.2. Performance Analysis for Simulation

This study analyses 3 scenarios for thermal analysis of LED armatures. These scenarios has been named:

– Space between surfaces: 0 – without air flow (*A1* – *P1*);

– Space between surfaces: 0.5 cm – without air flow (*A2* – *P2*);

– Space between surfaces: 0.5 cm – with air flow (*A3* – *P3*).

The simulation prepared by the finite element method was run. In the results of the thermal analysis of the top layer aluminium (*A1*, *A2*, *A3*), the bottom layer polyethylene surface (*P1*, *P2*, *P3*) is shown in Figs. 5, 6 and 7. The space between surfaces: 0 cm – without air flow (*A1* – *P1*) scenario, as a result of the analysis in *ANSYS*, Fig. 5 shows the temperature distribution on the aluminium plate and the polyethylene plate, respectively.

As can be seen from Fig. 6, if there is a 0.5 cm air flow between the upper aluminium surface and the lower polyethylene surface, the heat rises very quickly. Since there is no air flow in the 0.5 cm air space between the plates, it is seen that the value of 22 °C of the polyethylene plate given as the boundary condition is exceeded even at $t = 1$ sec. In the (*A2* – *P2*) scenario, it was observed that the temperature reached 22.46 °C for $t = 1$ sec on the aluminium plate and 26.22 °C on the polyethylene plate. In other words, regardless of the threshold temperature value, it produced air insulation. Such LED luminaries should not be used.

As can be seen from Fig. 7, if there is a gap between the upper aluminium surface and the lower polyethylene surface with an air flow of 0.5 cm, the heat does not increase. As the air flow occurred in the 0.5 cm air space between the plates, the temperature of the polyethylene plate of 22 °C, which was given as a boundary condition, allowed the plate to be exposed to low temperature. In the simulation, the maximum temperature rose to 22.02 °C. Under the conditions shown in Fig. 6, it is seen that the temperature in an armature with an air flow will not rise. A passive cooling method can be used to prevent the LED luminaries from heating up. This situation can be seen in Fig. 7. If the IPX protection standards are met, LED luminaires in the (*A3* – *P3*) scenario exposed to air flow prevent heating. In Fig. 7 it is seen that the aluminium surface does not
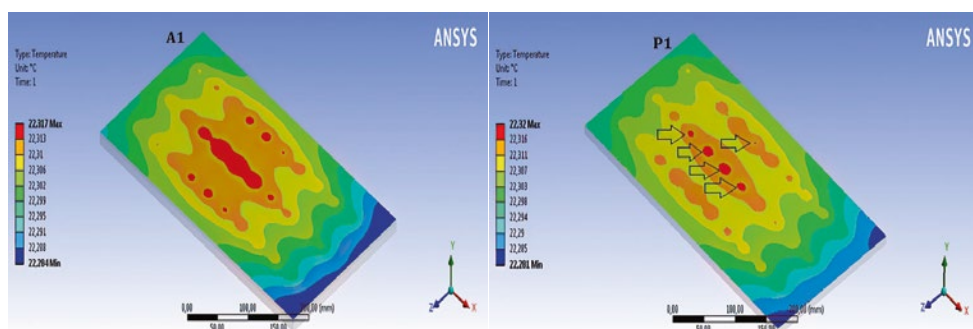
Fig. 5. The temperature distribution on the aluminium plate (*A1*) and the polyethylene plate (*P1*)
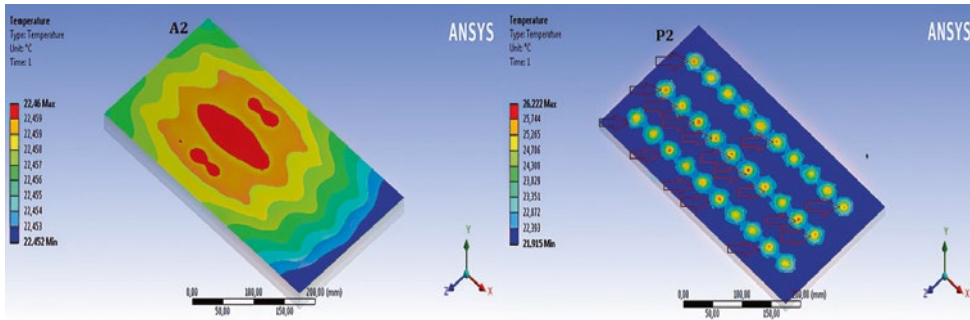
Fig. 6. The temperature distribution on the aluminium plate (*A*2) and polyethylene plate (*P*2) for the (*A*2 – *P*2) scenario
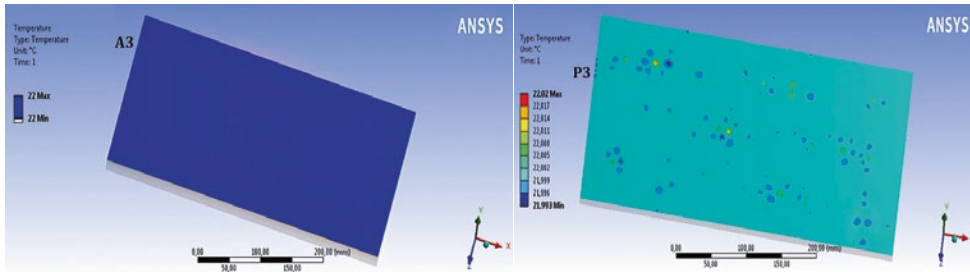
Fig. 7. The temperature distribution on the aluminium plate (*A*3) and the polyethylene plate (*P*3) for the (*A*3 – *P*3) scenario
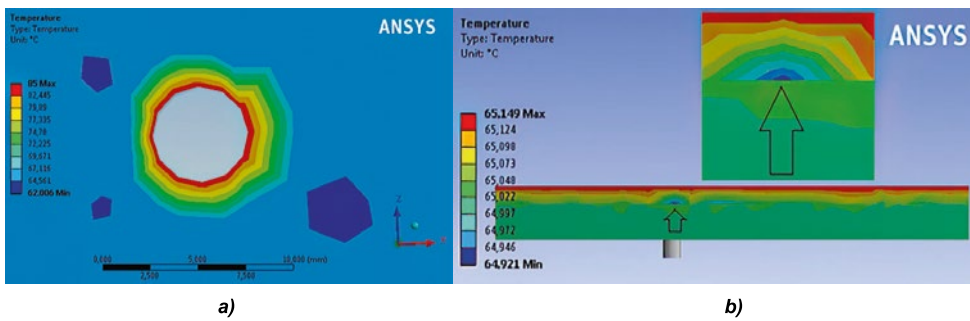
Fig. 8. Top and side heat dissipation for an LED chip, side cross-sectional temperature distribution for an LED chip(*a*), and overhead heat distribution for an LED chip (*b*)
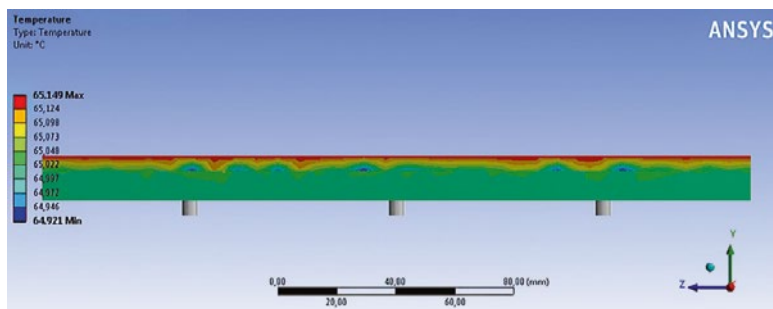
Fig. 9. Front section heat distribution for the LED luminaire

get heat up. In the (*A*3 – *P*3) scenario, although it is in equal conditions, it is seen in Fig. 7 that no LED on the polyethylene surface exceeds the threshold value. Whatever the threshold value, it does not isolate air. On the contrary, it makes air cooling. In this respect, cheaper materials can be used instead of aluminium on the upper cooling surface.

5. RESULTS AND DISCUSSIONS

When the scenarios were evaluated, the presence of an air gap layer brought the temperature to the highest level. Because it had the effect of air isolation. Therefore, there should be no air between the aluminium layer and the polyethylene layer in the LED armatures. For this purpose, thermal paste or thermal gel should be used.

As can be seen from Fig. 5, 5 LEDs exceeding the threshold temperature values were detected in $t = 1$ sec. There is no air gap between the aluminium plate and the polyethylene plate. It is clear that the aluminium layer will make sufficient cooling for the transfer.

However, in Fig. 6, if there is air in the closed area between the aluminium transfer surface and the polyethylene surface, cooling does not occur.
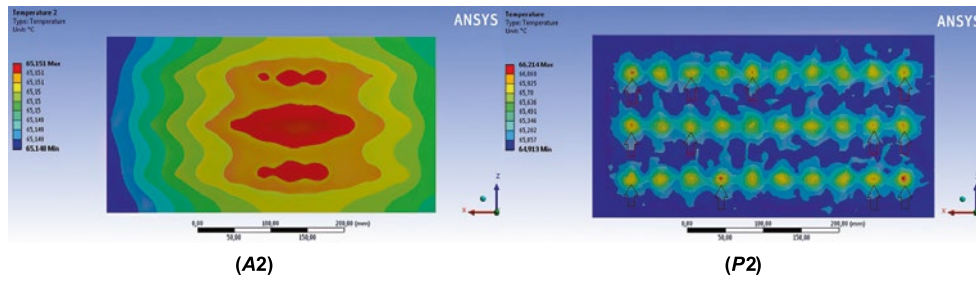
(A2)   (P2)

Fig. 10. The temperature distribution on the aluminium plate (*A2*) and the polyethylene plate (*P2*) for the (*A2 – P2*) scenario (air temperature within armature 65 °C)

Because air is a very good insulating material. If the air flow does not occur, that is, if the air inside is stationary, then you can see that the polyethylene plate is subjected to more heat. As can be seen from Fig. 6, 17 LEDs exceeded the threshold temperature value specified in the simulation in $t = 1$ sec. As the LED armature operates, the temperature will continue to increase, and it is clear that the temperatures will be reached, which will deteriorate the LED, regardless of the threshold temperature value.

This was repeated for 65 °C specified in *ASSIST* standards in the simulation environment. In the simulation, the temperature of the threshold in the closed area was accepted as 65 °C under the conditions shown in Fig. 6. Fig. 8 shows top and side heat dissipation for the LED chip.

As can be seen from Fig. 9, when the air temperature inside the LED armature is 65 °C, the temperature covered the aluminium transfer surface. Due to the isolation of the air in the closed area, the temperature exceeds the threshold value in $t = 1$ sec. So, as soon as the LEDs started working, heating started. This shows that the temperature will increase over time. Since the air is in a closed area, it does not transfer the heat outside, like the double glass effect on the windows. The heat generated by the LED chips increases on the polyethylene layer and causes the LEDs to fail. It shows air insulating properties for the aluminium surface. Therefore, aluminium cannot transfer heat. Fig. 9 shows front section heat distribution for LED luminaire.

Fig. 10 shows that the aluminium surface heats up much more at a indoor temperature of 65 °C. However, it has an air isolation effect. Therefore, the heat transfer rate decreases. So, 12 LED chips exceed 65 °C in $t = 1$ sec. You can see that over time, this temperature will rise too much and cause the LEDs to malfunction. Fig. 10 shows the temperature distribution on the aluminium plate and the polyethylene plate for the (*A2 – P2*) scenario (air temperature within armature 65 °C).

6. CONCLUSION

The main factors affecting the junction temperature are the ambient temperature and the LED chip thermal power.

In this study, LED chips heat the polyethylene surface and the air inside the luminaire. Therefore, the LED chips on the polyethylene surface, which get too hot decay. The flowless air gap between the layers acts as an insulator and causes the temperature to rise more. Therefore, there should be no gap between aluminium and polyethylene plates. If there is a gap, heating can be prevented with thermal paste or thermal gel.

In addition, the heat can be reduced by applying passive cooling in LED armatures. If the flow of air accumulated in the gaps is provided, then cooling is provided. This situation can be seen in the simulation in Fig. 7.

The thermal power of the LED chip is the most effective parameter. As the LED chip's thermal power increases, the amount of heat released increases. When the LED armature system is examined in a holistic way, the heat emitted from the LED chip is transferred to the armature body and then to the ambient air. Increased heat in the armature in the indoor area damages the LEDs. This situation can be seen in the simulations in Fig. 6 and Fig. 10.

As a result, every parameter is important in high power LED luminaires.

REFERENCES

1. Yurtseven M.B., Mete S. ve Onaygil S. The effects of temperature and driving current on the key parameters of commercially available, high-power, white LEDs. Lighting Research and Technology, 2016. V48, #8, pp. 943–965.

2. Jayawardena A., Liu Y., Narendran N., Analysis of three different junction temperature estimation meth-

ods for AC LEDs, Solid State Electronics, 2013. V86, pp. 11–16.

3. Yurtseven M.B., LED Işık Kaynaklı Armatür Isıl Modellenmesi ve Isıl Tasarımı Etkileyen Faktörlerin İstatistiksel Analizi, İstanbul Teknik Üniversitesi, Enerji Enstitüsü, Doktora Tezi, Haziran 2017.

4. Yurtseven M.B., Onaygil S., Ogus G. Thermal simulation and validation of LED based luminaires using two-resistor compact thermal model, Lighting Research and Technology, 2014. V46, #5, pp. 576–586.

5. Cengiz M. S., Thermal Design Calculations for LED Luminaires, International Journal of Engineering Research and Development, 2018. V10, #2, pp. 69–75.

6. ASSIST Assist Program. 2020, http://www.lrc.rpi.edu/programs/solidState/ ASSIST/index.asp

7. Çıbuk M., Cengiz M.S., Determination of Energy Consumption According to Wireless Network Topologies in Grid-Free Lighting Systems. Light & Engineering, 2020. V28, #2, pp. 67–76.

8. Çıbuk M., Reducing Energy Consumption in Single-Hop and Multi-Hop Topologies of Road Lighting Communication Network, Light & Engineering, 2020. V28, #4.

9. Efe S. B., UPFC Based Real-Time Optimization of Power Systems for Dynamic Voltage Regulation. Computer Modeling in Engineering & Sciences, 2018. V116, #3, pp. 391–406.

10. Efe S. B., Cebeci M., Power Flow Analysis by Artificial Neural Network. International Journal of Energy and Power Engineering, 2013. V2, #6, pp. 204–208.

11. Cengiz M. S., Simulation and Design Study for Interior Zone Luminance In Tunnel Lighting. Light & Engineering, 2019. V27, #2, pp. 42–51.

12. Cengiz M. S., Effects of Luminaire Angle and Illumination Topology On Illumination Parameters In Road Lighting. Light & Engineering, 2020. V28, #4.

13. Cengiz M. S., Cengiz Ç., Numerical Analysis of Tunnel LED Lighting Maintenance Factor. IIUM Engineering Journal, 2018. V19, #2, pp. 154–163.

14. Cengiz M. S., The Relationship between Maintenance Factor and Lighting Level in Tunnel Lighting. Light & Engineering, 2019. V27, #3, pp. 75–88.

15. Poppe A. Lasance C.J. On the standardization of thermal characterization of LEDs. Semiconductor Thermal Measurement and Management Symposium, 200925th Annual IEEE, 15–19 Mart 2009, San Jose, CA, ABD.

16. Petroski, J. Thermal Challenges in LED Cooling. 2020, https://www.electronics-cooling.com/2006/11/thermal-challenges-inled-cooling/

17. ANSYS: Engineering Simulation & 3D Design Software, https://www.ansys.com/, 2020.

18. Oms Lighting (2014). Cold lumens versus hot lumens. http://www.omslighting.com/ledacademy/579/4-leds-controls/41-coldlumens-versus-hot -lumens

19. Ateş S., Yurtseven M.B., Onaygil S. Design of A Chip on Board (COB) LED Based Industrial Luminaire With Thermal Simulations. Light & Engineering, 2019. V27, #2, pp. 78–87.

Mehmet Sait Cengiz,
Ph.D. He served as Director of Research and Development in the years 2000–2010. He had got his Master Degree in 2011 and Ph.D. in 2016. His spesialization area is electrical-electronics engineering (light). He still works in the field of applied lighting

Seda Yetkin,
M. Sc. She received her Master's Degree in Fırat University (2017), faculty of technology, Department of Mechatronics Engineering. Now she is a Ph.D. student in the same department. She is currently working as a lecturer at Bitlis Eren University, Vocational School of Technical Sciences, Department of Biomedical Device Technologies

ENERGY-SAVING LED LIGHTING SYSTEM WITH PARALLEL POWER SUPPLY BY PHOTOVOLTAIC MODULES AND BY NETWORK

Pavel V. Tikhonov

Federal Scientific Agroengineering Center VIM, Moscow
E-mail: ptikhonov@inbox.ru

ABSTRACT

The current state of LED lighting systems with parallel power supply by photovoltaic modules and central power supply network is analysed. The approach to implementation of parallel operation of LED luminaire powered by two sources of power is presented. It is simple, cheap and highly reliable as compared to the existing solutions. Based on this approach, four diagrams are developed which are applicable correspondingly to lighting applications and characteristics of photovoltaic modules and power consumers. The first and the second diagrams contain minimal quantity of transformers, but a number of operational constraints shall be taken into account when using them. The third diagram contains standard transformers and implies minimal number of various constraints, which makes it an optimal solution for the low-power lighting system being designed. The fourth diagram is expensive due to utilisation of equipment with automatic maximum power point tracking (the *MPPT* technology); it provides maximum possible energy efficiency of the lighting systems but the advantages of the *MPPT* technology apply only to high-power systems.

It is preferable to use such objects where lighting is mostly required during daytime as consumers of such systems (shopping malls, underground passages, storage facilities, poultry farms, etc.). A positive aspect is increase in reliability of consumer power supply since power supply of LED luminaires will be also provided by an additional source.

The proposed approach leads to reduction of power consumption for LED lighting, saving of fossil energy sources and therefore to ecologisation of the environment.

Keywords: solar radiation, photovoltaic module, direct current micro-grid, voltage stabiliser, current stabiliser, parallel operation, LED lighting

1.INTRODUCTION

The sphere of application of photoelectric transformers (PET) has been continuously expanding. Large-scale introduction of photoelectric systems is mostly promoted by reduction of the cost of PET [1–3] and growth of tariffs for electric energy generated using conventional sources of energy. Development of photovoltaic energy is also affected by environmental issues [3, 4] and development of energy-efficient electronics and direct-current lighting devices.

Application of photovoltaic modules (PVM) as sources of energy allows us to connect direct current consumers directly without an inverter establishing a direct current micro-grid. Such concept is being studied constantly throughout the world [5–7] and relevant technologies will become more popular and be introduced all over the world as soon as the cost of photovoltaic energy drops.

Many devices use direct current for operation in our homes and offices. A significant part of household and office appliances and other electric equipment operates using direct current being supplied by the alternate current network thanks to built-in power transformers. These devices are technically capa-
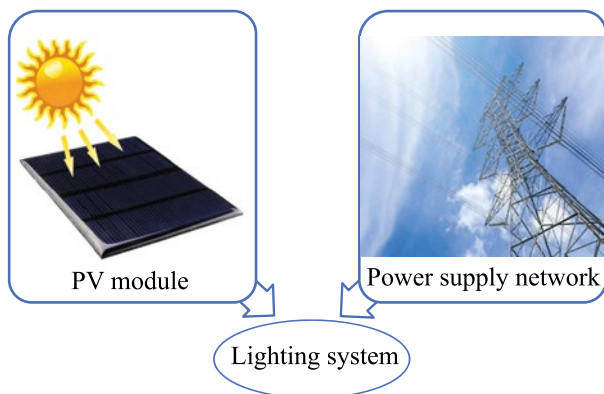
Fig. 1. Lighting system with parallel power supply by two sources

Fig. 2. Wiring diagram of the lighting system with combined power supply

ble to use direct current directly; however, manufacturers do not design such functionality. Devices that are capable to use AC and DC networks for operation simultaneously can be rarely encountered recently, but the number of such devices will increase following the observed trend. It is important that it does not lead to significant technical complication of devices and to rise in their prices. They will operate in hybrid DC and AC networks [8].

With consideration of the above described circumstances and trends, photovoltaic systems supplying direct-current loads will allow to reduce customers' expenses for power supplied by power network operators. A system of lighting by means of LED-based luminaires with parallel power supply by PET and general-use power network (Fig. 1) is one of distinctive examples.

2. METHODS

Various methods of matching parallel operation of a lighting system powered by a PVM and an electric network are possible. For instance, one of the designs comprises super capacitors and a relay for switching between sources of energy [9]. With such approach, relays suffer large load – due to frequent switching, their operation cycle will be short and will require frequent replacement of elements. Moreover, transition processes occurring in case of fast and frequent switching will impair quality of power. Another design comprises application of a special control device (driver) which matches parallel operation of LED sources powered by the network and by PVM by means of a high-frequency transformer [10]. This device also operates as an inverter outputting excessive energy to the network. However, the quality of output power does not com-

ply with standards. There is one common disadvantage of the two above mentioned systems: their complexity and expensiveness.

This article proposes a different approach to parallel operation of LED sources which is significantly different from similar solutions being very simple and less expensive. The method comprises of matching two parallel sources of power by voltage level (Fig. 2).

With such connection, it is important that nominal voltage of photovoltaic modules (PVM) is higher than nominal output voltage of the *AC-DC* network supply. Then the entire energy will be consumed by the luminaire with sufficient power generation by PVM. When output of PVM is not sufficient for supply of the luminaire, lack of photovoltaic energy is compensated by the network supply. Lack of photovoltaic energy will lead to decrease of voltage at input of the current stabiliser Stab. I (Fig. 2) of the luminaire, and the network supply will stabilise input voltage of this stabiliser compensating insufficient power at this moment. The current stabiliser is necessary for stabilisation of LED light source's operation in this diagram. In case the latter is equipped with a built-in current stabiliser, it will be removed from the diagram.

The diagram proposed above is the basic one, and some other variants are developed on its basis; the differences are primarily additional elements or
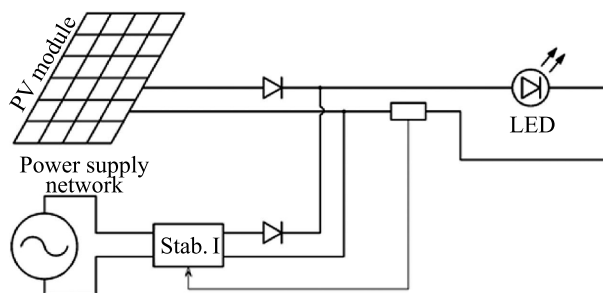
Fig. 3. Lighting system wiring diagram with the combined power supply and modernised network current stabiliser
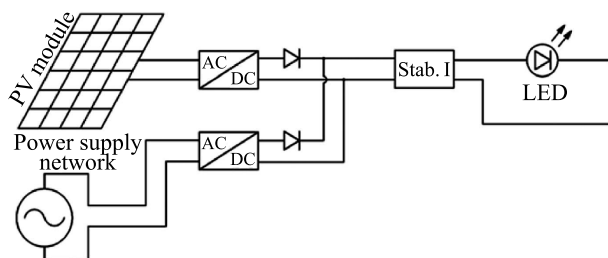
Fig. 4. Lighting system wiring diagram with combined
power supply and an up/down converter

modernisation of some elements. One of the variants is presented in Fig. 3. It is based on division between the network current stabiliser and its measurement unit. The measurement unit of the network current stabiliser is located at the input of the luminaire downstream of the connection point of two sources of power. Controlling current of the luminaire, the network transformer compensates lacking power from PVM (as required).

This variant looks very similar to the standard variant of LED-based luminaires powered by the network; the difference is just addition of another source of power and modification of the structure of the current stabiliser. Therefore, it is one of the cheapest variants of connection of a PVM to a conventional supply circuit of LED-based luminaires.

In search for compromises for low-power LED-based luminaires, a widely applicable variant is developed. It comprises application of step-up and step-down converters with voltage and current stabilisers (Fig. 4). With that, in the diagram for out-feed of energy generated by the PVM, an ordinary *DC-DC* voltage transformer-stabiliser is used.

In the case of high-power lighting systems, it is necessary to apply the *Maximum Power Point Tracking* (*MPPT*) technology; the power circuit of such system is shown in Fig. 5. The *MPPT* technology allows users to out-feed more power from the PVM. Different types of such devices (*MPPT* controllers) are being developed for LED-based lighting systems [11, 12].

3. RESULTS

The diagram variants presented above have advantages and disadvantages. Let us consider them in more details.

The variant with direct connection of PVM to a network supply (Fig. 2) has a number of disadvantages associated with impossibility of maximum out-feed of power from PVM and necessity

of its output voltage selection. The diagram is efficient only with correctly selected characteristics of elements.

In the second variant, with the modernised current stabiliser (Fig. 3), a minimal number of elements are required for functioning of the system. However, to prevent burnout of LEDs, peak power of PVM should not exceed operating power of LED. It is also possible to apply special limiter of PVM output power. Like in the previous variant of the diagram, it is important to select the PVM based on voltage: nominal voltage should be approximately equal to operating voltage of the luminaire.

After comparing the two above mentioned variants, it should be noted that the first one is preferable with PVM power comparable to that of a luminaire and the second one is preferable with PVM power less than that of a luminaire.

The third variant is preferable for low-power lighting systems. Its advantages are lack of mandatory necessity to select PVM and load voltage, which is necessary for the two previous variants. The PVM output voltage stabiliser operates within a broad range of input voltage and exceeds power out-feed from photoelectric transformers as compared to the first two variants, and the input current stabiliser of the luminaire protects its LED from burnout. Additional advantage of such diagram is capability to establish an AC micro-grid which may be supplemented with new sources and consumers of electric energy.

Although it is the most energy-efficient, the last diagram variant using the *MPPT* technology (Fig. 5) requires additional evaluation of feasibility of specific application due to its expensiveness. The advantages of this technology mostly manifest themselves in high-power lighting systems. For low-power systems, it is more beneficial to increase power of the photovoltaic part by means of additional photoelectric transformers than by means of a *MPPT* controller.
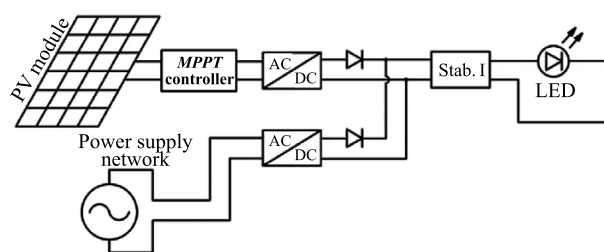
Fig. 5. Lighting system wiring diagram with combined
power supply and *MPPT* controller

The variant of a controller designed specifically for parallel operation with a PVM and an electric power is more promising; a *DC-DC* voltage transformer with the *MPPT* technology will be integrated with an *AC-AC* network supply.

The problems of optimal selection of equipment and comparison of different variants of the diagrams are more conveniently solved using special means of mathematical modelling like *MATLAB-Simulink* etc. Therefore, operation of these diagrams will be considered in detail with use of such means in further studies related to this subject.

A special attention shall be paid to unavailability of a battery in the circuits, which allows us to develop cost-efficient LED-based lighting systems, since the batteries would have significantly risen the price of generated power. And even application of lithium iron phosphate batteries which are optimal in terms of the cost of the charge/discharge cycle nowadays will not provide significant reduction of prime cost. However, application of batteries is necessary and feasible, for instance, in emergency lighting networks with LED-based luminaires. Also, application of low-capacity batteries is necessary for achievements of high characteristics in some cases, but it is necessary to solve problems of optimisation with consideration of specific criteria for this purpose. However, in any case, the power of batteries used for lighting will be minimal, which is caused by their inability to compete with PVM and electric network in terms of prime cost of energy.

4. CONCLUSION

Development of PET and lighting installations with LED-based luminaires leads to a large number of designs using them, but most of such installations are autonomous and accumulate energy throughout the day [13]. To make them cheaper, it is necessary to reduce capacities of batteries to a minimum and use general-use power networks as a guaranteed source of power. It is such approach that is implemented in LED-based luminaires with parallel supply from PVM and electric power under development, which reduces consumption of power from the general-use network and losses for transformation.

Moreover, complex supply circuits often have extensive functionality but their large costs lead to high expenses. In this context, it is very important to create simple solutions with their functionality limited to some extent which, however, solve major set problems and are efficient in terms of price and reliability. Therefore, different variants of supply circuits are developed, which are applicable depending on the objectives and distinctions of PVM and power consumers.

It is important to wisely select the loads; it appears that buildings with spaces requiring artificial lighting throughout the day are the most optimal. For instance, we would like to note shopping malls, underground passages, storage facilities and poultry farms. Reliability of power supply plays a very important role for such responsible consumers and is increased by LED-based luminaires being supplied by two to three sources of power (depending on power supply rating of a consumer).

As noted above, the price reduction of PVM over the last years has significantly increased their competitive ability as compared to other sources of energy [1–3]. In this view, a larger number of solar power plants operating directly for power networks have been appearing in Russia [14]. Nowadays, the prime cost of power generated by photovoltaic panels is able to compete with the cost of power from the network for enterprises in some regions. Consequently, such systems allow users to reduce consumption of power from the network in some cases even today allowing consumers to save on electric power bills and contributing to environmental safety growth.

REFERENCES

1. Global Market Outlook For Solar Power 2019–2023 / Aurélie Beauvais, Naomi Chevillard, Mariano Guillén Paredes, Máté Heisz, Raffaele Rossi, Michael Schmela. Belgium, Brussels: SolarPower Europe, 2019, 91 p. URL: https://www.solarpowereurope.org (date of reference: 09.09.19).

2. Stromgestehungskosten Erneuerbare Energien / Christoph Kost, Shivenes Shammugam, Verena Jülch, Huyen-Tran Nguyen, Thomas Schlegl. Deutschland, Freiburg: Fraunhofer-Institut für Solare Energiesysteme ISE, 2018, 41 p. URL: https://www.ise.fraunhofer.de (date of reference: 09.09.19).

3. Renewables 2018 global status report / Hannah E. Murdock, Rana Adib [et al.] France, Paris: REN21, 2018. – 324 p. – ISBN978–3–9818911–3–3 –URL: http://www.ren21.net/wp-content/uploads/2018/06/GSR_2018_Highlights_final.pdf (date of reference: 09.09.19).

4. Advancing the Global Renewable Energy Transition / Hannah E. Murdock, Rana Adib [et al.] – France, Paris: REN21, 2018, 51 p. ISBN978–3–9818911–2–6 – URL: http://www.ren21.net/wp-content/uploads/2018/06/GSR_2018_Highlights_final.pdf (date of reference: 09.09.19).

5. Wang B., Sechilariu M., Locment F. Intelligent DC microgrid with smart grid communications: control strategy consideration and design // IEEE Transactions on Smart Grid, 2012, 3(4), pp. 2148–2156. DOI: 10.1109/TSG.2012.2217764.

6. Dragičević T., Lu X., Vasquez J.C., Guerrero J.M. DC Microgrids-Part I: A Review of Control Strategies and Stabilization Techniques // IEEE Transactions on Power Electronics, 2016, 31(7, pp. 4876–4891. DOI: 10.1109/TPEL.2015.2478859.

7. Dragičević T., Lu X., Vasquez J.C., Guerrero J.M. DC Microgrids–Part II: A Review of Power Architectures, Applications and Standardization Issues // IEEE Transactions on Power Electronics, 2016, 31(5), pp. 3528–3549. DOI: 10.1109/TPEL.2015.2464277.

8. Justo J.J., Mwasilu F., Lee J., Jung J.W. AC-microgrids versus DC-microgrids with distributed energy resources: A review // Renewable and Sustainable Energy Reviews, 2013, Vol. 24, pp. 387–405. DOI: 10.1016/j.rser.2013.03.067.

9. De Zoysa H.B.H., Guruge P.A., Kalingamudali S.R.D., Kularatna N., Kanishka G. Designing and Constructing a DC Microgrid with Uninterrupted Power Supply Capability and Optimizing its Energy Usage by Smart Controlling System / IEEE Industrial-Electronics-Society (IES) International Conference on Industrial Electronics for Sustainable Energy Systems (IESES), New Zeland, Hamilton: IEEE, 2018, pp. 351–356.

10. Ali A., Lange J., Elrayyah A., Sozer Y., De Abreu-Garcia J.A., Mpanda A.A. Hybrid Flyback LED Driver with Utility Grid and Renewable Energy Interface / 33nd Annual IEEE Applied Power Electronics Conference and Exposition. USA, TX, San Antonio: IEEE, 2018, pp. 3377–3384.

11. Vieira J.A.B., Mota A.M. Implementation of a Stand-Alone Photovoltaic Lighting System with MPPT Battery Charging and LED Current Control / IEEE International Conference on Control Applications Part of 2010 IEEE Multi-Conference on Systems and Control, Japan, Yokohama: IEEE, 2010, pp. 185–190.

12. Shen C.L., Ko Y.X. Hybrid-input power supply with PFC (power factor corrector) and MPPT (maximum power point tracking) features for battery charging and HB-LED driving // Energy – Elsevier Ltd, 2014, Vol. 72, pp. 501–509. DOI: 10.1016/j.energy.2014.05.072.

13. Pandey A.K., Tyagi V.V., Selvaraj J.A.L., Rahim N.A., Tyagi S.K. Recent advances in solar photovoltaic systems for emerging trends and advanced applications // Renewable & Sustainable Energy Reviews, Elsevier Ltd, 2016, Vol. 53, pp. 859–884. DOI: 10.1016/j.rser.2015.09.043.

14. Solar Power Plants in Russia: Reality and Prospects [Solnechnyie elektrostantsii na territorii Rossii: realii i perspektivy] // Alternative Energy [web-site], 2019. https: //altenergiya.ru/sun/solnechnye-elektrostancii-v-rossii.html (date of reference: 09.09.19).

Pavel V. Tikhonov,
Ph.D. He graduated from the Mari-El State University (MarGU) with specialty in Power Supply in 2008. At present, he is a senior researcher with FNAC VIM. His key research interests: power supply systems based on photovoltaic modules (PVM) and cogeneration photoelectric heat modules, PVM-based micro-grids

FACADE OPTIMIZATION FOR AN EDUCATION BUILDING USING MULTI-OBJECTIVE EVOLUTIONARY ALGORITHMS

Arda Agirbas[1] and Ebru Alakavuk[2]

Department of Architecture, Yasar University, Izmir, Turkey
E-mails: [1]arda.agirbas@yasar.edu.tr, [2]ebru.alakavuk@yasar.edu.tr

ABSTRACT

Architectural design of a facade, both at the aesthetic point of view and from the point of view of internal daylighting performance of the building, can be considered as a complex task. In this study, we implement a multi-objective evolutionary algorithm to formally exploration the process of reconstruction of the education building's facade. The purpose of this research is to create a facade configuration by considering the size and location of elements and their materials when creating a suitable internal daylight distribution. The total construction cost of the building's exterior and the daylight performance of the building's interior are considered as objectives. The problem formulation includes two conflicting objectives, which are to increase daylighting aspect on each floor and reduce the total construction cost of the facade. To detect the approximation of Pareto fronts, including non-dominated solutions, we used a fast and elitist multi-objective genetic algorithm (NSGA-II). Computational and architectural results show that NSGA-II is efficient enough to demonstrate eligible facade design alternatives.

Keywords: facade design, multi-objective optimization, education building design, computational design

1. INTRODUCTION

The architectural design procedure is often described as a complex process because it requires the ability to respond to different needs of people at the same time. In addition, the design process involves making decisions on many parameters simultaneously in order to maximize objective performance while satisfying design constraints [1]. Decisions in this process affect final solutions.

In the discipline of architecture, educational buildings are one of the most multi-layered organizations types due to the diversity of spatial requirements in relation to the type of education. The existence of various persons, materials, providers, and high skilled qualifications to provide the service creates management issues [2]. The architectural design of an education building should be able to respond to different types of spatial requirements in relation to educational purposes. Educational building design relates to the design of the physical environment that includes interior layout and design (e.g., adjacencies and furnishing of different purposed spaces), internal environmental qualities (e.g., lighting) [3], and the building's exterior features (e.g. building's envelope, facade systems).

When designing educational buildings, building envelope systems can be considered as important architectural elements that have a positive contribution to daylight design [4] and should be carefully evaluated at the early stages of design. The existence of daylighting in enclosed spaces can improve the effectiveness of education and the quality of learning, while reducing stress [5]. In [6], the authors tried to prove the relationship between daylighting and human behaviour in a relative environment. Daylight autonomy [7] was used as a calculated metric in modelling to build a relationship between the probabilistic potential of daylight and

the comfort of lighting in relation to society. The influence of changes in window sizes, orientation, and glazing material on achieving satisfactory lighting values is studied. Experiments have shown that sufficient lighting can be achieved by a small amount of glazing in certain orientations. In [8], the authors demonstrated the influence of daylighting on users in addition to reducing the energy consumption of artificial lighting. In [9], authors presented an optimization study for a glazing system, considering the maximum useful daylight while reducing energy consumption. Based on the literature, one may argue that the optimization methodology is associated with parametric computer-based simulations to determine the glazing system design.

This paper aims to use parametric workflows and optimization methods to improve the design of the external glazing of the educational building. It focuses on optimizing the geometry of the external facade geometry of a building in Yasar University by configuring the placements and sizes of the elements for controlling solar penetration and improving daylight performance while reducing the overall cost of the structure. To investigate this problem, we employ the non-dominated sorting genetic algorithm II (NSGA-II).

In this study, the south-west and south-east facing facades of the education building at Yasar University campus are re-designed in order to increase the usage of daylighting inside the building. The building is in the district of Bornova, Izmir, Turkey,

Table 1. Initial Widths of the Glazing

Notations	Width, m
G_1	4.00
G_2	12.00
G_3	4.00
G_4	6.00
G_5	2.00
G_6	1.00
G_7	4.00

having 38° 27′ *N* latitude, 27° 12′ *E* longitude, and 17 m altitude. The dimensions and materials of existing facade elements are defined as decision variables in order to create daylight analysis.

In the rest of the paper, section 2 explains the parametric model, including decision variables and their impact on the geometric form-finding. Section 3 describes the problem formulation with constraints and objective functions. Section 4 highlights the key features of the algorithm that was used throughout the study. Section 5 presents computational and architectural results. Finally, in section 6, conclusions of the study are presented.

2. PARAMETRIC MODEL

The parametric model is generated in *Grasshopper* parametric modelling environment, which is a
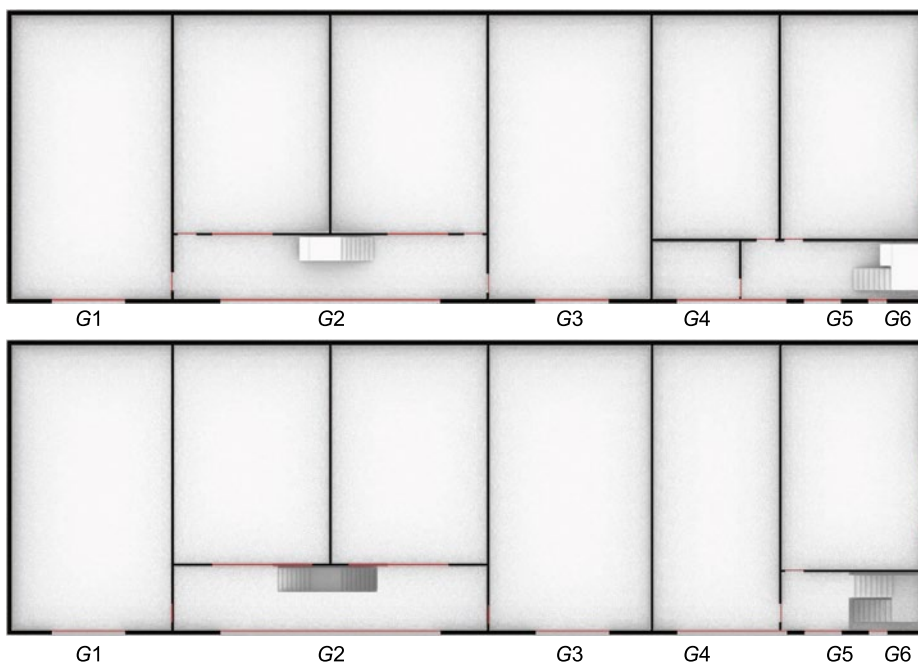
Fig. 1. Notations of the existing glazing

Fig. 2. The measuring grids glazing with their surroundings
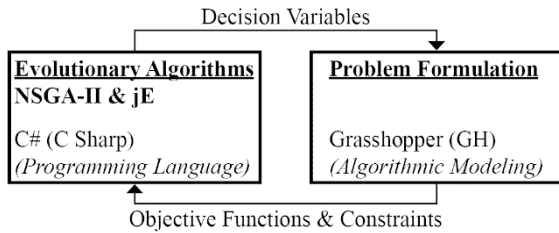
Fig. 3. The workflow diagrams

plug-in developed for *Rhinoceros 3D* software. In this study, we focus on a building within the boundaries of Yasar University campus that has measures of 50 m (width) and 16 m (depth).

As shown in Fig. 1, the building skin includes seven curtain-wall type glazing elements. The total height of the building is 5.80 m. The height of the glazing elements is fixed at 5.80 m, and widths are defined as decision variables.

The model considers the centrelines of each glazing as relative reference lines in the 1-D scal-

Table 2. Decision Variables

Notation	Type	Range, m
G_1	Real	[4.00, 10.00]
G_2	Real	[10.00, 16.40]
G_3	Real	[3.00, 10.00]
G_4	Real	[4.00, 7.40]
G_5	Real	[1.00, 3.00]
G_6	Real	[0.60, 1.70]
G_7	Real	[4.00, 13.00]

ing process, since the height of the building is fixed. A complete list of the initial dimensions of each glazing is presented in Table 1.

3. PROBLEM FORMULATION

3.1. Objective Functions

We consider two objective functions: minimizing of the facade system's construction cost $\left(C_{facade}\right)$ and increasing the penetration of the daylight into the foyer area. Measurement grids are created for each room in relation to their floors to measure and evaluate the daylight performance of each floor separately. Measurement grids are shown in Fig. 2. Daylight autonomy (*DA*) metric [10] is used to optimize the interior daylight distribution. The notations related to decision variables are shown in Table 2. We formulate the problem as a multi-objective optimization problem (MOP) as follows:

$$Min(\frac{1}{P_{DA}}, C_{facade}), \text{ where}$$

$$P_{DA} = \sum_{i=1}^{n} \begin{cases} 0, E_i < E_{min} \\ 1, E_i \geq E_{min} \end{cases}. \qquad (1)$$

$$C_{facade} = C_{glazing} + C_{wall}, \qquad (2)$$

where C_{facade} is the total construction cost of building facade, P_{DA} is the performance of daylight autonomy, $C_{glazing}$ is the total cost of glazing, C_{wall} is the total cost of exterior walls, E_{min} is the

Step 1: set $t = 0$ and construct a random parent population P_t with N size;

Step 2: generate offspring population Q_t with N size, perform *SBX* and *PM*;

Step 3: if termination criterion is satisfied, stop and return P_t;

Step 4: in order to combine parent and offspring populations, set $R_t = P_t \cup Q_t$;

Step 5: to find the non-dominated fronts $f_1, f_2, .., f_k$, apply the fast non-dominated sorting algorithm to R_t;

Step 6: for $i = 1, .., k$, do following steps:

    Step 6.1: for solutions in f_i, calculate crowding distance;

    Step 6.2: create P_{t+1} as follows:

- if $|P_{t+1}| + |f_i| \le N$, then set $P_{t+1} = P_{t+1} \cup f_t$;
- if $|P_{t+1}| + |f_i| > N$, then add the least crowded $N - |P_{t+1}|$ solutions from f_i to P_{t+1};

Step 7: use crowded tournament selection to choose parents from P_{t+1}. Then, employ *SBX* and *PM* to P_{t+1} in order to get offspring population Q_{t+1} with N size;

Step 8: set $t = t + 1$ and go to *step 3*.

Fig. 4. Steps of NSGA-II

specified threshold for daylight performance evaluation, E_i is the illuminance at a sample point in a specific hour provided that average spatial daylight autonomy is

$$sDA > 50\%. \qquad (3)$$

3.2. Daylight Objective

DA is considered as a metric for calculating daylight performance, mentioned in [10], which resulted in many discussions in the early 1900s. Later on, it was integrated into the building standards and considered as a standard for buildings since then [11]. *DA* is formulated as the percentage of annual daytime hours that a specific point is above a specified illuminance level. For this study, the specific illuminance threshold (E_{min}) is defined as 300 lx in relation to Leadership in Energy and Environmental Design (LEED) criteria.

DA is calculated using values that are obtained by using the simulation software named *Radiance*. To create a workflow between *Radiance* and *Rhinoceros* CAD program, *DIVA*, which is a plugin for *Grasshopper,* is used to calculate *DA* values. *DA* evaluates the hourly illuminance values for each measurement point in relation to the specified illuminance level, considering the working hours. For each hour, the values of 1 and 0 are assigned, considering their relationship to the specified threshold value. Hours above the threshold considered as 1, else are considered as 0, and the ratio is defined considering the summation of these hours and all working hours during the year. For this study, the working hours are defined as from 08:00 a.m. to 17:00 p.m. The *DA* calculation is expressed as follow:

$$DA(Point_a) = \sum_{i=1}^{n} \begin{Bmatrix} 0, E_i < E_{min} \\ 1, E_i \ge E_{min} \end{Bmatrix}. \qquad (4)$$

For daylight calculations, we adopt *DA* values. Since the calculation of DA includes direct sunlight calculations, thus leads to more accurate results considering obsolete metrics, such as daylight factor [11]. The building has two south-facing elements, this situation creates a suitable environment for using *DA* to calculate daylight performance of a focused building, since it includes the direct sunlight calculations as well as the location of the building. For our study, we define the measurement grid as 0.5 m from each wall and 0.8 m above the floor plates. Our objective is determined to obtain the LEED criterion that achieves a minimum of 50 % of the space above 300 lx during working hours throughout the year [11].
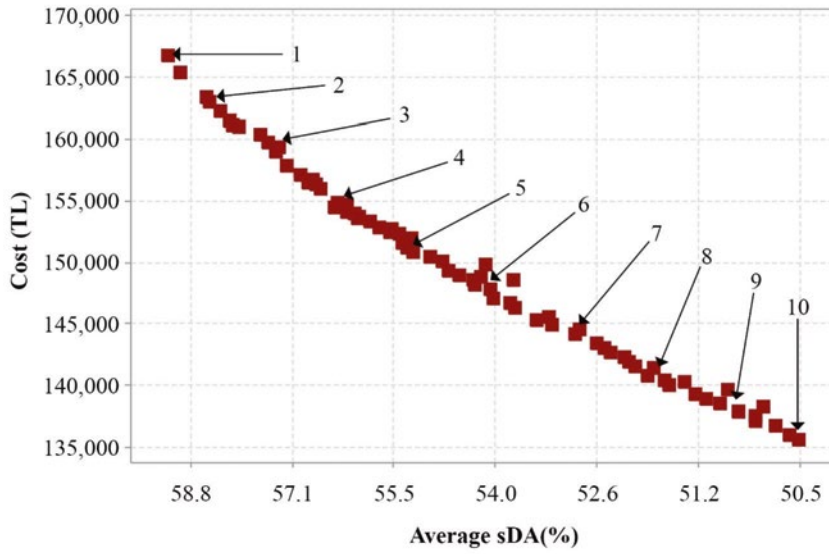
Fig. 5. Pareto front chart of non-dominated solutions at the 50th generation
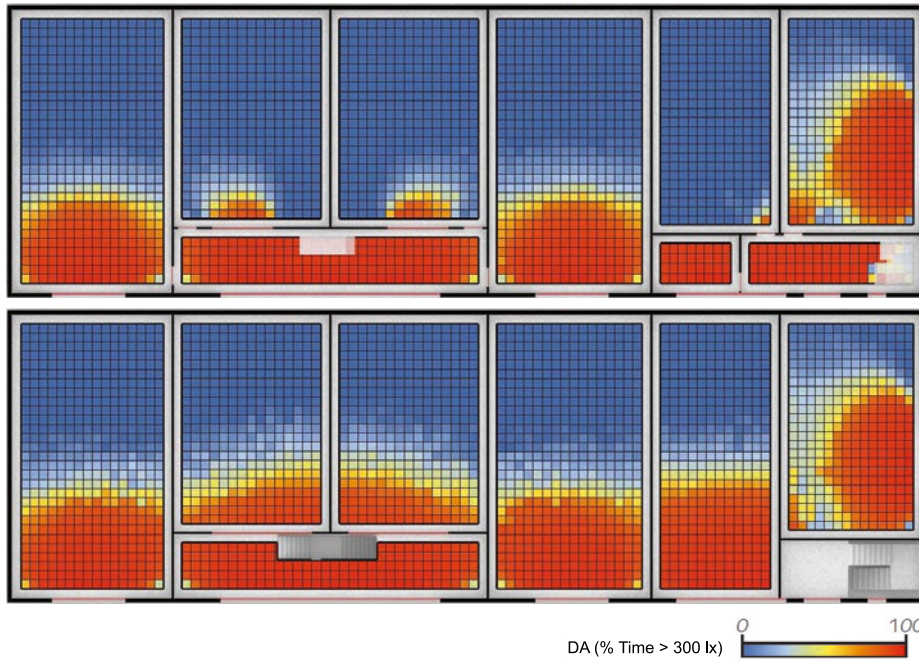
Fig. 6. *DA* measurement results of the initial state of the building

3.3. Cost Objective

As shown in the eq. (5), C_{facade} can be found by adding the total construction cost of walls (C_{wall}) and the total cost of glazing elements ($C_{glazing}$).

$$C_{facade} = C_{wall} + C_{glazing}. \qquad (5)$$

$$C_{wall} = C_{uw} \cdot A_{wall}. \qquad (6)$$

$$C_{glazing} = C_{ug} \cdot A_{glazing}. \qquad (7)$$

where A_{wall} is the total area of exterior walls, $A_{glazing}$ is the total area of glazing, C_{uw} is the unit price of glazing per sq. m, C_{ug} is the unit price of wall per sq.m.

These costs depend on the area of the relative element in relation to the unit cost per square meter.

3.4. Constraint

As shown in eq. (3), there is a constraint related to the calculated *DA* values. In order to satisfy the LEED criterion [11], the minimum value of spatial daylight autonomy (*sDA*) should be larger than 50 %.
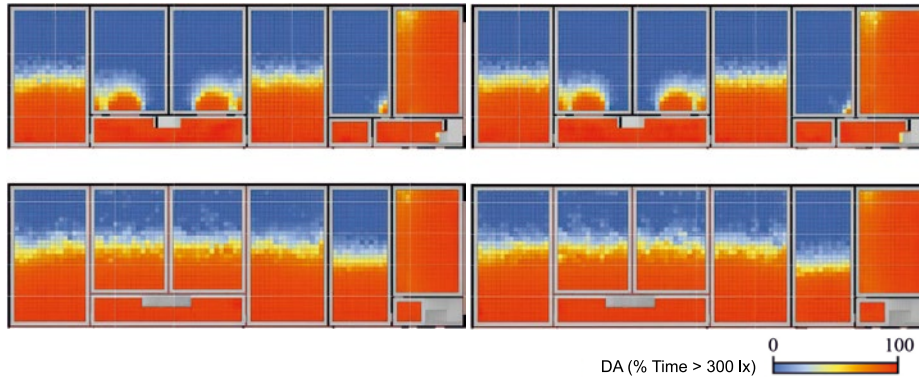
Fig. 7. *DA* measurement results for case 1 and case 2

DA (% Time > 300 lx)
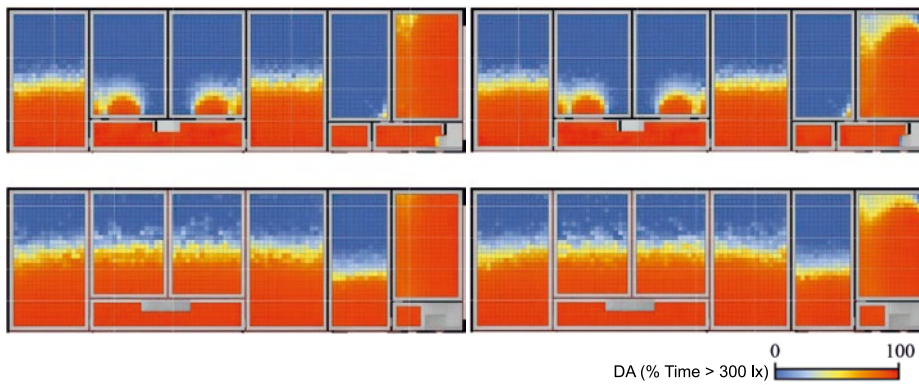
Fig. 8. *DA* measurement results for case 3 and case 4

DA (% Time > 300 lx)
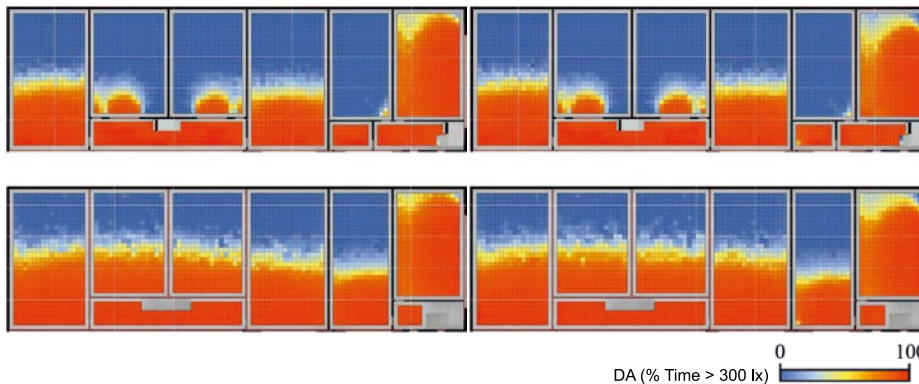
Fig. 9. *DA* measurement results for case 5 and case 6

DA (% Time > 300 lx)

4. EVOLUTIONARY ALGORITHM

In the current literature, there are various studies, which include the multi-objective optimization problems (MOPs). In terms of optimization algorithms, evolutionary algorithms (EAs) can be considered as an effective optimization algorithm type due to its unique way to deal with problems. In this respect, multi-objective evolutionary algorithms (MOEAs) are defined as the implementations of EAs within MOPs. In this research area, NSGA-II [12] and SPEA2 [13] are well-known and effective algorithms. Implementing genetic operators of EAs to MOEAs, several MOEAs are developed for multi-objective architectural problems (MOAPs) [14–20], also in [21]. The process diagram of the workflow shows how to integrate the NSGA-II algorithm into our parametric model in Fig. 3.

In terms of MOEAs, NSGA II, which is developed by [12], can be considered as one of the most powerful algorithms. The outline of NSGA-II is shown in Fig. 4. NSGA-II is known as being capable of dealing with very difficult MOPs. Key features of this algorithm are expressed as follows:

1. To discover non-dominated solutions, it employs $O(MN^2)$ sorting algorithm;

2. In terms of the cuboid volume neighbouring between elements that attend for the same rank value, it calculates the "crowding distance";

3. Using a crowding distance, superior of feasibility, as well as ranking for diversity preserving through binary tournament selection;
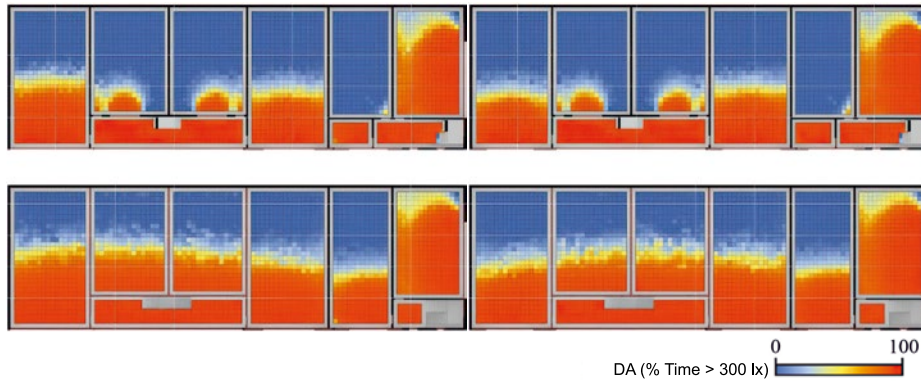
Fig. 10. *DA* measurement results for case 7 and case 8

DA (% Time > 300 lx) 0 — 100
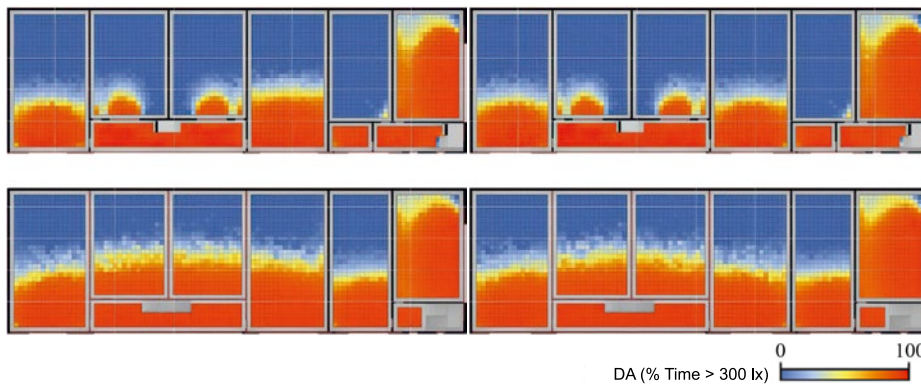
Fig. 11. *DA* measurement results for case 9 and case 10

DA (% Time > 300 lx) 0 — 100

4. Elitism strategy specifically, using the combination of elite parents and offspring members;

5. Utilization of the genetic operator namely, "simulated binary crossover (SBX)" [12];

6. Utilization of polynomial mutation operator (PM) [12].

5. COMPUTATIONAL AND ARCHITECTURAL RESULTS

For calculations, a computer with a data processing speed of 4.4 GHz and 32 GB of DDR4 RAM is used. The population sizes are defined as 100 people. Since the development of a single individual during the optimization process takes approximately 150 s, the algorithm is stopped at the 50th generation that defines our termination criteria. For 5000 function evaluations of the algorithm, the computer is run for approximately 209 hours. The Pareto front chart of non-dominated solutions at the 50th generation for 100 population size is given in Fig. 5.

After the optimization process concluded, we observed that NSGA-II discovered cost values within a range (135617.54–166798.34) TL. In terms of daylight performance, the algorithm suggested results within a range (50.02–59.20) %. The average values for total construction cost and daylight performance are 149499.92 TL and 54.50 %, respectively. Ten results are selected uniformly from the Pareto front and compared with each other, as well as the initial state of the building. In terms of daylight performance and cost objectives, a statement can be made that the decision variables, which are the widths of the exterior glazing elements have a significant effect on total construction cost and interior daylight distribution.

In terms of daylight performance of the building's initial state, the *sDA* values 28 % and 31 % are achieved for the ground floor and the first floor, respectively. The *DA* distribution in relation to the respective floors is shown in Fig. 6 and the values of relative decision variables and objectives for the initial state of the building are presented in Table 3. According to these results, it can be argued that opaque interior walls prevent sunlight to penetrate spaces that do not have a glazing surface. Therefore, both floors are below the daylight constraint $sDA > 50 \%$. The *DA* distribution in relation to the respective floors for each case is shown in Figs. 7–11. The values of relative decision variables and objectives for each case are presented in Table 4 and Table 5.

For the optimization problem, the unit cost of glazing per sq·m (C_{ug}) is defined as 400 TL, and

Table 3. The Decision Variables and Objectives for Initial State of the Building

Notations	Value		Notations	Value
G_1	4.00 m		G_6	1.00 m
G_2	12.00 m		G_7	4.00 m
G_3	4.00 m		sDA	29.5 %
G_4	6.00 m		C_{facade}	–
G_5	2.00 m		R_w	35.7 %

Table 4. The Decision Variables and Objectives for Each Case from 1 to 5

	Case 1	Case 2	Case 3	Case 4	Case 5
C_{facade}	166798.34	163086.34	161044.74	154919.94	150465.54
sDA	59.2 %	58.5 %	58.01 %	56.43 %	55.01 %
R_w	77.8 %	73.1 %	70.6 %	63.5 %	58.8 %
G_1	10.00 m	10.00 m	9.80 m	10.00 m	10.00 m
G_2	16.40 m	16.40 m	16.40 m	16.40 m	16.40 m
G_3	9.60 m	9.80 m	9.80 m	9.80 m	6.00 m
G_4	7.40 m	5.20 m	4.40 m	5.00 m	5.00 m
G_5	1.00 m	1.40 m	1.00 m	1.00 m	1.00 m
G_6	1.00 m	0.60 m	0.60 m	0.60 m	0.60 m
G_7	12.60 m	12.60 m	12.80 m	8.80 m	10.20 m

the unit cost of wall per sq. m (C_{uw}) is defined as 80 TL. Added construction costs, transportation, workmanship, etc. are not taken into account. To enhance the daylight performance results, translucent partition walls (P_T) are employed on the first floor. For the exterior glazing clear glass material is used, which has transmittance value (E_{mat}) of 88 %. For the translucent interior partition walls, double-pane glass material, which has E_{mat} of 65 % is employed.

In terms of daylight performance and cost objectives, a statement can be made that some of the decision variables have a significant effect on total construction cost and interior daylight distribution in comparison to others. For the width of the glazing 2 (G_2) the algorithm selected the largest value of the range in each example. It can be argued that it is a required condition to satisfy the daylight constraint, otherwise the results would be below the required minimum value. Furthermore, for the width of the glazing 7 (G_7), the algorithm did not suggest any values below 8.60 m. Although the minimum value in its range is 4.00 m, the algorithm employed higher values in this range due to glazing 7's loca-

tion and relation to the sunlight has a substantial effect on interior daylight distribution.

On the other hand, for the width of the glazing 6 (G_6), the algorithm employed the minimum value of its range. It can be argued that the effect of G_6 to the interior daylight distribution is relatively small than the other variables. Considering their range, the algorithm selected the maximum possible values for decisions variables of G_1, G_2, G_4. In comparison, the decision variables of G_5 and G_6 are defined in relation to the minimum values of their ranges. According to these results, we can consider that G_5 and G_6 have almost no effect on interior daylight distribution whereas, it greatly affects the total construction cost. The other decision variables mediated between their range to find suitable design solutions.

6. CONCLUSION

In this study, the NSGA-II algorithm is implemented for a building facade design problem in an education building, which described as a real-parameter constrained MOP. We formulated the de-

Table 5. The Decision Variables and Objectives for Each Case from 6 to 10

	Case 6	Case 7	Case 8	Case 9	Case 10
C_{facade}	147867.14	144897.54	140814.34	137844.74	135617.54
sDA	54.1 %	53.2 %	51.9 %	50.7 %	50.0 %
R_w	56.1 %	53.2 %	49.3 %	46.7 %	44.7 %
G_1	10.00 m	10.00 m	5.20 m	4.20 m	4.60 m
G_2	16.40 m	16.40 m	16.40 m	16.40 m	16.40 m
G_3	7.20 m	5.60 m	6.40 m	6.40 m	4.60 m
G_4	4.00 m	4.20 m	5.00 m	4.40 m	4.60 m
G_5	1.20 m	1.00 m	1.00 m	1.00 m	1.00 m
G_6	0.60 m	0.60 m	0.60 m	0.60 m	0.60 m
G_7	8.40 m	8.40 m	8.60 m	8.60 m	8.60 m

sign task to reach the minimum value of the total construction cost, while contributing to the daylighting aspects of interior space, using the daylight autonomy as the performance metric. Throughout the study, seven decision variables related to glazing widths and one constraint are taken into consideration to develop the best possible set of solutions for two objectives. As the results show, considering the termination criteria, the algorithm is efficient enough to demonstrate eligible facade design alternatives.

The implementation of numerous important design aspects that the facade design process contains is achieved. However, additional incorporation of various aspects related to performance may bring benefits. As an example, an investigation of using different construction materials for glazing parts of the facade can be a direction for further study. Last but not least, dynamic metrics for daylight performance, such as the daylight autonomy (*DA*), presents more accurate results, but the simulation takes longer time. There is no doubt that static metrics, mainly daylight factor (*DF*), require less computation time compared to *DA*. At this point, dealing with such a long simulation time for these metrics should be discussed, considering the local climate and the buildings' direct exposure to sunlight.

REFERENCES

1. Sariyildiz I. Performative computational design. in Keynote speech in: Proceedings of ICONARCH-I: International congress of architecture-I, Konya, Turkey, 15–17 November 2012. 2012. Selcuk University.

2. Cruz-Correia R., et al., Integration of Hospital data using Agent Technologies–a case study. Ai Communications, 2005. V18, #3, pp. 191–200.

3. Joseph A. and M. Rashid, The architecture of safety: hospital design. Current opinion in critical care, 2007. V13, #6, pp. 714–719.

4. Walch J.M., et al. The effect of sunlight on postoperative analgesic medication use: a prospective study of patients undergoing spinal surgery. Psychosomatic Medicine, 2005. V67, #1, pp. 156–163.

5. Ulrich R.S., et al. Stress recovery during exposure to natural and urban environments. Journal of Environmental Psychology, 1991. V11, #3, pp. 201–230.

6. Pechacek C.S., M. Andersen, and S.W. Lockley Preliminary method for prospective analysis of the circadian efficacy of (day) light with applications to healthcare architecture. Leukos, 2008. V5, #1, pp. 1–26.

7. Nabil A. and J. Mardaljevic Useful daylight illuminances: A replacement for daylight factors. Energy and buildings, 2006. V38, #7, pp. 905–913.

8. Aripin S. 'Healing architecture': A study of daylight in public hospital designs in Malaysia. 2010.

9. Shikder S.H., M. Mourshed, and A.D. Price, Optimisation of a daylight-window: hospital patient room as a test case. 2010.

10. Moon P. and D.E. Spencer, Illumination from a non-uniform sky. Illuminating Engineering, 1942. V37, #10, pp. 707–726.

11. Mardaljevic J., L. Heschong, and E. Lee, Daylight metrics and energy savings. Lighting Research and Technology, 2009. V41, #3, pp. 261–283.

12. Deb K., et al. A fast and elitist multiobjective genetic algorithm: NSGA-II. IEEE transactions on evolutionary computation, 2002. V6, #2, pp. 182–197.

13. Zitzler E., M. Laumanns, and L. Thiele. SPEA2: Improving the strength Pareto evolutionary algorithm. in Eurogen. 2001.

14. Ekici B., et al. Addressing the high-rise form finding problem by evolutionary computation. in 2015 IEEE Congress on Evolutionary Computation (CEC). 2015. IEEE.

15. Ugurlu C., et al. Evolutionary computation for architectural design of restaurant layouts. in 2015 IEEE Congress on Evolutionary Computation (CEC). 2015. IEEE.

16. Ugurlu C., et al. Identification of sustainable designs for floating settlements using computational design techniques. in 2015 IEEE Congress on Evolutionary Computation (CEC). 2015. IEEE.

17. Cubukcuoglu C., et al. Multi-objective harmony search algorithm for layout design in theatre hall acoustics. in Evolutionary Computation (CEC), 2016 IEEE Congress on. 2016. IEEE.

18. Cubukcuoglu C., et al., A Multi-Objective Harmony Search Algorithm for Sustainable Design of Floating Settlements. Algorithms, 2016. V9, #3, p. 51.

19. Cubukcuoglu C., et al. Multi-objective optimization through differential evolution for restaurant design. in Evolutionary Computation (CEC), 2016 IEEE Congress on. 2016. IEEE.

20. Dursun O., B. Ekici, and S. Sarıyıldız. Time-cost optimization at the conceptual design stage using differential evolution: Case of single family housing projects in Germany. in 2015 IEEE Congress on Evolutionary Computation (CEC). 2015. IEEE.

21. Kirimtat A., et al. Multi-objective optimization for shading devices in buildings by using evolutionary algorithms. in Evolutionary Computation (CEC), 2016 IEEE Congress on. 2016. IEEE.
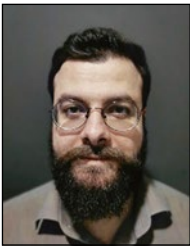
Arda Agirbas,
M. Sc., Artiyans Architecture. His research interests include digital design methods and multi-objective evolutionary optimization in the field of architecture. With a special focus on digitally-driven architectural form-finding and optimization studies, he especially explores the effects of digital concepts and methods in the context of architectural design

Ebru Alakavuk,
Ph.D., Yasar University. She studies on sustainable buildings, advanced facade systems and advanced construction systems

COMPARATIVE ASSESSMENT OF LIGHT-BASED INTELLIGENT SEARCH AND OPTIMIZATION ALGORITHMS

Bilal Alatas[*] and Harun Bingol

Department of Software Engineering, Firat University, Turkey
E-mail: [*]balatas@firat.edu.tr

ABSTRACT

Classical optimization and search algorithms are not effective for nonlinear, complex, dynamic large-scaled problems with incomplete information. Hence, intelligent optimization algorithms, which are inspired by natural phenomena such as physics, biology, chemistry, mathematics, and so on have been proposed as working solutions over time. Many of the intelligent optimization algorithms are based on physics and biology, and they work by modelling or simulating different nature-based processes. Due to philosophy of constantly researching the best and absence of the most effective algorithm for all kinds of problems, new methods or new versions of existing methods are proposed to see if they can cope with very complex optimization problems. Two recently proposed algorithms, namely ray optimization and optics inspired optimization, seem to be inspired by light, and they are entitled as light-based intelligent optimization algorithms in this paper. These newer intelligent search and optimization algorithms are inspired by the law of refraction and reflection of light. Studies of these algorithms are compiled and the performance analysis of light-based intelligent optimization algorithms on unconstrained benchmark functions and constrained real engineering design problems is performed under equal conditions for the first time in this article. The results obtained show that ray optimization is superior, and effectively solves many complex problems.

Keywords: optimization, optics inspired optimization, ray optimization, artificial intelligence

1. INTRODUCTION

Optimization is present everywhere in our lives – from engineering to industrial design, from business planning to travel planning [1]. Optimization has played an even more important role in our lives recently. Evolutionary and population-based optimization methods are very popular and widely used in many engineering fields [2]. These optimization techniques choose the best of the many available options intelligently, and they provide a suitable environment for the solution of problems [1]. Most optimization algorithms require a mathematical model for the system model. Establishing a mathematical model for complex systems is often difficult. Even if the model is established, the solution time cannot be used due to the huge cost [3]. That is, the design of an optimization algorithm has a challenging process, which is caused by physical events to obtain appropriate global and local search operators [2].

Classical optimization methods may be insufficient and unsuitable for solving complex nonlinear large scaled search and optimization problems. Classical methods are not effective in adapting them to the problems of interest. This, in many cases, requires some assumptions that may be difficult to confirm. Often, due to the natural solution mechanisms of solving classical search methods, the problem concerned is modelled such that the method will manage it. The strategy for solving classical methods usually depends on the types of objectives and constraints, as well as on the types of decision variables. Their effectiveness also strongly depends

on search space, the number of constraints, and the number of decision variables. Another important shortcoming is that they do not stand for common target strategies for different types of constraint functions and variables. In other words, classical methods solve models that have a specific type of objective function or constraint functions. However, many optimization problems, such as management, sports, engineering, economy, computer require concurrent different types of objective functions, constraint functions, and decision variables, simultaneously. Intelligent optimization and search algorithms are proposed and efficiently used in many different fields, because they are computationally powerful, and their transformations are easy [3].

General purposed artificial intelligence optimization algorithms are divided into various groups, such as biology-based, social-based, chemical-based, physics-based, music-based, mathematics-based, sports-based, swarm-based, plant-based, light-based, and water based. Their combinations can also be considered as a hybrid category. OIO and RO are the newest artificial intelligence optimization algorithms inspired by the light behaviour. OIO is inspired by the optical characteristics of convex and concave mirrors that can be used for searching the best solutions for different types of optimization and search problems. When the light rays fall on the convex mirror, they are reflected from the principal axis, and divergence occurs. When they hit a concave mirror, these rays are reflected in the direction of the principal axis, and convergence occurs. The exploration and exploitation capabilities of OIO are adjusted considering the convex and concave mirror phenomena [4, 5]. According to light refraction law of Snell, light is refracted when it passes through environments with different luminance factors. Inspired by this feature of the light in the RO, it uses the light as a candidate solution. The transition of the ray is used to obtain the optimal solutions [6].

RO was used to reduce the weight of truss under necessary constraints by Kaveh and Khayatazad in 2013 [7]. During this study, numerical results were compared for the five truss structure, and it was observed that the obtained truss weight was at a satisfactory level. RO gave better results than GA [8], ACA [9], BBBC [10], and PSO [11] algorithms. However, its performance was slightly lower than HPSACO [12], which is a hybrid method. Kaveh and his colleagues developed RO in 2013 and ad-

opted a new approach to produce new candidate solutions that had no restrictions on the number of variables of the problem interested. That is why there was no need to group the variables in the algorithmic process of RO [13]. With this new RO developed, a better balance between the exploration and exploitation was achieved. In addition, the algorithm was improved considering transport constraints [14]. Using the RO in 2014, an effective hybrid method for the shape and size optimization of the truss structures was implemented [14]. For this hybrid developed algorithm where PSO, HS, and RO were used together [14]. In this hybrid method, PSO algorithm was used as the main engine. While the movement vector was developed by the RO, HS was used to enhance the local search skill. The experimental results of this hybrid method showed that it gives better results than the existing mathematical and artificial intelligence optimization algorithms [14].

The OIO algorithm was applied to constrained problems, namely mechanical real engineering problems by Kashan in 2015 [5]. These tests were performed with five real-world engineering problems. The performance of OIO was compared with many artificial intelligence optimization methods, such as CPSO [15], PSRE [16], RSPSO [17], IHS [18], FSA [19], and SES [20]. OIO was reported as the outperformed algorithm among others [5]. In 2015, a master thesis was presented on the development of a new method for solving combinatorial optimization problems with permutation-based solution structures using the OIO method [21]. In 2015, a master thesis was published on the design of image processing methods using OIO [22]. In 2015, the OIO algorithm was used to solve the traveling salesman problem by Badrloo and Kashan [23]. In 2015, Badrloo and Kashan used the OIO method to solve the combinatorial quadratic assignment problem [24]. In 2016, OIO algorithm was used for routing and clustering in wireless sensor networks [25]. The cluster head choice and routing problem in wireless sensor networks is a known optimization problem due to the high computational complexity of large-scale networks. In their study, OIO was adapted for cluster head choice problem considering distance, energy, and node level parameters.

The OIO based routing method was proposed to calculate the path to the base station from each cluster head, considering the same parameters, such as distance, energy, and node level. The perfor-

mance evaluation of OIO was extensively evaluated and compared with other routing methods. OIO algorithm was shown to be more successful than the other techniques [25]. The conventional techniques, such as HF [26], EADC [27], and DHCR [28] were not suitable for cluster head choice and routing problems. As the size of the network increased, the performance of these conventional techniques rapidly fell. In recent studies, it was suggested that artificial intelligence method could be developed that maximizes the coverage area and distributes the nodes to minimize the number of nodes [25]. In 2016, optimal load frequency controller gains were optimized by Ozdemir and Ozturk using an OIO algorithm in a two-area power system. In this application, OIO was used to find optimal controller parameters of PID that controlled the frequency in a two-area power system [29]. The performance of the OIO for this problem was compared with the performance of the PSO and bacteria foraging optimization algorithm [30]. It was noted that OIO is better than these algorithms in terms of values of maximum blackout and settlement time. It was suggested that the optimal PID that adjusts itself could be performed to increase the practical work on the use of OIO in this way [30].

Intelligent algorithms for optimization and search for solutions for effective solution of problems of interest are proposed. One of the important current trends in the field of intelligent algorithms is the development of new search methods based on light. Concepts, events, and processes in light behaviours seem to be an inspiring guide for the development of effective optimization algorithms. This work aims to review the most important concepts of new existing two light-based intelligent optimization methods and their specific characteristics in the frame of complex optimization problems. The performances of light-based artificial intelligence optimization algorithms are also compared for the first time under equal conditions using unconstrained benchmark problems and constrained real engineering problems in this study.

2. METHODS

Nature has always been a good teacher for people. For instance, the invention of radar has been possible by the behaviour of the bats. Intelligent optimization methods inspired by the behaviour of natural beings or natural phenomena are used

to solve problems that take a long time or mathematical models cannot be derived. In many problems, the solution search space is infinite or so large that all candidate solutions cannot be evaluated. For this to be acceptable, it is necessary to evaluate the solutions and find a good solution. Evaluating solutions in such a way that they are acceptable for such problems means evaluating "some solutions" in the entire solution space. The way some solutions are chosen and how they are selected varies based on artificial intelligence method [31].

The solution proposed by artificial intelligence optimization techniques for solving the problem may be perceived as good, global, or near-global optimal solution [31]. Artificial intelligence optimization algorithms are computational methods that are defined to find what is effective from various alternative actions to achieve any purpose or reach a specified goal.

Artificial intelligence optimization algorithms are categorized according to whether they are inspired by nature or not, a number of candidate solution they iterate is one or more, the objective function is dynamic or static, the memory structure is used or not, and they use single or multiple neighbourhood structures.

The reasons for the need to use artificial intelligence optimization algorithms are:

a) The optimization problem may have a structure in which the optimal solution finding process cannot be defined;

b) In terms of clarity, intelligent search algorithms can be much simpler in terms of decision makers;

c) Intelligent optimization algorithms can be used as part of the learning and precise solution finding process;

d) Definitions made using mathematical formulas often ignore the most difficult parts of real-world problems; inaccurate data used to determine model parameters can lead to greater errors than the suboptimal solution that the artificial intelligence optimization approach can produce [32].

General purposed artificial intelligence optimization algorithms are divided into various groups, such as biology-based, social-based, chemical-based, physics-based, mathematics-based, music-based, sports-based, swarm-based, plant-based, light-based, and water based. Their combinations can also be considered as hybrid category.
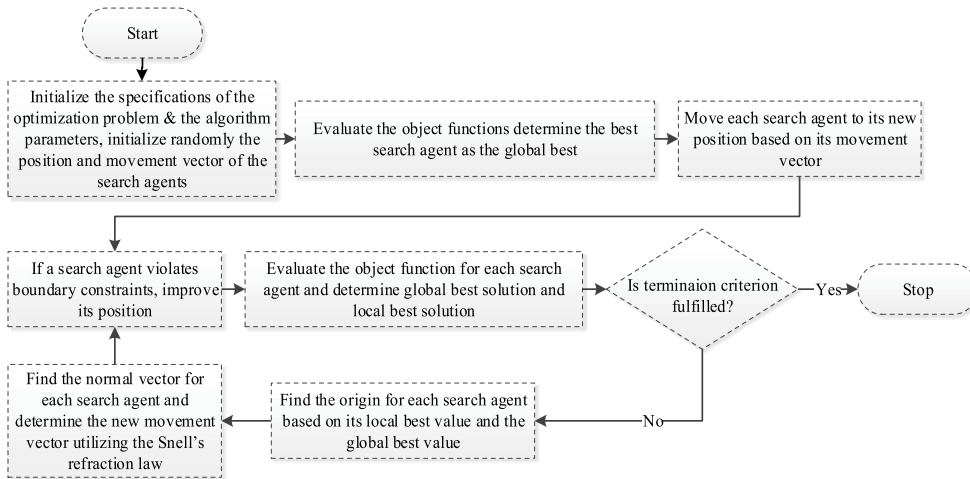
Fig. 1. The flowchart of the RO

All these population-based iterative methods follow a balance between exploitation and exploration as iterations progress. In general, exploration will be more effective in the first stages of the iteration, but exploitation will be strengthened towards the final iterations.

2.1. Ray Optimization

RO is a population-based general purposed stochastic artificial intelligence optimization and search algorithm proposed by Kaveh and Khayatazad in 2012 [6]. The light, which is also a natural event, is refracted and changes direction according to the law of refraction of light when passing from the light environment into a dark environment. Inspired by this feature of the light in the RO, it uses rays belonging to the light as a candidate solution. This behaviour of light helps to explore the search space in the first iterations, while it helps converge to the optimal solution in the last stages [6]. The optimization process ends when predetermined criteria are satisfied. If the criteria are not met, the optimization process continues, and the candidate solutions are moved to their new location. The steps are iterated until one of the defined criteria is met. The flowchart of the RO is shown in Fig. 1 [6].

2.2. Optics Inspired Optimization

OIO is a light-based physics inspired artificial intelligence optimization algorithm proposed by Kashan [4, 5]. Optics examines light properties, its behaviour, and interaction with matter. Practical applications of optics include mirrors, lenses, telescopes, microscopes, technology. The curved or spherical mirror has a curved concave or convex reflective surface. Most curved mirrors are shaped like a spherical piece.

Since the exploration and exploitation capabilities of OIO are controlled by mirror phenomena [4, 5], as described in the introduction, the reflection surface of the mirror functions as a search function. The flowchart of OIO is shown in Fig. 2.
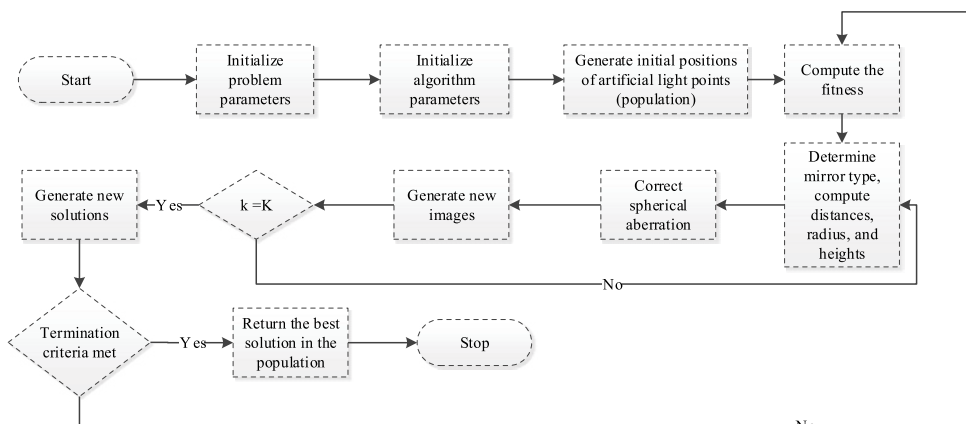
Fig. 2. The flowchart of OIO

Table 1. Algorithm Performances in Benchmark Functions

Benchmark function	Optimization algorithms				
	GEN	*GEN_S*	*GEN_S_M_LS*	*OIO*	*RO*
Griewank *n*=2	18838(0.91)	3111(0.91)	1652(0.99)	1825.94	1091(0.98)
Sphere *n*=3	9900	3040	1281	506.72	452
Goldstein and Price *n*=2	1478	1478	1325	1071.4	451
Exponential *n*=2	938	936	807	572.14	136
Exponential *n*=4	3237	3237	1496	1376.18	382
Exponential *n*=8	3237	3237	1496	2889.08	1287
Exponential *n*=16	8061	8061	1945	28994.14	17236(0.46)
Cosine Mixture *n*=4	2105	2105	1539	1673.7	802
Bohachevsky 1 *n*=2	3992	3356	1615	567.36	677
Bohachevsky 2 *n*=2	20234	3373	1636	620.7	582
Rastrigin *n*=2	1533(0.97)	1523(0.97)	1381	753	1013(0.98)

3. RESULTS

3.1. Results within Unconstrained Benchmark Functions

Researchers often use benchmark functions to compare the search and optimization algorithms [33]. There are many benchmark problems that are defined as unimodal, multimodal, and composite. In addition to complex mathematical expressions, the benchmark functions have many local and global minimums. Because of these features, the performance of artificial intelligence optimization algorithms is evaluated under equal conditions. In this paper, the performances of light-based intelligent search and optimization algorithms within Griewank, Cosine Mixture, Goldstein and Price, sphere, exponential, Bohachevsky1, Bohachevsky2, and Rastrigin benchmark functions were compared.

The performance comparison of OIO and RO, which are light-based optimization algorithms, is shown in Table 1 using benchmark functions. Light-based optimization algorithms are also compared with genetic algorithm and some of its variants in this table [6]. The number of function evaluations to achieve the predefined accuracy rate ($\varepsilon = f_{min} - f_{final} = 10{-}4$) is listed in this Table. Values written in parentheses in Table 1 show the ratio of successful runs of the algorithms according to this predefined accuracy rate. The absence of the parentheses shows that the algorithm is successful in all runs. During the experiments, problem dimension for sphere function was defined as 3, problem dimension for the Cosine mixture function was de-

fined as 4, and problem dimension for other functions was defined as 2. The number of populations was 20, the number of function evaluations (NFE) was 20000, and the number of independent runs was selected as 50. In addition, the performance of light-based optimization algorithms was measured by choosing the exponential test function dimension 2, 4, 8, 16 to check the performance in high problem dimensions. When the problem dimension is 16 and the population number is 100 in the exponential function, NFE is determined to be 50000 and the obtained results are listed in Table 1. In this Table, GEN, GEN_S, GEN_S_M_LS are variants of genetic algorithms whose performance has been reported promising [10].

When examined in detail in Table 1, it is seen that RO in the Griewank test function gives better results than all other artificial intelligence optimization algorithms. The OIO algorithm produced better solutions in terms of the ratio of successful runs. Light-based optimization algorithms are much more successful than other methods within sphere, Goldstein and Price, Bohachevsky 1, Bohachevsky 2, and exponential for *n*= 2 and *n*= 4. For exponential *n*=8, RO was seen to perform better than all other methods. However, it is impossible to generalize that the light-based methods are better than all other methods, because the OIO algorithm performed worse results in the exponential test function than the GEN_S_M_LS algorithm. It was seen that RO was the most successful method in the cosine mixture test function. However, it was that the OIO algorithm was more successful than the GEN and GEN_S algorithms, but it was observed that it

Table 2. Obtained Optimum Results from Different Methods for Tension/Compression Spring Design Problem

Method	Design variable and cost			
	x_1	x_2	x_3	f_{cost}
RO	0.051370	0.349096	11.76279	0.0126788
OIO	0.054557	0.429089	8.053812	0.0128404
Belegundu	0.050000	0.315900	14.250000	0.0128334
Arora	0.053396	0.399180	9.185400	0.0127303

was more unsuccessful than the GEN_S_M_LS algorithm. OIO seemed the best algorithm for Rastrigin function.

3.2. Results within Real-World Engineering Design Problems

The Tension/Compression Spring Design engineering design problem was first introduced by Belegundu and Arora [7]. Minimizing the weight of a tension/compression spring subjected to constraints on a minimum deflection, surge frequency, and shear stress [7] was aimed at this problem. The problem has four non-linear inequality constraints. It also has three continuous variables.

During the experiments, the number of populations was 40, NFE was 10000, and the number of independent runs was 50. The performance of light-based optimization algorithms under equal conditions were evaluated. The design variable values of the problem and the best cost values are shown in Table 2. In addition, mean values and standard deviation values obtained from the algorithms for this problem are listed in Table 3.

As shown in Table 2, RO performance is better than OIO algorithm for best results (f_{cost}). It cannot be concluded that all the light-based optimization algorithms are better than the other algorithms. Because during the experiments, OIO algorithm did not find better results than Belegundu and Arora [34]. However, as shown in Table 3, OIO gave more stable results than the RO algorithm according to the obtained standard deviation values and mean values.

The main object in welded beam engineering problem is to obtain minimum manufacturing cost of the welded beam subjected to constraints on shear stress, bulking load, bending stress, end deflection, and side constraint [7, 30, 35]. It also has four continuous variables.

During the experiments, the number of populations was 40, NFE was 10000, and the number of

Table 3. Mean and Standard Deviation Values for Tension/Compression Spring Design

Method	Mean and standard deviation	
	f_{mean}	*Std. dev.*
RO	0.13547	0.001159
OIO	0.01326	0.000297

independent runs was 50. The performance of the light-based optimization algorithms was tested under equal conditions. The design variable values of the problem and the best cost values are shown in Table 4. In addition, obtained mean values and standard deviation values are shown in Table 5. The success of light-based optimization algorithms was compared with other mathematical optimization algorithms.

As shown in Table 4 and Table 5, RO was more successful than OIO algorithm in terms of best cost result and mean cost result, respectively. Table 5 shows that light-based optimization algorithms are much more successful than other methods such as Approx, David, Simplex, and Random [35]. As shown in Table 4, light-based optimization algorithms were experimentally demonstrated that they are less fitted to the local minimum and better converged to the global minimum than other methods used in testing in real-world engineering problems.

4. DISCUSSION

For real world optimization problems, there are many intelligent methods that have been inspired by nature or other phenomenon. Almost all of the intelligent optimization algorithms perform with meta-heuristic population-based search procedures that incorporate random selection and variation. These algorithms should have two key components: exploration and exploitation.

RO and OIO are two of the methods inspired by the concepts, events, and processes in light behaviours, and they are entitled as light-based in-

Table 4. Optimum Results for Welded Beam

Method	Design variable and cost				
	x_1	x_2	x_3	x_4	f_{cost}
RO	0.2037	3.5285	9.0042	0.2072	1.7353
OIO	0.1914	3.8049	9.1382	0.2052	1.7605
Approx	0.2444	6.2189	8.2915	0.2444	2.3815
David	0.2434	6.2552	8.2915	0.2444	2.3841
Simplex	0.2792	5.6256	7.7512	0.2796	2.5307
Random	0.4575	4.7313	5.0853	0.6600	4.1185

Table 5. Mean and Standard Deviation for Welded Beam

Method	Mean and standard deviation	
	f_{cost}	Std Dev
RO	1.9083	0.173744
OIO	2.0381	0.167309

telligent optimization algorithms in this paper. According to the experimental results obtained, RO algorithm seems better than OIO in both unconstrained benchmark test functions results and constrained real-world engineering problems. However, it is not the best algorithm when compared the other methods. According to the No-Free-Lunch theorem, there is no single universally most efficient method for every types of optimization problem. Though theoretically solid, No-Free-Lunch theorem may have limited impact in practice because solving all problems and taking average performance are not needed. One of the main targets of optimization problems in practice is to inquire to obtain high-quality possible or optimal solution in an acceptable duration. For some types of problem, some methods can outperform the others. Furthermore, balance between exploration and exploitation is needed so that a method can achieve good performance. However, obtain such a balance is not resolved. No method claims that such a balance has been achieved. This balancing is a hyper optimization problem that depends on many factors, such as the working mechanism of a method, its parameter settings, controlling of these parameters. Furthermore, such balance may not universally exist, and it may depend on the interested problem.

Researchers do not aim to develop a single most successful method to solve all types of problems. They intend to propose more successful versions of the methods and more new methods based on untested phenomena in the nature. Furthermore,

values of parameters of the algorithms affect the performance. Setting the right fine-tuned values is essential for better performance. Setting parameters is still an active research area.

4. CONCLUSIONS

Light-based optimization methods and literature reviews based on these algorithms were compiled for the first time in this study. The performances of these algorithms were tested using unconstrained benchmark functions and constrained real-world engineering problems. Light-based optimization algorithms were also compared with other intelligent search and optimization methods, such as GA and its variants. The success of light-based optimization algorithms was experimentally proven.

The performance of light-based optimization algorithms in constrained real-world engineering problems was evaluated. During these tests, welded beam problem and tension/compression spring design problem were used. The performances of light-based optimization algorithms were compared for the first time under equal conditions. In the tension/compression spring design problem, RO outperformed all other methods, including the OIO algorithm. However, in this problem, the OIO algorithm could not obtain better results than other methods. In this context, all the light-based optimization algorithms did not yield better results than the other artificial intelligence methods in the literature within the problem of the tension/compression spring design. In the welded beam problem, it was seen that the light-based optimization and search methods better converged to the global minimum than the other methods. Another important consequence of this is that an artificial intelligence method that yields good results in a constrained real engineering problem cannot be proven to yield good results

in all other constrained and unconstrained problems and functions.

To the best of our knowledge, there is not any light-based artificial intelligence optimization algorithm developed in the literature other than the RO and OIO algorithms. In terms of performance of light-based optimization algorithms, RO algorithm, when both unconstrained benchmark test functions result and constrained real-world engineering problems tests are taken into consideration, usually converges better to the global solution. Light-based optimization algorithms are very new, and the obtained results are based on their classical main versions. In future works, better results can be obtained by proposing new distributed, hybrid, adaptive, and parallel versions using optimized parameters. Chaos theory and quantum computing features and capabilities can also be built into these methods to improve performance.

REFERENCES

1. Hussain K., Salleh M.N. M., Cheng S., Shi Y., "Metaheuristic research: a comprehensive survey", 2018, Artificial Intelligence Review, pp. 1–43.

2. Nabaei A., Hamian M., Parsaei M.R., Safdari R., Samad-Soltani T., Zarrabi H., A. Ghassemi, "Topologies and performance of intelligent algorithms: a comprehensive review", Artificial Intelligence Review, 2018. V49, #1, pp. 79–103.

3. Alatas B., "Chaotic bee colony algorithms for global numerical optimization", Expert Systems with Applications, 2010. V37, #8, pp. 5682–5687.

4. Kashan A. H., "A new metaheuristic for optimization: Optics inspired optimization", Computers & Operations Research, 2015. V55, pp. 99–125.

5. Kashan A. H., "An effective algorithm for constrained optimization based on optics inspired optimization (OIO)", Computer-Aided Design, 2015. V63, pp. 52–71.

6. Kaveh A., Khayatazad M., "A new meta-heuristic method: ray optimization", Computers & structures, 2012. V112, pp. 283–294.

7. Kaveh A., Khayatazad M., "Ray optimization for size and shape optimization of truss structures", Computers & Structures, 2013. V117, pp. 82–94.

8. Tsoulos I. G., "Modifications of real code genetic algorithm for global optimization", Applied Mathematics and Computation, 2008. V203, pp. 598–607.

9. Camp C. V., Bichon J., "Design of space trusses using ant colony optimization", Journal of Structural Engineering, 2004. V130, pp. 741–51.

10. Camp C. V., "Design of space trusses using big bang–big crunch optimization", Journal of Structural Engineering, 2007. V133, pp. 999–1008.

11. Perez R. E., Behdinan K., "Particle swarm approach for structural design optimization", Computers & Structures, 2007. V85, pp. 1579–88.

12. Kaveh A., Talatahari S., "Particle swarm optimizer, ant colony strategy and harmony search scheme hybridized for optimization of truss structures", Computers & Structures, 2009. V87, pp. 267–83.

13. Kaveh A., Ghazaan M.I., Bakhshpoori T., "An improved ray optimization algorithm for design of truss structures", Periodica Polytechnica, Civil Engineering, 2013. V57, #2, p. 97.

14. Kaveh A., Javadi S.M., "Shape and size optimization of trusses with multiple frequency constraints using harmony search and ray optimizer for enhancing the particle swarm optimization algorithm", Acta Mechanica, 2014. V225, #6, pp. 1595–1605.

15. He Q., Wang L., "An effective co-evolutionary particle swarm optimization for constrained engineering design problems", Engineering Applications of Artificial Intelligence, 2007. V20, #1, pp. 89–99.

16. Yildiz A. R., "A novel particle swarm optimization approach for product design and manufacturing", The International Journal of Advanced Manufacturing Technology, 2009. V40, pp. 5–6.

17. Wang J., Yin Z., "A ranking selection-based particle swarm optimizer for engineering design optimization problems", Structural and Multidisciplinary Optimization, 2008. V37, #2, pp. 131–147.

18. Mahdavi M., Fesanghary M., Damangir E., "An improved harmony search algorithm for solving optimization problems", Applied mathematics and computation, 2007. V188, #2, pp. 1567–1579.

19. Hedar A. R., Fukushima M., "Derivative-free filter simulated annealing method for constrained continuous global optimization", Journal of Global Optimization, 2006. V35, #4, pp. 521–549.

20. Mezura-Montes E., Coello C.C., Landa-Becerra R., "Engineering optimization using simple evolutionary algorithm", In 15th IEEE International Conference on Tools with Artificial Intelligence, 2003. Pp. 149–156.

21. Badrloo S., "A new method for solving combinatorial optimization problems with permutation based solution structure using optics inspired optimization", Azad University, Science and Research Branch, Iran, 2015.

22. Moghadasi M., "Design of image processing methods using league championship algorithm and optics inspired optimization", Azad University, Science and Research Branch, Iran, 2015.

23. Badrloo S., Kashan A.H., "A new method for the travelling salesman problem based on Optics Inspired Optimization", International Conference on Modern Research in Management and Industrial Engineering, Iran, 2015.

24. Badrloo S., Kashan A.H., "A new method for the quadratic assignment problem based on Optics Inspired Optimization", International Conference on Modern Research in Management and Industrial Engineering, Iran, 2015.

25. Lalwani P., Banka H., Kumar C., "CRWO: Clustering and routing in wireless sensor networks using optics inspired optimization", Peer to Peer Networking and Applications, 2017. V10, #3, pp. 453–471.

26. Abdulla A. E., Nishiyama H., Kato N., "Extending the lifetime of wireless sensor networks: A hybrid routing algorithm", Computer Communications, 2012. V35, #9, pp. 1056–1063.

27. Yu J., Qi Y., Wang G., Gu X., "A cluster-based routing protocol for wireless sensor networks with non-uniform node distribution", AEU-International Journal of Electronics and Communications, 2012. V66, #1, pp. 54–61.

28. Sabet M., Naji H.R., "A decentralized energy efficient hierarchical cluster-based routing algorithm for wireless sensor networks", AEU-International Journal of Electronics and Communications, 2015. V69, #5, pp. 790–799.

29. Ozdemir M. T., Ozturk D., "İki bölgeli güç sistemininin optikten esinlenen optimizasyon algoritması ile optimal yük frekans kontrolü", Fırat Üniversitesi Mühendislik Bilimleri Dergisi, 2016. pp. 28–2.

30. Muller S. D., Marchetto J., Airaghi S., Koumoutsakos P., "Optimization based on bacterial chemotaxis", IEEE Transactions on Evolutionary Computation, 2002. V6, pp. 16–29.

31. Altay E. V., Alatas B., "Bird swarm algorithms with chaotic mapping", Artificial Intelligence Review, 2020. Pp. 1–42.

32. Alatas, B., "Sports inspired computational intelligence algorithms for global optimization". Artificial Intelligence Review, 2019. V52, #3, pp. 1579–1627.

33. Bingol H., Alatas B., "Chaotic league championship algorithms", Arabian Journal for Science and Engineering, 2016. V41, #12, pp, 5123–5147.

34. Belegundu A. D., Arora J.S., "A study of mathematical programming methods for structural optimization. Part I: Theory", International Journal for Numerical Methods in Engineering, 1985. V21, #9, pp. 1583–1599.

35. Ragsdell K. M., Phillips D.T., "Optimal design of a class of welded structures using geometric programming", Journal of Engineering for Industry, 1976, V98, #3, pp. 1021–1025.

Bilal Alatas,
Ph.D. He received his Ph.D. degree from Firat University. Now he works as professor of software engineering at Firat University, Turkey. His research interests include artificial intelligence, data mining, social network analysis, metaheuristic optimization, and machine learning. Prof. Alatas has published over 150 papers in many well-known international journals and proceedings of the refereed conference since 2001. He has been editor of twelve journals three of which are indexed in SCI and reviewer of sixty SCI-indexed journals

Harun Bingol,
M. Sc. He is a Ph.D. student in Software Engineering at Firat University. His research interests include artificial intelligence, optimization, data mining, social network analysis, and machine learning

A NOVEL COST-EFFICIENT DAYLIGHT-BASED LIGHTING SYSTEM FOR PUBLIC BUILDINGS: DESIGN AND IMPLEMENTATION

Murat Ayaz[1,1], Ugur Yucel[2], Koray Erhan[3], and Engin Ozdemir[4]

[1]Kocaeli University, Department of Electric and Energy, Kocaeli, Turkey
[2]Kocaeli University, Mechatronics, Kocaeli, Turkey
[3]Istanbul Gedik University, Department of Electrical and Electronics Engineering Istanbul, Turkey
[4]Kocaeli University, Energy Systems Engineering, Kocaeli, Turkey
Email: [1]murat.ayaz@kocaeli.edu.tr

ABSTRACT

In this study, design and implementation of a new cost-efficient daylight-based lighting control system is proposed to provide energy saving in a public building with a conventional lighting system. Energy gain recovery and regional daylight utilization coefficients are obtained by conducting daylight measurements in all indoor spaces of the building where the proposed lighting system will be applied. Daylight value is continuously transferred to the control system through the pyranometer placed outside and the need for artificial lighting is calculated by using sectional daylight utilization coefficients. Thereby, maximum benefit from daylight is realized when unnecessary energy consumption for artificial lighting is reduced. Experimental measurement results show that the proposed daylight-based lighting control system provides an average energy efficiency of the building at the level of 60 %. Additionally, the required investment, such as operating cost and payback period for converting an existing conventional lighting system into the proposed system, are discussed in detail. Cost analysis shows that the payback period of the proposed system can be reduced by 5 years compared to the conventional system.

Keywords: energy-efficient buildings, daylight harvesting, lighting control system, energy efficiency, energy saving, cost-efficient systems, automation system design

1. INTRODUCTION

Getting a better quality of life requires environmental protection and the efficient use of natural resources. Achieving energy efficiency by applying new technologies in lighting is essential not only to reduce energy costs, but also to promote environmental and economic sustainability [1, 2]. The energy consumed for the lighting of buildings constitutes a large part of the energy consumption. Electricity lighting covers 19 % of the total electricity production in the world [3]. Commercial and office buildings are in the group of high energy-consuming buildings. While 14 % of total electricity consumption in commercial buildings is spent on lighting, 11 % of the energy consumed in houses is used for lighting and small appliances [4, 5]. It is determined as (100–1000) kWh/m^2 per year depending on the location of office buildings, equipment used, working hours, ventilation use, and type of lighting. Approximately 40 % of the total electricity consumed in office buildings is used for lighting [6–8].

New materials and systems are necessary to reduce the need for lighting and preserve the lighting comfort of users [9, 10]. By using energy-saving lamps, 40 % of energy savings are achieved by using a combination of occupancy lighting with presence and absence sensors and utilizing daylight [11–13]. The rapid development of detection and microcontroller technologies has enabled the de-

sign and use of high energy efficient lighting systems built on new smart lighting platforms. Control of artificial lighting standardizes user comfort while reducing energy consumption [14–19]. Open or closed-loop controlled lighting can be used as a control tool [20]. In the study conducted by Chew et al., a closed-loop controlled lighting system has been established and autonomously shaped based on the data received from the light sensors installed together with the LED lighting system. Luminaire luminous flux is provided by amplitude modulation depending on the sensor feedback information. The system saves 55 % of energy in continuous use under test conditions. In addition, the system is commercially 31.52 % cheaper compared to a system having manual dimming and a PIR detector [14]. In another study, Sahana et al. designed a daylight-based system using LDR (light-dependent resistance) and PIR (passive infrared sensor) sensors. In the developed system, when there is no user in any room or if the daylight level is sufficient, artificial lighting is turned off and electricity consumption is reduced. Artificial lighting control was carried out by determining different reference voltage levels for daylight range depending on the seasonal changes. The low-cost controller with both sensors integrated was implemented to a small room for lighting control and high efficiency was achieved [16]. Like the studies mentioned above, Dun carried out a study aimed at optimizing smart lighting in the university classroom and reducing energy consumption. In the study, the fuzzy model reference adaptive system (FMRAS) control algorithm was used. It has found that FMRAS has better control performance, higher steady state accuracy, lower overload rate, and higher response rate than typical fuzzy controllers currently used [18]. In another study on classroom lighting control, a lighting control system based on machine vision technology has been proposed to increase energy efficiency. It was found that a different number of signals could comprehensively control the level of illuminance created by classroom luminaires, and save energy used in classroom lighting [19].

The use of daylighting saves energy used for lighting, achieve high luminous flux, low heat dissipation compared to high illuminance level, protects the environment, better quality visual lighting compared to artificial lights, reduces stress and increases efficiency in workspaces since its human-friendly feature [15, 21–24]. When the literature is examined, it is seen that (20–60) % of the energy used for lighting is saved by using daylight harvesting systems (DHS) [25]. The study performed by Pandharipande et al. aimed to provide lighting comfort and energy saving for users in an office by optimizing artificial light sources with changing daylighting, and it is proposed to use sensors in the user platform as an alternative to the sensors used in the armature platform. If the sensors are placed at the user level, the illuminance level has been measured 10 % lower and consequently more energy is consumed. If the occupancy rate of the office space is above 25 %, it is seen that the control system should be disabled due to the decrease in the illuminance level of the working spaces [26]. In the study performed by Tang et al., daylight harvesting system is applied by using a smartphone in smart home systems. The illuminance level of a room with 3 luminaires is measured by using the light sensor feature of the smartphones, the luminaire luminous flux are controlled by amplitude modulation in the *Arduino* processor, and *Raspberry Pi* is used to connect the system with the mobile application editor.

Fig. 1. Study object
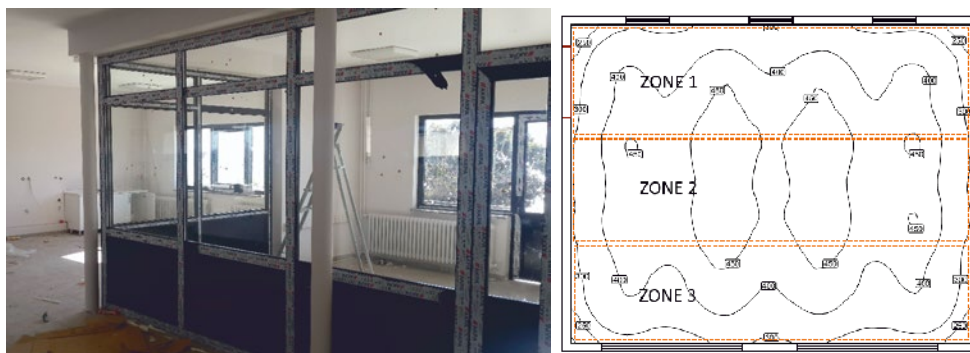
Fig. 2. Material laboratory and isolines on the working surface

54.7 % of energy savings are achieved on sunny days [27]. In another study of daylight-based lighting system, Meugheuvel et al. used a light sensor, which provides information about the local illuminance level under each luminaire in an open space office, and occupancy sensor. A control device is used to adjust the dimming level of the luminaire. According to the readings of light sensors, it is aimed to achieve the standard illumination levels for working zones and unused zones by using PI control. Two scenarios are applied. In the first scenario, each controller is operated independently, and it is found that the desired reference value could not be achieved in each case. The lighting reference value is captured through the PI controllers on the network, while a high saving in power consumption is achieved [28].

In this study discusses the energy savings, which can be achieved with a daylight-based lighting system for a building with a conventional lighting system, and recovery period of installation cost. Sections and utilization coefficients are determined by performing daylighting measurements in all indoor areas of the building within the specified time. The proposed lighting system components and control algorithm have been formed based on the number of sections The results obtained in the course of experimental measurements and analysis of the results are described in detail in the conclusion.

2. EXPERIMENTAL METHOD

2.1. Application Building

The building where the daylight-based lighting control system will be installed consists of 10 independent laboratories and offices. It has a total indoor area of 641 m². In the building shown in Fig. 1, the application laboratories are located on the ground floor, and the personnel departments are located on the first floor. The lighting installation for offices and laboratories consists of 75 luminaires (4×18 W) with fluorescent lamps using with on/off control. The instantaneous power consumption is 5.4 k·W, and the energy consumption for lighting for 8 hours shift is 43.2 kW·h.

2.2. Daylight Measurements

Measurements are performed over three months to find the utilization rate of daylight during the working hours in all the internal spaces in the building. Zones of lighting are specified by using individual daylighting measurement values for each office and laboratory. 26 zones of lighting have appeared for 10 detached internal spaces inside the building. The measurements for material laboratory of the building with different facades are detailed below.

In the material laboratory shown in Fig. 2, lighting installation consists of 16 pieces of luminaires (4×18 W) with fluorescent lamps. In addition, the laboratory has a window area of 7.56 m², due to which daylighting can make a significant contribution to illuminance of workspaces. The area is divided into 3 zones, considering luminaire layout and the distribution of daylighting. The first zone is the farthest from the windows and there are 4 luminaires with a total power of 288 W. The third zone is the closest to the window, and total artificial lighting power is 288 W. In the zone defined as zone 2, there are 8 luminaires with a total power of 576 W.

The contribution of daylighting on 3 zones in the material laboratory between (09:00–17:00) working hours is shown in Fig. 3. The desired level of illuminance in the laboratory should be 500 lx of the reference value. In this respect, the daylight utilization rate and the need for artificial lighting are specified by comparing the change of daylighting in zones without artificial lighting and reference value. When the graphs given in Fig. 3 are examined, daylight-
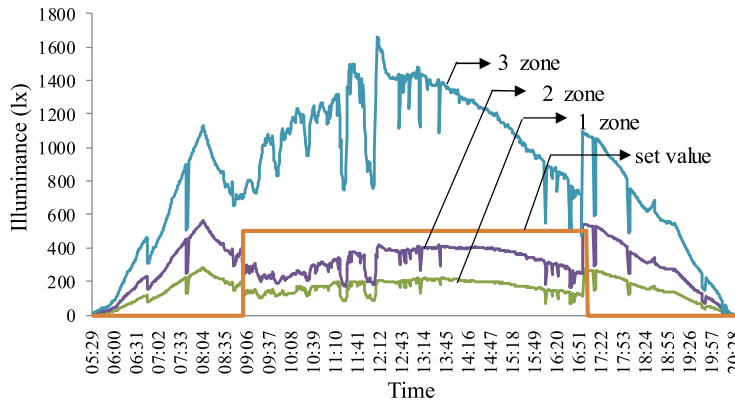
Fig. 3. The contribution of daylight in the material laboratory during working hours

ing contributes to the illuminance of the zones by 36 % at the first zone, 64 % at the second zone, and 100 % at the third zone. The energy requirement for lighting the first zone during working hours is 2304 W·h. While 830 W·h of that energy is supplied by daylighting, 1474 W·h of energy must be supplied through the network. In the second zone, 3000 W·h of the total energy demand of 4608 W·h is met by daylighting and 1608 W·h of energy is withdrawn from the network. In the third zone, artificial lightening is not required due to the high contribution of daylighting in the specified time.

3. DAYLIGHT-BASED LIGHTING SYSTEM

3.1. Daylight Automation System

In daylight-based lightening systems, the correct measurement or calculating the effect of daylighting on the indoors is of great importance for lighting control. In this context, the most used method is closed-loop controlled structures. In such systems, sensors are placed in each designated indoor space to transfer the level of illuminance to the control system instantly. Although the use of multiple sensors allows an easier and correct control, it poses a major disadvantage in terms of installation

cost. Furthermore, the need to verify each sensor by checking their calibration regularly leads to increased operating costs. In this context, the system recovery time can be shortened by reducing installation and operating costs through the installation of an open-loop controlled lighting system. Moreover, the conversion of conventional lighting systems into a daylight-controlled automation structure can be achieved with fewer components via open-loop control.

In this study, the proposed daylight-based lighting system is constituted with an open-loop control structure, and the control block diagram is given in Fig. 4. In the proposed system, daylighting is transferred to the control system instantly by using a pyrometer placed in the outdoor environment. The transfer coefficient of daylighting in each designated indoor zone is determined with experimental measurements. The need for artificial lighting is calculated for each zone by evaluating instant daylighting.

The controller calculates the amount of artificial lighting for areas where there is insufficient daylighting regionally. The required voltage rating in the luminaires is specified to meet the need for artificial lighting. The proposed lighting control system is installed in the Industry 4.0 laboratory. 6 existing luminaires (4×18 W) with T8 type
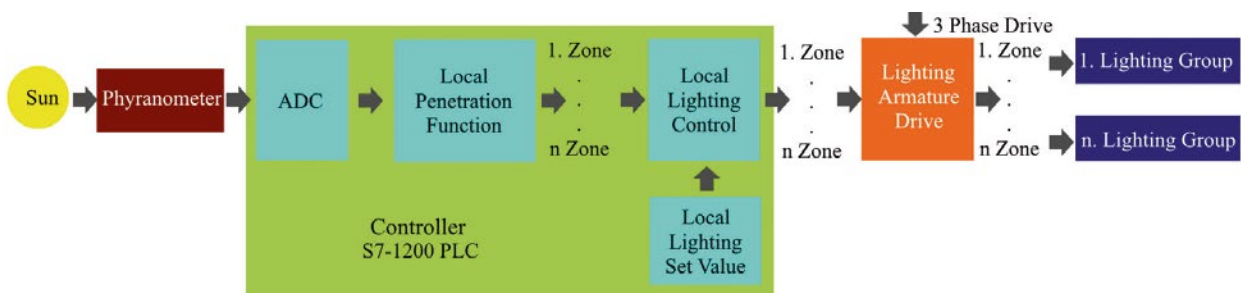
Fig. 4. Lighting automation system control block diagram

Fig. 5. Daylighting automation panel and Industry 4.0 laboratory

fluorescent lamps are removed and replaced with 6 LED luminaires 35 W by *Ledova*. The luminaires are grouped in pairs concerning their distance from windows that are a daylighting source, location of existing luminaires and workspaces, and a total of 3 lines are formed. The value of the analogue voltage (0–5) V obtained from the pyranometer is transferred to the system via the *S7–1200 PLC* analogue input unit on the control panel shown in Fig. 5. One pyranometer is used for outdoor daylighting radiance measurement. In the PLC, the luminaires are controlled in the range of (0–10) V in line with the created algorithm by calculating the amount of required artificial lighting based on the amount of daylighting. Total current, voltage and power values of the network and each line are measured with the analyser. Measured values are transmitted from the analyser to the PLC via Ethernet. All measured values can be read from the panel. Data can be saved to the memory card on the pan-

el. Also, the system can be accessed and intervened via the internet.

The measured values should be made as linear as possible to produce daylight saving coefficient in each zone specified in Industry 4.0 laboratory. Zone coefficients can be calculated based on time, as well as calculated by considering the effect value of the amount of daylighting. In this study, the coefficients are determined by considering the effect of daylighting on the zones. Measured values are categorized according to the first zone, where daylighting has the least effect, and the voltage ratings of luminaires in line with the needs of the zones are determined. The number of categories has kept high due to the eye-straining effect of sudden changes in the level of illuminance. A smooth transition is provided to increase or decrease the level of illuminance received from artificial light sources. Table 1 shows the determined groups of illuminance levels, the amount of daylighting impacting zones,
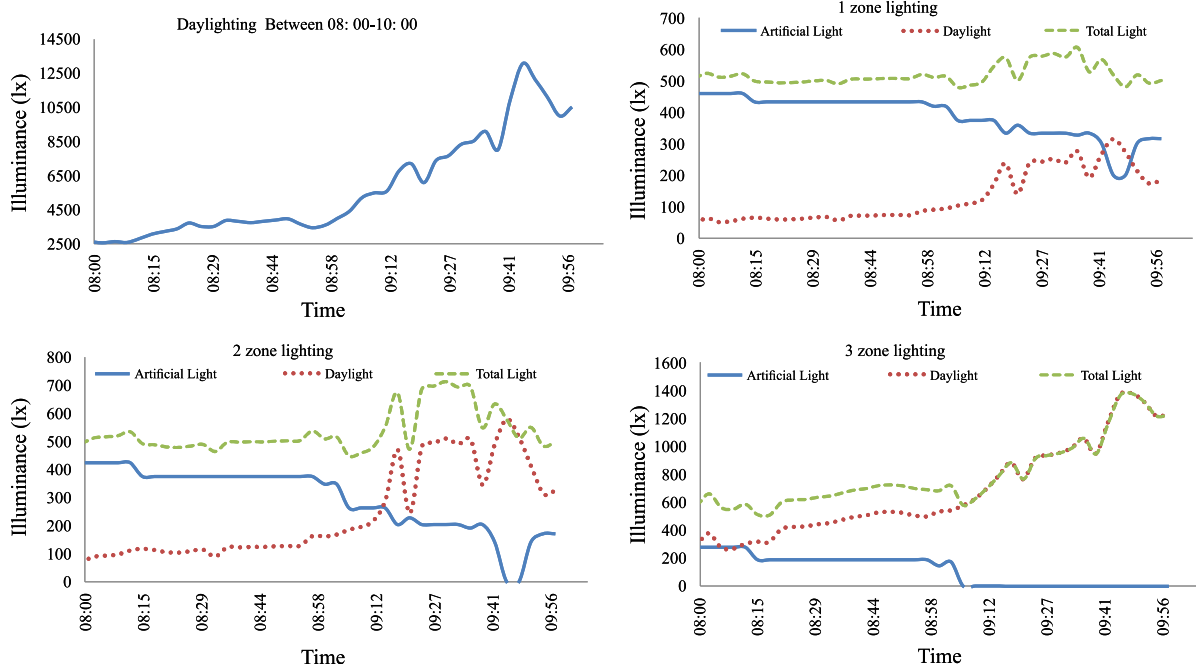
Fig. 6. Illuminance between (08:00–10:00)

64
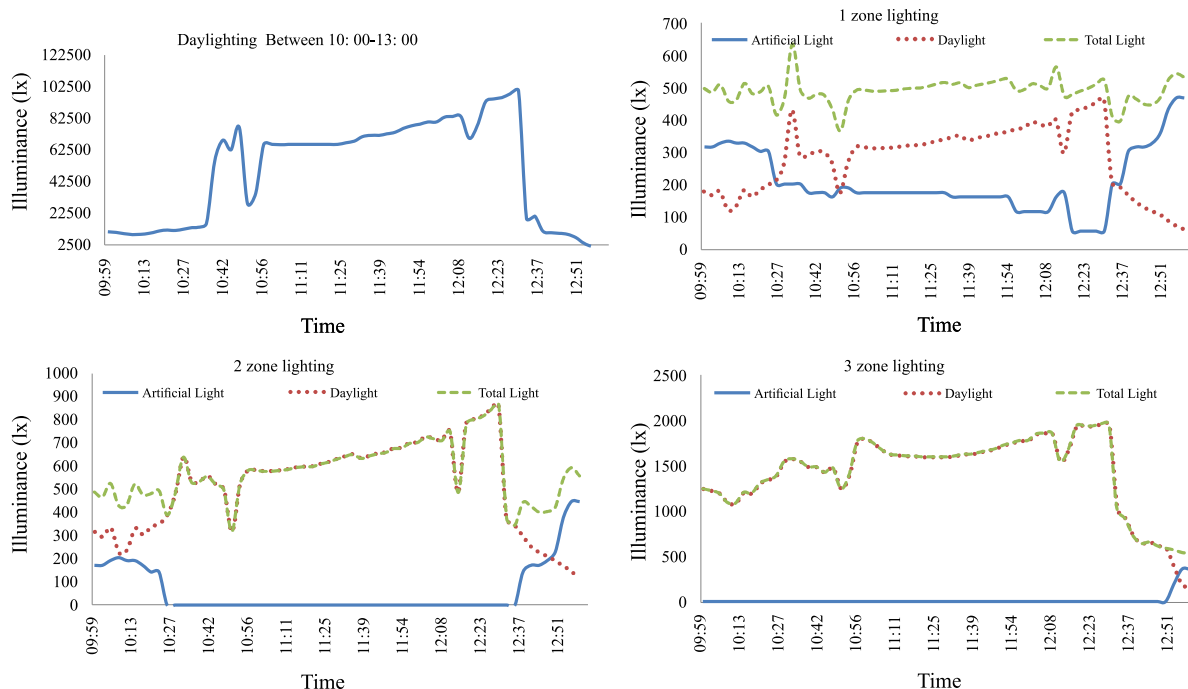
Fig. 7. Illuminance between (10:00–13:00)

the amount of artificial lighting required for these zones, and the analogue voltage rating that the controller should apply to the luminaires to obtain the artificial lighting.

3.2. Experimental Performance of Daylight Automation System

The proposed lighting control system is operated in line with the coefficients specified in the previous section. The measurement is performed by placing luxmeters in each zone for measuring the system can achieve the desired illuminance level in designated areas. As a result of the measurements, daylighting illuminance values are divided according to time, and the measured levels of illuminance readings for each zone during the working hours are shown in Fig. 6 and Fig. 7. For modelling have examined and graphed the hours between (08:00–10:00) and (10:00–13:00). Segmentation is made depending on the change for daylighting. Between (08:00–10:00), the amount of daylighting increases slightly, but illuminance produced by daylighting increaseы significantly between (10:00–13:00).

The level of illuminance at zone 1 is taken between (8:00–10:00). The low amount of daylighting increases the need for artificial light sources. A delay is added to the system due to the negative effects of sudden illuminance changes on eye health, thus the total illuminance level increases up to 590 lx.

Daylighting has a higher impact on zone 2, and the need for artificial lighting has decreased. The third zone is the area that makes the most use of daylighting, since it is located next to the window. The need for artificial lighting is minimal. The required artificial lighting decreases with increasing daylighting. It is seen that the power consumption decreases according to time by zones. By 09:05, the power consumption in zone 3 was 0 W.

If LED luminaires are installed instead of existing 6 luminaires (4×18 W) with fluorescent lamps in Industry 4.0 laboratory, the installed power capacity decreases from 432 W to 210 W. Table 2 shows that the energy consumption during the 8-hours working hour decreased from 3456 W·h to 1680 W·h. Using LED luminaires instead of luminaires with fluorescent lamps saved 48 % of energy.

In the proposed lighting control system, LED luminaire is used instead of luminaires with fluorescent lamps, and the illuminance level of the outdoor area is measured by a sensor and LED luminaires are turn on as necessary. It is experimentally shown that the desired illuminance level for each zone is realized due to the maximum use of daylighting. The electrical energy consumed by the lighting system during the day is measured and given in Table 2. The percentage of energy efficiency may vary depending on parameters such as weather conditions, seasons, glass pollution. The Table shows that the target lighting system provides (33–83) % ener-

Table 1. DIM Voltages to Be Applied to Obtain Required Artificial Lighting in Industry 4.0 Laboratory

Daylighting range (klx)	The amount of daylighting affecting the zones (lx)			The amount of artificial lighting needed in the zones (lx)		
	1 zone	2 zone	3 zone	1 zone	2 zone	3 zone
0–0.2	0	0	0	500	500	500
0.2–0.9	8	15	50	492	485	450
0.9–1.9	31	55	141	469	445	359
1.9–2.9	39	75	220	461	425	280
2.9–3.9	66	124	310	434	376	190
3.9–4.8	80	151	353	420	349	147
4.8–5.7	125	236	499	375	264	1
5.7–6.9	140	271	602	360	229	0
6.9–8.8	165	295	850	335	205	0
8.8–9.7	171	308	974	329	192	0
9.7–10.9	183	328	1136	317	172	0
10.9–11.9	197	357	1220	303	143	0
11.9–19.0	298	519	1410	202	0	0
19.0–55.4	310	535	1500	190	0	0
55.4–69.7	325	597	1623	175	0	0
69.7–78.7	338	622	1652	162	0	0
78.7–83.7	383	710	1826	117	0	0
83.7–100.0	444	820	1948	56	0	0
100.0–120.0	490	944	2183	10	0	0

gy efficiency in the zones and 59 % energy efficiency on average.

Depending on the results of the study conducted in the Industry 4.0 laboratory, the installed power of the workspaces consisting of 10 laboratories and offices in the building, the amount of energy spent on an 8 hours shift, and the effect of daylighting on the regions are determined. Table 3 shows operating and percentage values of the installed power in the workspaces with daylight, the amount of consumption from 09:00 hours to 17:00 hours, the contribution of daylighting. 79 pieces of the existing luminaires (4×18 W) with T8 fluorescent lamps are used, and the installed power is 5688 W. If the luminaires are continuously active and on/off controlled for 8 hours shift, then the consumed energy is 45504 W·h.

The power and energy consumption values are determined in case of replacing 79 existing luminaires in all work environments with built-in panel LED luminaires ((600×600) mm Ledova PL1400125 Olea, 35 W), used in Industry 4.0 laboratory and controlling the luminous flux depending on the daylighting received from a single sensor. If the LED luminaires are operated in on/off mode, the consumption in 8 hours will be 22120 W·h, and the energy consumption through daylighting control is decreased to 13228 W·h.

4. COST ANALYSIS

The system is designed for 10 independent zones used in central laboratories and student affairs building and can be used to improve energy efficiency by lighting control. In the study, there was no control system work for corridors, storage areas, archives, and toilets. Cost analysis is performed for the areas where the daylighting control system is installed. There is a total of 79 luminaires (4×18 W) with fluorescent lamps in the controlled areas.

In conventional lighting systems, luminaires are controlled by using on/off switches. In the case of illuminance of laboratories using different lighting methods, the required expenditures are shown in Table 4. The installation cost for lighting the spaces requiring control in our building by conventional methods is 3884 $. LED luminaires are used in conventional daylight-based lighting systems, and

Table 2. Comparison of Daylight-Controlled Lighting System Designed with on/off Control

		1 zone Energy consumption (W·h)	2 zone Energy consumption (W·h)	3 zone Energy consumption (W·h)	Total Energy consumption (W·h)
1	On/off controlled consumption (fluorescent)	1152	1152	1152	3456
2	On/off controlled consumption (LED)	560	560	560	1680
3	Daylighting control for LED luminaires	375	218	95	688
	Comparison of on/off controlled existing lighting installation and on/off controlled LED lighting installation	48 %	48 %	48 %	48 %
	Comparison of on/off controlled LED lighting installation and daylighting control LED lighting installation	33 %	61 %	83 %	59 %

Table 3. The Effect of Daylighting on Workspaces

Laboratory and Offices	Installed power (W)	Installed system consumption (W·h)	Power of LED luminaires (W)	Energy consumption of LED luminaires (W·h)	Contribution of daylighting on zones (%) avg.	Contribution of daylighting on zones (W·h)	LENI factor with daylighting control (W·h)/m²
Materials laboratory	1000	9000	560	4000	70 %	2500	26.1
Casting laboratory	864	6912	420	3360	63 %	2128	28.4
Electric Engine laboratory	864	6912	420	3360	63 %	2128	31.4
Industry 4.0 laboratory	432	3456	210	1680	60 %	1008	3.1
Robotics laboratory	432	3456	210	1680	64 %	1087	23.4
Academic staff room	432	3456	210	1680	56 %	936	26.7
Student affairs main office	168	4032	245	1960	61 %	1196	26.5
Documentation office	432	3456	210	1680	40 %	663	17.6
Management office	288	2304	140	1120	80 %	896	44.8
Support office	288	2304	140	1120	22.5 %	252	12.6
Total	**5688**	**45504**	**2765**	**22120**	**59 %**	**13228**	

Note to Table 3: The lighting energy numerical indicator (LENI) method provides an alternative way of calculating the lighting energy performance of a building. Whereas each luminaire is usually assessed for its energy efficiency (for example a luminaire with no controls should have a minimum efficiency of 60 luminaire lumens per circuit watt), the LENI method calculates the actual energy used in kW·h per square meter per year. This figure is then assessed against a maximum benchmark value depending on the illuminance (lx) required within a room.

there is a sensor that measures the illuminance level in every workspace or under each luminaire. The use of a controller is mandatory for processing sensor information and driving luminaires. The controller also provides data monitoring and remote access to the system. Using an energy analyser to measure site data enables the measurement of energy savings. Luminaires must be suitable for DIM operation. LED luminaires are appropriate for control structure. The system must have a sensor that can measure the illuminance level of 10 closed areas, and a control structure that can drive 26 zone luminaires. In the case of lighting zones with conventional daylight-based lighting system, the cost

Table 4. Cost Analysis Table

	Components	On/off lighting system (fluorescent)	On/off lighting system (LED)	Conventional daylight-based lighting system	Proposed daylight-based lighting system
1	Luminaries	2756 $	3635 $	9042 $	9042 $
2	Sensors and detectors	–	–	4500 $	450 $
3	Controller and components	–	–	5350 $	4919 $
4	Cabling infrastructure	615 $	615 $	1285 $	1117 $
5	Installation work	513 $	513 $	1010 $	945 $
	Total		**4763 $**	**21187 $**	**16473 $**

of installation is 21187 $. Unlike conventional daylight-based lighting system, the proposed system uses a single sensor. Using a single sensor saves the inputs of the controller. The proposed single-sensor daylight-based control system has an installation cost of 16473 $.

According to the 2019 tariff applied in schools in Turkey, the cost of 1 kW·h of electricity reflected to the consumer is 14.89 ₵ [29]. If the LED luminaire is used instead of the luminaire with T8 fluorescent lamps, an added 879 $ will be added to the installation cost. In case of using LED luminaire instead of the luminaire with fluorescent lamps, the excess cost can be compensated within 1 year. If a conventional (sensor in each working area) daylight-based lighting system is installed instead of a luminaire with T8 fluorescent lamps, an added investment of 17303 $ is required.

5. CONCLUSION

A single sensor and open-loop control system is created as an alternative to conventional daylighting control systems. Daylighting illuminance levels are measured depending on daylight in indoors spaces where control system will be applied. Daylight factors of these spaces are determined accordingly. The experimental system has been installed in the Industry 4.0 laboratory. Existing luminaires are replaced with DIM controlled LED luminaires, and their operating performance is examined depending on/off operating mode and daylighting. The performance of current conventional luminaires, LED luminaires and daylight-controlled LED luminaires are compared. When the LED luminaires are operated in on/off mode, it is found that they are 48 % more efficient than conventional lighting systems. Daylighting value is measured with a single sensor placed outdoors, and the luminaires are dimmed depending

on daylighting. Empirically, 59 % energy savings are achieved. The cost analysis is performed and compared with the current conventional lighting if the system is installed throughout the building. It is seen that the start-up costs of current conventional lighting systems are lower than the daylighting control systems; however, a single-sensor open-loop controlled daylighting control system achieved high energy efficiency. Despite its high cost, daylight-controlled lighting systems support a fixed illuminance level at low daylighting values and supply lighting comfort for users. Since the aim of the study is energy efficiency, shading studies have not been conducted in cases where the daylighting value is high. It has been found that the payback period can be reduced by 5 years with the proposed system compared to conventional daylighting control systems. Also, the proposed system supplies advantages such as 59 % energy savings, instant data monitoring of system current, voltage, power, and illuminance, as well as remote intervention.

REFERENCES

1. Paz J.F.D., Bajo J., Rodríguez S., Villarrubia G., Corchado J.M., Intelligent system for lighting control in smart cities, Information Sciences, 2016. V372, pp. 241–255.
2. Radulovic D., Skok S., Kirincic V., Energy efficiency public lighting management in the cities, Energy, 2011. V36, #4, pp. 1908–1915.
3. Zou H., Zhou Y., Jiang H, Chien Z.C., Xie L., Spanos C.J., WinLight: A WiFi-based occupancy-driven light-

ing control system for smart building, Energy and Buildings, 2018. V158, pp. 924–938.

4. Rosenberg E., Calculation method for electricity end-use for residential lighting, Energy, 2014. V66, pp. 295–304.

5. Yahiaoui A., Experimental study on modelling and control of lighting components in a test-cell building, Solar Energy, 2018. V166, pp. 390–408.

6. Darula S., Review of the current state and future development in standardizing natural lighting in interiors, Light & Engineering, 2018. V26, #4, pp. 5–26.

7. Santamouris M., Dascalaki E., Passive retrofitting of office buildings to improve their energy performance and indoor environment: the office project, Building and Environment, 2002. V37, pp. 575–578.

8. Chi D. A., Moreno D., Navarro J., Correlating daylight availability metric with lighting, heating and cooling energy consumptions, Building and Environment, 2018. V132, pp. 170–180.

9. Doulos L., Tsangrassoulis A., Topalis F.V., Multi-criteria decision analysis to select the optimum position and proper field of view of a photosensor, Energy Conversion and Management, 2014. V86, pp. 1069–1077.

10. Barbón A., Pardellas A., Fernández-Rubiera J.A., Barbón N., New daylight fluctuation control in an optical fiber-based daylighting system, Building and Environment, 2019. V153, pp. 35–45.

11. Ovcharov A.T., Selyanin Y.N., Antsupov Y.V., A hybrid illumination complex for combined illumination systems: concepts, state of the problem, practical experience, Light & Engineering, 2018. V26, #2, pp. 20–28.

12. Dubois M.C., Blomsterberg A., Energy saving potential and strategies for electric lighting in future North European, low energy office buildings: A literature review, Energy and Buildings, 2011. V43, pp. 2572–2582.

13. Shen E., Hu J., Patel M., Energy and visual comfort analysis of lighting and daylight control strategies, Building and Environment, 2014. V78, pp. 155–170.

14. Chew I., Kalavally V., Oo N.W., Parkkinen J., Design of an energy-saving controller for an intelligent LED lighting system, Energy and Buildings, 2016. V120, pp. 1–9.

15. Yu X., Su Y., Daylight availability assessment and its potential energy saving estimation –A literature review, Renewable and Sustainable Energy Reviews, 2015. V52, pp. 494–503.

16. Sahana S., Roy B., Development and performance analysis of a cost-effective integrated light controller, Light & Engineering, 2019. V27, #6, pp. 73–81.

17. Alexei K. Soloviev, Nina A. Muraviova, Sergei V. Stetsky, Comfort light environment under natural and combined lighting method of their characteristics definition with subjective expert appraisal using, Light & Engineering, 2018. V26, #3, pp. 124–131.

18. Dun W., Optimization of intelligent illumination in university classroom based on FMRAS control algorithm, Light & Engineering, 2018. V26, #2, pp. 52–59.

19. Cheng R., Classroom lighting energy-saving control system based on machine vision technology, Light & Engineering, 2018. V26, #4, pp. 143–149.

20. Jain S., Garg V., A review of open loop control strategies for shades, blinds and integrated lighting by use of real-time daylight prediction methods, Building and Environment, 2018. V135, pp. 352–364.

21. Pandharipande A., Caicedo D., Smart indoor lighting systems with luminaire-based sensing: A review of lighting control approaches, Energy and Buildings, 2015. V104, pp. 369–377.

22. Soori P.K., Vishwas M., Lighting control strategy for energy efficient office lighting system design, Energy and Buildings, 2013. V66, pp. 329–337.

23. Nikolaevich A. V., Light desynchronosis and healt, Light & Engineering, 2019. V27, #3, pp. 14–25.

24. Ihm P., Nemri A., Krarti M., Estimation of lighting energy savings from daylighting, Building and Environment, 2009. V44, #3, pp. 509–514.

25. Gentile N., Dubois M, Laike T., Daylight harvesting control systems design recommendations based on a literature review, Environment and Electrical Engineering (EEEIC), 2015 IEEE15th International Conference on Rome, Italy, 10–13 June, ISBN: 978–1–4799–7994–3, 2015. pp. 632–637.

26. Pandharipande A., Willems F.M.J., Daylight-adaptive lighting control using light sensor calibration prior-information, Energy and Buildings, 2014. V73, pp 105–114.

27. Tang S., Kalavally V., Ng K.Y., Parkkinen J., Development of a prototype smart home intelligent lighting control architecture using sensors onboard a mobile computing system, Energy and Buildings, 2017. V138, pp. 368–376.

28. Meugheuvel N.V.D.M., Pandharipande A., Caicedo D., Hof P.P.J.V.D., Distributed lighting control with daylight and occupancy adaptation, Energy and Buildings, 2014. V75, pp. 321–329.

29. Türkiye Cumhuriyeti Enerji Piyasası Düzenleme Kurumu [Republic of Turkey Energy Market Regulatory Authority]. URL: https://www.epdk.org.tr/Detay/Icerik/3–0–1/tarifeler (referance date: 29.10.2019)

Murat Ayaz,
Ph.D. He received his B.S., M.S., and Ph.D. degrees from the Department of Electrical Education, Kocaeli University, Kocaeli, Turkey, in 2005, 2008, and 2015, respectively. Between 2005 and 2009, he worked as a project engineer in Beck & Pollitzer, Kocaeli, Turkey. From 2009 to 2015, he served as a research assistant in the Electrical Education Department of Kocaeli University, Kocaeli. Currently, he is an assistant professor at Electric and Energy Department of Kocaeli University. He has several researches on electric machine design and industrial automation system design. His research activities include electric machines, electromechanical systems, hybrid electric vehicles and industrial automation systems

Ugur Yucel,
M. Sc. He received his B. Sc. degree from the Department of Electrical Education, Gazi University, Ankara, Turkey, in 1993. Then, he received his M. Sc. degree from the Department of Energy Systems Engineering, Kocaeli University, Turkey in 2019. He is currently a Ph.D. candidate in the Department of Energy Systems Engineering, Kocaeli University. Between 1994 and 2001, he worked as a technical teacher in industrial vocational high school under the Ministry of National Education. Since 2001, he works as a lecturer in Kocaeli University, Hereke Vocational School Mechatronics Program. His research activities include lighting control systems, LEDs and industrial automation systems

Koray Erhan,
Ph.D. He was born in 1987 in Turkey. He received his B. Sc. in Electrical Engineering from Yildiz Technical University, Turkey in 2010. Then he completed his M. Sc in Electrical Engineering at Istanbul Technical University in 2013. Finally, he got his Ph.D. at Department of Energy Systems Engineering, Kocaeli University in 2018. He became a research assistant in 2010 at Istanbul Technical University and in 2013 at Kocaeli University. He is currently holding position of System Engineer at AVL R&D Company, Turkey. His research interests are electric and hybrid electric vehicles, photovoltaic power generation systems, renewable energy sources, energy storage technologies, and smart grid integration and automation systems

Engin Ozdemir,
Ph.D. He is a professor in Kocaeli University, Faculty of Technology Department of Energy System Engineering Department in Kocaeli in Turkey. He has received his B. Sc., M. Sc., and Ph.D. in Electrical Engineering in Turkey. He has strong background in power electronics, renewable energy and energy storage technologies and its application in industry. His research interests are power electronics, renewable energy, energy storage and industrial automation

COMPARATIVE ANALYSIS OF THE CHARACTERISTICS OF LED FILAMENT LAMPS FOR HOUSEHOLD LIGHTING

Nina P. Nestyorkina[1], Yulia A. Zhuravlyova[2], Olga Yu. Kovalenko[1], and Svetlana A. Mikayeva[2]

[1]N.P. Ogarev Mordovia State University
[2]MIREA – Russian Technological University
E-mail: ulypil@mail.ru

ABSTRACT

This paper examines the characteristics of LED filament lamps from various manufacturers: LLC " Lisma "(Russia), an American company with production in China " GENERAL LIGHTING CO. LTD", a joint Chinese-Russian company " Uniel "and Taiwan company" Smartbuy " in the A60 bulb – the time of stabilization of characteristics, luminous flux, colour temperature, colour rendering index, flicker index, radiation spectrum during 6000 hours of burning. The research was carried out on the Gooch&Housego measuring system. The results of experimental studies that showed that the clear leader in the test results is the lamp SDF-8 (LISMA), according to GOST of all tested samples of led filament lamps, it can be recommended for lighting in lighting devices for household lighting.

Keywords: luminous flux, luminous efficacy, colour temperature, colour rendering index, radiation spectrum, luminous intensity distribution curves (LIDCs), lighting, stabilization time, household premises

1. INTRODUCTION

LED lamps are considered the most energy-efficient, reliable and promising light sources (LS) nowadays. There is a wide range of these LSs on the market, including filament LED lamps (FLED), which allow these products to select rationally with consideration of their purpose and major characteristics [1–6]. The purpose of this work is to compare light and engineering characteristics of FLED lamps for household applications in order to increase rationality of selection of these LSs primarily for replacement of incandescent lamps.

2. THE STUDY OF CHARACTERISTICS OF FLED LAMPS WITH *A60* BULBS

For the comparative study, FLED lamps manufactured by Lisma LLC (Russia), the American company with PRC-based production facilities *General Lighting Co., Ltd*, the joint Chinese and Russian company *Uniel* and the Taiwan company *Smartbuy* were selected. The power of the studied lamps was equal to 5,8 W and 10 W, the bulb type was *A60*, the cap type was *E27*.

The studies were conducted in the Light Engineering Metrology laboratory (Electronics and Light Engineering Institute of the N.P. Ogarev Mordovia State University) using the measurement system by *Gooch & Housego* consisting of the *OL IS7600* photometer sphere with diameter of about 2 m, the *OL 770 VIS/NIR* spectroradiometer, the *OL410–200 PRESISION LAMP SOURCE* DC supply unit (for supply of an auxiliary lamp), fasteners for lamps and a PC [7].

Stabilisation time of the compared characteristics of the FLED lamps was defined. For *GLDEN-A60S-10–230-E27–2700 (General Lighting Co., Ltd)* and SDF-8 (LISMA) it was equal to 5 min, for *SKY-A60–8–30K-E27* lamps (*Uniel*) it was equal
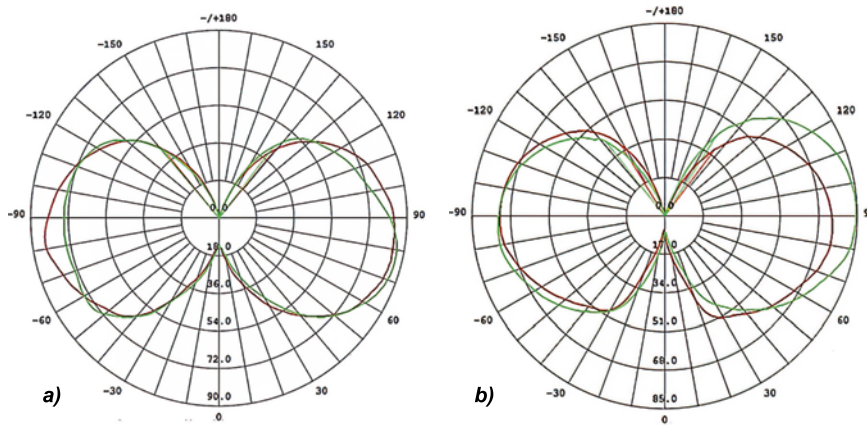
Fig. 1. LIDCs of the lamps:
a: SDF-A60–8–27K-E27 (Lisma); *b*: GLDEN-A60S-10–230-E27–2700 (*General Lighting*)
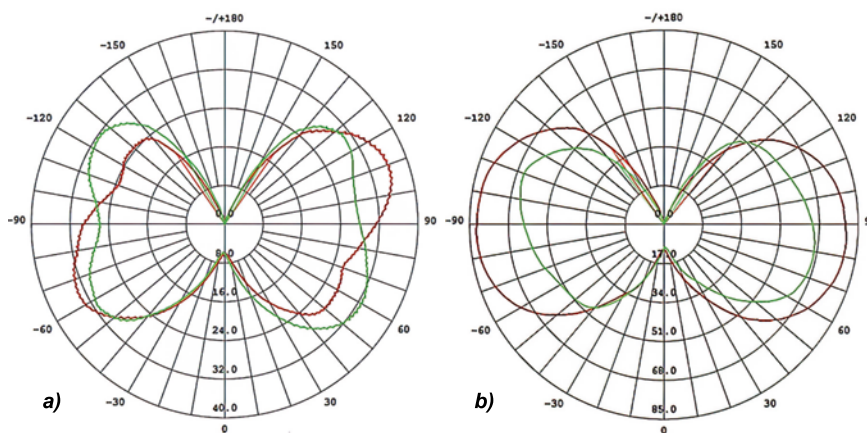
Fig. 2. LIDCs of the lamps:
a: *SBL-A60F-5–30K-E27* (*Smartbuy*); *b*: *SKY-A60–8–30K-E27* (*Uniel*)

to 7 min, and for *SBL-A60F-5–30K-E27* (*Smartbuy*) it was equal to 4 min.

Lamp parameters were measured by means of the photometer sphere in accordance with standards [8, 9]. Light flickering level was measured by means of a TKA-PKM 08 illuminance and flicker meter that measures flicker index k_f in the (380–760) nm spectral region.

Table 1 summarises the results of measurements of characteristics of the studied lamp samples and the values of the characteristics declared by manufacturers.

The analysis of the results showed that the measured values of luminous flux Φ_v for lamps manufactured by Lisma LLC (780 lm) and *General Lighting Co., Ltd* (890 lm) correspond to the declared values (770 lm and 870 lm respectively) and are significantly lower (655 lm and 355 lm) than the declared values (800 lm and 480 lm respectively) in lamps manufactured by *Uniel* and *Smartbuy*. The measured values of correlated colour temperature T_{cp} and general colour rendering index R_a of all lamps correspond to the declared ones. Only power of the lamp by LISMA was approximately equal

to the declared value while it was less than the declared value for the other lamps by 30 %. Actual power value of the lamp *GLDEN-10* (*General Lighting Co., Ltd*) which is less by 30 % does not affect the level of Φ_v: it corresponds to the declared one; reduction of power by 32.5 % in lamps by *Smartbuy* led to reduction of Φ_v by 18.1 % and reduction of power by 35.6 % for lamps by *Uniel* led to reduction of Φ_v by 26 %. Luminous efficacy η_v of all studied lamps turned out to exceed the declared values. k_f of the lamps by LISMA LLC and by *General Lighting Co., Ltd* turned out to be much less than the declared values (0.2 %); it was within the specification limits in the lamp *SKY-8* (*Uniel*) and equalled at least 35 % in the lamp *SBL-5* (*Smartbuy*).

Radiation spectra of the lamps were studied by means of the *OL 770VIS/NIR* spectroradiometer. Radiation spectra of FLED lamps are continuous, it occupies the entire visible region and its peak wavelength lies within the yellow-orange part of the spectrum providing warm white light of the lamps. Based on CIE (Commission International d'Eclairage) 1931 standard colorimetric sys-
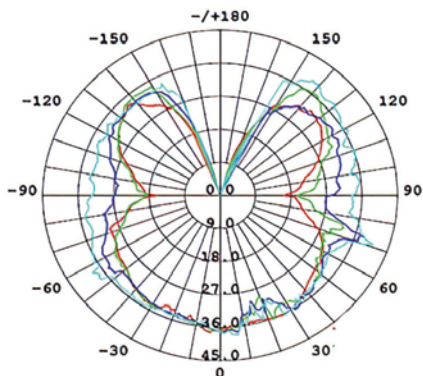
Fig. 3. LIDCs of the B230–40 incandescent lamp
(with A60 bulb)

tem, chromaticity coordinates of the lamp SDF-8 (LISMA) are (0.4558, 0.4104), which corresponds to T_{cp} of 2,700 K; the chromaticity coordinates of the lamp *SKY-A60–8–30K-E27* (*Uniel*) are equal to (0.4338, 0.4009), which corresponds to T_{cp} of 3,000 K.

Using the goniophotometer set *GO 2000A* (*Everfine*), LDCs of the studied lamps were registered (Figs. 1 and 2). The figures show that the shapes of LIDCs are primarily sine [10]; maximum luminous intensity of SDF-A60–8–27K-E27 is equal to 87 cd, maximum luminous intensity of *SBL-A60F-5–30K-E27* is equal to 35 cd, maximum luminous intensity of *GLDEN-A60S-10–230-E27–2700* is 84 cd and that of the lamp *SKY-A60–8–30K-E27* is 83 cd. As a comparison, Fig. 3 shows LIDC of a B230–40 incandescent lamp (with *A60* bulb) [11]. As we can see, LIDCs of FLED lamps are merely different from LIDC of an incandescent lamp.

Table 2 summarises the results of measurements of the characteristics of FLED lamps after 1,000, 2,000, 3,000, 4,000 and 6,000 hours of continuous work and the results of calculation of the luminous flux retention factor of the lamps after *n* hours of work (*L*) using the formula from standard [8]:

$$L = (\Phi_{v,n} / \Phi_{v,o}) \cdot 100, \%,$$

where $\Phi_{v,o}$ is the initial Φ_v, $\Phi_{v,n}$ is the Φ_v after *n* hours of work. The lamp *GLDEN-A60S-10–230-E27–2700* (*General Lighting Co., Ltd*) was out of service after 3,466 hours of work.

Fig. 4 shows the graphs of changes in Φ_v of the lamps in the course of continuous work.

Standard [8] sets 5 categories based on *L*: A, B, C, D and E and each of them is characterised by reduction of nominal Φ_v by 10 % as compared to a previous category, with $\Phi_{v,o}$ at 0 hours.
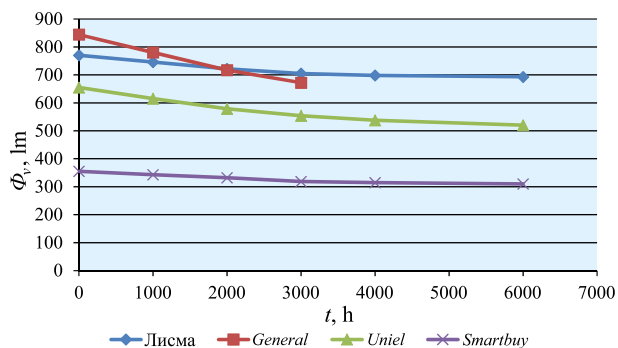
Fig. 4. Reduction dynamics of luminous flux of the compared lamps

Based on the results of the tests, after 6000 hours of operation, the lamp SDF-8 (LISMA) may be categorised as *A*-category, the lamp *SKY-A60–8–30K-E27* (*Uniel*) may be categorised as *B*-category, and the lamp *SBL-A60F-5–30K-E27* (*Smartbuy*) may be also categorised as *A*-category, however, its k_f is too high.

3. ANALYSIS OF THE RESULTS OF LAMP CHARACTERISTICS COMPARISON

As a result of the studies of the lamps conducted in the course of 6,000 h of continuous operation, the following conclusions may be drawn:

– SDF-8 lamp (Lisma) has the highest *L* (90 %) and the least k_f;

– *SBL-A60F-5–30K-E27* lamp (*Smartbuy*) has $L = 87.3$ % and the highest k_f which exceeds the acceptable value by 7 times and more;

– *L* of *SKY-A60–8–30K-E27* lamp (*Uniel*) is equal to 79.4 % and k_f does not exceed the standardised value;

– T_{cp} of all lamps virtually did not change (with consideration of acceptable errors).

As noted above, the lamp *GLDEN-A60S-10–230-E27–2700* (*General Lighting Co., Ltd*) was broken after 3466 hours of operation, its *L* was equal to 79.6 % after 3000 hours of operation and k_f did not exceed the standardised value. As a result, this FLED lamp cannot be recommended for lighting of living premises due to low service life and *L*. According to standard [8], it may be categorised as *C*.

SDF-8 (LISMA) is the only lamp which may be categorised as *A* as per standard [8] and it may be recommended for application in household lighting devices.

Table 1. Parameters of the Lamp Samples

Lamp type	*SDF-8* (Lisma)		*GLDEN-A60S-10–230-E27–2700* (General Lighting)		*SKY-A60–8–30K-E27* (Uniel)		*SBL-A60F-5–30K-E27* (Smartbuy)	
Parameters	declared values	measured values	declared values	measured values	declared values	measured values	declared values	measured values
Φ_v, lm	780	770	890	870	800	655	480	355
T_{cp}, K	2,700	2,736	2,700	2,717	3,000	2,991	3,000	2,946
R_a	> 80	85	> 80	85	> 80	83	> 80	81
Power, W	8.0	7.6	10.0	7.0	8.0	5.4	5.0	3.22
η_v, lm/W	97.5	101.3	89.0	124.2	100.0	121.0	96.0	110.0
k_f,%	< 1	0.2	< 5	0.2	< 5	3.5	< 5	35

Table 2. Time Behaviour of Lamp Parameters

Lamp type	Parameters	Operation duration, h					
		0.25	1,000	2,000	3,000	4,000	6,000
SDF-8 (Lisma)	Φ_v, lm	770	746	722	705	700	693
	k_f,%	5	0.5	0.5	2	0	0.5
	L,%		96.9	93.8	91.6	90.9	90.0
GLDEN-A60S-10–230-E27–2700 (General Lighting)	Φ_v, lm	844	771	702	672		
	k_f,%	5	0.2	2	3.5		
	L,%		91.4	83.2	79.6		
SKY-A60–8–30K-E27 (Uniel)	Φ_v, lm	655	605	579	554	529	520
	k_f,%	5	3.5	3.5	0.5	0	
	L,%		92.4	88.4	84.6	80.8	79.4
SBL-A60F-5–30K-E27 (Smartbuy)	Φ_v, lm	355	343	332	319	315	310
	k_f,%	5	35	35	30	25.5	26
	L,%		96.6	93.5	89.9	88.7	87.3

REFERENCES

1. Zheleznikova O.E., D. Mohammad S.D., Mikhalkova A.N., Mikaeva S.A. Lighting with led light sources / automation. Modern technology// 2019. T. 73. # 12, pp. 540–543.

2. Zheleznikova, O. E. on the effectiveness of LED lighting for visual work / / O. E. Zheleznikova, S.A. Amelkina, L.V. Sinitsina// Light & Engineering, 2018, #2, pp. 6–10.

3. Zhuravleva Yu.a., Kovalenko O. Yu., Mikaeva S.A., Atishev A.V., Nemov V.V. Investigation of the influence of the form factor of led lamps for household lighting on their lighting characteristics // Energy Security and Energy Saving, 2019, No. 6, pp. 24–27.

4. GOST R54815–2011/IEC/PAS62612: 2009. LED lamps with a built-in control device for General lighting at a voltage of more than 50 V. Operational requirements, Entered 2012–07–01, Moscow: Standardinform, 2012, 16 p.

5. GOST R55702–2013. Light sources are electric. Methods for measuring electrical and light parameters. "Yes," I said. 2013–11–08, Moscow, Standardinform, 2013. 44 p.

6. GOST R54350–2015. Lighting devices. Lighting requirements and test methods. – Entered 2016–01–01. Moscow: Standardinform, 2015, 45 p.

7. Nesterkina N.P. about the characteristics of led filament lamps with a power of 4, 6, 8 W / N.P. Nesterkina, A.S. Kondrashin / / in the collection: Problems and prospects of development of domestic lighting, electrical engineering and energy materials of the XIII All-Russian scientific and technical conference with international participation in the IV all-Russian lighting forum with international participation, 2017, pp. 358–366.

8. Mikaeva S.A., Zheleznikova O. E., Sinitsyna L.V. Complex of modern research equipment for light measurements / / automation and modern technologies, 2012, #12, pp. 33–36.

9. Appendix to certificate no. 64752 photocolorimetric measuring Installation. – [Electronic resource]. – Access mode: http://fundmetrology.ru/ 10_tipy_si/11/view.aspx?num=qJbKqJpWgBeM / – Title from the screen.

10. Nestyorkina N.P., Kovalenko O. Yu., Zhuravlyova Yu.A. Analysis of characteristics of led lamps with T8 bulb by various manufacturers// Light & Engineering, 2019, Vol. 27, № 6, pp. 82–87.

11. J. Liu, C. Xu, H. Zheng, and S. Liu, "Numerical analysis and optimization of thermal performance of LED filament light bulb," in 2017 IEEE67th Electronic Components and Technology Conference (ECTC), pp. 2243–2248, Orlando, FL, USA. – 2017.

12. C. Xu, Z. Zhang, J. Chu et al., "Thermal dissipation enhancement of LED filament bulb by ionic wind" in 2016 17th International Conference on Electronic Packaging Technology (ICEPT), pp. 1212–1215, Wuhan, China, 2016.

Nina P. Nestyorkina, engineer. In 1975, she graduated from N.P. Ogarev Mordovia State University with specialty in Light Engineering and Light Sources. Head of the laboratory and senior lecturer of the Light Sources sub-department of the Electronics and Light Engineering Institute of the N.P. Ogaryov Mordovia State Research University. Area of scientific interests: discharge and LED light sources, lighting installations, circuit engineering

Olga Yu. Kovalenko graduated from the Mordovia State University majoring in Lighting Engineering and Sources of Light in 1983. Professor of the Metrology, Standardisation and Certification sub-department of the Institute for Electronics and Lighting Engineering of the N.P. Ogarev Mordovia State University, Doctor of Technical Sciences, Associate Professor. Her research interests are measurement and monitoring of parameters of lighting and irradiating systems

Yulia A. Zhuravlyova graduated from the Mordovia State University majoring in Lighting Engineering and Sources of Light in 2010. Associate professor of the Light Sources sub-department of the Institute for Electronics and Lighting Engineering of the N.P. Ogaryov Mordovia State University, Candidate of Technical Sciences, associate professor. Associate professor of the Electronics sub-department of the Institute for Physics and Technology of RTU MIREA. Research interests: Energy-efficient lighting installations; parameters of contemporary small-size fluorescent lamps and LED light sources; vacuum equipment

Svetlana A. Mikaeva, Doctor of Technical Science, Associate professor. In 1988, graduated from N.P. Ogarev Mordovia State University with specialty in Light Engineering and Light Sources. Head of the Electronics sub-department of the Institute for Physics and Technology of RTU MIREA. Research interests: light engineering and light sources, instrument manufacturing technology, instrument monitoring and diagnostics, solid-state electronics, radioelectronic components, quantum-effect devices

DEVELOPMENT OF VISUAL THINKING OF STUDENTS SPECIALISING IN LIGHTING DESIGN AS PART OF THE LIGHT MODELLING PRINCIPLES AND METHODS DISCIPLINE

Natalia V. Bystryantseva[1], Ilya S. Smilga, Darya A. Chirimisina[1], and Valeria V. Lukinskaya

ITMO University, St. Petersburg
[1]E-mail: chirimisinad@gmail.com

ABSTRACT

Through the examples of global architecture, art and design schools of the 20th and 21st centuries, the authors conduct historical and comparative analyses of the methods of studying form-making elements of composition as a method of development of visual thinking of students. The article discusses applicability and efficiency of integration of a propaedeutic course on primary elements of composition in the Light Modelling Principles and Methods discipline (Lighting Design specialisation, ITMO University), describes the methodological basis of the discipline.

Keywords: lighting design, visual (figurative) thinking, primary elements of composition, light modelling, perception

1. INTRODUCTION

Nowadays, the profession of a designer is trendy and prestigious. This is evidenced by increase in the number of search queries on quick (from two weeks to several months) design training courses. Such design courses are mainly oriented on training technical tools, i.e. various graphics and visualising software, which is definitely important for professionals to know. However, it has long been known that design is directly associated with the functional side of the physical world and constructing of forms; it is primarily art, which solves aesthetic and artistic problems while creating new forms. Therefore, one of the main tasks of design art is to create a "vision", i.e. a reflection of sensory perception of things and phenomena as well as to design it for a spectator. "The artist is the hand through which the medium of different keys causes the human soul to vibrate", as Wassily Kandinsky wrote in his canonical book "On the Spiritual in Art" [1], where "the key" naturally represents the interaction between geometric forms and light affecting a spectator's perception. In order to create a vision in design, specific level of development of visual thinking and understanding of perception patterns are required and should be formed in future specialists.

L.G. Medvedev formulated a definition of visual thinking that is similar to ours noting that "Visual thinking is a dynamic process consisting of senses, perception, concepts, insights, imagination: it is a capability of human conscience to reflect the reality in a visual form" [2, 3, 4]. Its main function is to create visions and operate them while solving problems. One of the stages of development of visual thinking of a future designer is learning of a universal set of design methods and artistic expression means. This article describes practicability and efficiency of the method of studying of formal composition, one of the main tools of development of visual thinking in lighting designer training. The methodology is analysed on the basis of practical experience of visual thinking training of the first-year Master's degree students of the ITMO University Lighting Design programme as part of the Light Modelling Principles and Methods discipline.

**Table. Key Elements, Objectives and Principles of Propaedeutic Methodologies
of Bauhaus and VKHUTEMAS**

	Bauhaus	**VKHUTEMAS**
Elements of visual language	Line, point, spot, plane, volume, space	Line, spot, plane, volume, space
Objective of the course	Development of compositional and artistic thinking, formation of creative freedom including the sensory and emotional component	Training students in the language of plastic forms, patterns of form and colour making
Basic principles and approaches to training in the propaedeutic course	Comprehensive learning of elements of visual language related to programmes of further thematic workshops (sculpture, theatre etc.)	The method was designed as a creative concept of rationalism form-making with 'elements of architecture', from abstract to specific ones, being the basis of composition Modelling as a step of design. Division of plastic culture into separate disciplines used for training separate elements of visual language
Basis of the pedagogical system (artistic movements)	Expressionism, abstractionism, functionalism	Rationalism, constructivism "objective and formal method"

2. THE GENESIS OF FORMAL COMPOSITION TRAINING METHODOLOGY IN ARCHITECTURE AND DESIGN EDUCATION

Just like in the 1920s, when first design schools had been forming, nowadays professional education in the fields of design and architecture is to a large extent based on the principles of creative design that had been formulated and practically implemented by the two main schools: Bauhaus in Germany and VKHUTEMAS (Higher Art and Technical Studios) in Russia. In order to understand the dynamics of the goals of formal composition and primary elements studying, we should address the origins, since it is Bauhaus and VKHUTEMAS that created and applied these methods as propaedeutic disciplines. The main elements, goals and principles of propaedeutic methodologies of Bauhaus and VKHUTEMAS are summarised in the Table.

It is commonly believed that the German Bauhaus appeared due to changes of social and cultural conditions and social and political structure in the early 20th century. The new human attitude towards the world expressed in the art by avant-garde artists could not but influence the system of artistic education itself. The new training methods were originally proposed by J. Itten, a future lecturer of the school, in 1918 and then were integrated in the Bauhaus school education programme as part of the propaedeutic course.

W. Kandinsky, one of the ideologists and creators of the contemporary form-making theory, also played a special part in the history of creation of the Bauhaus propaedeutic course. Being an artist and an art theorist, W. Kandinsky created his own course which was based on scientific achievements of contemporary mathematics, psychology, physiology and other disciplines in order to create the 'Science of Art' (Kunstwissenschaft). His first step was to create a specific language of primary composition elements which allows people to talk about the inner emotional and spiritual meaning of a work of art, to form a spectator's perception corresponding to an artist's idea. He described this language in his book "Point and Line to Plane" [5]. This language consisting of several primary elements, "letters" (points, lines and planes), is analysed using the properties of these primary elements and their changes in the course of interaction in a composition. W. Kandinsky believed that the training methodology should be based on training to interpret primary elements of art and to use them.

At the same time in VKHUTEMAS, where its own art ideology had been forming, the training methodology was mainly based on the students completing research tasks using primary elements of composition as well as studying their proper-

ties and qualities. N.A. Ladovsky was the first in VKHUTEMAS to raise the question of necessity to research the psychology of human perception of architectural and artistic forms [6]. He also established a research laboratory where objective patterns of psychological and physiological perception of physical environment were experimentally studied. At the same time, thanks to N.A. Ladovsky, separate formal primary elements have begun to be studied in terms of their perception as part of specific composition combinations, which has definitely enhanced the artistic pedagogics of the school as well as has become a technique actively adopted by co-thinkers.

The analysis of the experience of architecture and design schools in their work with primary elements of the plastic language makes it clear that the set of the primary elements remains unchanged. In particular, the transformation involves the objectives of the training courses regarding the search for the language of formal composition which were considered as **the basis of creation of the theories of spaces** in the early 20th century. The situation changed in the 1950s, when P. Ya. Galperin developed the theory of step-by-step formation of mental efforts [7]. After acquiring the psychological and pedagogic grounds, propaedeutic methods reach the new educational level: **they are re-oriented from the result to the process**, i.e. **from creation of a product (project) to the course of the creative process, development of visual thinking.** Departure from ready techniques, experimenting in the course of creation common for the avant-garde movement has logically led to necessity of "search training" of new form-making patterns and mechanisms of visual thinking.

Many of contemporary educational institutions including architectural and design faculties of such universities as *Bauhaus-Universidad Weimar* (Germany), *Illinois Institute of Technology* (USA), *Iuav University of Venice* (Italy), *Yale University* (USA), MGUP (Moscow State University of Press) and MArkhI (Moscow Architectural Institute) are the successors of propaedeutic and creative traditions of VKHUTEMAS and Bauhaus. Development of the methodologies leads to concretising of form-making properties of compositions and their detail interpretation in specific areas of design activity; this article will specifically discuss the lighting design.

3. FORM-MAKING AS A PROPAEDEUTIC COURSE IN THE CONTEXT OF LIGHTING DESIGN

Form-making gains a new interpretation in the field of lighting design due to changes of requirements to the quality of lighting environment. The principles of construction of an object image become more complex; for instance, during interaction between artificial light and a form and material, an object's light image appears which is qualitatively different from its daylight image. The new requirements led to changes in methods of form making and a number of discoveries.

In 1971–1972, a team supervised by N.M. Gusev and N.M. Shchepetkov conducted a search for volumetric light modelling for the ensemble of the Cathedral of Saint Demetrius and the Dormition Cathedral in Vladimir [14]. The models were equipped with small light sources with adjustable luminance and power for modification of the structure of the light composition of the ensemble.

In 1977, the Methodological Recommendations on Design of Outdoor Architectural Lighting of Buildings and Structures handbook was published under supervision of G.V. Kamenskaya [8]. The handbook describes the methodology of selection of lighting and colour arrangement by means of modelling. In order to form luminance distribution over a building facade, a slide projection apparatus was developed for planar modelling of lighting. Luminance and colour of some fragments of the image were changed by means of a control board. The apparatus allowed to find optimal variants of a lighting and colour arrangement of a building or structure which shall be implemented in situ.

In her study, A.G. Batova conducted laboratory lighting modelling using a 1:10-scale model of a wall of the Solovetsky Monastery [19]. In the course of the experiment, optimal variants of light and composition parameters were found (luminance distribution and ranges of luminance contrasts). This work also studied the effect of artificial light on visual perception and interpretation of architectonics.

These methods include search for patterns of construction of a lighting composition of specific elements of an object or an architectural composition of an ensemble when changing the luminance ratio in the field of view. The effect of lighting parameters on changes in perception of spatial arrange-

ment gives a perspective of construction (recovery) of perception of the form of its visible components such as specific elements, building proportions and tectonics under natural lighting.

There are no many methods utilising formal properties of primary elements even in international practice; *Aalborg University* (Denmark) and *Jefferson University* (USA) are among the universities training such methods. Lighting design educational programmes are mostly focused on studying natural effects and materials (which are, in turn, also a fundamental element) [9,10,11,12].

In international practice (Hochschule Wismar (Germany), Royal Institute of Technology (Sweden)), form making is mostly considered within the framework of laboratory-based light modelling using architectural models.

In 1999, A.B. Matveev's article Aesthetics of Lighting was published. The author identified several important methods of work with light and primarily the necessity to find the limits for creation of the 'light language': "…light acts as one of components of the language by means of which the image of an environment is recreated. Like any language of a work of art, light and other expressive means should be used in accordance with the patterns and limitations natural for the language of this work" [16]. This points out not only to necessity of finding a language but also to understanding of "properties of this work of art", i.e. properties of composition in lighting aesthetics. This methodology has developed on the basis of architectural lighting principles, where, defining boundary parameters of specific elements of a building (portico, pillar, entablement, pediment, etc.), proportions of perception of the composition of classic form-making architecture were experimentally established [17].

In 2008, methods of space interpretation as a situation with specific environmental nature were developed in the Architectural Environment Design sub-department of MArhkI. As part of the Spatial Senses Pavilion task, the students, future architects and spatial light characteristic designers, used formal composition means when creating a model using the 'cut and bend' technique. The task aimed at creating a small object for 'increased sensing' based on solutions of architects of the 20th century, detail familiarisation with the principles of spatial arrangement of architecture using works of VKHUTEMAS and Bauhaus and some masters (F.L. Wright, Le Corbusier, T. Ando, S. Hall,

Fig. 1. "Volume, Contrast, Colour"
(Student A. Dubinovskaya; Lighting Design Programme, ITMO University, 2014)

Z. Hadid, etc.) as examples. Graphic analysis allows students to learn various compositions means when arranging the space and inspires them to create their own design solutions [15].

In 2015, N.V. Bystryantseva defended her thesis at the same sub-department under supervision of A.V. Efimov. This work suggested a method of design search for interaction between parameters of different types of lighting within the borders of a visual plan or spatial area based on primary means of light and composition construction, namely points, lines, spots and their structure as well as spectral and luminance characteristics taking information about urban environment into consideration [14]. Such approach supplemented the design with a new stage of search for form-making properties and light-composition interactions between elements inside spatial arrangement without reference to their urban-planning composition. It means that, while designing, an author uses not geometric patterns for constructing a form but perceptive ones which create visual and informational links using W. Kandinsky's 'inner composition' principle. The 'inner composition' principle seems to perfectly demonstrate the grounds for creative visual design: "life of exceptionally and perpetually artistic forms and forms randomly thrown on canvas" [18]; working with an abstract composition, an author may depart from artistic forming of details and work with the nature of form making (both the one existing inside an object after being put by an architect and the new one under artificial light). This technique provides an author with a capability not to 'look at a picture from outside' but 'to whirl inside a picture, to live inside it' [18]. In the context of such problem statement, not only interpretation of artistic properties of light-engineering and optical parameters but

MODELS OF SPATIAL SENSES PAVILION

Fig. 2. Models of the spatial senses pavilion, MARKHI, 2008

also change of attitude to urban architecture, its spatial arrangement, renewal of perception of its semantic meaning has become important. Definition of formal composition properties allowed to 're-set to zero' the decorative value of architecture and to work with basics of compositional arrangement using stable artistic paradigms: the classic, modern and post-modern ones [14].

This first step towards formation of a meta-language in lighting design is being further developed in the methodological course of the Lighting Design programme. Since 2014, this method has been being tested by the Lighting Design programme employees of the ITMO University as part of Principles and Methods of Light Modelling discipline. The methodology forms the basis of development of visual thinking in design. This means that, in the course of training, a lighting designer learns a set of compositional form-making elements, their properties, ways of their interaction in which light is used as the main material, Fig. 1. Being a tool, which is capable 'to create many different values of the same item via its light image, light form', [16], light, in turn, may supplement the methodology of the work with primary elements. A number of methodological approaches was tested in this course.

The first stage of testing of light modelling methods included the following tasks:

– Analysis of form-making principles (classic, modern, post-modern), their recognition and destruction or identification of the patterns of their light composition (picture, model, photo);

– Analysis of form-making principles of classic composition (plane, volume, space) and their inter-action with natural light at different daily changes and cloudiness (contrast, nuance, incidence angle), recreation of these effects when arranging a lighting environment (picture, model, photo);

– Analysis of interaction between form-making principles of space composition and their interaction with lighting techniques (recreation of effects in a model).

Analysis of an architect's own method (Tad-ao Ando, Le Corbusier, Kenzō Tange, Steve Hall, etc.), formation of a spatial senses pavilion (a pa-vilion where different light and space compositions are used to submerge people in specific emotional states and people acquire new experience of interaction with space) using this author's method (based on early practice of MArkhI: picture, model, pho-to), Fig. 2.

This methodology allowed us to formulate practical knowledge of the patterns of light composition construction in architectural lighting, namely to understand: the effect of incidence angle, luminance and lighting techniques on perception of the form of an object; distinctions and differences of artificial and natural lighting; interaction between an object's colour range and spectral characteristics of light sources. However, utilisation of specific existing lighting techniques, approach to visual forms of buildings in models and insufficient freedom to create optical effects have limited a capability to develop research experience and creative intuition of students. The scale of perception of a solution designed as a model did not allow us to gain specific practical experience for its utilisation in actual design.

Fig. 3. Paper plastics (Student A. Bondar; Lighting Design Programme, ITMO University, 2015)

Fig. 4. Vision of an object (Student A. Gafurov; Lighting Design Programme, ITMO University, 2015)

Fig. 5. A photo portrait (Student E. Smirnova; Lighting Design Programme, ITMO University, 2015)
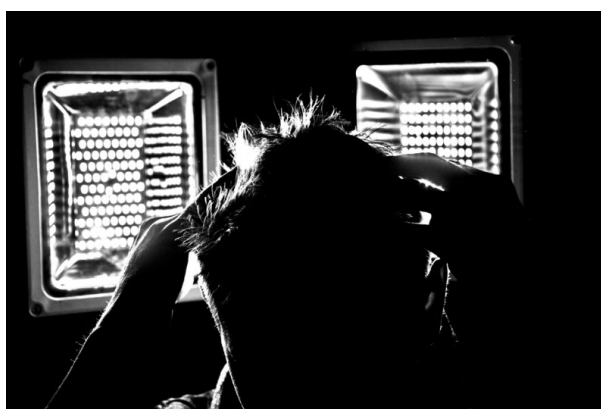
Fig. 6. A photo portrait (Student I. Domashkevich; Lighting Design Programme, ITMO University, 2015)

The second stage of testing was based on early practice of paper form making adopted in GHPA (Saint Petersburg Stieglitz State Academy of Art and Design). Its main principles are: departure from formal composition, work with "natural images (sunset, noon, fog, light spots), abstract volumetric and spatial construction of paper (analysis of: Kazimir Malevich – philosophical grounds of special interpretation of a plane in artistic space; Vladimir Tatlin – form beyond a flat canvas; Alexandr Rodchenko's paper plastics – volume interpretation of artistic space; V.F. Koleychuk – typology of constructive methods of plane transformation, Fig. 3. B.N. Rachmaninov's paper plastics course ("By squeezing paper you unchain your mind") plays a special role.

The work in accordance with this methodology includes:

– Formation of experience of interaction between a form and light and understanding of distinctions of light distribution over different shapes (round and rigid), design of a clear-obscure by the form of canvas itself (model, photo);

– Learning and formation of optical properties of light, understanding of a material via properties of paper (self-glowing, reflected, direct light), spectral characteristics and colour of light (experiments with scale models, results are shown using photos);

– Learning of primary elements of formal composition on a plane;
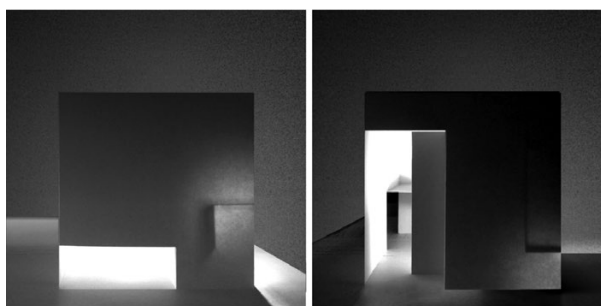
Fig. 7. External volume and Artificial lighting (Student A. Khvatova; Lighting Design Programme, ITMO University, 2018)

81

Fig. 8. Classics. Modernism and Postmodernism (Student L. Angelova; Lighting Design Programme, ITMO University, 2018)

– Learning of techniques: proportioning (fifth portions, module) and proportion of volumes in a planar and spatial composition, colour and graphic coding of information, learning of form-making principles (statics and dynamics, rhythm (changing repetition) and metre (repetition without changes), etc.);

– Experimental learning of capabilities of different materials, learning of composition patterns in the format of experiments, learning of techniques: scale, work with light and form, the effect of light graphics on perception of a form, and experimental modelling and compositional breakdown (model, photo);

– Experimental learning of changes of light and space, learning of techniques: contrast and nuance lighting, silhouette, creation of dynamics in a frame, work with a shade form and an object image (model, photo), Fig. 4;

– Formation of experience of meaning transition on the border between illustration and sign, transition from material and physical perception to formal and visual perception, establishment of conditions and factors exit from which always lies within the area of simplification and archetypisation, learning of compositional techniques: silhouette and background, large and small, contrast and nuance, statics and dynamics, graphics and sense, and understanding of distinctions of perception of natural light-and-dark structures (patterns) (meaning transition), and also work with the concepts of time, contrast, movement (graphics, model, photo), Figs. 5, 6.

This methodology allowed students to form research experience. In visual terms, students' works had broad nature, however, the experiments were not naturally determined; there was a lack of research and conclusions. It was necessary to reduce the amount of effects and to increase accuracy of used compositional techniques of natural changes identification during light modelling.

The third stage included alignment of formal composition with searching light modelling (plane, volume, space), concretising and studying of light-composition principles, studying of the effect of different characteristics of luminous flow (point, line, spot) on form-making properties of an environment, search for an author's artistic language, Fig. 7. Methodological objectives of the course are presented below.

• Learning of luminous flow modelling techniques by means of optics, reflectors, limiters. Analysis of techniques of work with light at a model level (incidence angle, reflection angle, luminance, spectre, natural patterns). Accumulation of a set of modelling techniques.

• Analysis of interaction between artificial lighting and plastic techniques of form making (classic,
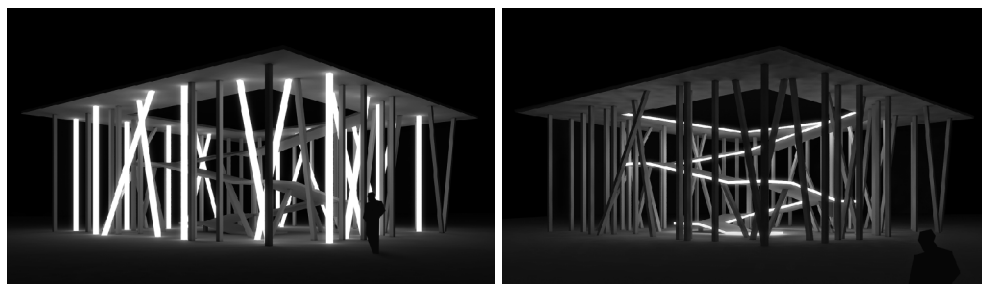
Fig. 9. The spatial senses pavilion (Student Yu. Lyubakova; Lighting Design Programme, ITMO University, 2016)
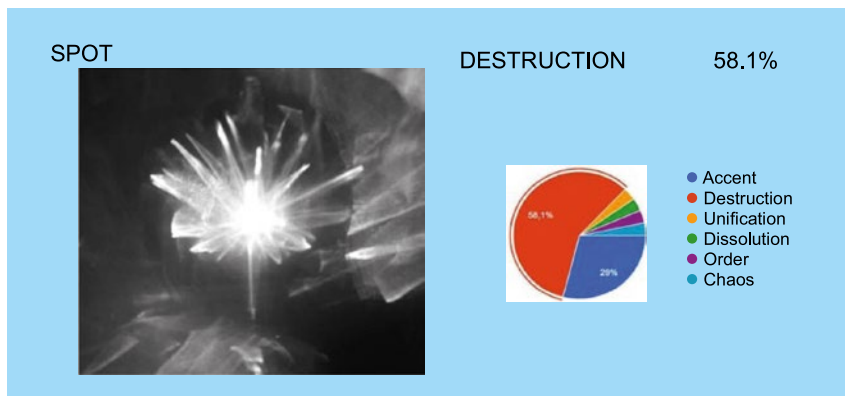
Fig. 10. The results of the questionnaire (Student M. Ivleva; Lighting Design Programme, ITMO University, 2018)

modern and postmodern) on a plane, in a volume and in a space, Fig. 8. Works are divided into separate light-composition tasks (rhythm – metre, statics – dynamics, symmetry – asymmetry, contrast – nuance, destruction – unification).

• Analysis of the effect of the sequence of perceived fragments, establishment of visual and informational links based on the principles of "inner composition" (semiotics, time, space, model, research and photo).

• Analysis and studying of authorial methods of architects, lighting designers and designers in their work with the spatial senses pavilion (presentation, model, photo), Fig. 9.

• Prototyping and search for new forms of interaction between light and various types of spaces, practical research of the effect of a light solution on emotional reactions of people (model, photo, research).

• Analysis and uncovering of patterns of perception of the received visual images by a user (social questionnaire), Figs. 10, 11.

This method demonstrated high results in terms of development of visual thinking of students, formation of their own artistic language as well as capability to understand the mechanism of formation of human psychological and physiological state by the effect of light and to control this mechanism.

4. CONCLUSION

Both light as a tool and work with it have a number of specific distinctions related to its nature.

– Light modelling is a continuous process of experimental search. Continuous practical studying of variability of light environment, unpredictable effects and nuances occurring in the course of works with optical lenses, stencils, reflecting and scattering materials pre-determine appearing of an unique image and develop a lighting designer's creative intuition.

– The differences in the nature of light as a tool are determined by its broader means of visual expressivity. This is associated with the fact that "keeping its conventional 'applied' function of one of the artistic expressivity means, over the 20th century, light had gradually acquired characteristics of a self-consistent form of creativity in synthesis with different types of art such as music, stage art, architecture, sculpture or, less frequently, with monumental painting" [13].

– It is important that properties and interactions between primary elements are studied not only using paint, marker pens, pencils but also using artistic qualities of light, a tool of future project work. Alongside with creation of an image in composition, the properties and nature of light are being studied, an authorial methodology is being established: students form their own "light language", individual technique of work with light and its nature.

– The most significant distinction of light as an instrument of creation of a formal composition is its spatial and temporal value in the course of interaction with a user. When we look at a light spot, we understand that there is a light source somewhere, we understand its intensity, the way it has passed between the source and the object, we can see the relation to a reflecting, absorbing or translucent surface. When creating visual and informational links within a light environment, we look at a series of light spots but see an image possessing specific information.

Capability to think with images, to construct relations and to understand their effect on a person is a basic category of formation of a lighting designer's professional mind-set. Moreover, compiling of a basic 'dictionary' of techniques for learning professional language of light is a methodological necessi-
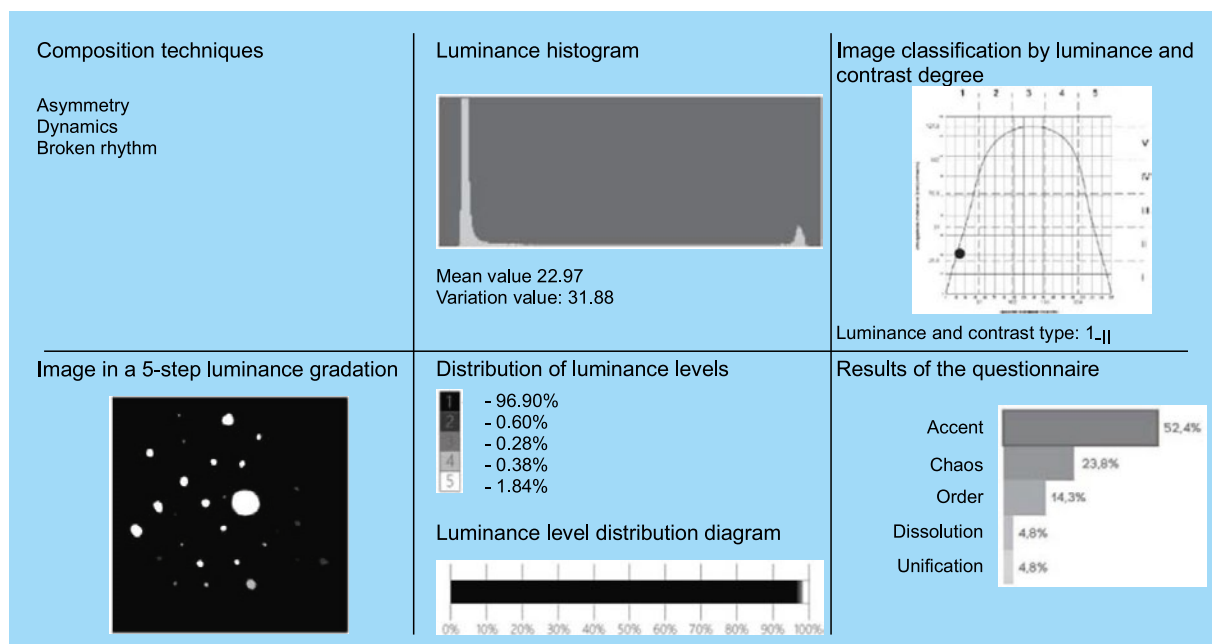
Fig. 11. Analysis of luminance and contrast (Student A. Khvatova; Lighting Design Programme, ITMO University, 2018)

ty when working with students having unequal level of art education. This is caused by different professional and educational experience: from designers, architects, actors to technical (laser opticians, engineers, IT) and natural-science (chemists, physicists) specialists. The question of differences between students' skills is important for many schools, which is determined by inter-disciplinary nature of lighting design as a subject of communication and cooperation between specialists in many professional areas.

In our opinion, the gap between technical and artistic skills and knowledge of students educated in different areas of science, art and design in the said schools can be closed and the balance between them can be found by integrating the disciplines studying human perception of light that determine the human-oriented approach to projects. However, application of the form-making methodology based on utilisation of primary properties of composition and artistic properties of light could significantly supplement formation of professional mind-set of future lighting designers, enhancement of their creative thinking and departure from template thinking.

REFERENCES

1. Kandinsky W. On the Spiritual in Art [O dukhovnom v iskusstve]. Moscow: Arkhimed, 1992, 112 p.

2. Medvedev L.G. Formation of a Graphic Imagery in Drawing Classes: A Study Guide for Students of Art and Graphic Faculties of Pedagogical Institutes [Formirovaniye graficheskogo khudozhestvennogo obraza na zanyatiyakh po risunku]. Moscow: Prosvechsheniye, 1986, 159 p.

3. Zinchenko V.P. Osip Mandelshtam's Walking Stick and Mamardashvili's Pipe. On Basics of Organic Psychology [Posokh Osipa Mandelshtama i trubka Mamardashvili. K nachalam organicheskoy psikhologii]. – Moscow: Novaya shkola, 1997, 336 p.

4. Yakimanskaya I.S. Main Lines of Visual Thinking Research [Osnovnyie napravleniya issledovaniy obraznogo myshleniya]. Moscow: Voprosy psikhologii, 1985.

5. Kandinsky W. Point and Line to Plane [Tochka i liniya na ploskosti] / trans. from German by E. Kozina. Saint Petersburg: Azbuka, 2001, 236 p.

6. Khan-Magomedov S.O. Architecture of Soviet Avant-Garde: in 2 books. Book One: Problems of Form Making. Masters and Movements [Arkhitektura sovetskogo avangarda: v 2 kn. Kniga pervaya: Problemy formoobrazovaniya. Mastera i techeniya]. Moscow: Stroyizdat, 1996.

7. Galperin P. Ya. Mind Action as a Basis for Formation of a Thought and an Image [Umstvennoye deistviye kak osnova formirovaniya mysli i obraza]. Voprosy psikhologii, 1957, Vol. 6.

8. Kamenskaya G.V. The Methodological Recommendations on Design of Outdoor Architectural Lighting of Buildings and Structures [Metodicheskiye rekomendatsii po proektirovaniyu naruzhnogo arkhitekturnogo osveshcheniya zdaniy i sooruzheniy] / G.V. Kamenskaya, L.I. Petrova et al. Moscow, TsNIIEP of Eng. Equipment, 1977, 63 p.

9. The MSC programme. URL: https://www.light.aau.dk/msc-education/ (date of reference: 15.09.2018).

10. Professional studies master programme lighting design. URL: https://studieren.de/fileadmin/europe/germany/_study/docs/Master_Lighting_Design.pdf (date of reference: 15.09.2018).

11. Lighting M.S. URL: http://catalog.rpi.edu/preview_program.php?catoid=11&poid= 2431&return-to=256 (date of reference: 15.09.2018).

12. Architectural lighting design courses. URL: https://www.kth.se/en/ studies/master/architectural-lighting-design/course-overview-1.268138 (date of reference: 15.09.2018).

13. Lekus E. Yu., Bystryantseva N.V. Lighting Design: Light as Material, Technology, Form: Joint Monograph [Svetovoy dizain: svet kak material, tekhnologiya, forma] // Proceedings of the international scientific conference "Material-Technology-Form as the Universal Triad in Design, Architecture, Fine and Decorative Arts". Moscow: Stroganov Moscow State Academy of Arts and Industry, 2018, 537 p.

14. Bystryantseva N.V. Comprehensive Approach to Establishment of a Light Environment in a Night-Time City: extended abstract of Cand. Arch. Dissertation [Kompleksniy podkhod v sozdanii svetovoy sredy vechernego goroda]. Moscow: Moscow Architectural Institute (State Academy), 2015, 27 p.

15. Sokolova M.A. View from Inside. Design of Architectural Space: Interior. Study Guide [Vzglyad iznutry. Proektirovaniye arkhitektirnogo prostranstva: interier]. – Moscow: BooksMArt, 2016.

16. Matveev A.B. Aesthetics of Lighting [Estetika osvashcheniya] // Svetotekhnika, 1995, Vol. 4–5, pp. 2–4.

17. Shchepetkov N.I. Lighting Design of a City [Svetovoy dizain goroda]. Moscow: Arkhitektura-S, 2006. – 317 p.

18. Feshchenko V., Koval O. Creation of a Sign. Articles on Linguistic Aesthetics and Semiotics of Art [Sotvoreniye znaka. Ocherki o lingvoestetike i semiotike iskusstva]. – Moscow: Yazyki slavyanskoy kultury, 2014.

19. Batova, A.G. Principles of Design of Outdoor Lighting of Architectural Objects: extended abstract of Cand. Arch. Dissertation [Printsipy proektirovaniya naruzhnogo osveshcheniya arkhitekturnykh obiektov]. Moscow: Moscow Architectural Institute (State Academy), 2012, 27 p.

Natalia V. Bystryantseva, Ph.D. She graduated from Gagarin Saratov State University (SGTU) and Moscow Architectural Institute (MArkhI). At present, she is a head of the international Master's Programme "Lighting Design" of the ITMO University and of the Light Environment workgroup of the Smart Saint Petersburg project management office, member of the RULD union of lighting designers, Moscow Government award winner in nomination of Architecture and Design 2014, author of 20 papers, developer of such disciplines as 'Problem-oriented Approach to Design of Lighting Solutions', 'Principles and Methods of Light Modelling', 'Creative Technologies', and co-developer of the concept of the international Master's degree programme Art & Science of the ITMO University

Ilya S. Smilga graduated from Saint Petersburg Stieglitz State Academy of Art and Design in 2001. At present, he is a head of the Production laboratory of the Higher School of Lighting Design of the ITMO University. His research interests: design and prototyping of multimedia installations and light objects

Darya A. Chirimisina, Master's degree (2018). Engineer with the ITMO University. Research interests: lighting design, visual and non-visual effect of light on person, BCI, interactive environments

Valeriya V. Lukinskaya, Master's degree (2018). Engineer with the ITMO University. Research interests: lighting design, visual and non-visual effect of light on person, perception, interactive environments

EVALUATION AND SELECTION OF COLOUR SPACES FOR DIGITAL SYSTEMS

Vera L. Zhbanova

The Branch of National Research University
Moscow Power Engineering Institute in Smolensk, Russia
E-mail: vera-zhbanova@yandex.ru

ABSTRACT

The research examined the changing of colour difference by the control colours depending on the choice of colour space when working with matrix photo detector. The spectral characteristics of photo detectors from different manufacturers noticeably differ from each other and from the addition functions of the working RGB system. This can explain the difference in colour quality between different digital devices. A software method for studying the colour rendition of the image obtained by digital devices based on the selection of an individual colour space for each matrix photo detector is proposed. To analyze and evaluate the capabilities of the spectral characteristics of matrix photo detectors, the control colour method based on the Mansell Atlas was used. The analysis of the obtained parameters of 14 colours was carried out according to various criteria for seven colour spaces: sRGB, AdobeRGB, DCI-P3 RGB, M1N1P1, PAL / SECAM, Wide Gamut RGB, ProPhoto RGB. Also studied the influence of the choice of colour space on the change in the coordinates of the source 6,500 K. Based on the colour differences of the control colours, it is possible to choose the optimal colour space for working with a specific matrix photo detector. The latter will reduce colour distortion at the initial stage of image registration. The ways for improving the colorimetric method of control colours are proposed as applied to digital devices at the software level.

Keywords: colour, colour space, colour difference, digital device, matrix photo detector, RGB

1. INTRODUCTION

The matrix, or the multi-element matrix photo detector (MPD), is one of the main electronic units of digital registering devices. The quality of obtained images depends on to a large extent of their characteristics. The process of colour separation in most image-capturing devices is conducted by MPD itself. Colour separation systems have been constantly developing, which requires large financial and temporal expenses [1]. Digital devices for registration and reproduction of colour images use different colour spaces. The variety of these spaces is related to capabilities of contemporary engineering. For instance, *ProPhoto RGB* is developed with digital capturing of photo film, *sRGB* is based on capabilities of reproducing systems, and *AdobeRGB* is based on capabilities of colour printing. Equipment manufacturers try to follow the established standards adjusting characteristics for correspondence with them. For instance, digital cameras with different spectral characteristics of MPD mostly utilise *sRGB* or *AdobeRGB* [2, 3] and colour distortions are compensated by different correction software. In the course of visualisation and printing of an input image, additional colour distortions occur, therefore, colour rendering in a ready picture becomes inadequate. That is why it is important to obtain the primary digital image which is "clean" to the maximum extent.

Advanced users use a special format to have an opportunity to select a colour space, *RAW*, which contains parameters of each primary colour: *R* (red), *G* (green) and *B* (blue) captured directly from the MPD and either not interpolated, or not digitally filtered. Then a user may set any colorimetric system using different software. Usually, such colour profiles as *Wide Gamut RGB* and *ProPhoto RGB* are selected because of their large colour gamut. However, sometimes application of a colour space with lesser gamut may allow us to obtain better results, which is mostly related to input colour data captured from MPD with different spectral characteristics of major colours.

Every year, newer methods of processing, transformation and improvement of images obtained by digital devices which are just the final stage of processing have been proposed [4–7]. All efforts of manufacturers aim at improvement of optics and software. At the same time, the effect of colour space interaction with MPD characteristics is omitted. Spectral characteristics of filters of camera colour separation systems significantly differ both from each other and from colour mixture curves of the applied standard colorimetric system.

In short, researchers try to solve the problem of colour distortions on a shallow level, without actually taking MPD characteristics into account.

The goal of this work was to study interaction of colour spaces with different spectral characteristics of MPD, and the objectives were to select and analyse spectral characteristics of MPDs by well-known manufacturers; to select and to describe colour spaces; to develop the study methodology; to analyse the obtained results; to formulate recommendations on interaction between colour spaces and spectral characteristics of PD.

2. THE PRESENTED MATRIX PHOTO DETECTORS

MPDs by three manufacturers were selected as study objects: *Sony, Kodak* and *Agilent* (Fig. 1) [3]. Their ideal spectral characteristics have smooth dome shape with single maximums at operational wavelength, λ. For instance, it is ideal when the peak of the green channel spectral curve corresponds to $\lambda = 555$ nm.

The curves of the *Sony* MPD are rather smooth and without secondary peaks. However, the peak of the green channel is at $\lambda = 540$ nm and the green

and blue channel curves cover slightly larger spectral areas. Transmission of blue and green shades of colour is especially important for human, since it is these shades that prevail in the environment (the sky, reflection at water surface, leaves, grass, etc.). The red channel curve corresponds to high transmittance level and its peak is split in two.

When the *Kodak* MPD spectral characteristics are analysed, secondary peaks of the red and blue channels covering each other can be seen. Probably such non-uniformities of the system are taken into account by the manufacturers at the software level and are somehow compensated. However, the original curves will be processed in the study.

The spectral characteristics of the *Agilent* MPD are similar to the previous ones. The curves of the red and blue channels have "tails" covering non-operating regions rather than secondary peaks. Moreover, the peaks of all curves are wide and not smooth, and it worsens the operating properties of MPD and
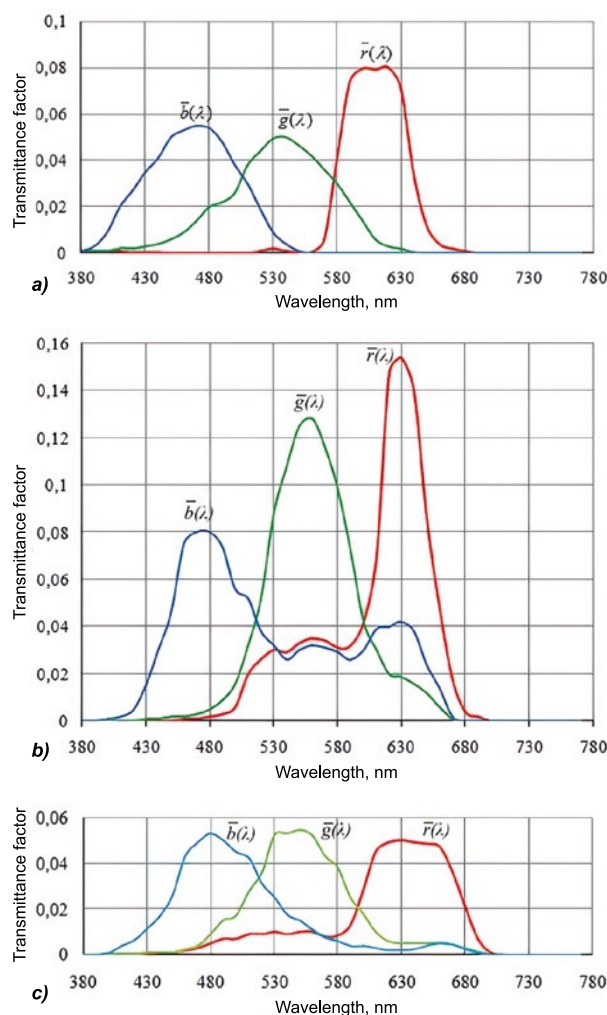
Fig. 1. Spectral characteristics of matrix photo detectors
Sony (*a*), *Kodak* (*b*) and *Agilent* (*c*)

transmission of "clear" colours. These curves correspond to low transmission as compared to the other MPDs, and since chromaticity of control samples is taken into account hereinafter rather than their colour, transmittance shall not affect the results.

This implied that the *Sony* MPD should have the least colour distortions among the analysed ones. But we will return to this assumption in the end of the study, below.

3. THE STUDIED COLOUR SPACES

The contemporary colour spaces *sRGB, AdobeRGB, DCI-P3 RGB, M1N1P1, PAL/SECAM, Wide Gamut RGB, ProPhoto RGB* [1, 2] with different colour gamut [CG] were selected for the study. The systems with reference white *D65* were selected mostly. *Wide Gamut RGB* and *ProPhoto RGB* are exceptions: they have the *D50* colour and have no analogues in terms of CG.

The *sRGB* system is developed as a standard for web and multimedia applications. This and the following colour spaces are actually the main ones for all digital image capturing devices.

The *AdobeRGB* space has increased colour gamut as compared to *sRGB* and is used for typographical and digital printing.

DCI-P3 RGB is the new colour space which imitates the colour palette of motion picture film. This system was developed by the community of cinema and TV engineers as a standard for digital cinemas. The colour gamut of the new space is larger than that of *sRGB* and is smaller than that of *Adobe RGB* in the green-yellow region and is larger than it in the yellow-red region. Nowadays, the *DCI-P3 RGB* system has been being introduced in smartphones and tablets. But will it be able to compete well with the previous two colour spaces?

The *M1N1P1* system was developed by the author and studied both at the software level and experimentally [8, 9]. The system has showed good results according to all criteria but still has not been compared to the leading colour spaces. *M1N1P1* is described as the colour space with maximum colour gamut but minimal negative colour mixture curves for better interaction with digital devices. The *M1N1P1* system has real main colours. When analysing a standard light source (SLS) *E* (with equi-energy spectrum of radiation), correspondence of *M1N1P1* with the CIE1931 *XYZ* was proven. The shape of the obtained spectral characteristics (curves) is better

than that of contemporary analogues and these characteristics will allow us to minimise losses in colour reproduction. Mathematical modelling and comparison of theoretical and practical curves have given satisfactory results.

The *PAL/SECAM* space is based on chromaticities of colour-forming stimuli recommended by the European video broadcasting standard. It is a standard of TV and video broadcasting systems.

The *Wide Gamut RGB* space has maximum possible colour gamut (78 %), clear main spectral colours (λ of 700 nm, 525 nm and 450 nm) and *D50* white point.

ProPhoto RGB almost completely covers the colour gamut of human eye; it is developed for storage of photos and images without losses of information if colour gamut of the used colour space is insufficient. Green and blue are nonphysical. The white point is *D50*.

The major colours of *RGB* systems are presented in Fig. 2.

4. THE METHOD OF COLOUR PARAMETERS CALCULATION

The tristimulus values of reference colours calculation method is based on integral calculation of colour values of an object illuminated by a light
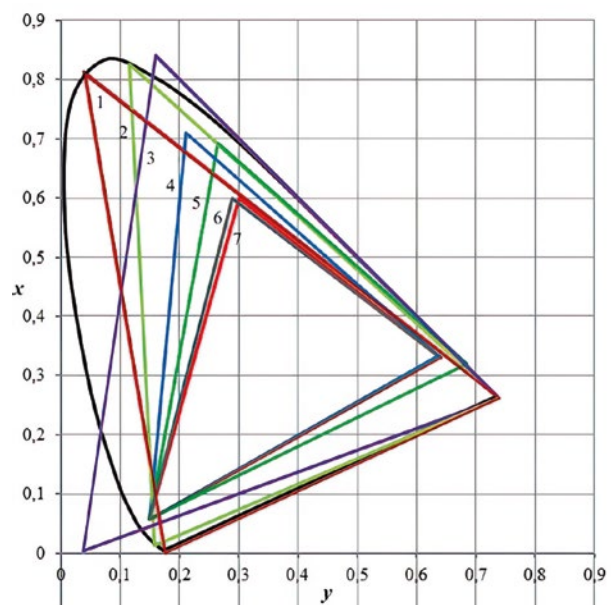
Fig. 2. The studied colour spaces on the *x, y* colour space:
1 – M1N1P1; 2 – Wide Gamut RGB; 3 – ProPhoto RGB;
4 – AdobeRGB; 5 – DCI-P3 RGB; 6 – PAL/SECAM;
7 – sRGB

source with specific spectrum registered by a MPD with specific spectral characteristics and further transformation into one of the colour spaces using the formulas [10, 11].

$$R' = \int\limits_{\lambda=400}^{770} \varphi(\lambda) S_R(\lambda) \bar{r}(\lambda) r_{N,\lambda} d\lambda,$$

$$G' = \int\limits_{\lambda=400}^{770} \varphi(\lambda) S_G(\lambda) \bar{g}(\lambda) r_{N,\lambda} d\lambda,$$

$$B' = \int\limits_{\lambda=400}^{770} \varphi(\lambda) S_B(\lambda) \bar{b}(\lambda) r_{N,\lambda} d\lambda,$$

where $\varphi(\lambda)$ is the spectral radiant flux; $S_R(\lambda)$, $S_G(\lambda)$, $S_B(\lambda)$ are the spectral characteristics of MPD; $\bar{r}(\lambda)$, $\bar{g}(\lambda)$, $\bar{b}(\lambda)$ are the colour mixture curves; $r_{N,\lambda}(\lambda)$ is the spectral luminance factor of the reference samples.

In this case, the tristimulus values in the *R', G', B' linear space will be obtained.* To present the tristimulus values in the required space, it is necessary to transform them into a non-linear *RGB* space, i.e. to take the γ transformation, luminance transformation, etc. into account. If necessary, colorimetric correction is also conducted. But these steps are not made in this study since all values shall be presented in the *XYZ* system.

Then the tristimulus values are transformed into *XYZ* from *RGB* using the expression

$$\begin{pmatrix} X \\ Y \\ Z \end{pmatrix} = \begin{pmatrix} X_R & X_G & X_B \\ Y_R & Y_G & Y_B \\ Z_R & Z_G & Z_B \end{pmatrix} \begin{pmatrix} R' \\ G' \\ B' \end{pmatrix},$$

where X_R, X_G, X_B, Y_R, Y_G, Y_B, Z_R, Z_G, Z_B are the coefficients for recalculation for a specific *RGB* system.

The recalculation coefficients were calculated in accordance with the method [10, p. 236–247, 249–256]. For instance, for the *PAL/SECAM* space, the coefficients were equal to 0.514, 0.265, 0.024, 0.324, 0.670, 0.123, 0.162, 0.065, and 0.853 respectively.

After transformation, the chromaticity coordinates are found:

$$\begin{cases} x = \dfrac{X}{X + Y + Z}; \\ y = \dfrac{Y}{X + Y + Z}. \end{cases}$$
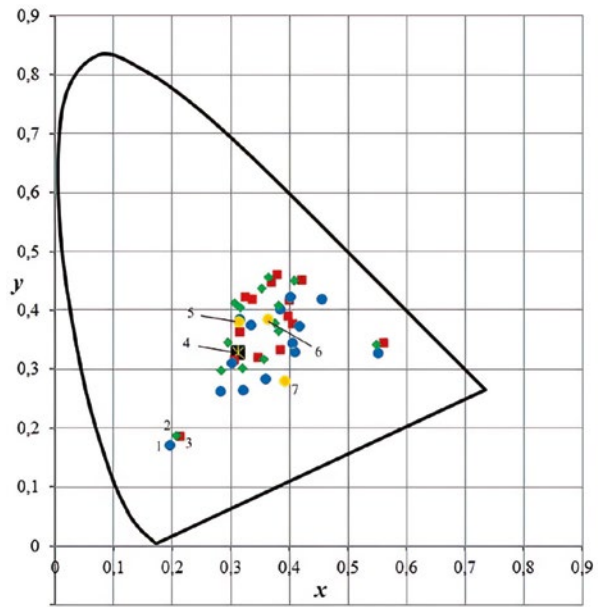
Fig. 3. Chromaticity coordinates of 14 colours from the Munsell Atlas in the *XYZ system: 1 – Sony; 2 – Agilent; 3 – Kodak; 4 – SLS D65; 5 – light source Agilent; 6 – light source Kodak; 7 – light source Sony*

The *XYZ* system is not a uniform chromaticity system, therefore, for adequate comparison of the obtained values with the theoretical data, the chromaticity coordinates shall be transformed into a uniform chromaticity colorimetric system in which colour difference threshold between two colours shall be the same over the entire colour space. According to the CIE recommendations, one of the large number of such systems may be selected: *CIEUVW, CIELUV, CIELAB,* and *CIECAM* [12, 13]. However, they all are oriented on determination of colour change, and if a colour space is selected based on MPD spectral characteristics, it is more necessary to aim at adequacy of chromaticity transmission. Many factors affect the tristimulus values in a real digital system: the dynamic range, the size of the sensitive surface, noises, etc. Colour depends on brightness, while chromaticity is constant. Therefore, in order to be capable to compare the results of the mathematical study with the experimental results, it was decided to analyse colour difference based on chromaticity by means of the 1976 *u'v'* uniform-chromaticity-scale diagram, where, as opposed to the 1960 *u, v* diagram, the yellow, orange and red chromaticities are more balanced.

The ratio of chromaticity coordinates on the *x, y* and *u', v'* colour diagrams is defined as

Table 1. Example of Colour Difference of the Samples for *Sony* MPD from *sRGB* Sample

Chromaticity coordinates		Numbers of the reference colours													
Groups		Medium saturation								Higher saturation				Special	
Colour		Light grey-red	Grey-yellow	Yellow-green	Light-green	Light-magenta	Light-blue	Light-violet	Purple	Red	Yellow	Green	Blue	Pinkish (skin colour)	Green (colour of foliage)
		1	2	3	4	5	6	7	8	9	10	11	12	13	14
X		21.58	18.14	15.78	14.40	16.99	18.81	21.32	23.92	12.72	35.78	9.19	4.56	38.57	6.12
Y		17.30	16.20	16.51	16.07	17.25	17.32	17.47	18.74	7.49	32.64	11.20	3.94	32.49	6.37
Z		13.70	9.12	6.83	12.39	21.68	29.98	27.31	23.75	2.79	9.80	8.73	14.59	23.73	3.41
x		0.4104	0.4174	0.4035	0.3359	0.3038	0.2845	0.3226	0.3602	0.5531	0.4574	0.3155	0.1974	0.4069	0.3847
y		0.3290	0.3727	0.4220	0.3750	0.3085	0.2620	0.2642	0.2822	0.3258	0.4173	0.3845	0.1706	0.3428	0.4009
Δx		0.0129	0.0134	0.0172	0.0411	0.0375	0.0342	0.0236	0.0130	0.1159	0.0026	0.0558	0.0400	0.0145	0.0188
Δy		0.0197	0.0074	0.0365	0.0281	0.0016	0.0225	0.0379	0.0455	0.1341	0.0260	0.0328	0.0227	0.0076	0.0265
u'		0.2680	0.2515	0.2224	0.1968	0.1994	0.2041	0.2335	0.2543	0.3812	0.2580	0.1807	0.1698	0.2583	0.2185
v'		0.4832	0.5054	0.5234	0.4943	0.4556	0.4230	0.4304	0.4483	0.5052	0.5295	0.4956	0.3300	0.4897	0.5124
$\Delta u'$		0.0008	0.0123	0.0225	0.0340	0.0262	0.0178	0.0002	0.0155	0.2943	0.0093	0.0420	0.0285	0.0067	0.0207
$\Delta v'$		0.0128	0.0012	0.0105	0.0063	0.0065	0.0218	0.0324	0.0343	0.0699	0.0097	0.0060	0.0315	0.0061	0.0076
Δe		0.0128	0.0123	0.0248	0.0346	0.0270	0.0282	0.0324	0.0376	0.3025	0.0134	0.0424	0.0425	0.0090	0.0221
$\Delta \bar{e}_{u'v'}$		0.0262								0.1002				0.0156	

Table 2. Set of Correction Filters

Sony MPD	Δx	Δy
sRGB	0.080	−0.050
AdobeRGB	0.027	−0.019
DCI-P3 RGB	0.063	−0.034
PAL/SECAM	0.071	−0.048
M1N1P1	0.011	−0.053
Wide gamut RGB	0.030	−0.045
ProPhoto RGB	−0.004	−0.015

$$\begin{cases} u' = \dfrac{4x}{-2x+12y+3}; \\ v' = \dfrac{9y}{-2x+12y+3}. \end{cases}$$

The change in chromaticity was defined as an Euclidean distance in the uniform-chromaticity-scale area along the shortest way between colour points, i.e. the distance which is essentially the length of a particular curved way between the corresponding colour points in the CIE1931 space,

$$\Delta e_{u'v'} = \sqrt{\left(u'_{\mathrm{p}} - u'_{\mathrm{T}}\right)^2 + \left(v'_{\mathrm{p}} - v'_{\mathrm{T}}\right)^2},$$

where u'_{p}, v'_{p} are the chromaticity coordinates obtained in the course of interaction of spectral characteristics of MPD with the colour space; u'_{T}, v'_{T} are the chromaticity coordinates obtained in the *XYZ* space without the effect of MPD.

A *D65* SLS was selected as an emitter (CCT of 6,500 K) [14] with standardised radiation spectrum close to that of daylight at noon.

Fourteen colours of the Munsell Atlas applied for calculation of general colour rendering index R_{a} were selected as reference samples. Average val-

ues of colour difference Δe were analysed using the groups of samples with medium saturation (from 1 to 8), higher saturation (9 to 12) and special samples: No. 13 (face skin) and No. 14 (foliage).

The entire algorithm of the calculation method was implemented in *MATLAB*. Fig. 3 presents the chromaticity coordinates of 14 reference colours for the studied MPDs when using the *sRGB* space. An example of output tristimulus values for the *Sony* MPD and the *sRGB* space is summarised in Table 1 where Δx, Δy and $\Delta u'$, $\Delta v'$ are the differences between chromaticity coordinates of the reference samples calculated in the *XYZ* system without turning the MPD on and in the *sRGB* with turning the MPD on transformed into *XYZ* by means of the recalculation coefficients. In accordance with GOST [14], the values of chromaticity coordinates for SLS should not exceed 0.01. For the *Sony* MPD, none of the spaces meet this requirement to *D65* SLS (Tables 2 and 3).

When calculating coordinates of the light source in these spaces, it is necessary to conduct the γ correction, as a result of which the colour will probably correspond to the theory to maximum extent. For *sRGB*, the γ indicator is not uniform over the entire space, which complicates such manipulation. Probably, this is the reason why white balance in digital devices is based also on specific reference colours and not on the source itself. As seen from Table 2, the best result was obtained for *ProPhoto RGB*, and the worst one was obtained for *sRGB*. As a result of software calculation, the values of colour differences were obtained and their average values in particular groups of samples were found; they are presented in Tables 3–5.

Similar calculations and transformations were conducted for the *Kodak* and *Agilent* MPD's (Ta-

Table 3. Chromaticity Coordinates of *Sony* MPD

Colour spaces	Average value of Δe of different colour groups					Δe of LS
	Nos. 1–14	Nos. 1–12	Nos. 1–8	Nos. 9–12	Nos. 13 and 14	
sRGB	*0.0458*	*0.0509*	*0.0262*	*0.1002*	0.0156	*0.0862*
AdobeRGB	0.0361	0.0410	0.0173	0.0886	**0.0065**	0.0278
DCI-P3 RGB	0.0400	0.0443	0.0227	0.0877	0.0138	0.0626
M1N1P1	0.0325	0.0350	**0.0176**	0.0699	*0.0177*	0.0426
PAL/SECAM	*0.0445*	0.0496	0.0249	*0.0991*	0.0141	*0.0776*
Wide gamut RGB	**0.0279**	**0.0304**	**0.0134**	**0.0643**	0.0130	0.0466
ProPhoto RGB	**0.0321**	**0.0367**	0.0173	0.0757	**0.0045**	**0.0095**
Mean value	**0.04**	**0.04**	**0.02**	**0.08**	**0.012**	**0.05**

Table 4. Chromaticity Coordinates of *Kodak* MPD

Colour spaces	Average value of Δe of different colour groups					Δe of LS
	Nos. 1–14	Nos. 1–12	Nos. 1–8	Nos. 9–12	Nos. 13 and 14	
sRGB	**0.0588**	0.0650	0.0425	*0.1099*	**0.0218**	**0.0366**
AdobeRGB	0.0653	0.0691	*0.0506*	0.1059	0.0426	0.0570
DCI-P3 RGB	0.0622	0.0665	**0.0492**	0.1013	0.0361	0.0440
M1N1P1	0.0614	**0.0627**	**0.0492**	**0.0895**	0.0541	0.0427
PAL/SECAM	**0.0584**	0.0644	0.0420	*0.1091*	**0.0227**	**0.0346**
Wide gamut RGB	0.0611	**0.0627**	**0.0520**	**0.0840**	0.0520	0.0460
ProPhoto RGB	*0.0730*	*0.0752*	*0.0644*	0.0967	*0.0598*	*0.0743*
Mean value	**0.06**	**0.07**	**0.05**	**0.10**	**0.04**	**0.05**

Table 5. Chromaticity Coordinates of *Agilent* MPD

Colour spaces	Average value of Δe of various colour groups					Δe of LS
	Nos. 1–14	Nos. 1–12	Nos. 1–8	Nos. 9–12	Nos. 13 and 14	
sRGB	**0.0557**	**0.0612**	**0.0368**	*0.1099*	**0.0232**	**0.0302**
AdobeRGB	0.0653	0.0683	0.0489	0.1071	0.0473	0.0699
DCI-P3 RGB	0.0584	0.0621	0.0427	0.1010	0.0366	0.0493
M1N1P1	0.0650	0.0655	0.0507	0.0950	0.0624	0.0606
PAL/SECAM	**0.0558**	**0.0609**	**0.0367**	*0.1092*	**0.0254**	0.0344
Wide gamut RGB	0.0616	0.0624	0.0500	**0.0872**	0.0569	0.0586
ProPhoto RGB	*0.0780*	*0.0799*	*0.0678*	0.1041	*0.0664*	*0.0848*
Mean value	**0.06**	**0.07**	**0.05**	**0.10**	**0.05**	**0.06**

ble 3–5). The Tables present average values for the three main groups: Nos. 1–8, 9–12 and 13–14 as well as the average value for all colours and for Nos. 1–12, and the best and the worst results of calculations are marked.

5. ANALYSIS OF THE RESULTS

Analysis of the described MPDs and colour spaces was conducted within the framework of this study only.

For the *Sony* MPD, *Wide Gamut RGB* and *ProPhoto RGB* colour spaces turned out to be the best (Table 3) and *sRGB* and *PAL/SECAM* turned out to be the worst. Despite the fact that both the latter systems are rather close to each other in terms of major colour coordinates, *PAL/SECAM* is still better than *sRGB*. The other systems have shown the good but not excellent results.

DCI-P3 RGB, *M1N1P1* and *Wide Gamut RGB* (Table 4) proved themselves as the best ones for the *Kodak* MPD. These systems have good values in several groups. *ProPhoto RGB* is the worst space for application with this MPD despite its large colour gamut. As could be expected, the worst results were seen in the group with higher saturation. The MPD has secondary maximums in different regions of the spectre not allowing us to identify a "clear" colour in the saturated shades. As a result, in *Wide Gamut RGB* demonstrated the only good result in terms of average saturation. Combined with the *Kodak* MPD, the spaces *sRGB* and *PAL/SECAM* have both advantages and disadvantages although these spaces have the best light source values.

SRGB and *PAL/SECAM* may also be noted for the *Agilent* MPD. *AdobeRGB*, *DCI-P3 RGB*, *M1N1P1* and *Wide Gamut RGB* (Table 5) have demonstrated acceptable values and the *ProPhoto RGB* space turned out to be the worst, since this MPD, like the *Kodak* MPD, has spectral characteristics with secondary maximums.

Therefore, the more secondary maximums has MPD spectral characteristic curve, the less colour gamut should be (with large negative branches which probably compensate these secondary maximums).

Table 6. Average Chromaticity Values of MPDs

Colour space	MPD	Value $\overline{\Delta e}_{u'v'}$ of the sample groups			Changes of $\overline{\Delta e}_{u'v'}$ of the sample groups with respect to the indicators of *Wide Gamut RGB*:		
		medium saturation, Nos. 1–8	higher saturation, Nos. 9–12	Nos. 13 and 14	medium saturation, Nos 1–8	higher saturation, Nos. 9–12	Nos. 13 and 14
sRGB	*Sony*	0.0262	0.1002	0.0156	1.96	1.56	1.20
	Kodak	0.0425	0.1099	0.0218	3.17	1.71	1.68
	Agilent	0.0368	0.1099	0.0232	2.75	1.71	1.78
Adobe RGB	*Sony*	0.0173	0.0886	0.0065	1.29	1.38	0.50
	Kodak	0.0506	0.1059	0.0426	3.78	1.65	3.28
	Agilent	0.0489	0.1071	0.0473	3.65	1.67	3.64
DCI-P3 RGB	*Sony*	0.0227	0.0877	0.0138	1.69	1.36	1.06
	Kodak	0.0492	0.1013	0.0361	3.67	1.58	2.78
	Agilent	0.0427	0.1010	0.0366	3.19	1.57	2.82
M1N1P1	*Sony*	0.0176	0.0699	0.0177	1.31	1.09	1.36
	Kodak	0.0492	0.0895	0.0541	3.67	1.39	4.16
	Agilent	0.0507	0.0950	0.0624	3.78	1.48	4.80
PAL/ SECAM	*Sony*	0.0249	0.0991	0.0141	1.86	1.54	1.08
	Kodak	0.0420	0.1091	0.0227	3.13	1.70	1.75
	Agilent	0.0367	0.1092	0.0254	2.74	1.70	1.95
Wide gamut RGB	*Sony*	0.0134	0.0643	0.0130	1	1	1
	Kodak	0.0520	0.0840	0.0520	3.88	1.31	4.00
	Agilent	0.0678	0.1041	0.0664	5.06	1.62	5.11
Pro Photo RGB	*Sony*	0.0173	0.0757	0.0045	1.29	1.18	0.35
	Kodak	0.0644	0.0967	0.0598	4.81	1.50	4.60
	Agilent	0.0678	0.1041	0.0664	5.06	1.62	5.11

It follows from Table 6 that the colour spaces *DCI-P3 RGB* and *M1N1P1* may be identified as the best ones since they do not have any issues and even demonstrate some best results for all the MPD's. As opposed to that, the *Sony* MPD combined with the *Wide Gamut RGB* colour space turned out to be the best option since it has the least colour distortions in all groups of the reference samples. Table 6 demonstrates by many times the colour differences of other MPDs combined with different colour spaces exceed that of the *Sony* MPD combined with *Wide Gamut RGB*. As we can see, *Agilent MPD has demonstrated the worst results.* Generally, the *Sony* MPD proved itself as the best detector (the best results in all indicators as compared to the other two), and the colour spaces *DCI-P3 RGB* and *M1N1P1* proved themselves as the best colour spaces (without issues). This means that the new colour system *DCI-P3 RGB* may be highly competitive with *sRGB* and *AdobeRGB*. And yet it is necessary to keep developing new colour spaces, since the *M1N1P1* system also demonstrated good results and a number of advantages [9].

CONCLUSION

The colour spaces *sRGB*, *AdobeRGB*, *DCI-P3 RGB*, *M1N1P1*, *PAL/SECAM*, *Wide Gamut RGB*, and *ProPhoto RGB* were studied on the basis of spectral characteristics of the *Sony*, *Agilent*, *Kodak* MPDs for digital systems. The shapes of spectral characteristics of MPDs directly affect the results of colour resolution. Larger colour gamut does not always demonstrate the best results, and many factors depend on the MPD. However, as the study results have shown the disadvantages of the MPD spectral characteristic curves may be reduced by selecting a specific colour space. This may be foreseen

by preliminary calculation of colour difference of reference colours. But there are still no methods of digital system evaluation at the software level. The reference colour method is applicable more to the transmitting colour systems. And colour scales and profiling test objects are designed for digital registering devices, which is not applicable at the software level.

The colorimetric method of separate colours may be taken as the basis of the method. However:

– It is necessary to widen the list of reference colours of (saturated) yellow, green and magenta, since it is these shades which human sight system reacts the most to accurate representation of as compared to red and blue colours;

– It is necessary to have at least 5 different colours for each major colour, since equal-chromaticity-scale systems in which colour differences are found are not ideal and each of them causes its own deviations of colour threshold for each shade, and it is important to create a method, which would take the disadvantages of the systems into account for result processing and in which the reference colours would be selected with a specific periodicity, e.g. with difference by 2 or 4 tones;

– It is also possible to start using such atlases as *Pantone* and *RAL* which are widely used in polygraphy and design respectively.

Such method will allow us to test MPDs as early as at the stage of spectral characteristics development and then to compare the calculation data with the experimental results obtained using real samples of reference colours.

It is planned to conduct the studies with a selection of 24 reference samples using MPDs with different spectral characteristics by the same manufacter. In particular, this will allow us to conduct a more detailed analysis of nonlinearity of colour spaces. Moreover, colour difference will be conducted using *CIELAB* and "intensity" of MPD spectral characteristics will be taken into account.

REFERENCES

1. Zhbanova, VL. Colour separation systems for matrix pho-todetectors: monograph (Sistemy cvetodeleniya matrichnyh fotopriemnikov) [In Russian]. Smolensk: Universum. 2018. 186 p. ISBN978–5–91412–392–2

2. Domasev, M.V., Gnatyuk, S.P. Colour, colour management, colour calculations and meas-urements (Cvet, upravlenie cvetom, cvetovye raschety i izmereniya) [In Russian]. Saint Pe-tersburg, ''Piter ''. 2009. P. 224.

3. Richard F. Lyon, Paul M. Hubel. Eyeing the Camera: into the Next Century. IS&T Re-porter "The window on imaging". 2002. Vol. 17. № 6.

4. Cepeda-Negrete, J. Dark image enhancement using per-ceptual colour transfer / J. Cepeda-Negrete, R. Sanchez-Yanez, F. Correa-Tome, R. Lizarraga-Morales / IEEE Access. 2018. Vol. 6. P. 14935–14945. DOI: 10.1109/ACCESS.2017.2763898.

5. Lozhkin, L.D., Osipov, O.V., Voronoj, A.A. Colour Correction in Tri-Colour Colour Devic-es (Cvetokorrekciya v trekhcvetnyh ustrojstvah cvetovosproizvedeniya) [In Russian]. Computer optics. 2017. T. 41, № 1. P. 88–94. DOI: 10.18287/2412–6179–2017–41–1–88–94.

6. Gao, H. An improved gray-scale transformation method for pseudo-colour image en-hancement / H. Gao, W. Zeng, J. Chen. Computer Optics. 2019. Vol. 43, Issue. 1. P. 78–82. – DOI: 10.18287/2412–6179–2019–43–1–78–82.14.

7. Kanaeva, I.A. Colour and brightness correction methods for creating panoramic images [In Russian]. I.A. Kanaeva, Yu.A. Bolotova. Computer optics. 2018. T. 42, № 5. P. 885–897. DOI: 10.18287/2412–6179–2018–42–5–885–897.

8. Zhbanova, V.L. Research into methods for determining colour differences in the CIELAB uniform colour space // Light & Engineering, 2020,. Vol. 28, #3, pp. 53–59.

9. Zhbanova, V.L, Parvuyusov Yu.B. Experimental investigation of the colour-separation system of photodetector array // Journal of Optical Technology, 2019, Vol. 86, #6, pp. 177–182 (DOI (CrossRef): 10.1364/JOT.86.000177).

10. Zhbanova, V.L., Nubin V.V. A method of improving colour rendition of digital photo- and videocameras // Light & Engineering, 2014, Vol. 22, # 2, pp. 84–89.

11. Krivosheev, MI, Kustarev, AK. Colour measurements [In Russian]. Moscow "Ener-goatomizdat", 1990. 240 p.

12. CIE (Commission Internationale de l'Eclairage). Publication № 116. Industrial colour difference evaluation, 1995.

13. CIE (Commission Internationale de l'Eclairage). Publication № 135/2:1999. Colour rendering (TC133 closing remarks).

14. GOST 7721–89 Illuminants for colour measurements. Types. Technical requirements. Marking.

Vera L. Zhbanova,
in 2011, she graduated from the Moscow Power Engineering Institute (TU), specialty 05.11.07, "Optoelectronic Devices and Systems", in 2016 received a degree – candidate of technical sciences, works as an docent in The Branch of National Research University "Moscow Power Engineering Institute" in Smolensk, Research interests: colorimetry, digital image processing, radiation receivers, 3D design

METHODS OF INCREASING SPECTRAL RESOLUTION OF IMAGING SPECTROMETERS BUILT ON THE BASIS OF MULTI−CHANNEL RADIATION DETECTORS

Anastasiya V. Guryleva*, Alexei M. Khorokhorov, and Vitaly S. Kobozev

N.E. Bauman Moscow State Technical University (MGTU), Moscow
*E −mail: *guryleva.av@gmail.com*

ABSTRACT

The article proposes the methods of object shooting by means of a spectrometer based on a multi-channel radiation detector and further processing of its results allowing spectral resolution of such spectrometers significantly to increase with the same original spatial resolution. The mathematical model of the shooting process is provided. It is determined that restoration of spectral radiance of objects based on the shooting data using the proposed method is a mathematically incorrect inverse task. The Greville method, the method of wavelet transformation, the Tikhonov regularisation method, and the Godunov method were considered as methods for its solution. The results of computational modelling of the considered methods are shown and it is found that restoration of spectral radiance of objects based on the shooting data using the considered methods is possible and relative error of restoration is at a fraction of per cent scale. It is determined that the wavelet transformation method is an optimal method of solution of the incorrect spectral radiance restoration task. It is also shown that the proposed method of imaging spectrometry is applicable both when using matrix radiation detectors with increased number of narrow-band filters and when using widely spread standard three-channel matrix *RGB* detectors of radiation.

Keywords: imaging spectrometry, incorrect tasks, multi-channel shooting, spectrum restoration, optical filters

1. INTRODUCTION

Imaging spectrometers are rather actively used in science and industry. The key distinction of imaging spectrometers is the capability to record spectral characteristics of each point of a two-dimensional image of an object. For conventional representation of a data array acquired when measuring by means of an imaging spectrometer, the data cube concept is used [1]. The data cube is a three-dimensional structure formed by spectral characteristics of radiation reflected from the studied surface on one plane and by corresponding spatial coordinates on the two other planes.

In terms of the number of spectral channels used for measurement and spectral resolution, imaging spectrometers are conventionally identified as multispectral and hyperspectral ones. The multispectral instruments are the ones registering radiation in 4 to 100 spectral channels with resolution less than 10 nm [2, 3]. The instruments with high spectral resolution have the best specifications among hyperspectral instruments [4, 5]. They have over 1000 spectral channels and their resolution is better than 1 nm. In order to reach high resolution, these hyperspectrometers are equipped with dispersing systems of various types or built based on the principle of a Fourier spectrometer [6–9]. Due to the said distinctions and high requirements to the elements of the structures of dispersing and interference systems, these instruments have large dimensions, low operational characteristics and high cost [10–11]. Moreover, for processing of information and formation

of the data cube, it is necessary to provide a mechanism of scanning in one of the coordinates of the cube: either spatial or spectral one.

Imaging spectrometers with 100 up to 1000 channels and resolution of 1 nm to 10 nm are classified as medium-resolution spectrometers.

Multispectral instruments are the simplest imaging spectrometers with the best operational characteristics [12, 13]. They comprise a combination of a lens and a sensing matrix installed on the image plane. The sensors (micro pixels) are equipped with narrow-band selective filters with their positioning on the matrix defining the type of the matrix radiation detector (RD): band, tile or mosaic-type. In terms of construction of imaging spectrometers, mosaic-type matrix RD's are preferred with groups of micro pixels with selective filters united into one macro pixel, i.e. the same principle is used as in standard *RGB* matrices, however, the number of spectral channels is increased from 3 to 4, 8, 16, etc. Increase of spectral resolution of such instrument is reached by increasing the number of channels in a macro pixel, but it increases the dimensions of a macro pixel and, therefore, reduces spatial resolution [14]. The method under consideration allows us to increase spectral resolution of a multispectral instrument up to the level common for a medium-resolution hyperspectrometer with the same spatial resolution.

The method is based on shooting of a studied object through several filters with known spectral characteristics of transmission and then the parameters of the obtained images are processed mathematically to find spectral characteristics of the object within each macro pixel with spectral resolution significantly exceeding capabilities of a multispectrometer. The article also demonstrates that not only multispectral matrix RDs operating in four or more channels can serve as a basis for an imaging spectrometer utilising the proposed method but also standard three-channel *RGB* RDs can, and final spectral resolution can reach several nanometres.

2. THE METHOD

Determination of spectral characteristics of continuous, uniformly illuminated and diffusively reflecting objects using data from imaging spectrometers based on multispectral RDs is a problem of interpretation of the input relation using results of indirect measurements [15, 16] such as response

of RD to an input signal [17]. The article analyses reconstruction of a spectral characteristic, namely spectral radiance (SR) $L_e(\lambda)$ of the objects, based on the signal quantity U from pixels of the multispectral RD using known functions of spectral responsivity of corresponding channels $S(\lambda)$. Quantities of signals from pixels of a matrix RD within a single macro pixel are written as linear integral equations:

$$
\begin{cases}
\int_{\lambda_1}^{\lambda_2} S_1(\lambda) \cdot L_e(\lambda) d\lambda = C \cdot U_1, \\
\int_{\lambda_1}^{\lambda_2} S_2(\lambda) \cdot L_e(\lambda) d\lambda = C \cdot U_2, \\
\quad \vdots \qquad\qquad = \qquad \vdots \\
\int_{\lambda_1}^{\lambda_2} S_m(\lambda) \cdot L_e(\lambda) d\lambda = C \cdot U_m,
\end{cases}
$$

where U_1, U_2, U_m are the signals values of a pixels corresponding to a specific channel obtained when shooting an object by means of a camera; $S_1(\lambda)$, $S_2(\lambda)$, ... $S_m(\lambda)$ are the functions of spectral responsivity of a matrix RD pixel in each channel; λ_1 и λ_2 are the boundaries of operating range of wavelengths; m is the number of channels; C is the ratio not depending on λ and defined by parameters of equipment and conditions of shooting (diameter of the lens entrance pupil, distance to the object, field of view, etc.).

For approximate calculations of corresponding integrals with constant increment $\varDelta\lambda$, the following system of equations is used

$$
\begin{cases}
\sum_{i=1}^{n} L_e(\lambda_i) \cdot S_1(\lambda_i) \cdot v(\lambda_i) = C \cdot U_{1rj}, \\
\sum_{i=1}^{n} L_e(\lambda_i) \cdot S_2(\lambda_i) \cdot v(\lambda_i) = C \cdot U_{2rj}, \\
\quad \vdots \qquad\qquad = \qquad \vdots \\
\sum_{i=1}^{n} L_e(\lambda_i) \cdot S_m(\lambda_i) \cdot v(\lambda_i) = C \cdot U_{mrj},
\end{cases} \tag{1}
$$

where $L_e(\lambda_i)$ are the values of SR of the object at discrete points of the operating region of the spectrum; $S_1(\lambda_i)$, $S_2(\lambda_i)$, ... $S_m(\lambda_i)$ are the discrete values of the pixel spectral responsivity with narrow-band filter of the matrix RD; $v(\lambda_i)$ is the weighting factors of the increment depending on the method of numerical integration: triangular method, trapezoidal method, the Simpson method, etc.; U_1, U_2, ... U_m are the signal quantities of pixels acquired when shooting the object by means of a multispectral camera; m is the number of narrow-band filters; n is the

number of split points over the spectrum; i is the split step number.

With the known functions $S_1(\lambda)$, $S_2(\lambda)$, $S_m(\lambda)$ and values U_1, U_2, U_m, the system (1) resolves itself to a system of linear equations in the set of selected values $L(\lambda_i)$. With that, the number of values $L_e(\lambda_i)$ is defined by the value of n. The error of these values is mainly defined by the constructive matrix of equations of the system (2) and the nature of changes of the function $L(\lambda)$. Usually, the system (1) does not allow to recover information on the function $L_e(\lambda)$ with required accuracy, therefore, in order to obtain additional information on SR of the object, it is suggested to make several additional shots through special optical filters with known spectral transmission functions $\tau_j(\lambda)$ ($j = 1, 2...p$). The system of equations (1) is also supplemented by $m \times p$ more similar equations:

$$\begin{cases} \sum_{i=1}^{n} L_e(\lambda_i) \cdot S_1(\lambda_i) \cdot v(\lambda_i) \cdot \tau_j(\lambda_i) = C \cdot U_{1\tau j}, \\ \sum_{i=1}^{n} L_e(\lambda_i) \cdot S_2(\lambda_i) \cdot v(\lambda_i) \cdot \tau_j(\lambda_i) = \\ \quad = C \cdot U_{2\tau j}, \quad j = 1...p \\ \quad \cdot \qquad\qquad \cdot \\ \quad \cdot \qquad = \qquad \cdot \\ \quad \cdot \qquad\qquad \cdot \\ \sum_{i=1}^{n} L_e(\lambda_i) \cdot S_m(\lambda_i) \cdot v(\lambda_i) \cdot \tau_j(\lambda_i) = C \cdot U_{m\tau j}, \end{cases} \quad (1+)$$

where $U_{1\tau j}$, $U_{2\tau j}$, ... $U_{m\tau j}$ are signal quantities of the pixels acquired when shooting the object by means of a camera with corresponding narrow-band filters through a filter with transmission function $\tau_j(\lambda_i)$. The system of equations (1+) may be enhanced by including the system (1) in it. For this purpose, it is necessary to introduce the value of the parameter $j = 0$ in the system (1+) and to take $\tau_0(\lambda_i) = 1$, i.e. to consider that the object is being shot without a filter.

Selection of the required number of filters and optimal nature of their transmission functions is defined by necessary accuracy of determination of the function $L_e(\lambda_i)$, required dynamic characteristics of the image processing system and other parameters of the design specification.

For modelling and computational solution, it is convenient to write the system of equations (1+) in the matrix form:

$$S \cdot l = u, \quad (2)$$

where S is a $m \cdot (p + 1) \cdot n$-order matrix taking into account spectral responsivity of the pixels of the matrix RD, known spectral functions of transmission $\tau_j(\lambda_i)$ and weighting factors of increment $v(\lambda_i)$; l is the vector consisting of n elements defining SR of the object; u is the vector consisting of $m \cdot (p+1)$ defining the signal quantities of pixels acquired when shooting the object by means of a multispectral camera itself and with additional filters.

2.1. The Greville Method

With high requirements to spectral resolution of an imaging spectrometer and natural strive to their technical implementation, the amount of unknown values of $L_e(\lambda_i)$ turns out to be large and sometimes significantly exceeds the number of equations (1+).

With that, the problem (2) may either have no solution or have a non-unique solution [18–20], i.e. it may be set mathematically incorrectly, therefore, a pseudo solution is used in such cases [21–23], i.e. such vector l that measures up the following functional [24]:

$$\|S \cdot l - u\|^2 \to min.$$

On the other hand, in consequence of the known theorem on perpendicular, the normal pseudo solution is determined with a single value and may be found using the equation

$$l = S^+ \cdot u, \quad (3)$$

where S^+ is a pseudo-inverse matrix obtained by means of pseudo-inversion of the matrix S.

Pseudo-inversion may be understood as solution of the problem of the best approximation using the least squares method. The pseudo-solution method is one of the simplest ways to restore spectral radiance of objects using the data of multichannel shooting, and the pseudo-inverse matrix was found using the Greville method in this work.

2.2. The Wavelet Transformation Method

The equation (2) is an inverse incorrect problem [25, 26], and its solution written as (3) is a simple one but has a grave disadvantage. It resides in the fact that the distinctions of the problem discussed in this article often make the matrix S ill-conditioned (due to linear dependence between the rows

of the matrix and therefore low stability of the solution to errors of the right-hand side of the equation (2)). In order to eliminate this factor of accuracy reduction of original luminance spectre reconstruction, wavelet transformation of the function may be used [27, 28].

Wavelet transformation of a regular signal is its representation in the form of a generalised series or a Fourier integral over the system of basic functions constructed from the mother (original) wavelet $\psi(\lambda)$ with specific properties gained using operations of time shift b and change of time scale a. For the set values of parameters a and b the function $\psi_{ab}(\lambda)$ is the wavelet generated by the mother wavelet $\psi(\lambda)$ [29]. Wavelets are used for shortening excessive information in this article. Each row of the matrix S is expanded in the basis and then not the elements of the matrix S, the number of which is defined by the amount of points of split over the spectrum and may reach tens and hundreds, are used in the solution of the equation (2) relative to l but the wavelet coefficients of its expansion in the basis the number of which is defined by the number of functions included in the basis, which ultimately reduces the condition number μ by orders of magnitude. The erf integral $\psi(\lambda) = \mathrm{erf}(\lambda)$ was used as a mother function of wavelets in this article and the expansion basis consisted of 8 functions (i.e. $k = 8$) and was written in the following form:

$$
\begin{cases}
\psi_0(x) = 1, \\
\psi_1(x) = \mathrm{erf}(2 \cdot x), \\
\psi_2(x) = \mathrm{erf}\left(4 \cdot \left(x - \dfrac{1}{2}\right)\right), \quad \psi_5(x) = \mathrm{erf}\left(8 \cdot \left(x + \dfrac{1}{2}\right)\right), \\
\psi_3(x) = \mathrm{erf}\left(4 \cdot \left(x + \dfrac{1}{2}\right)\right), \quad \psi_6(x) = \mathrm{erf}\left(8 \cdot \left(x - \dfrac{3}{4}\right)\right), \\
\psi_4(x) = \mathrm{erf}\left(8 \cdot \left(x - \dfrac{1}{4}\right)\right), \quad \psi_7(x) = \mathrm{erf}\left(8 \cdot \left(x + \dfrac{3}{4}\right)\right),
\end{cases}
\tag{4}
$$

where x is a variable representing wavelength λ normalised to the standard interval $[-1; 1]$ similar to [30].

SR of the object with use of wavelet transformation of the matrix S was defined using the following formula acquired from the expression (3)

$$
l = \Phi \cdot (S \cdot \Phi)^+ \cdot u,
$$

where Φ is the matrix of the values of basic functions from the expressions (4) with order of $(k \times n)$;

$(S \cdot \Phi)^+$ is the matrix acquired by pseudo inversion of the matrix $S \cdot \Phi$.

2.3. The Tikhonov Regularisation Method

Since it is impossible to obtain an accurate solution of the equation (2) stable to minor changes of input data due to the incorrect nature of the problem of radiance spectrum reconstruction, it is necessary to search for some approximated solution [31]. The equation (2) being solved is an operator equation of the first kind [32]; in [25; 33], it is shown that its solution is equivalent to the solution of the problem of functional minimisation:

$$
M^{\acute{a}}(l, u) \equiv \|S \cdot l - u\|^2 + \alpha \cdot \|l\|^2 \to \min, \tag{5}
$$

$$
l \in L, \quad \alpha > 0,
$$

where $M^{\alpha}(l, u)$ is the Tikhonov smoothing functional, α is the regularisation parameter.

The regularised solution of the problem (2) is determined as the only solution of the Euler equation [25, 31]

$$
(S' \cdot S + \alpha \cdot E) \cdot l = S' \cdot u + \alpha \cdot u^*,
$$

where E is the unity matrix of the n degree.

The canon form of the regularisation method which was used in this article corresponds to the case $u^* = 0$.

When practically applying this method, the algorithmic methods of α parameter selection are very important. One of them is based on the paper [34] and comprises selection of α using the values of the functional $M^{\alpha}(l, u)$ on the regularised solutions from the constraint (5). The solution of such problem is found based on the principle of generalised residual [35] using Newton step-by-step approximation on the α grid:

$$
\alpha_{s+1} = \alpha_s + \beta; \; s = 0, 1, 2 \ldots; \beta = 0.001.
$$

2.4. The Godunov Method

According to [36, 37], application of additional information about the fact that the desired solution has not too large second derivatives allows us to supplement it in such a way when compiling the system of linear equation, that such supplementation significantly lowers the condition number and

makes the system solvable. In such case, the system of equations (1+) is written as the system

$$\begin{bmatrix} (1-\tau)\cdot S \\ \tau \cdot B \end{bmatrix} \cdot l = \begin{bmatrix} (1-\tau)\cdot u \\ 0 \end{bmatrix}, \qquad (6)$$

where B is the matrix with n order with its elements (b_{ij}) being such that

$$b_{ij} = \frac{-2}{\left(1/n-1\right)^2} \text{ при } i = j;$$

$$b_{ij} = \frac{-1}{\left(1/n-1\right)^2} \text{ при } i = j-1 \text{ и } i = j+1;$$

$$b_{ij} = 0 \text{ при } |i-j| \geq 2;$$

τ is the ratio defined from the expression $\tau = 1/(n-1)^2$.

It was expected that, provided the above conditions of calculations of the elements of the matrix B and the ratio τ are complied with, the normal solution of the system (6) which may be written as

$$((1-\tau)^2 \cdot S' \cdot S + \tau^2 \cdot B' \cdot B)\cdot l = (1-\tau)^2 \cdot S' \cdot u,$$

would be proximate to the vector we are interested in [24].

2.5. The Modelling Procedure

The described method of determination of the object SR using the data of indirect measurements was checked using computational modelling in accordance with the expression (1+). Uniform diffusely scattering coloured plates were used as test samples. The SR curves of these samples, $L_{e1}(\lambda_i)$, $L_{e2}(\lambda_i)$ and $L_{e3}(\lambda_i)$, were determined by means of a certified device: spectrophotometer *Perkin Elmer Lambda 950* (Fig. 1).

Each sample was modelled separately. Multichannel mosaic-type matrix RD's are manufactured with macro pixels consisting of some fixed number of pixels with specific filter (i.e. the number of channels is m). Two RDs were considered in the course of modelling: a standard *RGB* matrix with three channels ($m = 3$) and a multispectral eight-channel mosaic-type matrix RD with its macro pixels consisting of eight pixels with narrow-band filters ($m = 8$). Computational modelling was conducted separately for each matrix. The curves of spectral responsivity of the *RGB* matrix, $S_R(\lambda)$, $S_G(\lambda)$ and
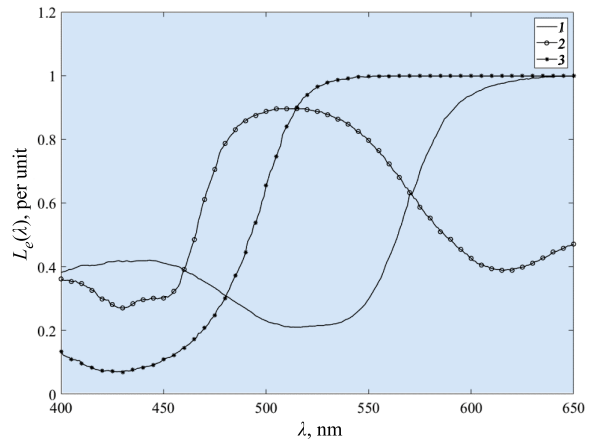
Fig. 1. Relative SR curves of samples 1 (*1*), 2 (*2*) and 3 (*3*)

$S_B(\lambda)$, and of the multispectral eight-channel matrix, $S_1(\lambda)$, $S_2(\lambda)$, …, $S_8(\lambda)$, are shown in Fig. 2, a and b, respectively.

Colour glasses ZhZS-5 (ЖЗС-5), ZhZS-18 (ЖЗС-18), SZS-16 (СЗС-16) and SS-1 (СС-1) were selected from the optic glass catalogue and used as optic filters in the course of computational modelling; their transmission functions, $\tau_1(\lambda_i)$, $\tau_2(\lambda_i)$, $\tau_3(\lambda_i)$, and $\tau_4(\lambda_i)$ ($p = 4$), complied with Standard 9411–91. The said colour glasses were selected using the classic method comprising of selection of filters with maximum difference between the shapes of transmission curves and uniform covering of the entire operational range of λ [38].

At the first stage of modelling, the signal quantities of the pixels of the standard *RGB* matrix $U_R \tau_j$, $U_G \tau_j$, $U_B \tau_j$, ($j = 0,…p$) are determined from the direct solution of the equation (1+) using the known parameters, namely spectral responsivity of the pixels of the matrix RD with Bayer filters $S_R(\lambda_i)$, $S_G(\lambda_i)$, $S_B(\lambda_i)$, SR of the samples $L_e(\lambda_i)$ and transmission functions $\tau_j(\lambda_i)$ of additional p filters ($j = 1, 2,…p$). The signal quantities of the pixels of the standard *RGB* matrix are defined for each sample, i.e. for $L_{e1}(\lambda_i)$, $L_{e2}(\lambda_i)$, $L_{e1}(\lambda_i)$. The corresponding values of signal quantity of the pixels of the multispectral RD are obtained in the similar way. In such case, another quantity p of additional optical filters is used. To provide sufficient accuracy of modelling, the increment of split over spectrum was 1 nm for all functions, which corresponded to the total number of points of $n = 251$ for the spectral region of (400–650) nm.

The second stage of modelling comprised determination of SR, $L_{e1}^*(\lambda_i)$, $L_{e2}^*(\lambda_i)$ and $L_{e3}^*(\lambda_i)$, of each sample at n points using one of the above-men-
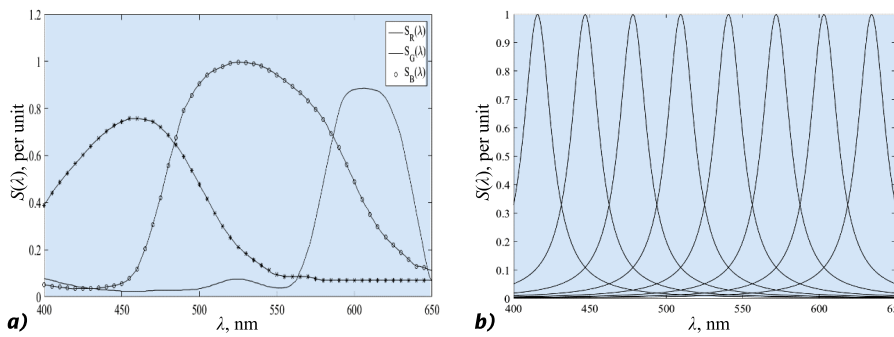
Fig. 2. Relative SR curves of pixels with Bayer filters of the three-channel *RGB* matrix (*a*) and the eight-channel multi-spectral matrix (*b*)

tioned methods of solution of the inverse incorrect task (2). Moreover, SR of the samples was defined separately for the two variants of modelling: with three-channel ($m = 3$) and eight-channel ($m = 8$) matrix RDs. Relative error expressed in per cent was the measure of concordance with the spectrum reconstructed in such a way.

3. RESULTS

The main results of mathematical modelling of the methods to determine the sample SR are presented below.

1. It appears to be impossible to solve the inverse incorrect task of determination of the object SR with accuracy specific for a medium-resolution spectrometer without using additional optical filters by means of any of the presented methods. Relative errors of the reconstructed and original SR of the samples are equal to tens of per cent. This is applicable to both multi-channel and *RGB* RDs.

2. Utilisation of additional filters for shooting of the object allows us to increase accuracy of SR definition with required spectral resolution. In most cases, one or two additional filters are sufficient for multispectral systems depending on the number of channels. It is appropriate to use the value $p = 2$ for the eight-channel radiation detector used for calculation in this article. It is found that the method of imaging spectrometry based on multi-channel RDs yields good results not only for matrix RDs with the number of channels increased as compared to the standard one, which was expected [39], but also for widely used three-channel matrix RDs. In the latter case, the number of optical filters involved in multi-channel shooting (p) is increased but remains within technically feasible limits and appears to be justified [40, 41]. The value $p = 4$ is assumed in this article.

3. Fig. 3 illustrates the results of reconstruction of the original SR using the Greville method, wavelet transformation, the Godunov method, and Tikhonov regularisation. The graphs demonstrate that all considered methods of solution of the equation (2) appear to be applicable for definition of SR of different samples. At the boundaries of the spectral region, almost all methods demonstrate some deviation between the original and the reconstructed curves, and this aspect shall be taken into account when using the methods in practice. The main challenge when using the Tikhonov method is calculation of the optimal value of the regularisation parameter α. In the course of modelling, the values of this parameter were calculated using the Newton step-by-step approximation method. They were equal to 0.0616 at $m = 3$ and 0.1481 at $m = 8$. The wavelet transformation method provides a more single-valued representation of the shape of the SR curve; therefore, in the problems requiring further integration of the values at specific points of the reconstructed curves in the calculations, it is preferable to use the method of wavelet transformation due to its less relative error of SR reconstruction.

4. The Table contains the values of relative error of restoration of SR of three objects using the above described methods of solution of incorrect inverse task. The Table makes it clear that computational modelling of the discussed method of multi-channel imaging spectroscopy and the methods of further data processing yield positive results and the original SR of the samples is reconstructed with low error. It may seem that the results listed in the Table are too optimistic but it should be noted that we are talking about just the errors of reconstruction of spectral curves in terms of the methods of solution of inverse problems. When using the Greville and the Godunov methods, deterioration of the results with increase of the number of matrix channels is observed, which is explained by high sen-
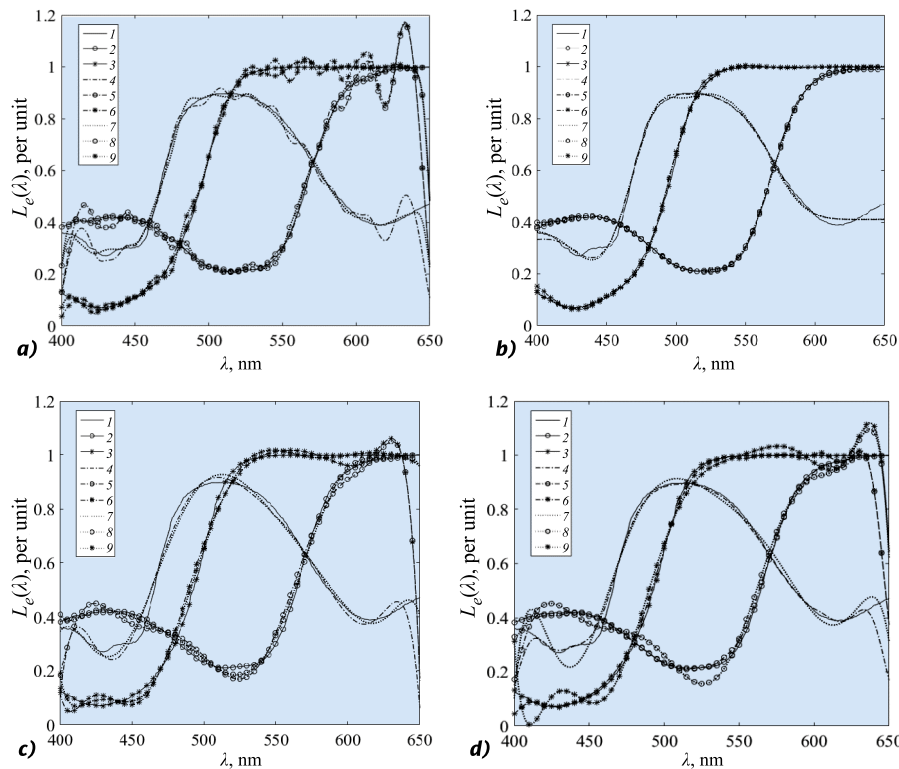
Fig. 3. Relative SR curves: original and reconstructed using the Greville method (*a*), wavelet transformation (*b*), Tikhonov regularisation (*c*) and the Godunov method (*d*). Original sample curves – *1, 2, 3*; the curves reconstructed using the three-channel shooting data ($m = 3$, $p = 4$) – *4, 5, 6*; the curves reconstructed using the data of eight-channel shooting ($m = 8$, $p = 2$) – *7, 8, 9*

sitivity of these methods to ill-conditioning of the matrix *S* included in the calculation; however, the Godunov method demonstrates more preferable results as compared to the Greville method. On the other hand, the methods of wavelet transformation and Tikhonov regularisation are applicable better with high condition number of the matrix *S*, which serves as an important factor in solution of incorrect tasks, and with increase of the number of equation included in the system (1+), relative error of calculation with use of these methods lowers. The wavelet transformation method allows us to reduce the condition number (μ) of the matrix *S* at $m = 3$, $p = 4$ from $8.4 \cdot 10^2$ down to $0.3 \cdot 10^2$, and down to $0,1 \cdot 10^3$ from $1.4 \cdot 10^3$ at $m = 8$, $p = 2$ and to obtain the mean value with respect to three samples not exceeding 0.40 % at $m = 3$, $p = 4$ and 0.17 % at $m = 8$, $p = 2$, which is obviously the best result.

3. DISCUSSION AND CONCLUSIONS

The article considers the methods of shooting of objects by means of an imaging spectrometer based on a multi-channel RD with corresponding software processing of the shooting results allowing to define SR of objects with increased spectral resolution and original spatial resolution by obtaining additional information on spectral characteristics of an object in the course of its shooting through special optical filters. Mathematical modelling of the shooting process confirming theoretical grounds of the method is conducted. In the course of the work it is found that the problem of results processing is not trivial, therefore the results of modelling of its solution using different methods are given in the article. It is found that the method of wavelet transformation is the most universal method of solution of the incorrect problem of object SR curves reconstruction. As a result of computational modelling, it is found that relative error of SR reconstruction based on the data of multi-channel shooting using the proposed method is about 0.17 % and is satisfactory. It is also shown that the discussed method of multi-channel imaging spectroscopy is applicable both to multispectral eight-channel matrix RDs and to widely used standard three-channel matrix RDs. When three-channel RDs are used, the number of optical filters used for shooting appears to be technically feasible and justified.

It appears that the main advantages of the described method of multi-channel shooting are simplicity of its technical implementation, low sensitivity to external factors (increased vibrations, significant temperature drops, etc.) and capability of the imaging spectrometer to obtain data in three coordinates of the cube without scanning with

Table. The Results of Modelling of Reconstruction of Spectral Radiance Based on the Data of Multichannel Shooting

Sample number	Relative error, %							
	Greville Method		Wavelet Transformation Method		Tikhonov Regularisation Method		Godunov Method	
	$m=3$	$m=8$	$m=3$	$m=8$	$m=3$	$m=8$	$m=3$	$m=8$
	$p=4$	$p=2$	$p=4$	$p=2$	$p=4$	$p=2$	$p=4$	$p=2$
1	0.96	2.86	0.62	0.25	1.33	0.77	0.65	1.61
2	0.91	2.55	0.29	0.11	1.20	0.61	0.42	1.33
3	0.61	2.00	0.30	0.15	1.11	0.56	0.55	1.54

high spectral and spatial resolution. The considered method allows a large number of variations (e.g. by changing the number of shooting channels and optical filters involved in it, transmission spectra of these filters, etc.). In consequence of such variability, optimisation of the values of the said parameters and their combinations as well as consideration of the effect of measurement errors on the results of object SR reconstruction using the data of indirect measurements should be the subject matter of further research.

REFERENCES

1. Golovin, A.D., Dyomin, A.V. The Imitation Model of the Multi-channel Offner Hyperspectrometer [Imitatsionnaya model mnogokanalnogo giperspectrometra Offnera] // Kompyuternaya optika, 2015, Vol. 39, # 4, pp. 521–528. Doi 10.18287/0134–2452–2015–39–4–521–528.

2. Larar Allen M. et al. Multispectral, hyperspectral, and ultraspectral remote sensing technology, techniques, and applications III // Proc. SPIE International Society for Optical Engineering. 13–14 October 2010. Incheon, Korea Republic, 2010, Vol. 7857.

3. Rodionov, I.D., Rodionov, A.I., Vedeshin, L.A., Vinogradov, A.N., Egorov, V.V., Kalinin, A.P. Aviation Hyperspectral Installations for Remote Sensing Applications [Aviatsionnyie giperspektralnyie kompleksy dlya resheniya zadach distantsionnogo zondirovaniya] // Issledovaniye zemli iz kosmosa, 2013, Vol. 6, pp. 81–93.

4. Gorbunov, G.G., Chikov, K.N., Shlishevskiy, V.B. Interferential Hyper and Ultraspectral Videospectrometers for Remote Sensing Applications [Interferentsionnyie giper- i ultraspektralnyie videospektrometry dlya zadach distantsionnogo zondirovaniya] // Bulleting of SGUGiT, 2016, Vol. 1, # 33, pp. 70–94.

5. Vilaseca M., Schael B., Delpueyo X., Chorro E., Perales E., Hirvonen T., Pujol J. Repeatability, reproducibility, and accuracy of a novel pushbroom hyperspectral system // Color Research & Application, 2013, Vol. 39, No. 6, pp. 549–558. Doi 10.1002/col.21851.

6. Pozhar, V.E., Machikhin, A.S., Gaponov, M.I., Shirokov, S.V., Mazur, M.M., Sheryshev, A.E. Hyper-spectrometer Based on an Acousto-optic Tuneable Filters for UAVS // Light & Engineering, 2019, Vol. 27, # 3, pp. 99–104.

7. Palto, S.P., Alpatova, A.V., Geyvandov, A.R., Blinov, L.M., Lazarev, V.V., Yudin, S.G. Fourier Spectroscopy as a Method of Studying of Photoelectric Properties of Organic Systems [Furye-spektroskopiya kak metod izucheniya fotoelektricheskikh svoistv organicheskikh sistem] // Optika i spektroskopiya, 2018, Vol. 124, # 2, pp. 210–220. Doi 10.21883/OS.2018.02.45526.209–17.

8. Zavarzin, V.I., Mitrofanova, Yu.S. Schematic Solutions for Advanced Hyperspectral Systems [Skhemnyie resheniya dlya perspektivnoy giperspektralnoy apparatury] // Opticheskiy zhurnal, 2017, Vol. 84, # 4, pp. 12–16.

9. Golovin, A.D., Dyomin, A.V. The Imitation Model of the Multi-channel Offner Hyperspectrometer [Imitatsionnaya model mnogokanalnogo giperspectrometra Offnera] // Kompyuternaya optika, 2015, Vol. 39, # 4, pp. 521–527. Doi 10.18287/0134–2452–2015–39–4–521–528.

10. Balashov, A.A., Vagin, V.A., Golyak, I.S., Morozov, A.N., Nesteruk, I.N., Khorokhorin, A.I. Visible and Near-IR Range Fourier Spectrometer [Furye-spektrometr vidimogo i blizhnego IK diapazonov] // Radiostroeniye, 2017, Vol. 6, pp. 27–38. Doi 10.24108/rdeng.0617.0000124.

11. Arkhipov, S.A., Zavarzin, V.I., Lee, A.V. // Reflective Optical Systems for Low-dimension Hyperspectral Systems of Remote Sensing of Earth [Zerkalnyie opticheskiye sistemy dlya malogabaritnoy giperspektralnoy apparatury distantsionnogo zondirovaniya zemli iz kosmosa] // From the collection Acoustic-optic and Radar Methods of Measurement and Information Processing. Proceedings of the 10th International Science and Tech-

nical Conference. A.S. Popov Russian Society of Radio Engineering, Electronics and Communication (NTORES), 2017, pp. 262–264.

12. Veys C., Davies P., Hibbert J., Grieve B. (2017). An Ultra-Low-Cost Active Multispectral Crop Diagnostics Device. 1005–1007. Paper presented at IEEE Sensors 2017 Conference, Glasgow, United Kingdom. Doi. org/10.1109/ICSENS.2017.8234211.

13. Burns P.D., Berns R.S. Analysis Multispectral Image Capture // Color Imaging Conferenct 1996, # 1, pp. 19–22.

14. Khorokhorov, A.M., Vvedenskaya, A.V., Shirankov, A.F., Kobozev, V.S., Algorithm of Enhancement of Matrix Radiation Detectors with Bayer filters [Algoritm rasshireniya vozmozhnostey matrichnykh priyomnikov izlucheniya s filtrami Bayera / Int. Conf. Applied Optics 2018, Saint Petersburg: D.S. Rozhdestvensky Society of Optics, 2018, Vol. 2.

15. Varentsova, S.A., Trofimova, V.A., Troshchiyev, Yu.V. Reconstruction of a Signal and Dynamics of its Spectral Characteristics with a Non-regular Set of Measurements [Vosstanovleniye signala i dinamiki ego spektralnykh kharakteristik pri neregulyarnom nabore izmereniy] // J. tech. phys. 2008, Vol. 78, # 7, pp. 57–68.

16. Zhuchko, O.V., Pytyev, Yu.P. Reconstruction of Functional Dependence Using Theoretical and Possibility Methods // J. comp. math. and math. phys. 2003, Vol. 43, # 5, pp. 767–783.

17. Hardeberg J. Acquisition and reproduction of color images: colorimetric and multispectral approaches. USA: Dissertation.com, 2001.

18. Vapnik, V.N. Reconstruction of Dependences Using Empirical Data [Vosstanovleniye zavisimostey po empiricheskim dannym], Moscow: Nauka, 1979, 448 p.

19. Ivanov, V.K., Vasin, V.V., Tanana, V.P. The Theory of Linear Incorrect Problems and its Application [Teoriya lineynykh nekorrektnykh zadach i eyo prilozhenie], Moscow: Nauka, 1978, 206 p.

20. Sizikov, V.S., Lavrov, A.V. Contemporary Sustainable Mathematical and Software Methods of Distorted Spectra Reconstruction [Sovremennyie ustoichivyie matematicheskiye i programmnyie metody vosstanovleniya iskazhonnykh spektrov] // Science and Technical Bulletin of Information Technologies, Mechanics and Optics, 2018, Vol. 18, # 6.

21. Sydikhov, A. Sh., Arapov, S. Yu., Arapova, S.P. Pseudoinverse Processing of the Data of Multispectral Shooting in Stationary Zones of an Image [Psevdoinversnaya obrabotka dannykh multispektralnoy fotosyomki v statsionarnykh zonakh izobrazheniya] / Int. Conf. of Students, Postgraduates and Young Scientists Information Technologies, Telecommunications and Control Systems: book of reports, Ekaterinburg: UrFU, 2015, pp. 179–185.

22. El-Rifai I. et al. Enhanced Spectral Reflectance Reconstruction Using Pseudo-Inverse Estimation Method // Int. J. Image Process. IJIP, 2013, Vol. 7, # 3, pp. 278–285.

23. Barliani, A.G. Development of Algorithms of Equalisation and Evaluation of Accuracy of Unconstrained and Constrained Geodetic Networks Based on a Pseudonormal Solution [Razrabotka algoritmov uravnivaniya i otsenki tochnosti svobodnykh i nesvobodnykh geodezicheskikh setey na osnove psevdonormalnogo resheniya, Novosibirsk: SGGA, 2010, 135 p.

24. Morozov, V.V., Grebennikov, A.I. Methods of Solution of Incorrectly Set Problems. The Algorithm Aspect [Metody resheniya nekorrektno postavlennykh zadach. Algoritmicheskiy aspekt]. – Moscow: Moscow University Press, 1992, 319 p.

25. Vogel C.R. Computational Methods for Inverse Problems. SIAM. Philadelphia, 2002, 179 p. Doi 10.1137/1.9780898717570.

26. Gurylyova, A.V., Khorokhorov, A.M., Latyshev V.I. Comparative Analysis of Methods of Solving Incorrect Reverse Problems for Multi-channel Hyperspectroscopy [Sravnitelnyi analiz metodov resheniya nekorrektnykh obratnykh zadach dlya mnogokanalnoy giperspektrometrii] // Optika i spektroskopiya, 2019, Vol. 127, # 4, pp. 551–557. Doi 10.21883/ OS.2019.10.48356.171–19.

27. Arapov, S. Yu., Arapova, S.P., Dubinin, I.S., Sergeev, A.P. Reconstruction of Reflection Spectra of Test Fields Based on Data of Multispectral Shooting [Vosstanovleniye spektrov otrazheniya testovykh poley po dannym multispektralnoy fotosyomki] / Transmission, Processing, Perception of Text and Graphic Information: proceedings of the International Science and Practical Conference. – Ekaterinburg: UrFU, 2015. – P. 21–33.

28. Arapov, S. Yu., Tarasov, D.A., Sergeev, A.P., Kolmogorov, Yu.N. Modelling of Reflection Spectra Using the Basis of Erf Functions [Modelirovaniye spektrov otrazhaniya na osnove bazisa iz funktsiy tipa integrala oshibok] // Izvestiya vysshykh uchebnykh zavedeniy. Problemy poligrafii i izdatelskogo dela, 2012, Vol. 6, pp. 17–29.

29. Novikov, L.V. Spectral Analysis of Signals in Wavelet Basis [Spektralnyi analiz signalov v bazise veivletov] // Nauchnoye priborostroeniye. 2000, Vol. 10, # 3, pp. 70–77.

30. Tarasov, D.A. Modelling of Reflection Spectra by Polynome Superposition [Modelirovaniye spektrov otrazheniya superpozitsiey polinomov] // Izvestiya

vysshykh uchebnykh zavedeniy. Problemy poligrafii i izdatelskogo dela, 2012, Vol. 5, pp. 59–66.

31. Tikhonov, A.N., Arsenin, V. Ya. Methods of Solving of Incorrect Problems [Metody resheniya nekorrektnykh zadach]. Moscow: Nauka, 1986, 288 p.

32. Calvetti, D., Morigi, S., Reichel, L., Sgallari, F. Tikhonov regularization and the L-curve for large discrete ill-posed problems // J. Comput. Appl. Math. 2000, Vol. 123, pp. 423–446.

33. Hansen, C.A. Matlab Package for Analysis and Solution of Discrete Ill-Posed Problems // Numerical Algorithms, 1994, Vol. 6, pp. 1–35.

34. Morozov, V.A. Linear and Non-linear Incorrect Problems [Lineynyie i nelineynyie nekorrektnyie zadachi] // Itogi nauki i tekhniki. Ser. Math. anal. 1973, Vol. 11, pp. 129–178.

35. Goncharskiy, A.V., Leonov, A.V., Yagola, A.G. Generalised Residual Principle [Printsip obobshchyonnoy nevyazki] // J. Comp. Math. & Math. Phys. 1973, Vol. 13, # 2, pp. 294–302.

36. Godunov, S.K., Antonov, A.G., Kirilyuk, O.P., Kostin, V.I. Guaranteed Accuracy of Solution of a System of Linear Equations in Euclidean Spaces [Garantirovannaya tochnost resheniya sistem lineynykh uravneniy v evklidovykh prostranstvakh]. Novosibirsk: Nauka: Sib. branch, 1988, 456 p.

37. Vapnik, V.N., Mikhalskiy, A.I. On Searching of Dependences Using the Method of Ordered Risk Minimisation [O poiske zavisimostey metodom uporyadochennoy minimizatsii riska] // Automat. & telemech. 1974, Vol. 10, pp. 10–21.

38. Connah, D., Alsam, A., Hardeberg, J.Y. Multispectral imaging: How many sensors do we need? // J. Imaging Sci. Technol. 2006, Vol. 50, #. 1, pp. 45–52. Doi 10.2352/j.imagingsci.technol. (2006)50:1(45).

39. Helling, S., Seidel, E., Biehlig, W. Algorithms for spectral color stimulus reconstruction with a seven-channel multispectral camera / Proc. of CGIV (2nd European Conference on Color in Graphics, Imaging and Vision). 2004, Vol. 2, pp. 254–258.

40. Imai, F.H., Berns, R.S. Spectral estimation using trichromatic digital cameras // Proc. Int. Symp. Multispectral Imaging and Color Reproduction for Digital Archives. Chiba: Society of Multispectral Imaging of Japan, 1999, pp. 42–48.

41. Masahiro, Y., Hideaki, H., Nagaaki, O. Beyond Red–Green–Blue (RGB): Spectrum-Based Colour Imaging Technology // J. Imaging Sci. Technol. 2008, Vol. 52, #. 1, pp. 1–15.

Anastasiya V. Guryleva,
engineer. In 2017, she graduated from N.E. Bauman Moscow State Technical University (MGTU). At present, she is postgraduate student of the Laser and Optoelectronic Devices sub-department of N.E. Bauman Moscow State Technical University (MGTU). Her research interests: photonics, optical engineering, spectrometry

Alexei M. Khorokhorov,
Ph.D. In 1968, he graduated from N.E. Bauman Moscow State Technical University (MGTU). At present, he is Associate Professor of the Laser and Optoelectronic Devices sub-department of N.E. Bauman Moscow State Technical University (MGTU) and Honoured Worker of the Higher Education of the Russian Federation. His research interests: photonics, optical engineering, laser equipment

Vitaly S. Kobozev,
5-th year student of the Laser and Optoelectronic Devices sub-department of N.E. Bauman Moscow State Technical University (MGTU). His research interests: optics, optoelectronic devices

APPLICATION OF SOLAR MAPS IN DESIGN OF GENERAL-POSITION SHADING DEVICES

[a] Alexander T. Dvoretsky[1], [b]Oleg V. Sergeychuk[2], and [c]Alexander V. Spiridonov[3]

[1] *V.I. Vernadsky Crimean Federal University, Simferopol, Russian Federation*
[2] *Kiev National University of Construction and Architecture, Kiev, Ukraine*
[3] *Structure Physics Research Institute of the Russian Academy of Architecture and Construction Sciences, Moscow, Russian Federation*
E-mails: [a] erces_crimea@mail.ru, [b] ovsergeich@mail.ru, [c] spiridonov_aleks@list.ru

ABSTRACT

For insolation calculations and design of shading devices (SD) comprising plane sections or fins, the method based on solar maps shall be preferred because of its high descriptiveness and universality. The article describes the algorithm of design of a general-position SD using a solar map and a shade clinometer. An example of calculation of SD geometry parameters such as fin slopes with the horizontal plane and the facade plane, distance between the fins with consideration of screening of the translucent structure during the building cooling period and of transmission of solar radiation during its heating period is given in the article. A simplified formula of a general-position SD energy efficiency calculation is proposed.

Keywords: solar map, shade clinometer, shadow mask, shading device geometry parameters, preferable insolation zone, overheating zone, building cooling period

1. INTRODUCTION

The decisive impact on temperature mode in premises is caused by the Sun. Even in moderate climate areas, increase of solar heat through windows may be excessive in summer. In summer, overheating of premises may be lowered by the following means: 1) turning the building's facade with the largest number of windows to the North: in this case, however, passive solar heating through windows significantly lowers in winter; 2) application of special glass units operating as heat filter, which also lowers heat transmission not only in summer but also in winter; 3) application of shading devices (SD) with optimised geometry.

A rationally designed SD screens solar radiation during overheating periods, promotes better application of natural daylight, prevents blinding action and provides transmission of solar heat to the premises in winter.

2. ANALYSIS OF THE LATEST ACHIEVEMENTS AND PUBLICATIONS

A shadow mask is a simple tool for definition of the shaded part of the sky at a specific model point (design point) on a solar map. With any set of shading objects, their shadow mask may be placed onto the solar map to show how the design point is irradiated by the Sun at any time of the year [1]. Shadow masks may be built by means of shade clinometers. They are described in [2] for horizontal and vertical shading elements.

The article [3] describes calculations and analysis of SD protective characteristics which allow us to form preliminary guidelines on energy efficiency of different types of SD. However, it is only possible to define SD energy efficiency correctly by means of comprehensive solar maps identify-
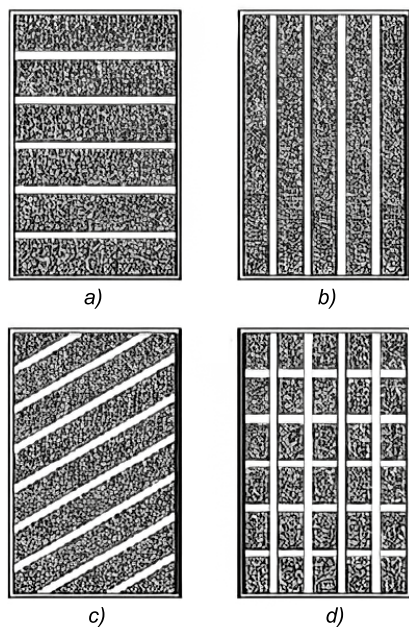
Fig. 1. Different positions of SD shading elements:
a – horizontal; *b* – vertical; *c* – general position;
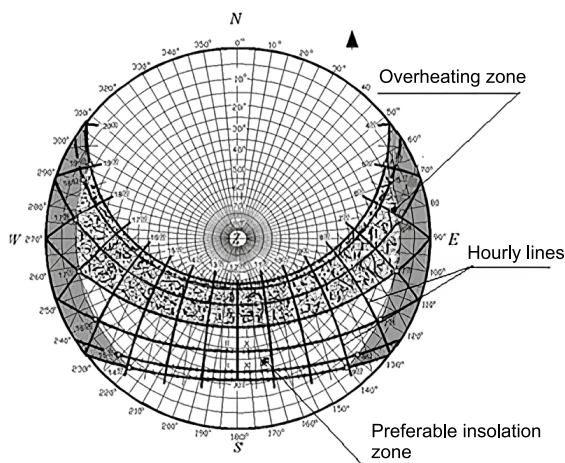*d* – combined

Fig. 2. The solar map with overheating and preferable insolation zones for Simferopol

ing the zones of preferable and non-preferable insolation [4].

The guideline [5] specifies major requirements to SD's of buildings and rules of their design in the Russian Federation applicable to construction, reconstruction and repair of residential, public and production buildings. This regulation specifies major types of SD based on their locations, structural features, materials and adjustment methods to meet standard requirements to heat insulation, solar radiation protection and daylighting in premises for different purposes. The method of solar maps is proposed for design of stationery SDs with rational shape. For insolation calculations and design of SDs comprising plane sections or fins, the method based on solar maps shall be preferred because of its high descriptiveness and universality [5]. The positions of shading elements of SDs, Fig. 1, in this case, are defined by means of a solar map and depend on latitude and facade orientation [5].

Solar maps are used for evaluation of necessity of air heating and conditioning in premises located in different climatic zones. The climatic parameters affecting selection of the type of SDs are considered in the article [6].

The building heating periods form the preferable insolation zone on a solar map and the building cooling periods form the zone of non-preferable insolation or the overheating zone. A solar map with the overheating zone and the preferable insolation zone within the period between March 22 and September 22 with cumulative annual solar radiation on a horizontal plane in conditions of actual cloudiness for the IV and V climatic zones, Fig. 2, is taken from the guideline [5].

This article describes development of the method of definition of geometry parameters of optimised SDs and evaluation of their energy efficiency by means of solar maps and shade clinometers.

3. SOLAR RADIATION AND THE BUILDING COOLING PERIOD

Solar radiation incident on a building facade comprises the direct, diffused and reflected components. Reflected radiation is mostly dependent on surrounding development and it is rather difficult to take it into account in the course of design. The direct and diffused radiation parameters were taken from the climatic handbook [7].

The building cooling periods in Simferopol lasts for almost five months: from May 10 to September 28 [8, Table A.2]. This corresponds to the overheating zone on the solar map (Fig. 2). The article [9] contains the graphs of direct and diffused radiation for these months (Fig. 3), which demonstrate that diffused radiation changes insignificantly during this period.

With accuracy sufficient for evaluation calculations, we may consider that SD screens only direct solar radiation. This corresponds to the guideline in the national standard [10]: "Unless otherwise is determined nation-wide, calculation of shading re-
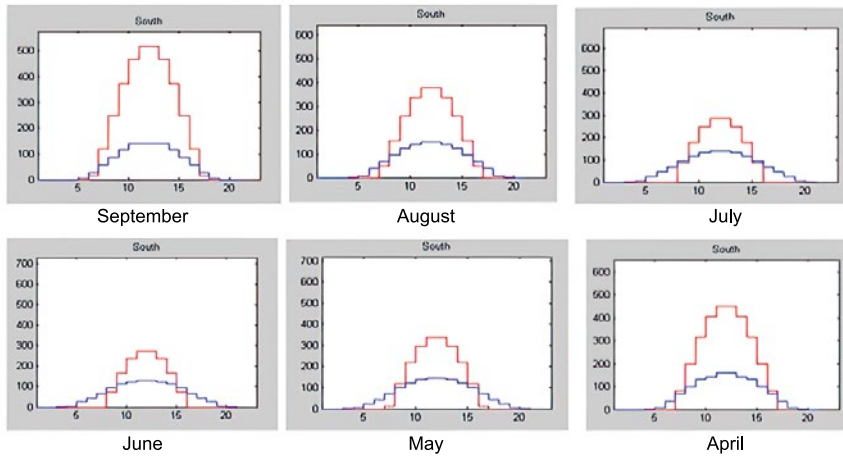
Fig. 3. Direct and diffused radiation with actual cloudiness in Simferopol (W/m²)

duction factors shall be based on the following assumptions. Direct solar radiation is absorbed by an obstruction; diffused radiation and radiation reflected from the Earth remain unchanged. It is identical to obstructions which reflect the same amount of solar radiation as they absorb."

In the general case, the SD efficiency coefficient $F_{sh,0}$ is defined as [10]

$$F_{sh,0} = \frac{I_{sol,ps,mean}}{I_{sol,mean}},$$

where $I_{sol, ps, mean}$ is the irradiance of the surface under consideration due to solar radiation with available shading taken into account, W/m²; $I_{sol, mean}$ is the average irradiance of the surface under consideration if shading is not available.

The article [11] proposed the formulae for calculation of efficiency coefficients of horizontal (F_{ov}) and vertical (F_{fin}) SDs:

$$F_{ov} = \frac{S \cdot k + D \cdot \cos\alpha + 0,25 \cdot Q \cdot r \cdot (1 - \cos\alpha) + R}{S + D + R};$$

$$F_{fin} = \frac{\begin{bmatrix} S \cdot k + 0,5 \cdot D \cdot (1 + \cos\beta) + 0,5 \cdot D^{\perp} \cdot (1 - \cos\beta) + \\ + 0,25 \cdot Q \cdot r \cdot (1 + \cos\beta) + 0,5 \cdot R^{\perp} \cdot (1 - \cos\beta) \end{bmatrix}}{S + D + R},$$

where S, D, R are the values of irradiance of the irradiated surface by direct, diffused and reflected solar radiation respectively, W/m²; Q is the irradiance of Earth surface by total solar radiation, W/m²; r is the albedo of the Earth surface (defined with consideration of snow cover); k is the direct solar radiation transmittance factor of SD; $D^{\perp}$ is the irradiance of a fin by diffused solar radiation, W/m²; $R^{\perp}$ is the irradiance of a fin by reflected (from the Earth surface) solar radiation, W/m²; α is the canopy shading angle; β is the vertical fin shading angle.

For calculation of $F_{sh,0}$ of a general-position SD, the simplified formula may be proposed:
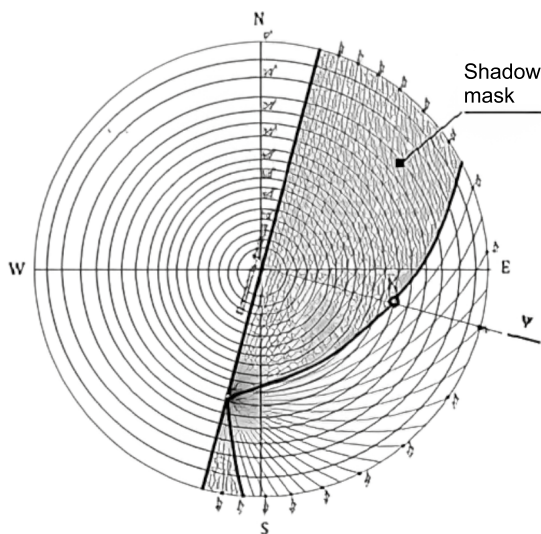
Fig. 4. An example of a shade clinometer for general-position fins with the applied SD shadow mask
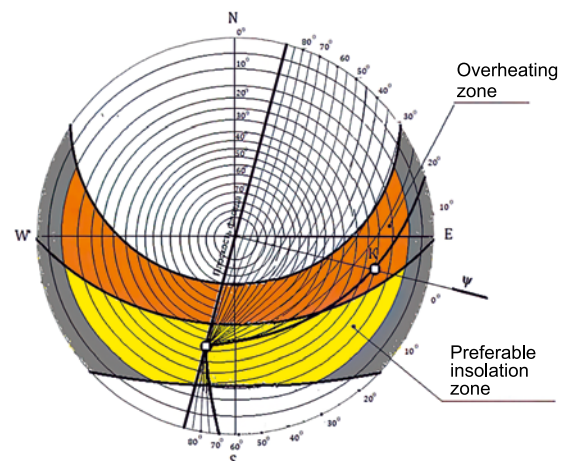
Fig. 5. Example of definition of a rational shadow mask of a general-position SD

Fig. 6. Geometry parameters and general view of a general-position SD:
h – fin width; l – distance between fins; δ – aperture angle; δ_Z – inverse aperture angle; θ – fin slope with the facade plane; μ – shading element slope with the horizontal plane

$$F_{sh,0} = \frac{S \cdot k + D + R}{S + D + R},$$

where the values of S, D and R are defined with consideration of facade orientation using the handbook [7] or the data of meteorological observations.

4. SD STRUCTURAL PARAMETERS CALCULATION

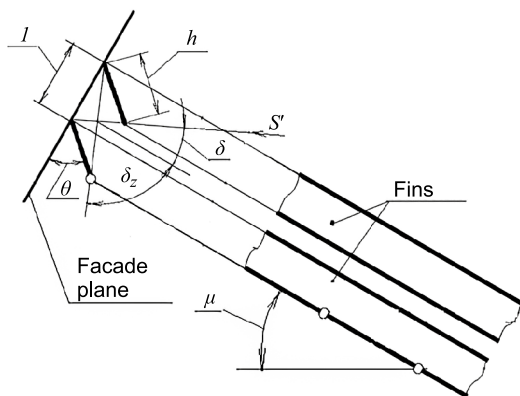A solar map is a graphical tool for design of SD and determination of the insolation period. For insolation calculations and design of SD's comprising plane sections or fins, the method based on solar maps shall be preferred [12].

A part of the celestial sphere between the curve of the selected aperture angle and the facade plane is called the shadow mask of SD, Fig. 4. Such insolation angle should be selected the shadow mask of which covers the non-preferable insolation zone the most efficiently with minimal covering of the preferable insolation zone and the neutral part of the celestial sphere.

__Example.__ A SD for windows of a building in Simferopol with azimuth of 105° is required to be designed. ***The algorithm of efficient SD geometry calculation*** is as follows:

1. Shade clinometers are put onto the solar map with the facade shadow mask on it so that the facade plane on the clinometer corresponds to the facade plane on the shadow mask. The shade clinometers for calculation of different SD types are attached to the guideline [5, Annex I].

2. A shade clinometer is selected so that the shadow mask covers the overheating zone to the maximum extent and does not cover the most part of the preferable radiation zone (Fig. 5). For the design facade orientation, general-position shading elements (fins) are necessary to be applied. Fig. 5

depicts application of a shade clinometer with fin slope with the horizontal plane equal to $\mu = 30$ °.

3. The aperture angle $\delta = 20$ ° and the inverse aperture angle $\delta_Z = 70$ ° are defined based on the selected shade clinometer.

4. The fin slope with the facade plane θ is selected (Fig. 6). Nowadays, brackets allowing us to install fins with facade slope of 90 °, 60 ° and 45 ° are manufactured. Using them, the value $\theta = 45°$ closest to the value of $\delta = 20$ ° may be provided.

5. If we apply the fin width $h = 145$ mm (the dimension from the practically applied standard size of fins) in the designed SD, the distance between the shading elements l is calculated as

$$l = h \cdot (\cos\theta + \sin\theta \cdot \mathrm{tg}\delta) =$$
$$= 145 \cdot \cos 45^\circ \cdot (1 + \mathrm{tg} 20^\circ) \approx 140 \ (mm).$$

Maximum facade insolation will be on the vertical ray plane ψ perpendicular to the facade plane. To design SD with sloped fins, it is necessary to know Solar altitude angle φ on the plane ψ. The latter corresponds to the zero orientation on the shade clinometer. φ on the plane ψ is defined by the almucantarat crossed by the aperture angle curve. In Fig. 5, the point K is the point of crossing of the $\delta = 20°$ curve with the plane ψ. In this case, $\varphi = 23$ °.

The described SD is installed on an experimental building in the outskirts of Simferopol (Fig. 6).

CONCLUSIONS

The structure of SD shall primarily correspond to the facade orientation providing screening of high solar rays during the building cooling period and transmission of solar rays during the heating period. The method based on solar maps and shade clinometers shall be preferred because of its high descriptiveness and universality. This method

allows to define parameters of SD shape and position (in particular slopes of fins with the horizontal plane and the facade plane and the distance between the fins) at which high energy efficiency of SD will be provided.

REFERENCES

1. Marsh A.J. The Application of Shading Masks in Building Simulation / 9th Int. IBPSA Conf. "Building Simulation 2005", Montreal, Canada, 2005.

2. Harkness, E.L., Mehta, M.L. Solar Radiation Control in Buildings [Regulirovaniye solnechnoy radiatsii v zdaniyakh]; Trans. from Eng. by G.M. Ayrapetova, Moscow: Stroyizdat, 1984, 177 p.

3. Kupriyanov, V.N., Spiridonov, A.V. Calculation of Shading Device Parameters [Raschyot parametrov solntsezachshitnykh ustroystv] // Stroitelstvo i rekonstruktsiya, 2019, Vol. 3 (83), pp. 54–62.

4. Spiridonov, A.V., Dvoretsky, A.T. Insolation and Shading [Insolyatsiya i solntsezachshita] / Light Engineering Handbook [Spravochnaya kniga po svetotekhnike]. 4th issue / Edited by Yu.B. Eisenberg and G.V. Boos. Moscow: Editorial Board of the Svetotekhnika journal, 2019, pp. 553–566.

5. SP 370.1325800.2017 Solar Shading Devices in Buildings. Design rules.

6. Dvoretsky A.T., Spiridonov A.V., Shubin I.L., Klevets K.N. Accounting of Climatic Features in Designing Solar Shading Devices // Light & Engineering, 2018, Vol. 26, # 2, pp. 162–166.

7. Scientific and Applied Handbook on Climate in the USSR [Nauchno-prikladnoy spravochnik po klimatu SSSR]. Series 3. Long-Term Data. Parts 1–6. Issue 1–34, Leningrad: Gidrometeoizdat, 1989–1998.

8. Dvoretsky, A.T., Spiridonov, A.V., Mirofanova, S.A., Denisova, T.V. On Necessity of Determination of Degree-Days of the Building Cooling Period in Russia [O neobkhodimosti opredeleniya graduso-sutok perioda okhlazhdeniya zdaniy na territorii Rossii] // Zhilishchnoye stroitelstvo, 2019, Vol. 8, pp. 46–49.

9. Sergeychuk, O.V. Geometry Computer Model of Atmospheric Radiation for Energy-Efficient Contruction [Geometrichna komp'yuterna model Atmospheric Radiation dlya energoeffektivnogo budivnitstva] // Energozberezhennya v budivnitstve ta arkhitekturi, 2011, Vol. 1, pp. 22–28.

10. ISO 52016–1:2017 "Energy performance of buildings – Energy needs for heating and cooling, internal temperatures and sensible and latent heat loads – Part 1: Calculation procedures".

11. Sergeychuk, O.V., Buravchenko, V.S., Andropova, O.V. et al. Features of the Method of Calculation of Solar Access in the National Annex to DSTU B EN ISO 13790 [Osobennosti metodiki raschyota postupleniy v natsionalnom prilozhenii k DSTU B EN ISO 13790] // Energoefektivnist' v budivnitstve ta arkhitekturi, 2014, Vol. 6, pp. 267–272.

12. Dvoretsky, A.T., Morgunova, M.A., Sergeychuk, O.V., Spiridonov, A.V. Methods of Design of Stationery Shading Devices [Metody proektirovaniya statsionarnykh solntsezachshitnykh ustroystv] // Stroitelnyie materialy, oborudovaniye, tekhnologii XXI veka, 2018, Vol. 11–12, pp. 6–10.

Alexander T. Dvoretsky, Prof., Dr. of Technical Science, graduated from Donetsk Polytechnic Institute in 1971. At present, he is the head of the Chair "Geometric and Computer Modelling of Energy Efficient Buildings" of Academy of Civil Engineering and Architecture of the Crimean Federal University named after V.I. Vernadsky, counsellor of Russian Academy of Architecture

Alexander V. Spiridonov, Ph.D., graduated from MPEI in 1975 as specialist in light and engineering and sources of light. At present, he is a head of laboratory "Energy saving technologies in construction" NIISF RAASN, President of Association of Energy Effective Windows Manufacturers, Laureate of the Russian Federation Government prize in the field of science and technology

Oleg V. Sergeichuk, Prof., Doctor of Technical Science, graduated from the Kiev National University of Construction and Architecture in 1975. The professor of the architectural department of the Kiev National University of Construction and Architecture

THE EFFECT OF SCATTERED RADIATION ON CAPABILITIES OF LASER BEAM GUIDANCE

Gennady A. Kaloshin[1], Vladimir P. Budak[2], Sergey A. Shishkin[1,3],
and Vladislav V. Zhukov[4]

[1]*V. E. Zuev Atmospheric Optics Institute of the Siberian Branch
of the Russian Academy of Sciences, Tomsk*
[2]*NIU MEI, Moscow*
[3]*JSC «Research Institute «Ekran», Samara*
[4]*Tomsk Polytechnic University, Tomsk*
E-mails: [1]gkaloshin@iao.ru

ABSTRACT

The paper discusses the possibility of remote detection of a continuous laser beam propagating in a scattering continental and coastal atmosphere, when it is recorded outside the axial zone. In the single scattering approximation, estimates of the radiance at the registration site are carried out, which are compared with the threshold characteristics of existing photodetectors in the visible and IR spectral regions. It is shown that the laser radiation (LR) of the beam is reliably recorded in the range of angles (0–180)° at metrological range of visibility equal (5–20) km at night conditions. At twilight, under the same conditions, detection capabilities are significantly reduced.

A significant increase of the LR beam radiance contrast with a decrease in its divergence has been shown experimentally in the field observations.

At twilight, a decrease in the beam's radiance contrast is seen. A beam with a divergence equal to 2′ ceases to be distinguishable at angles equal to (80–90)°, and a beam with a divergence of 4′ – at angles (60–70)°.In this case, the contrast difference reaches up to 10 times.

Keywords: aerosol scattering, indicatrices, contrast transfer, laser beam, photometer, continental and coastal atmosphere

INTRODUCTION

Many of applications in the fields of sensing, communication, and monitoring are performed by active and passive optical locator stations (OLS). They use powerful sources of laser radiation (LR) with propagation distance of several kilometres in the most dynamic part of the atmosphere: surface air. It is desirable to know the location and direction of a LR beam. In [1–5], it is shown that LR is detectable due to scattering by aerosols and a beam may be displayed by photodetectors (PD). It follows from these works that intensity of LR scattering is corresponds to the prediction based on Mie scattering [6–9] for coastal and continental aerosols. It is known that concentration of aerosol varies significantly depending on regional and local weather conditions [10–13]. For example, increased moisture increases concentration of aerosols and, typically, scattering of LR [14–18]. In typical conditions (mist, thin fog, etc.), even at low altitude, scattering is slight and hardly detectable if there is a background. This poses special requirements, on the one hand, on the PD characteristics: sensitivity, response time, and spectral responsivity range, and, on the other hand, on information about the optical properties of the atmosphere and mostly the aerosol as the main component affecting the attenuation and scattering of LR in atmospheric transparency windows
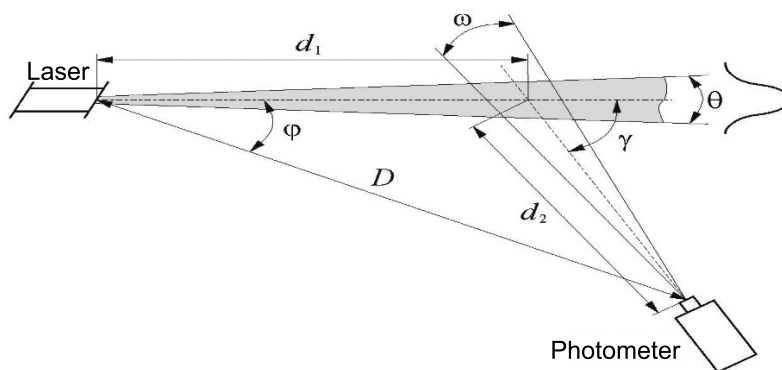
Fig. 1. Diagram of scattered laser radiation detection

[19, 20]. Despite the fact that there are different methods of predicting signal variations at entrance pupils of OLS, it is necessary to further enhance the existing methods and approaches and to develop new methods of remote detection of LR in real operating conditions. This is due to both the development of LR sources and PD's [21–23] and enhancement of aerosol models of surface air [24–27].

The main goals of this work are the study of off-axis detection of LR and measurement of LR radiance contrast, including during field measurements.

The goal of the work is to study patterns of aerosol scattering when estimating capabilities of off-axis detection of LR in continental and near-coast conditions in case of changes of beam parameters, meteorological visibility (MV), time of the day, and distances to LR source.

The work included theoretical evaluations of one-time scattered radiation based on the *MaexPro* aerosol model [28, 29], where sea salt consists of water droplets and salt particles, and aerosol of continental haze with particles radii (0.01-100) μm as the most optically active in wavelength band ORS of (0.2-12) μm. For the following basic conditions of numerical calculations: height above sea level H = (0-25) m; wind speed U = (3-18) m/s; wind speed U = (3-18) m/s; The rest of the conditions are given in the text at the place of mention. In the calculations, we used computer programs [30–33], as well as a program for experimental estimates of the intensity contrast of LR in field conditions [34].

1. RESULTS OF CALCULATIONS

Radiance of scattered LR in surface air is selected as the main magnitude allowing to specifically evaluate capabilities of off-axis detection of a laser beam. Contemporary photometers (spectroradiometers) allow to confidently detect superweak signals within the spectral range of (0.35–1.1) μm by means of non-cooled silicon photodiode detectors and photomultipliers within the spectral range of (0.35–0.93) μm with responsivity thresholds at level of 3σ (depreciation factor is 6) $(3 \cdot 10^{-10})$ W/nm and $(3 \cdot 10^{-14})$ W/nm, respectively. These spectroradiometers manufactured by instrument systems [35] have threshold responsivity of $(10^{-6} - 10^{-7})$ lx within the spectral range of (0.2–5) μm, which allows to register the background of moonless starry sky at $(3 \cdot 10^{-4})$ lx or, for example, light of Sirius at 10^{-5} lx. For cooled photomultipliers operating within spectral range of (0.35–0.93) μm with *GaAs* photocathode, noise equivalent power equals to 10^{-13} W/(cm²·sr·nm) and luminance responsivity is of approximately 10^{-3} cd/m².

The work considers the model of off-axis scattering of LR for optimizing the detector characteristics and predicting the luminous efficacy of its operation in coastal areas when moving the optical axis of a PD perpendicular to and along the beam axis along a horizontal path in night and twilight conditions with different VS.

The diagram of the numerical experiment for the two-dimensional case to determine the distance of off-axis detection of continuous LR passing through a scattering environment is shown in Fig. 1. The Gaussian LR beam with wavelength of λ, initial power of P_0, and divergence of θ at the level of 0.5 is directed in parallel to the earth's surface in direction φ relative to the PD. PD is located at distance D from the source of LR with angle of view ω. Scattered LR is seen at angle of γ.

The distances D and d_2 at which the condition $L / L_t \geq 1$ where L_t is the threshold radiance for a specific PD is met, for LR scattered towards the radiance PD L, are taken as distance of off-axis detection.
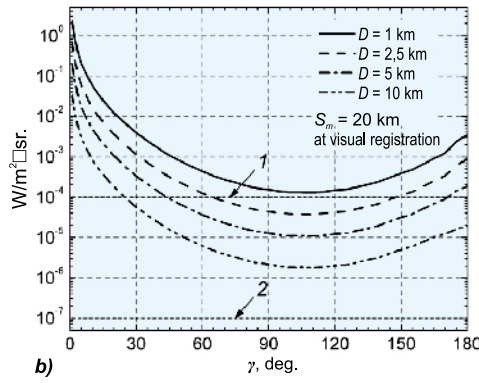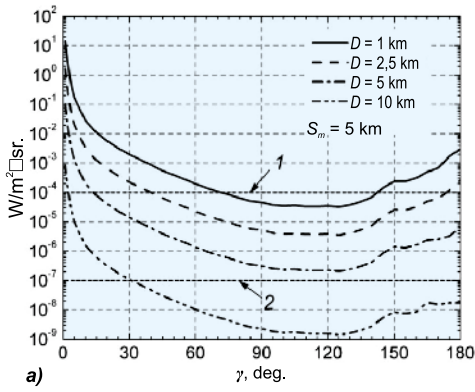
Fig. 2. Change of radiance of a laser beam L by $\lambda = 0.52$ μm at $P_0 = 1$ W and $\theta = 3'$ depending on scattering angle γ in the course of scanning of PD field-of-view axis along the beam axis with different distances D from the emitter with $S_m = 5$ km (*a*) and $S_m = 20$ km (*b*)

L was calculated for one-time scattering, which is reasonable for small optical thicknesses when solving atmospheric problems [17]. Molecular scattering was assumed to be low.

L at the cross-section with the PD field of view axis was calculated as

$$L = \frac{10^{-3}}{4\pi} \cdot \frac{\chi(\gamma) \cdot \exp\left[-\sigma(\lambda) \cdot d_2 \cdot 10^{-3}\right]}{\sin\gamma} \int\limits_{-R}^{R} E(r) dr, \quad (1)$$

where $\sigma(\lambda)$ is spectral coefficient of aerosol scattering, λ is LR wavelength, $\chi(\gamma)$ is directional aerosol light scattering coefficient, γ is scattering angle; d_2 is distance between PD and the sight point at the beam axis, $E(r)$ is irradiance formed by the laser beam at the given point, r is beam radius in a plane of the sight point.

$E(r)$ was defined using the formula

$$E(r) = \frac{2P_0}{\pi \cdot r^2} \cdot \exp(-\sigma(\lambda) \cdot d_1 \cdot 10^{-3}) \cdot \exp\left(-2\frac{r^2}{r_e^2}\right), \quad (2)$$

where P_0 is LR power at entrance of the environment, d_1 is the distance between the laser and the point of sight, $r_\theta = r_0 + d_1 \cdot \mathrm{tg}(\theta/2)$ is the beam radius at divergence level θ in the plane of the sight point,

r_0 is the beam radius at aperture exit, θ is beam divergence at level of 0.5 rad; $R = d_2 \cdot \mathrm{tg}(\omega/2)$ is the distance across the beam limited by the PD field of view; ω is the vision angle of PD.

Using the eqs. (1) and (2), the values of L were calculated for coastal mist with MV S_m of 5 km and 20 km with different geometry of the detection scheme (D, φ) and scattering angles γ in range (0–180)°. The obtained values were compared with threshold radiance responsivity of the selected PD's (for evaluation of the distance of off-axis detection). The following values of LR beam parameters were taken as $P_0 = 1$ W, $\lambda = 0.52$ μm and 1.06 μm, $\theta = 3'$, and $r_0 = 2$ mm. The factors $\sigma(\lambda)$ and $\chi(\gamma)$ were calculated using the data of the *MaexPro* model [28, 29]. For example, at $\lambda = 0.52$ μm and $S_m = 5$ km and 20 km, $\sigma = 0.83$ km^{-1} and 0.75 km^{-1}, respectively, and at $\lambda = 1.06$ μm, it equals to 0.21 km^{-1} and 0.11 km^{-1}, respectively. Some values of the factors $\chi(\gamma)$ (at $\gamma = 1°$, $3°$, $5°$, $45°$, $90°$ and $135°$) are given in Table 1.

The threshold responsivity of PD was selected using the data of [35] with consideration of transformation of energy quantities into luminous quantities using spectral luminous efficacy $V(\lambda)$ at $\lambda = 0.52$ μm. The values of L_t at $\lambda = 0.52$ μm for night and twilight conditions were equal to 10^{-7} W/(m^2·sr)

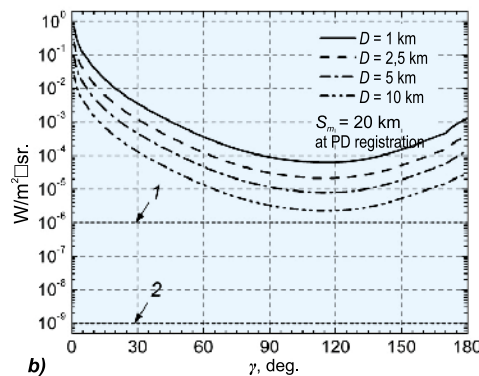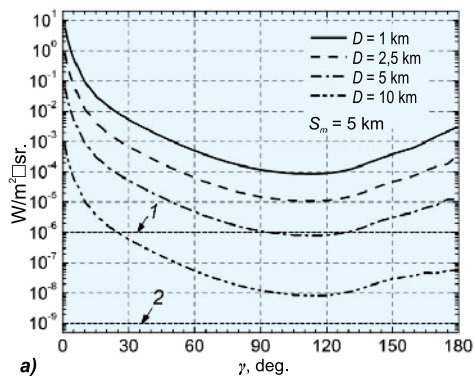
Fig. 3. Change of radiance of a laser beam L by $\lambda = 1.06$ μm at $P_0 = 1$ W and $\theta = 3'$ depending on scattering angle γ in the course of scanning of *PD* field-of-view axis along the beam axis with different distances D from the emitter with $S_m = 5$ km (*a*) and $S_m = 20$ km (*b*)

Table 1. The Values (Selected) of the Coefficients χ(γ) Taken for Calculation

S_m, km	λ LR, µm	$\chi(\gamma)$, km^{-1}·sr^{-1}					
		$\gamma = 1°$	$\gamma = 3°$	$\gamma = 5°$	$\gamma = 45°$	$\gamma = 90°$	$\gamma = 135°$
5	0.52	20	3.7	1.2	0.032	0.0038	0.0029
	1.06	8.1	6.2	3.8	0.087	0.0098	0.0092
20	0.52	6.7	4.5	3.0	0.13	0.026	0.025
	1.06	3.5	3.3	3.0	0.22	0.027	0.017

and 10^{-4} W/(m²·sr), respectively, and at $\lambda =$ = 1.06 µm, they were equal to 10^{-9} W/(m²·sr) and 10^{-6} W/(m²·sr), respectively. The angle ω in this case was equal to 20°.

As an example, the Figs. 2 and 3 show the results of calculation of L depending on γ in the visible ($\lambda =$ 0.52 µm) at visual registration and the near-IR ($\lambda =$ 1.06 µm) regions of the spectre when scanning the PD axis along the axis of the beam at $S_m = 5$ km and 20 km and different values of D.

The calculation results show that the possibilities of detecting scattered LR in the visible range with visual registration at Sm=20 km (Fig. 2b) are higher than at Sm=5 km (Fig. 2a) for all scatteringangles angles.This is explained by the greater attenuation due to scattering at lower Sm on particles of atmospheric haze (Mie particles). The threshold brightness levels in Fig. 2 are indicated by lines 1 and 2 for twilight and night conditions, respectively. In the near-IR range during PD registration with a decrease in the background level by two orders of magnitude to the values indicated in Fig. 3 by lines 1 and 2, the possibilities of detecting scattered LR beams are much higher. The figures show that at night conditions, at $S_m = 5$ m, the LR beam will be detected at distance $D = 10$ km at $\gamma = 45°$. At $\gamma = (110–120)°$ (minimal values of L), the distance of detection D at $S_m = 5$ km reduces to 5 km, and at

$S_m = 20$ km, the LR beam is confidently detected at D exceeding 10 km. In the twilight, at the same values of γ, capabilities of detection reduce significantly down to $D = 1$ km for both 5 km and 20 km.

2. RESULTS OF FIELD MEASUREMENTS

In 2015–2018, to confirm the results of the calculations, the field measurements were conducted in night and twilight conditions at the test area of the V.E. Zuev Atmospheric Optics Institute of the Siberian Branch of the Russian Academy of Sciences. During the measurements, the background luminance was 10^{-2} cd/m² (night) and 0.5 cd/m² (twilight), respectively. During the measurements, the sky was cloudy, and the Moon was below the horizon. MV varied within the range of (12–15) km.

2.1. Scheme of the Experimental Installation

The emitter model (Fig. 4) contained a semiconductor laser *DTL-313* ($\lambda = 0.527$ µm, $P_0 = 117$ mW, $\theta = 1$ mrad, $d_0 = 2$ mm) and the telescopic beam collimation system for adjustment of θ. To measure L, *LS-110* PD by *Konica Minolta* was used (the range of luminance measurements of (0.01–999,
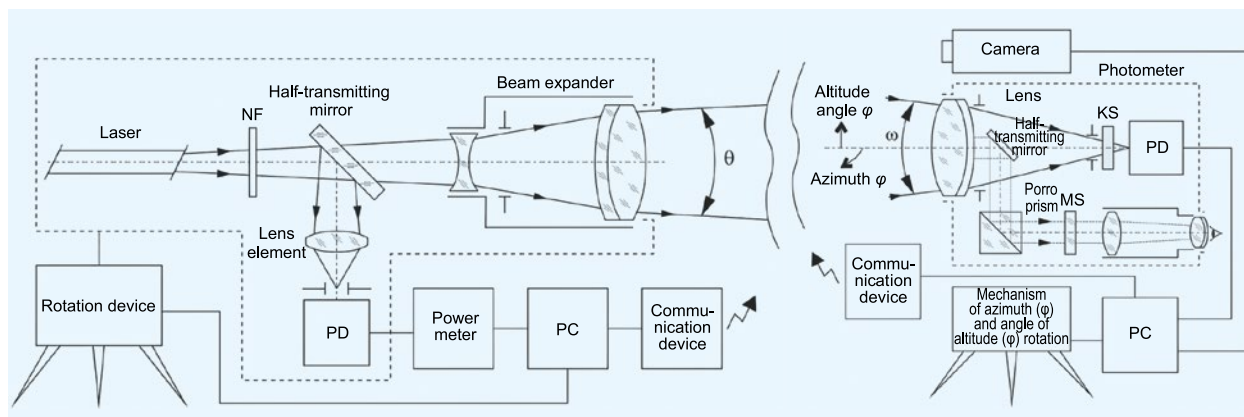

Fig. 4. Diagram of the experimental installation for measurement of luminance of scattered laser radiation
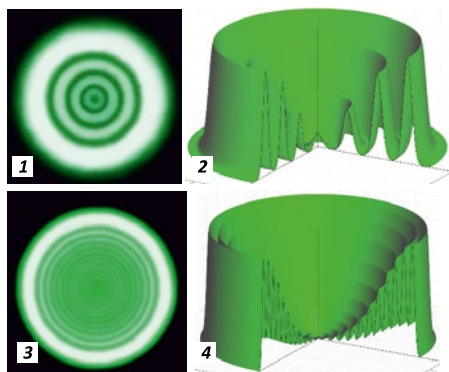
Fig. 5. Cross-sectional distribution of luminance of laser radiation beams in the form of 4 and 12 concentric rings (photos *1* and *3* respectively) and the results of photometry of the same beams (*2* and *4*)

900) cd/m², $\omega = 1/3°$) with a *Canon EOS6D* camera (resolution of 20 *Mpx* (megapixels), EF (24–105) mm lens, *f/4L*). The equipment was installed on a rotating platform to move along the azimuth and angle of altitude. The measurement data was registered by a PC and processed by means of the developed software [36, 37].

The measurements were conducted following the scheme shown in Fig. 1. The directional light scattering coefficient γ was registered in the range of angles of $\gamma = (0.5–179.5)°$ with a step of 5° at the set values of D and φ. Due to structural features, the PD did not reach the border values of γ at 0.5°. The beam passed at altitude of about 2 m above the earth surface. Before commencement of measurement, a standard pegging-out of the area was conducted to define the parameters of the LR path and

to define the places of PD installation so that their optical axes were in one plane and crossed each other.

The structure of laser beams used for measurements is shown in Fig. 5.

Recently, LR beams with circular structure of intensity distribution, which may be well approximated cross-sectionally by the Gaussian function are of interest. Fig. 5 shows that the external ring of both types of beams has the highest radiance, which reduced to the centre of the beam according to the law close to the Gaussian distribution. The main power of the beam is concentrated in the first two rings. In Fig. 5, white colour depicts maximum intensity and black colour depicts zero intensity. Here, cross-sectional distribution of intensity is presented as concentric 4 rings and 12 rings with $\theta = 2'$ и $4'$, respectively.

An example of an image of beams shot from one side is shown in Fig. 6. The geometry of the detection scheme was as follows: $D = 150$ m, $\varphi = 2°$, $\gamma = 45°$.

2.2. Results of Measurement of LR Beam Luminance Contrast

The measured luminance of LR beams in direction perpendicular to their axis is shown in Fig. 7 at two values of angular detection directions $\gamma = 45°$ and 90°. In the shot of the LR beams (Fig. 6), the detector axis was located near the centre of the image along the axis of a respective beam.

Fig. 6. The image of laser radiation beams ($\lambda = 0.527$ μm, $P_0 = 117$ mW), side view, on a near-surface path, with beam divergence $\theta = 2'$ (*a*) and $4'$ (*b*)

a)

b)
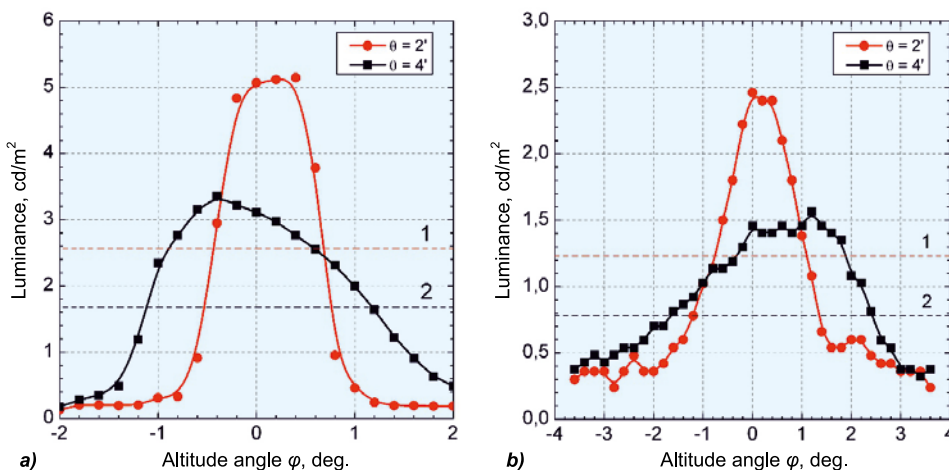
Fig. 7. Change of luminance of the laser radiation beams ($\lambda = 0.527$ μm, $P_0 = 117$ mW) with divergence of $\theta = 2'$ and $4'$ when displacing the field-of-view axis of the photometer perpendicular to the beam axis at acceptance angles $\gamma = 45°$ (*a*) and 90° (*b*)
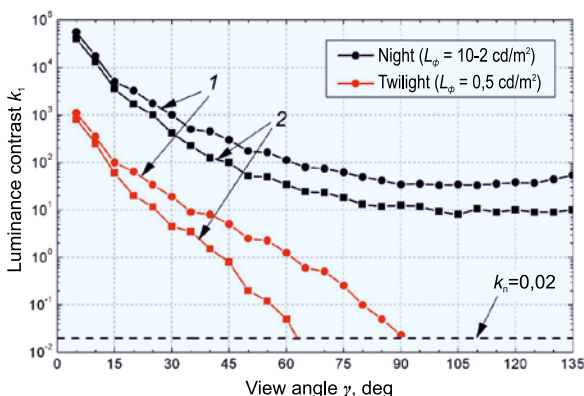
Fig. 8. Change of luminance contrast k of the laser beam ($\lambda = 0.527$ μm, $P_0 = 117$ mW) with divergence of $\theta = 2'$ (curves *1*) and $4'$ (curves *2*) at night and twilight conditions when the field-of-view axis of the photometer is displaced angularly along the beam axis

The capability of guidance along the LR beam was evaluated by the value of luminance contrast k defined using the expression

$$k = (L_0 - L_b)/L_b, \qquad (3)$$

where L_0 is luminance of the scattered LR beam; L_b is background luminance. At $k \rightarrow 1$, the observed LR beam is extremely contrast, and the case of $k \rightarrow 0$ corresponds to complete scattering of the LR beam. For definition of k of the LR beam, the value of the beam luminance L_0 was selected on the level of $0,5 \cdot L_{max}$ depicted by horizontal lines 1 (at $\theta = 2'$) and 2 (at $\theta = 4'$) in Fig. 7. At $\gamma = 45°$, the values of k calculated using (3) were equal to 0.51 and 0.33 for LR beams with $\theta = 2'$ и $4'$, respectively. At $\gamma = 90°$, $k = 0.33$ for the LR beam with $\theta = 2'$ and $k = 0.12$ for the LR beam with $\theta = 4'$. Therefore, Fig. 7 illustrates a significant reduction of k of the beam with increasing θ.

To evaluate the detection capabilities of the LR beam, several series of the beam k were measured at different values of γ depending on background observation conditions. The measured background luminance L_b was equal to about 10^{-2} cd/m2 and 0.5 cd/m^2 for the night and twilight conditions, respectively. The selected detection scheme was as follows: $D = 1200$ м, $\varphi = 5°$, $\gamma = (5-135)°$.

Changes in k of the LR beams at $\theta = 2'$ и $4'$ are shown in Fig. 8. The horizontal line here depicts the level of threshold luminance contrast k_t, which was selected equal to 0.02 as per the recommendations [38, 39] for approximate calculations.

3. DISCUSSION OF THE RESULTS

The results show (Fig. 7) that k of LR beams significantly reduces with increase of θ. This is caused by an increase in background radiation due to multiple scattering of the beam itself. Moreover, it follows from Fig. 8 that k of LR beams at night conditions is much higher than k_t within the entire range of angles γ, which confirms that they are found reliably. The initial sections of the beams up to (15–20)° are especially contrast and were also perceived visually the same in both beams. With increase of the angles γ, the beam with $\theta = 2'$ was seen more contrast, and its k was (3–5) times higher than that of the beam with $\theta = 4'$.

At twilight conditions, a significant decrease in k of both beams was seen. The beam with $\theta = 2'$ becomes not detectable at (80–90)°, and the beam with $\theta = 4'$ becomes not detectable at (60–70)°. In this case, the difference between the values of k becomes 10-fold.

4. CONCLUSIONS

The results of the calculations and field measurements show that the values of k of the selected types of LR beams strongly depend on θ and S_m.

It is demonstrated that LR is reliably detected within the range of angles of (0–180)° at (5–20) km at night and twilight conditions with background luminance of 10^{-2} cd/m^2 and 0.5 cd/m^2, respectively.

Field experiments have showed that k of the LR beam significantly reduces with decrease of its θ. In twilight conditions, significant reduction of k of both beams was seen. The beam with $\theta = 2'$ becomes not detectable at (80–90)°, and the beam with $\theta = 4'$ becomes not detectable at (60–70)°. In this case, the difference between the values of k ultimately becomes 10-fold.

REFERENCES:

1. Roy N., Reid F. Off–axis laser detection model in coastal areas, Optical Engineering, 2008. V47, pp. 1–11.

2. Cariou J.P. Off-axis detection of pulsed laser beams: simulation and measurements in the lower atmosphere, Proceedings of SPIE, 2003. V5086, pp. 129–138.

3. Michulec J. K., Schleijpen R. Influence of aerosols on off-axis laser detection capabilities, Proceedings of SPIE, 2009. V7463, pp. 1–12.

4. DeGrassie John S. Modeling off-axis laser scattering: effects from aerosol distributions, Proceedings of SPIE, 2012. V8517 (85170V).

5. Mendoza–Yero, O. Effects of off–axis laser beam propagation on beam parameters, Proceedings of SPIE, 2014. V5622.

6. Kaloshin G.A., Piazzola J. Influence of the large aerosol particles on the infrared propagation in coastal areas, Proceedings of 23rd International Laser Radar Conference, 2006. pp. 429–432.

7. Kaloshin G.A., Piazzola J., Shishkin S. Numerical modeling of influence of meteorological parameters on aerosol extinction in the marine atmospheric surface layer, Proceedings of 16th International Conference on Nucleation and Atmospheric Aerosols (ICNAA), 2004. p. 352–354.

8. Kaloshin G.A. Modeling the Aerosol Extinction in Marine and Coastal Areas, IEEE Geoscience and Remote Sensing Letters, 2020, april. URL: https://ieeexplore.ieee.org/document/9052468 (date of reference: 20.06.2020); doi: 10.1109/LGRS.2020.2980866.

9. Kaloshin G.A. Method of Building of a Visual Landing-and-Takeoff System by Means of Vortex Laser Beams, Patent of Russia No. 2695044, 2018. V32.

10. Gathman S.G. Optical properties of the marine aerosol as predicted by the Navy aerosol model, Optical Engineering, 1983. V22, #1, pp. 57–62.

11. Gathman S.G. J. van Eijk A.M. and Cohen L.H. Characterizing large aerosols in the lowest levels of the marine atmosphere, Proceedings of SPIE, 1998. V3433, pp. 41–52.

12. Shettle E.P. Models of aerosols clouds and precipitation for atmospheric propagation studies, Proceedings of AGARD Conference: Atmospheric Propagation in the UV Visible IR and MM–Wave region and Related Systems Aspects, 1989. V454, pp. 15–1 – 15–13.

13. Weichel H. (ed.) Laser Beam Propagation in the Atmosphere. – SPIE Bellingham WA. – 28.09.1990.

14. Zuev V.E. Propagation of Visible and Infra-Red Waves in Atmosphere [Rasprostranenie vidimykh i infrakrasnykh voln v atmosfere]. – Moscow: Sovetskoye radio, 1970. 496 p.

15. Zuev V.E. Propagation of Laser Radiation in Atmosphere [Rasprostranenie lazernogo izlucheniya v atmosfere]. Moscow: Radio i svyaz, 1981. 288 p.

16. Zuev V.E., Krekov G.M. Optical Models of Atmosphere [Opticheskiye modeli atmosfery]. – Leningrad: Gidrometeoizdat, 1986. 256 p.

17. Zuev V.E., Kabanov M.V., Saveliev B.A. Propagation of Laser Beams in a Scattering Environment [Rasprostranenie lazernykh puchkov v rasseivayushchey srede], Applied Optics, 1969. V8, #1, pp. 137–141.

18. Deymerdjan D. Scattering of Electromagnetic Radiation by Spherical Polydisperse Particles [Rasseyanie elektromagnitnogo izlucheniya sfericheskimi polidispersnymi chastitsami]. – Moscow: Mir, 1971. 290 p.

19. Jensen D.R., Gathman S.G., Zeisse C.R., Littfin K.M. EOPACE overview and initial accomplishment, Journal of Aerosol Science, 1999. V30, #1, pp. 53–54.

20. Jensen D.R., Gathman S.G., Zeisse C.R., Leeuw G., de Smith M.H., Frederickson P.A., Davidson K.L. Electrooptical Propagation Assessment in Coastal Environments (EOPACE): summary and accomplishments, Optical Engineering, 2001. V40, #8, pp. 1486–1498.

21. Kaloshin G.A., Gordienko A.I. Laser aids to navigation (methods), IALA Bullletin. 2003. V3, pp. 46–51.

22. Kaloshin G.A. Gordienko A.I. Laser aids to navigation (technologies), IALA Bullletin, 2004. #1, pp. 42–49.

23. Gordienko A.I. Kaloshin G.A. Laser leading beacons: summaries and perspectives, Proceedings of XV Conference IALA "Navigation and the Environment", 2002. pp. 150–158.

24. Jensen D.R. Gathman S.G. Zeisse C.R. and Littfin K.M. EOPACE (Electrooptical Propagation Assessment in Coastal Environments) Overview and Initial Accomplishments /Proceedings of Millennium Conference on Antennas and Propagation (AP2000). – Davos Switzerland, 2000.

25. Nilsson B.A. Meteorological influence on aerosol extinction in the 0.2–40 μ wavelength range, Applied Optics, 1979. V18, pp. 3457–3472.

26. Nilsson B.A. Model of the relation of IR aerosol extinction to weather parameters, Proceedings of SPIE: Infrared Technology XVIII, 1992. V1762, pp. 238–250.

27. Lewis E.R., Schwartz S.E. Sea salt aerosol production: Mechanisms methods measurements and models – a critical review. Geophys. Monograph. Washington DC: AGU, 2004. 413 p.

28. Kaloshin G.A., Grishin I.A. An aerosol model of the marine and coastal atmospheric surface layer, Atmosphere, Ocean, 2011. V49, #2, pp. 112–120.

29. Kaloshin G.A. Development of the Aerosol Model of the Near-Earth Layer of Marine and Coastal Atmosphere [Razvitiye aerozolnoy modeli prizemnogo sloya morskoy i pribrezhnoy atmosfery]. Optika atmosfery i okeana, 2018. V31, #11, pp. 881–887.

30. Kaloshin G.A., Shishkin S.A. The Range Software Package for Calculations of Optical Radiation Propagation with Consideration of Aerosol Attenuation in the Near-Surface Layer of the Continental Marine and Coastal Atmosphere [Programmno-tekhnologicheskiy paket

Range dlya provedeniya raschyotov rasprostraneniya opticheskogo izlucheniya s uchyotom aerozolnogo oslableniya v prizemnom sloye kontinentalnoy morskoy i probrezhnoy atmosfery], Certificate of State Registration of Computer Software No. 2012616944 dated on 08/03/2012.

31. Kaloshin G.A., Shishkin S.A. MaexPro Software Package for Calculation of Spectral Aerosol Attenuation Coefficients in the Near-Surface Layer of Marine and Coastal Atmosphere [Programma dlya raschyota spektralnykh koeffitsientov aerozolnogo oslableniya v prizemnom sloye morskoy i pribrezhnoy atmosfery MaexPro] / Certificate of State Registration of Computer Software No. 2012616945 dated 08/03/2012.

32. Kaloshin G.A., Shishkin S.A. MieCalc Software Package for Calculation of Complex Refractive Indices of a Material of Marine and Coastal Aerosol Particles [Programma dlya raschyota kompleksnykh pokazateley prelomleniya veshchestva chatits morskogo i pribrezhnogo aerozolya MieCalc]. Certificate of State Registration of Computer Software No. 2012616943 dated 08/03/2012.

33. Kaloshin G.A., Shishkin S.A. Zhukov V.V. Microphysical and Optical Characteristics of Marine and Coastal Aerosol [Mikrofizicheckiye i opticheskiye kharakteristiki morskogo i pribrezhnogo aerozolya]. Certificate of State Registration of a Database No. 2015621775 dated 12/14/2015.

34. Kaloshin G.A., Shishkin S.A. Zhukov V.V. Characteristics of scattered radiation in off–axis recording of laser radiation under field conditions, Proceedings of SPIE25th Intern. Symp. on Atmospheric and Ocean Optics: Atmospheric Physics, 2019. V11208, P. 112081C.

35. Instrument Systems. URL: http://www.instrument systems.com/ (date of reference: 20.06.2020).

36. Kaloshin G.A., Shishkin S.A., Zhukov V.V. Software Package for Control and Processing of the Data of Spectroradiometry Measurements of Scattered Radiation of Laser Beams in Atmosphere [Programma dlya upravleniya i obrabotki dannykh spektroradiometricheskikh izmereniy resseyannogo izlucheniya lazernykh puchkov v atmosfere] / Certificate of State Registration of Computer Software No. 2015618954 dated 08/20/2015.

37. Kaloshin G.A., Shishkin S.A., Zhukov V.V. Software for Control of Measurements of Laser Beam Luminance Contrast in Scattering Environments [Programma upravleniya izmereniyami kontrasta yarkosti lazernykh puchkov v rasseivayushchikh sredakh] Certificate of State Registration of Computer Software No. 2015663204 dated 12/14/2015.

38. Meshkov V.V., Matveev A.B. Basics of Light Engineering: Study Guide for Higher Education Institutions: in 2 parts. P. 2. Physiological Optics and Colourimetry [Osnovy svetotekhniki: uchebnoye posobiye dlya vuzov: v 2 ch. Ch. 2. Fiziologicheskaya optika i kolorimetriya].

2nd edition, revised and supplemented. Moscow: Energoatomizdat, 1989, 432 p.

39. Luizov A.V. Eye and Light [Glaz i svet]. – Leningrad: Energoatomizdat, Leningrad Branch, 1983. 144 p.

Gennady A. Kaloshin, Ph.D (phys.-math.) He graduated from Tomsk State University with specialty in Radiophysics and Quantum Electronics in 1972. Leading Scientist Researcher of V.E. Zuev Atmospheric Optics Institute of the Siberian Branch of the Russian Academy of Sciences

Vladimir P. Budak, Professor, Doctor of Technical Sciences. In 1981, he graduated from the Moscow Power Engineering Institute (MPEI). At present, he is the Editor-in-chief of the Svetotekhnika / Light & Engineering journal, Professor of the Light Engineering sub-department of NRU MPEI. Corresponding member of the Academy of Electrotechnical Sciences of Russia

Sergey A. Shishkin is Leading engineer, Head of department. He graduated from Tomsk University of Control Systems and Radioelectronics in 2000. He works at Joint Stock Company "Research Institute "Ekran", Samara and V.E. Zuev Institute of Atmospheric Optics SB RAS

Vladislav V. Zhukov graduated from Tomsk Polytechnic University, Tomsk. Now he is engineer at Tomsk Polytechnic University

DETERMINATION OF EFFICIENT MODES OF OPTICAL RADIATION EXPOSURE FOR CONTROL OF HUMAN CIRCADIAN ACTIVITY

Alexander V. Leonidov

E-mail: avleonidoff@mail.ru

ABSTRACT

The article describes the stages of transformation of the direct and diffused components of solar radiation in the short-wave and long-wave spectral channels of the human circadian activity control path. The method of determination of the dependences of irradiance on Solar altitude angle as well as the values of radiant exposure in the circadian region of the optical spectre required for efficient control of human circadian activity. An example of utilisation of the developed method is provided. Correspondence between the results of calculations based on the proposed method and the results of independent experimental studies is demonstrated. The developed method allows us to formulate major light-engineering requirements to characteristics of emitting installations controlling human circadian activity, preventing and eliminating its deregulations.

Keywords: circadian activity, Solar altitude angle, components of solar radiation, thermodynamic temperature, spectral channels, effective irradiance, radiant exposure, effect modes, calculation method

1. INTRODUCTION

Daily changes of the characteristics of optical radiation of the Sun reaching the surface of the Earth are the main physical factor affecting human circadian activity (CA). These changes of characteristics of solar radiation (SR) are caused by current position of the Earth in the course of its orbital movement around the Sun as well as its current altitude angle common for a specific calculation point of the Earth surface.

When conducting light-engineering and biological studies, it is necessary to have information on the dependence of effective[1] irradiance E affecting CA of human body on Solar altitude angle h at a particular point of the Earth surface. This information as well as the values of radiant exposure H at different calculation points of the Earth surface is also necessary for design of specialised emitting installations for prevention and elimination of circadian deregulations.

Prevention and elimination of circadian deregulations allows us to save psychosomatic health and maintain necessary level of general and visual performance of human and provides maintenance of daily intellectual activity.

This work aims at development of the method of determination of effective energy characteristics of Solar and artificial radiations affecting human body CA.

2. INPUT DATA

Spectral density of radiant exitance of the Sun photosphere $m_{eS}(\lambda, T)$ described by the Planck function [1] is used as the model of Solar radiation:

$$m_{eS}(\lambda,T) = C_1 \lambda^{-5} \left(\exp\frac{C_2}{\lambda T} - 1 \right)^{-1},$$

---

[1] Hereinafter "effective" means the value of human body reaction to the effect of irradiance and spectral irradiance formed by SR in the circadian region of the spectre as well as to radiant exposure within the range of Solar altitude angles corresponding to CA control.

where λ is the radiation wavelength, T is the thermodynamic temperature of blackbody radiation, $C_1 \approx$ $\approx 3.742 \cdot 10^{-16}$ W·m^2 and $C_2 \approx 1.439 \cdot 10^{-2}$ m·K [2].

Spectral irradiance (SI) formed by SR normally incident on a site located at the upper border of the Earth atmosphere is expressed as [3]:

$$e_{eS}(\lambda, T) = \left(\frac{r}{R}\right)^2 m_{eS}(\lambda, T), \qquad (1)$$

where T is the average thermodynamic temperature of SR with respect to the Sun photosphere, $r = 6.96 \cdot 10^5$ km is the Sun equatorial radius, $R = 1.496 \cdot 10^{12}$ km is the radius of circular orbit of the Earth [4, 5].

The value T depends significantly on the year number n within the Schwabe's 11-year cycle of Solar activity [6] and is expressed as [3]

$$T(n) = T_{aver}\left[1 + 0,027\sin\left(\frac{2\pi n}{11} - \frac{\pi}{2}\right)\right],$$

where $T_{aver} = 0.5 \cdot (T_{min} + T_{max})$, $T_{min} \approx 5480$ K, $T_{max} \approx 5780$ K are the values of thermodynamic temperature of SR at the upper border of the atmosphere corresponding to the minimum and maximum Solar activity, $0 \leq n \leq 11$.

As a result of SR distribution over the atmosphere, there are two components of the radiation formed at the Earth surface: the direct (*Dir*) component and the diffused (*Diff*) component. The values of thermodynamic temperature of the direct and diffused components of SR during daytime at a design point of the Earth surface depend on the Solar altitude angle, i.e. $T_{Dir} = T_{Dir}(h, n)$ and $T_{Diff} = T_{Diff}(h, n)$.

The functions $T_{Dir}(h, n)$ and $T_{Diff}(h, n)$ may be written as approximate dependences.

$$T_{Dir(Diff)}(h, n) \approx T_{Dir(Diff)}(h) + T(n). \qquad (2)$$

Analysis of literature with respect to experimental data on the dependences $T_{Dir}(h, n)$ and $T_{Diff}(h, n)$, in particular, [7], etc. as well as approximation of this data demonstrated that $T_{Dir(Diff)}(h)$ in (2) may be written as

$$T_{Dir(Diff)}(h) = a_{Dir(Diff)}\exp(-b_{Dir(Diff)}h). \qquad (3)$$

The values of spectral radiance of the direct and diffused components at the Earth surface formed by SR are written as

$$e_{eS,Dir(Diff)}\left[\lambda, T_{Dir(Diff)}(h, n)\right] =$$

$$= \left(\frac{r}{R}\right)^2 \tau_{Dir(Diff)}(h) C_1 \lambda^{-5} \left(\exp\frac{C_2}{\lambda T_{Dir(Diff)}(h, n)} - 1\right)^{-1}, \quad (4)$$

where $T_{Dir(Diff)}(h, n)$ are the dependences (2), $\tau_{Dir(Diff)}(h)$ are the dependences of integral transmittance factors of the direct and diffused components of SR in the spectral window of the atmosphere $300 \leq \lambda \leq 1200$ nm [8] with different atmosphere cloudiness.

The dependence $\tau_{Dir(Diff)}(h)$ in (4) has the form [3]

$$\tau_{Dir(Diff)}(h) =$$

$$= \tau_{Dir(Diff)}(90°)0,5\left[1 + \sin\left(d_{Dir(Diff)}h - g_{Dir(Diff)}\right)\right], \quad (5)$$

where $\tau_{Dir(Diff)}(90°)$ are the integral transmissivity factors of normal SR incidence on the Earth surface (maximum Solar altitude angle $h = 90°$ is seen at the equator at noon of the vernal or autumnal equinox days), the factors $d_{Dir(Diff)}, g_{Dir(Diff)}$ for different cloudiness of atmosphere are given in [9].

SI of the direct and the diffused components of SR on the Earth surface as per the relation (4) are received by retinal detectors characterised by the function of relative spectral circadian efficiency (FRSCE) in the following form [10]

$$c(\lambda) = c_1(\lambda) + c_2(\lambda) = \frac{\alpha_1}{\sigma_1\sqrt{2\pi}}\exp\left[-\frac{(\lambda - \lambda_{1max})^2}{2\sigma_1^2}\right] +$$

$$\frac{\alpha_2}{\sigma_2\sqrt{2\pi}}\exp\left[-\frac{(\lambda - \lambda_{2max})^2}{2\sigma_2^2}\right], \quad (6)$$

obtained after approximating the results of independent experimental studies by G.K. Brainard and K. Thapan and their contributors, in particular, [11–14].

The graphs of the function (6) and its components $c_1(\lambda)$ and $c_2(\lambda)$ are shown in Fig. 1. The differences between FRSCE obtained by Brainard and Thapan are just in relation between the maximums of the functions $c_1(\lambda)$ and $c_2(\lambda)$.

3. RESULTS

The functions $c_1(\lambda)$ and $c_2(\lambda)$ form the short-wave (*SW*) and the long-wave (*LW*) spectral channels of the *CA* control path [10] and conduct spectral
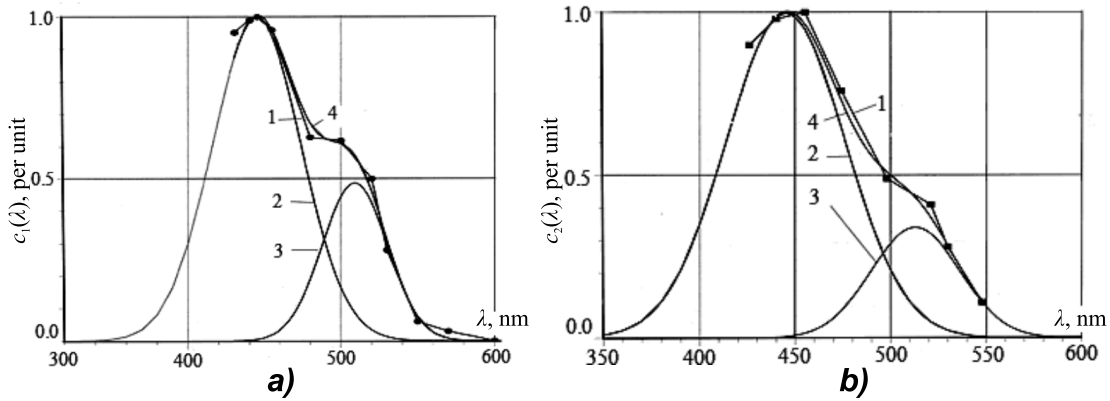
Fig. 1. FRSCEs obtained by Brainard (a) and Thapan (b), functions $c_1(\lambda)$, $c_2(\lambda)$ in the relation (9) and the sum $c_1(\lambda) + c_2(\lambda)$:
1 – results of the experimental studies [11–14], *2* – the function $c_1(\lambda)$, *3* – the function $c_2(\lambda)$, *4* – the function $c_1(\lambda) + c_2(\lambda)$
approximating the results of the studies [11–14]

and selective transformations of SR SI (4) described by the multiplications

$$e_{\text{eS,Dir(Diff),SW(LW)}}\left[\lambda, T_{\text{Dir(Diff)}}(h,n)\right]c_{1(2)}(\lambda) =$$

$$= \left(\frac{r}{R}\right)^2 \tau_{\text{Dir(Diff)}}(h)C_1\lambda^{-5}\left(\exp\frac{C_2}{\lambda T_{\text{Dir(Diff)}}(h,n)} - 1\right)^{-1} \times$$

$$\times\, c_{1(2)}(\lambda) \qquad (7)$$

with isolation of the $350 \leq \lambda \leq 540$ nm spectral region from the broadband spectra (4) with spectral selection by only blue-sensitive (*B*) retinal cones, isolation of the $450 \leq \lambda \leq 570$ nm spectral region with spectral selection by only retinal rods, and isolation of the $350 \leq \lambda \leq 570$ nm spectral region with cooperative spectral selection by the *B* cones and rods of the retina. Obviously, after spectral and selective processing of the function (4) by the functions $c_1(\lambda)$, $c_2(\lambda)$, $c_1(\lambda) + c_2(\lambda)$ using the relation (7), the shape of the obtained spectrum is defined only by non-variable spectral characteristics of these functions which do not depend on Solar altitude angle.

Modification of $T_{\text{Dir(Diff)}}(h, n)$ on the Earth surface with changes of Solar altitude angle during daytime leads not only to changes in chromaticity of SR (4) but also to λ-related displacement of the spectral maximum (4) based on the Wien's displacement law: $\lambda_{\max}\cdot T(h, n) = C_3 \approx 0.2898\cdot10^{-2}$ m·K [2].

Changes of values of $\lambda_{\max}$ with respect to the λ-fixed position of the functions $c_1(\lambda)$, $c_2(\lambda)$, $c_1(\lambda) + c_2(\lambda)$ and unchanged spectral form (7) leads to dependence of the energy characteristics (7) on Solar altitude angle.

Determination of the dependence of energy characteristics (7) on Solar altitude angle is based on two-step transformation of the arguments in (7). At the first step, we shift from the λ scale to the $\lambda_{\max}$ scale by means of linear (identity) transformation of the argument λ into the argument $\lambda_{\max}$. At the second step, $\lambda_{\max}$ is non-linearly functionally transformed into Solar altitude angle h using the Wien's displacement law by means of an inverse function of the function (2).

Functional transformation of the arguments in (7) is conducted using the known rule, e.g. [15, 16]:

$$S(y) = S(x)\left|\frac{dx}{dy}\right| = S[\varphi(y)]\left|\frac{d\varphi(y)}{dy}\right|, \qquad (8)$$

where x is the basic argument, y is the new argument, $x = \varphi(y)$ is the inverse function of the original function $y = f(x)$.

At the first step of transformations of the argument λ into $\lambda_{\max}$, the argument $\lambda_{\max}$ directly substitutes λ in (4):

$$e_{\text{Dir(Diff),SW(LW)}}\left(\lambda_{\max,\text{Dir(Diff)}}h, n\right)\cdot c_{1(2)}\left(\lambda_{\max,\text{Dir(Diff)}}\right) =$$

$$= \left(\frac{r}{R}\right)^2 \tau_{\text{Dir(Diff)}}(h,n)C_1\lambda_{\max,\text{Dir(Diff)}}^{-5} \times$$

$$\times \left(\exp\frac{C_2}{\lambda_{\max,\text{Dir(Diff)}}T_{\text{Dir(Diff)}}(h,n)} - 1\right)^{-1} \times$$

$$\times \left|\frac{d\lambda}{d\lambda_{\max,\text{Dir(Diff)}}}\right|c_{1(2)}\left(\lambda_{\max,\text{Dir(Diff)}}\right). \qquad (9)$$

In the relation (9), the modulus of the derivative is $\left|\dfrac{d\lambda}{d\lambda_{\max,\mathrm{Dir(Diff)}}}\right| = 1$ and the (9) itself describes the spectral form remaining homothetic with all values of h and n since this form is defined only by the functions $c_1(\lambda)$, $c_2(\lambda)$ or $c_1(\lambda) + c_2(\lambda)$.

The energy characteristics of the dependence of the function

$$e_{\mathrm{Dir(Diff)},\mathrm{SW(LW)}}\left(\lambda_{\max,\mathrm{Dir(Diff)}}h,n\right)\cdot c_{1(2)}\left(\lambda_{\max,\mathrm{Dir(Diff)}}\right)$$

on the Solar altitude angle are defined using the Wien's displacement law.

With non-linear functional transformation, the Wien's displacement law $\lambda_{\max} \to h$ is written as

$$\lambda_{\max,\mathrm{Dir(Diff)}}\left(h,n\right) = C_3\left[T_{\mathrm{Dir(Diff)}}\left(h\right) + T\left(n\right)\right]^{-1}. \quad (10)$$

In the non-linear transformation of the arguments $\lambda_{\max} \to h$ in the relation (9) using the rule (8), multipliers $\left|\dfrac{d\lambda_{\max,\mathrm{Dir(Diff)}}}{dh}\right| c_{1(2)}\left(h,n\right)$ are inserted instead of multipliers $\left|\dfrac{d\lambda}{d\lambda_{\max,\mathrm{Dir(Diff)}}}\right| c_{1(2)}\left(\lambda_{\max,\mathrm{Dir(Diff)}}\right)$.

The relation (9) is simply applied to the other multipliers.

The derivatives $\left|\dfrac{d\lambda_{\max,\mathrm{Dir(Diff)}}}{dh}\right|$ are written as

$$\left|\frac{d\lambda_{\max,\mathrm{Dir(Diff)}}}{dh}\right| =$$

$$C_3\left|\frac{d\left[T_{\mathrm{Dir(Diff)}}\left(h\right)\right]}{dh} \cdot \frac{1}{\left[T_{\mathrm{Dir(Diff)}}\left(h\right) + T\left(n\right)\right]^2}\right|. \quad (11)$$

After applying (10) and (11) to the relation (9), it describes just the dependence of its form on the values h and n per unit:

$$e_{\mathrm{Dir(Diff)},\mathrm{SW(LW)}}\left\{C_3\left[T_{\mathrm{Dir(Diff)}}\left(h\right) + T\left(n\right)\right]^{-1}\right\}\Big|_{\mathrm{rel}} =$$

$$= \left(\frac{r}{R}\right)^2 \tau_{\mathrm{Dir(Diff)}}\left(h,n\right)C_1 C_3^{-5}\left[T_{\mathrm{Dir(Diff)}}\left(h\right) + T\left(n\right)\right]^5 \times$$

$$\times \left(\exp\frac{C_2}{\left\{C_3\left[T_{\mathrm{Dir(Diff)}}\left(h\right) + T\left(n\right)\right]^{-1}\right\}} - 1\right)^{-1} \times$$

$$\times C_3\left|\frac{d\left[T_{\mathrm{Dir(Diff)}}\left(h\right)\right]}{dh} \cdot \frac{1}{\left[T_{\mathrm{Dir(Diff)}}\left(h\right) + T\left(n\right)\right]^2}\right| c_{1(2)}\left(h,n\right). \quad (12)$$

Simplification of (12) transforms it into

$$e_{\mathrm{Dir(Diff)},\mathrm{SW(LW)}}\left(h,n\right)\Big|_{\mathrm{rel}} =$$

$$= e_{\mathrm{Dir\,eS}}\left(h,n\right)\left|\frac{dT_{\mathrm{Dir(Diff)}}\left(h,n\right)}{dh}\right| c_1\left(h,n\right)\Big|_{\mathrm{rel}} =$$

$$= \left(\frac{r}{R}\right)^2 \tau_{\mathrm{Dir(Diff)}}\left(h,n\right)C_1 C_3^{-5} \times$$

$$\times \left[T_{\mathrm{Dir(Diff)}}\left(h\right) + T\left(n\right)\right]^5 \left(\exp\frac{C_2}{C_3} - 1\right)^{-1} \times$$

$$\times C_3\left|\frac{d\left[T_{\mathrm{Dir(Diff)}}\left(h\right)\right]}{dh} \cdot \frac{1}{\left[T_{\mathrm{Dir(Diff)}}\left(h\right) + T\left(n\right)\right]^2}\right| c_{1(2)}\left(h,n\right). \quad (13)$$

For illustrative purposes, the products $C_3 C_3^{-5}$, $\left[T_{\mathrm{Dir(Diff)}}\left(h,n\right)\right]^5$ and $\dfrac{1}{\left[T_{\mathrm{Dir(Diff)}}\left(h,n\right)\right]^2}$ in (12) and (13) are not simplified.

The curve (13) is nearly bell-shaped, with its maximums at different combinations of the direct and diffused components of SR and *SW* and *LW* spectral channels, i.e. at $h_{\max,\,\mathrm{Dir(Diff)},\,\mathrm{SW\,(LW)}}$.

Introduction of the product $c_{1(2)}(\lambda)$ from (9) in (13) as an additional multiplier allows us to obtain the dependences of SI (per unit) on two variables (h and λ) in the form of a three-dimensional control
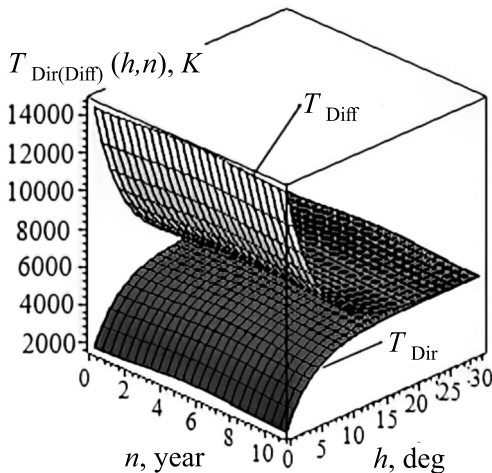

Fig. 2. The graphs of the functions $T_{\mathrm{Dir}}(h, n))$ and $T_{\mathrm{Diff}}(h, n)$ at a random design point of the Earth surface in the 11-year cycle of solar activity

121

signal $e_{SW(LW)}(\lambda,h,n)|_{\mathrm{rel}}$ at input of the *suprachiasmatic nucleus of hypothalamus* (SCN):

$$e_{\mathrm{Dir(Diff),SW(LW)}}\left(\lambda,h,n\right)\big|_{\mathrm{rel}} =$$

$$\left(\frac{r}{R}\right)^2 \tau_{\mathrm{Dir(Diff)}}\left(h,n\right) C_1 C_3^{-5}\left[T_{\mathrm{Dir(Diff)}}\left(h\right)+T\left(n\right)\right]^5 \times$$

$$\times\left(\exp\frac{C_2}{C_3}-1\right)^{-1}\left|-\frac{dT_{\mathrm{Dir(Diff)}}\left(h,n\right)}{dh}\right| \times$$

$$\times\, c_{1(2)}\left(h,n\right)c_{1(2)}\left(\lambda\right). \tag{14}$$

Like that of the function (13), the graph of (14) per unit is also bell-shaped.

Dependences of absolute effective values of (13) on current values of Solar altitude angle with each possible combination of the direct and diffused components of SR with the functions $c_{1(2)}(h, n)$ are defined using the calculated values of $h = h_{\mathrm{max,\,Dir(Diff),\,SW\,(LW)}}$ corresponding to the maximum values of (13). Then the relation (13) is normalised by dividing its left and right sides by the values of (13) calculated at $h = h_{\mathrm{max,\,Dir(Diff),\,SW\,(LW)}}$, i.e. the following functions are defined

$$e_{\mathrm{norm,Dir(Diff),SW(LW)}}\left(h,n\right) =$$

$$=\frac{e_{\mathrm{Dir(Diff),SW(LW)}}\left\{C_3\left[T_{\mathrm{Dir(Diff)}}\left(h\right)+T\left(n\right)\right]^{-1}\right\}\big|_{\mathrm{rel}}}{e_{\mathrm{Dir(Diff),SW(LW)}}\left\{C_3\left[T_{\mathrm{Dir(Diff)}}\left(h=h_{\mathrm{max,\,Dir(Diff),SW(LW)}}\right)+\right.\right.}.$$

$$\left.\left.+T\left(n\right)\right]^{-1}\right\}\big|_{\mathrm{rel}} \tag{15}$$

Using the relation (7), the dependences of the absolute values of SI

$$e_{\mathrm{eS,Dir(Diff),SW(LW)}} \times$$

$$\times\left[\lambda,T_{\mathrm{Dir(Diff)}}\left(n,h=h_{\mathrm{max,Dir(Diff),SW(LW)}}\right)\right]c_{1(2)}\left(\lambda\right)$$

on λ are defined for the calculated values of Solar altitude angle $h = h_{\mathrm{max,\,Dir(Diff),\,SW(LW)}}$ corresponding to the maximum values of (13).

The dependences of absolute values of SI at input of SCN (3D-represented) are obtained using the relation (7) by multiplying

$$e_{\mathrm{eS,Dir(Diff),SW(LW)}} \times$$

$$\times\left[\lambda,T_{\mathrm{Dir(Diff)}}\left(n,h=h_{\mathrm{max,Dir(Diff),SW(LW)}}\right)\right]c_{1(2)}\left(\lambda\right)$$

by the normalised functions (15).

Maximum absolute values of SI at output of SCN (depending just on the values of h) are obtained using (7) from the product

$$e_{\mathrm{Dir(Diff),SW(LW)}}\left(\lambda,h\right) = e_{\mathrm{norm,Dir(Diff),SW(LW)}}\left(h,n\right)\times$$

$$e_{\mathrm{eS,Dir(Diff),SW(LW)}} \times$$

$$\times\left[\lambda,T_{\mathrm{Dir(Diff)}}\left(n,h_{\mathrm{max,Dir(Diff),SW(LW)}}\right)\right]c_{1(2)}\left(\lambda\right)$$

by inserting the values of λ equal to 445 nm and 505 nm corresponding to the maximum values of the functions $c_1(\lambda)$ and $c_2(\lambda)$. The dependences $e_{\mathrm{,\,Dir(Diff),\,SW(LW)}}(h, n)$ at SCN output obtained after the said substitution are the signals directly controlling daily activity of epiphysis, which releases melatonin to blood plasma. Daily variations of melatonin concentrations in blood plasma ultimately lead to daily control of human nonconscious biological reactions including CA. CA directly affects different characteristics of visual perception, which form the basis of static and dynamic building of the mental world model and uses this basis for control of human higher intellectual activity including concrete and abstract thinking.

The developed method and the product of the relations (7) and the normalised functions (15) allows us to obtain the dependences of irradiance within the circadian region of spectrum on Solar altitude angle ($E(h)$) which are important for experimental and theoretical studies of CA, as well as the values of radiant exposure H within the range $\Delta h = h_{\mathrm{fin}} - h_{\mathrm{init}}$ of modification of the function $E(h)$, where h_{fin} and h_{init} are the initial and final values of Solar altitude angle respectively.

Irradiance $E(h)$ is written as

$$E\left(h\right) = e_{\mathrm{norm,Dir(Diff),SW(LW)}}\left(h,n\right)\times$$

$$\times\int\limits_{\lambda_{\mathrm{init}}}^{\lambda_{\mathrm{fin}}} e_{\mathrm{eS,Dir(Diff),SW(LW)}}\left[\lambda,T_{\mathrm{Dir(Diff)}}\left(h_{\mathrm{max,Dir(Diff),SW(LW)}},n\right)\right]\times$$

$$\times\, c_{1(2)}\left(\lambda\right)d\lambda, \tag{16}$$

and radiant exposure is written as

$$H\left(\Delta h\right) = \int\limits_{\lambda_{\mathrm{init}}}^{\lambda_{\mathrm{fin}}}\int\limits_{0°}^{90°} e_{\mathrm{eS,Dir(Diff),SW(LW)}}$$

$$\left[\lambda,T_{\mathrm{Dir(Diff)}}\left(h_{\mathrm{max,Dir(Diff),SW(LW)}},n\right)\right]$$

$$c_{1(2)}\left(\lambda\right)e_{\mathrm{norm,Dir(Diff),SW(LW)}}\left(h,n\right)d\lambda dh. \tag{17}$$

In (16) and (17), λ_{init} and λ_{fin} are the values of λ limiting the considered spectral region defined by the functions $c_1(\lambda)$, $c_2(\lambda)$, $c_1(\lambda) + c_2(\lambda)$, 0° and 90° are the limits of the possible range of Solar altitude angle.

The example below contains the results of calculations using the developed method which describe processing of the direct and diffused components of SR in the *SW* spectral channel of the CA control path and define effective modes of the effect of radiation with maximum solar activity ($n = 5.5$), for instance, in conditions of clear sky.

In the conditions under consideration, the function $T_{h_{max}, Dir(Diff), SW(LW)}(h, n)$ (2) with (3) taken into account in the expression of spectral irradiance of the direct and diffused components (4) is written as

$$T_{Dir(Diff)}(h, n) \approx a_{Dir(Diff)} \exp\left(-b_{Dir(Diff)} h\right) + T(n). \quad (18)$$

In (18), $a_{Dir} = -3780$, $b_{Dir} = 0.2444$, $a_{Diff} = 8950$, $b_{Diff} = 0.2084$, $T(n = 5.5) = 5780$.

The graphs of the dependence (18) are shown in Fig. 2.

In (5), the values of the coefficients are as follows: $\tau_{Dir}(90°) = 0.73$, $d_{Dir} = 0.0348$, $g_{Dir} = 1.55$, $\tau_{Diff}(90°) = 0.13$, $d_{Diff} = 0.029$, $g_{Diff} = 1.04$, and the values of the coefficients in (6), for instance, with data from [13] are as follows: $\alpha_1 = 72.56 \times 10^{-9}$ m, $\sigma_1 = 28.99 \times 10^{-9}$ m, $\lambda_{1, max} = 445 \cdot 10^{-9}$ m, $\alpha_2 = 25.89 \times 10^{-9}$ m, $\sigma_2 = 21.21 \cdot 10^{-9}$ m, $\lambda_{2, max} = 505 \times 10^{-9}$ m.

In accordance with the Wien's displacement law, the expressions for $\lambda_{max, Dir}$ and $\lambda_{max, Diff}$ (10), with the expression (4) taken into account, are written as

$$\lambda_{max, Dir} = C_3 \left[-3780 \exp(-0,2444h) + 5780\right]^{-1}, \quad (19)$$

$$\lambda_{max, Diff} = C_3 \left[8950 \exp(-0,2084h) + 5780\right]^{-1}. \quad (20)$$

The derivatives in (9) are as follows:

$$\left|\frac{d\lambda_{max, Dir}}{dh}\right| = \frac{2,6773 \exp(-0,2444h)}{\left[-3780 \exp(-0,2444h) + 5780\right]^2}, \quad (21)$$

$$\left|\frac{d\lambda_{max, Diff}}{dh}\right| = \frac{5.4053 \exp(-0,2084h)}{\left[8950 \exp(-0,2084h) + 5780\right]^2}. \quad (22)$$

After inserting the expression (6) with its coefficients α_1, σ_1, $\lambda_{1, max}$, α_2, σ_2, $\lambda_{2, max}$ and the expressions (19)–(22) into the relation (13) (for maximum

values of the direct component of SR in the *SW* spectral channel), the expression $e(h, n)|_{rel}$ at input of SCN in expanded form is written as

$$e_{Dir, SW}(h, n)|_{rel} =$$

$$= \left(\frac{r}{R}\right)^2 0,73 \cdot 0,5\left[1 + \sin(0,0348h - 1,55)\right] \times$$

$$\times C_1 \left\{\frac{C_3}{\left[-3780 \exp(-0,2444h) + 5780\right]}\right\}^{-5}$$

$$\left[\exp\frac{C_2}{C_3} - 1\right]^{-1} \times$$

$$\times \frac{2,6773 \exp(-0,2444h)}{\left[-3780 \exp(-0,2444h) + 5780\right]^2} \frac{\alpha_1}{\sigma_1 \sqrt{2\pi}} \times$$

$$\times \exp\left[-\frac{\left(\dfrac{C_3}{\left[-3780 \exp(-0,2444h) + 5780\right]} - 445 \cdot 10^{-9}\right)^2}{2\sigma_1^2}\right]. \quad (23)$$

The similar expression for the diffused component of SR in the *SW* spectral channel is written as

$$e_{Diff, SW}(h, n) =$$

$$= \left(\frac{r}{R}\right)^2 0,13 \cdot 0,5\left[1 + \sin(0,029h - 1,04)\right] \times$$

$$\times C_1 \left\{\frac{C_3}{\left[8950 \exp(-0,2084h) + 5780\right]}\right\}^{-5} \times$$

$$\times \left[\exp\frac{C_2}{C_3} - 1\right]^{-1} \times$$

$$\times \frac{5,4053 \cdot \exp(-0,2084h)}{\left[8950 \cdot \exp(-0,2084h) + 5780\right]^2} \times$$

$$\times \left(\frac{\alpha_1}{\sigma_1 \sqrt{2\pi}}\right) \times$$

$$\times \exp\left[-\frac{\left(\dfrac{C_3}{\left[8950 \exp(-0,2084h) + 5780\right]} - 445 \cdot 10^{-9}\right)^2}{2\sigma_1^2}\right].$$

The dependence of SI on $\lambda_{max, Dir(Diff)}$ and h at input of SCN is written in the form

$$e_{\text{Dir(Diff)}}\left(\lambda_{\text{max,Dir(Diff)}}, h, n\right)\big|_{\text{rel}} =$$

$$= \left(\frac{r}{R}\right)^2 \tau_{\text{Dir(Diff)}}(h,n) C_1 \lambda_{\text{max,Dir(Diff)}}^{-5} \times$$

$$\times \left(\exp\frac{C_2}{\lambda_{\text{max,Dir(Diff)}} T_{\text{Dir(Diff)}}(h,n)} - 1\right)^{-1} \times$$

$$\times c_{1(2)}\left(\lambda_{\text{max,Dir(Diff)}}\right)\left|\frac{d\lambda_{\text{max,Dir(Diff)}}}{dh}\right| c_{1(2)}(h,n).$$

Solar altitude angle corresponding to the maximum value $e_{\text{Dir, SW}}(h)$, h_{max} calculated from the expression (23) equals to 16.14° and the corresponding maximum value of the function $e_{\text{Dir, SW}}(h)\big|_{\text{rel}}$ equals to 0.01533.

Integration of the function $e_{\text{eS, Dir, SW}}(\lambda, h)$ from the expression (7) over λ at $h_{\text{max}} = 16.14°$ gives the maximum value of irradiance:

$$E_{\text{Dir,SW}}\left(h_{\text{max}} = 16{,}14°\right) =$$

$$\int_{350 \cdot 10^{-9}}^{570 \cdot 10^{-9}} e_{\text{Dir,SW}}(\lambda)\big|_{h_{\text{max}}=16,14°} \, d\lambda = 6{,}915 \text{ W·m}^{-2}. \quad (24)$$

After multiplying the calculated value of the integral (24) by the normalised function $e_{\text{norm,Dir,SW}}(h,n)$ derived from $e_{\text{norm,Dir(Diff),SW(DW)}}(h,n)$ by means of the expression (15), the expression for the irradiance dependence $E_{\text{Dir, SW}}(h)$ formed by the direct component of SR in the *SW* spectral channel is written as

$$E_{\text{Dir,SW}}(h) = \frac{6{,}9145}{0{,}01533} e_{\text{Dir eS}}(h)\left|\frac{d\lambda_{\text{max,Dir}}}{dh}\right| c_1(h) =$$

$$= 4{,}5115 \cdot 10^2 \left(\frac{r}{R}\right)^2 \times$$

$$\times C_1 \left\{\frac{C_3}{\left[-3780\exp(-0{,}2444h)+5780\right]}\right\}^{-5} \times$$

$$\times \left[\exp\frac{C_2}{C_3} - 1\right]^{-1} \cdot 0{,}73 \times$$

$$\times 0{,}5\left[1+\sin(0{,}0348h-1{,}55)\right] \times$$

$$\times \frac{2{,}6773\exp(-0{,}2444h)}{\left[-3780\exp(-0{,}2444h)+5780\right]^2} \times$$
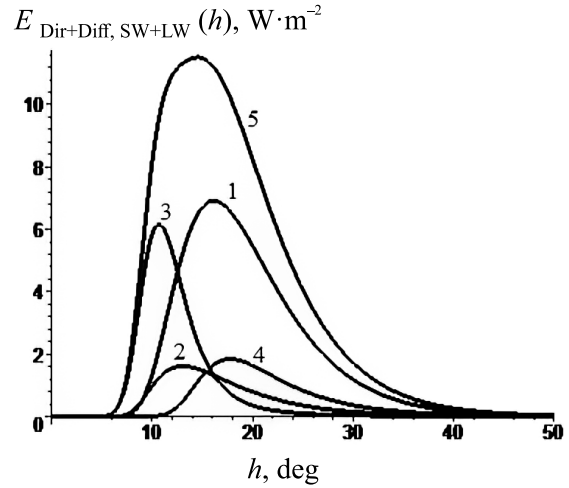
Fig. 3. The dependences of effective irradiance on Solar altitude angle under combined effect of direct and diffused components of SR simultaneously on the *SW* and *LW* spectral channels: *1* – irradiance under effect of the direct component of SR on the *SW* spectral channel, *2* – irradiance under effect of the direct component of SR on the *LW* spectral channel, *3* – irradiance under effect of the diffused component of SR on the *SW* spectral channel, *4* – irradiance under effect of the diffused component of SR on the *LW* spectral channel, *5* – irradiance corresponding to the sum of the direct and diffused components of SR simultenaously affecting the *SW* and *LW* spectral channels

$$\times \left(\frac{\alpha_1}{\sigma_1\sqrt{2\pi}}\right) \times$$

$$\times \exp\left[-\frac{\left(\frac{C_3}{\left[-3780\exp(-0{,}244h)+5780\right]} - 445\cdot10^{-9}\right)^2}{2\sigma_1^2}\right]. \quad (25)$$

The graph of the dependence of absolute values of effective irradiance on Solar altitude angle as per the expression (25) is shown in Fig. 3.

The absolute value of effective radiant exposure $H_{\text{Dir, SW}}(\Delta h)$ within the interval of Solar altitude angle which corresponds to the effect of the direct irradiance component $E_{\text{Dir, SW}}(h)$ on the *SW* spectral channel of the CA control path is calculated as

$$H_{\text{Dir,SW}}(\Delta h) = \int_{0°}^{90°} E_{\text{Dir,SW}}(h) \, dh = 91{,}218 \text{ W·m}^{-2}\cdot\text{deg.}$$

With combined effect of the direct and diffused components of SR on the *SW* and *LW* spectral channels simultaneously, the dependence of absolute values of effective irradiance on Solar altitude angle $E_{\text{Dir+Diff, SW+LW}}(h)$ is described by the sum

124

Table. Effective Modes of the Effect of Solar Radiation in the Circadian Region of Spectrum for Control of Human Body Circadian Activity

Energy characteristics → Types of effect ↓	h_{init}	h_{fin}	h_{max}	$E(h_{max})$, Wm^{-2}	H, Wm^{-2} deg
Direct SR in the *SW* spectral channel	7°	43°	16.14°	6.915	91.218
Direct SR in the *LW* spectral channel	6°	43°	13.04°	1.618	18.768
Diffused SR in the *SW* spectral channel	4.5°	34°	10.69°	6.164	38.100
Diffused SR in the *LW* spectral channel	10°	43°	17.78°	1.848	21.731
Direct and diffused SR in the *SW* spectral channel	4.5°	43°	12.56°	9.262	129.341
Direct and diffused SR in the *LW* spectral channel	6°	43°	16.75°	2.987	40.499
Direct SR in the *SW* and *LW* spectral channels	7°	43°	15.62°	8.263	109.987
Diffused SR in the *SW* and *LW* spectral channels	4.5°	43°	10.69°	6.164	59.858
Direct and diffused SR in the *SW* and *LW* spectral channels	4.5°	43°	14.10°	11.492	169.845

$$E_{Dir+Diff,SW+LW}(h) = E_{Dir,SW}(h) + E_{Dir,LW}(h) +$$

$$E_{Diff,SW}(h) + E_{Diff,LW}(h) =$$

$$= \frac{6{,}9145}{0{,}01533} e_{Dir\,eS}(h) \left| \frac{d\lambda_{max,Dir}}{dh} \right| c_1(h) +$$

$$+ \frac{1{,}6179}{0{,}09506} e_{Dir\,eS}(h) \left| \frac{d\lambda_{max,Dir}}{dh} \right| c_2(h) +$$

$$+ \frac{6{,}1639}{0{,}9512} e_{Diff\,eS}(h) \left| \frac{d\lambda_{max,Diff}}{dh} \right| c_1(h) +$$

$$+ \frac{1{,}8434}{0{,}07545} e_{Diff\,eS}(h) \left| \frac{d\lambda_{max,Diff}}{dh} \right| c_1(h), \quad (26)$$

the members of which are defined (similar to the expression (25)) using the developed method.

The graphs of the members of (26) $E_{Dir,\,SW}(h)$, $E_{Dir,\,LW}(h)$, $E_{Diff,\,SW}(h)$, $E_{Diff,\,LW}(h)$ and of their sum are shown in Fig. 3.

The absolute value of effective radiant exposure $H_{Dir+Diff,\,SW+LW}(\Delta h)$ within the interval of Solar altitude angle $0° \le h \le 43°$ which corresponds to simultaneous effect of the direct and diffused components of effective irradiance on the *SW* and *LW* spectral channels is expressed as

$$H_{Dir+Diff,SW+LW} = H_{Dir,SW} + H_{Dir,LW} + H_{Diff,SW} +$$

$$+ H_{Diff,LW} = 169{,}845 \text{ W} \cdot \text{m}^{-2} \cdot \text{deg.} \quad .$$

The Table summarises the values of energy characteristics of CA control signals with different combinations of effects of the direct and diffused components of SR on *SW* and *LW* spectral channels.

The last line of the table contains the values of irradiance and radiant exposure in the case of normal human health condition (without fatal failure of one of the CA control path spectral channels).

The fifth line of the table corresponds to fatal failure of the *LW* spectral channel and the sixth line of the table corresponds to fatal failure of the *SW* spectral channel.

It is worth noting that, according to the available experimental data, CA is controlled exceptionally under direct effect of SR on human body, i.e. within the period between sunrise and sunset. The data in the table completely complies with such provision: CA control commences (in the morning) and finishes (in the evening) at Solar altitude angle $h = 4.5°$.

It is also important that the daily value of superior culmination of the Sun h_{fin} approximately equal to 43° corresponds to non-availability of circadian deregulations in real cases of SR effect (lines 7–9 of the Table) and to cases of fatal failure of one of spectral channels (lines 5 and 6 of the Table), Fig. 3. At the same time it is seen from Fig. 3 and the Table that CA control ends at $h_{fin} \ge 43°$. Processing of the results of independent experimental studies has shown that the value $h_{fin} = 43.13°$ corresponds to complete non-availability of human circadian deregulations at arbitrary values of latitude and the day of a year [17]. Further increase of Solar altitude angle, e.g. with decrease of latitude on a random day of a year, does not lead to changes in CA [17].

Correspondence between the values of h_{fin} defined using the proposed method and obtained after processing of the results of independent experimental studies confirms practicability of this method.

Adequacy of the results of calculations obtained using the latter confirms that it may be used in theoretical and experimental studies of CA considering the effect of optical radiation on human body.

CONCLUSION

The values of effective irradiance and radiant exposure shown in Fig. 3 and the Table may be used in the course of experimental studies of nonconscious daily reactions of human body to levels of affecting irradiance and radiant exposure with different combinations of the direct and diffused components of optical radiation on the *SW* and *LW* spectral channels of the CA control path. Application of the proposed method allows us to define the values of irradiance and radiant exposure controlling human CA also at different cloudiness [9]. In particular, the results of this work may form a basis for research of circadian deregulations caused by trans-meridian flights and shift working in facilities with continuous production cycle. Moreover, the information obtained in the course of the work may be used for development of special emitting installations for prevention of circadian deregulations, correction of CA if they are available and for maintenance of proper human CA in conditions of daily CA deficiency, which is especially important for enhancement of protection of national security in sub-polar and polar regions and development of their economic use.

REFERENCES

1. Gagliardi, R.M., Karp, Sh. Optical Communications: trans. from Eng. / Eds. A.G. Sheremetyev. Moscow: Svyaz, 1978, 424 p.

2. Meshkov, V.V. Basics of Light Engineering: Study Guide for Higher Education Institutions. P. 1 [Osnovy svetotekhniki: ucheb. posobie dlya vuzov. Ch. 1]. 2nd edition, revised. Moscow: Energiya, 1979, 368 p.

3. Leonidov A.V. Changes in irradiance and illuminance on Earth surface during 11 – year solar activity cicle // Light & Engineering, 2020, Vol. 28, # 2, pp. 61–66.

4. Allen, C.W. Astrophysical Quantities (Handbook) [Astrofizicheckiye velichiny (Spravochnik)]. Trans. from Eng. Moscow: Mir, 1977, 279 p. (Allen C.W. Astrophysical quantities. – London: The Athlone Press, 1973, 279 p.)

5. Martynov, D. Ya. Practical Astrophysics Course [Kurs prakticheskoy astrofiziki]. – Moscow: Nauka, 1977.

6. Schwabe H. Sonnenbeobachtungen im Jahre 1843 // Astronomische Nachrichten, 1844, Vol. 21, p. 233.

7. Schwarzer, K. Lighting with Adjustable Colour – Study and Optimisation of Colour Lighting Control Systems / Summary Report, 2006. URL: http://www.bocom.eu/rus/catalog/downloads/Farblichtstadie.rus.pdf (date of reference: 07/30/2019).

8. Kononovich, E.V., Moroz, V.I. General Astronomy: Study Guide [Obshchiy kurs astronomii: uchebnoну posobie] / Eds. V.V. Ivanov. 2nd edition, revised. Moscow: Editorial URSS, 2004, 544 p.

9. Leonidov A.V. Calculation of the Natural Illumination of the Earth's Surface at Different States of Cloud Cover // Izvestiya – Atmospheric and Oceanic Physics. 2019, Vol. 55, # 11, pp. 1592–1601.

10. Leonidov A.V. On optical receivers in pathway implicated in control of human circadian rhythm Biophysics, 2016, Vol. 61, # 6, pp. 1002–1010.

11. Brainard G.C., Glickman G.L. The biological potency of light in humans: significance to health and behavior / CIE152: 2003.

12. Brainard, G.K., Glickman, G.L. Biological Effect of Light on Human Health and Behaviour [Biologicheskoye vliyaniye sveta na zdorovye i povedeniye cheloveka] // Svetotekhnika, 2004, Vol. 1, pp. 4–8.

13. Thapan K., Arendt J., Skene D.J. An action spectrum for melatonin suppression: evidence for a novel non – rod, non – cone photoreceptor system in humans // J. Physiol. 2001, Vol. 535, pp. 261–267.

14. Brainard G.C., Provencio I. Photoreception for the neurobehavioral effects of light in humans / CIE031:2006 "Proc. 2nd CIE Expert Symposium on "Lighting and Health", pp. 6–21.

15. Wentzel, E.S. Probability Theory [Teoriya veroyatnostey]. 2nd edition, revised and supplemented. Moscow: Fizmatgiz, 1962, 564 p.

16. Levin, B.R. Theoretical Basics of Statistical Radio Engineering [Teoreticheskiye osnovy statisticheskoy radiotekhniki]. Book one, Moscow: Sovetskoye radio, 1966, 728 p.

17. Leonidov, A.V. On conditions of occurrence of seasonal disorders in human circannual and circadian rhythm // Biophysics, 2014, Vol. 59, #1, pp. 157–161.

Alexander V. Leonidov,
Ph.D. in Technical Science, graduated from MPEI in 1970 by speciality light and engineering and sources of light. Currently, he is a retired freelance researcher

ANALYSIS OF FAILURE DETECTION AND VISIBILITY CRITERIA IN PANTOGRAPH-CATENARY INTERACTION

Sakir Parlakyıldız[1,1], Muhsin Tunay Gencoglu[2,2], and Mehmet Sait Cengiz[1,3]

[1]*Department of Technical Vocational School, Bitlis Eren University, Turkey*
[2]*Department of Electrical Electronics Engineering, Fırat University, Turkey*
E-mails: [1]sparlakyildiz@beu.edu.tr, [2]mtgencoglu@firat.edu.tr, [3]msaitcengiz@gmail.com

ABSTRACTS

The main purpose of new studies investigating pantograph catenary interaction in electric rail systems is to detect malfunctions. In the pantograph catenary interaction studies, cameras with non-contact error detection methods are used extensively in the literature. However, none of these studies analyse lighting conditions that improve visual function for cameras. The main subject of this study is to increase the visibility of cameras used in railway systems. In this context, adequate illuminance of the test environment is one of the most important parameters that affect the failure detection success. With optimal lighting, the rate of fault detection increases. For this purpose, a camera, and a LED luminaire 18 W was placed on a wagon, one of the electric rail system elements. This study considered CIE140–2019 (2nd edition) standards. Thanks to the lighting made, it is easier for cameras to detect faults in the electric trains on the move. As a result, in scientific studies, especially in rail systems, the lighting of mobile test environments, such as pantograph-catenary, should be optimal. In environments where visibility conditions improve, the rate of fault detection increases.

Keywords: rail system lighting, pantograph-catenary interaction, fault detection visibility, luminance, illuminance

1. INTRODUCTION

As in all areas, the biggest need for transportation is energy. Energy consumption is increasing day by day due to the needs of modern life, the increasing competition environment, and cultural and social developments. The area where electric energy is used in transportation systems is electric rail systems. Demand for railway transportation is increasing. The energy required to move the train comes from the power line. For the rail system vehicle to be continuously energized, there must be constant contact between the power line and the pantograph. Even a short-term non-contact between the pantograph and the catenary negatively affects the rail system vehicle and the electronic systems inside it. Therefore, the interaction between the pantograph and the catenary should be tested dynamically and statically at certain intervals. In order to detect malfunctions in the dynamic interaction of pantograph-catenary on the travel wire, the force applied by the pantograph mounted on the rail system vehicles and providing the necessary energy to the train set is measured. If this force is applied more than desired, it causes breaks due to the force of the electric line. If the applied force is small, the electric train causes arcing and mechanical damage to the pantograph while driving. Accelerometer sensor, load cell sensor and encoder or GPS system are required to perform these tests [1–6]. In this study, the lighting conditions of a recording system with a LED lamp and a camera mounted on a wagon using in an electric rail system were analysed.
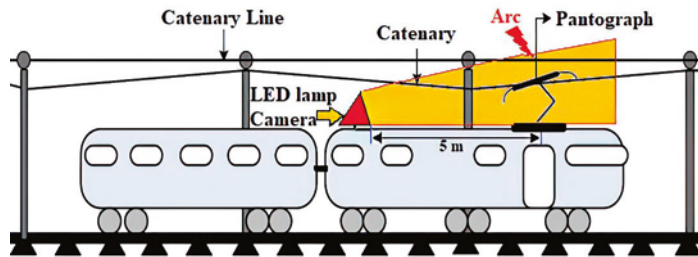
Fig. 1. System that records and illuminates the pantograph catenary image [1–4]

2. LIGHTING AREA

Electric rail systems have been used in transport for many years. The most important element in electric rail systems is the pantograph and the catenary. Compatibility between the pantograph and the catenary is one of the most important issues in these systems. The pantograph is a movable and catenary fixed element. These two elements are in contact with each other, and movement is provided in electric rail systems. Therefore, the pantograph-catenary interaction that moves and contacts each other increases the number of failures [1–6].

Current in the pantograph is the primary source of failure in electric rail systems. The pantograph is located on the roof of the train and collects current from the upper catenary line. The catenary line is fixed to poles with support points at regular intervals along the railway line [7–9]. When the train is moving, the pantograph moves along the catenary line to support energy continuity. When the speed in the electric rail systems increases, vibrations occur in the catenary line. This disrupts the interaction between the pantograph and the catenary. These vibrations negatively affect the contact between the pantograph and the catenary. Since the contact between the pantograph and the catenary is interrupted by electrical contact, wear and arc occur. In electric rail systems, elements other than pantograph-catenary are advantageous in terms of maintenance factor [7, 8]. So, they usually do not cause malfunctions. Therefore, care factor multipliers are high. The source of the malfunction is the pantograph catenary interaction elements. For this purpose, many studies are conducted in scientific studies that study the pantograph catenary interaction. However, the lighting conditions are not taken into consideration in recordings made with the camera in fault detection studies. Therefore, sufficient success is not achieved in fault detection. This study provides appropriate lighting for camera recording during a moving train. In this way, it has been un-

derstood that the camera can record (for the lighting class $M2$, 50 km/h < speed < 90 km/h) more accurately when the illuminance levels and luminance are selected appropriately [9, 10]. Fig. 1 shows the system that records and illuminates the pantograph catenary image.

2.1. Methods

In electric rail transport systems, arc and abrasions occur due to the horizontal movement-balance of the pantograph and the contact force applied by the pantograph to the catenary. If the interaction between the pantograph and the catenary is inappropriate, the contact is cut. Therefore, the train is de-energized. The vibrations of the contact wire and external effects cause malfunctions in the rail systems. It is important that periodic monitoring, fault detection, and necessary maintenance can be predicted in railway systems. Monthly checks of railway systems focus on two important points. These are the monitoring of the rail profile and the catenary line. Accidents are determined in advance by examining factors that cause accidents, such as abrasion, breaking, bending, catenary line stretching, contact condition, compatibility of catenary line, and pantograph axis of rails. Image processing based contactless methods have been developed using cameras to diagnose these faults. Nowadays, contactless condition monitoring methods are more preferred. With the cameras used in these methods, the railway line is monitored without contact, and the image processing algorithms developed, and malfunctions in the railway line are detected. Such methods are efficient methods that work faster, reducing workload.

• Various mathematical methods have been analysed using cameras to detect components and faults in rail systems. These methods are support vector machine, Gabor filter, basic image processing methods, deep learning, binary pattern matching base, wavelet transform, template matching, Hough trans-
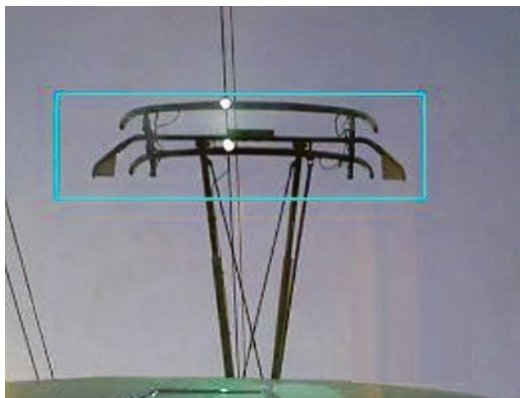
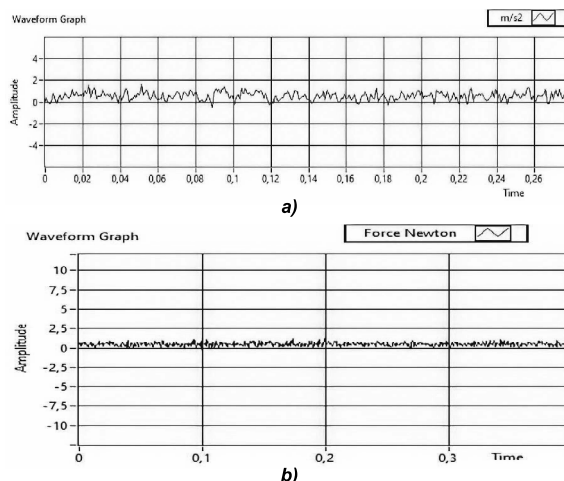Fig. 2. Pantograph-catenary arc failure in non-illuminated environment [1–5]

Fig. 3. When the electric train is stationary, signals from the accelerometer (*a*) and signals from the force sensor (*b*)

form, Sobel edge extraction, line segment detector, and batch algorithm conversion techniques [11–24].

• Images recorded with the camera were analysed by the black tree conversion technique to detect the rail faults with loose connections [25].

• To detect defects in the railway fasteners, analysis was done using machine vision methods using a camera [26–31].

• An analysis was conducted with basic image processing methods using camera for scissors detection malfunctions [32–34].

• HSV colour conversion, masking, edge extraction, and basic image processing methods were analysed using the camera for the detection of rail line tracking [35].

• Using the camera for surface detection; visual based methods, Haar-like method, Otsu method, machine vision method, adaptive background extraction, image segmentation, deep learning, deep convolutional neural network, gaussian filter, edge extraction methods, and object recognition techniques were analysed [36–47].

Although each study uses different methods, the common point of these studies is the use of camera images. However, none of these studies did not consider the vision conditions of the camera. In this case, troubleshooting has become difficult. Optimal lighting should be done to increase the rate of fault detection.

The most important problem here is that the camera cannot record clearly in any conditions. For the camera to record clear images in day or night conditions, the criteria specified in CIE road standards should in terms of illuminance level and luminance values. Because trains running on rail systems should be evaluated as road vehicles in motion. Any arc or malfunction between the pantograph and the

catenary during the movement of the electric train is recorded by the camera. For the camera to clearly detect this fault, parameters such as speed, surface type, reflection coefficient, luminous flux, distance, and maintenance factor must follow CIE-140 standards. So, a train in railway systems is like a vehicle on a highway [48, 49]. There are many studies in the literature that have been done using a fault detection camera. However, in no study was the visibility of test runs evaluated in terms of lighting. Arc and malfunctions caused by poor visual conditions are sometimes not detected by the camera. In other words, in experimental studies (if it is specific to each experiment), the most important parameters that affect visibility are optimal illuminance level and luminance values [50–52]. Fig. 2 shows the state of the pantograph-catenary arc failure in the non-illuminated environment.

2.2. Condition Monitoring and Fault Detection

Many contact and contactless methods have been developed for monitoring the components that make up the railway line. When reviewing current research in the literature, it is clear that non-contact methods are more profitable. Image processing-based methods are used to detect malfunctions in rail components and rail surfaces. Images are taken from the railway system via a camera. Status monitoring and diagnostics are performed on the acquired images using some image processing techniques. Experimental installations for the developing image processing-based methods are quite simple and do not require large costs. As a result of the
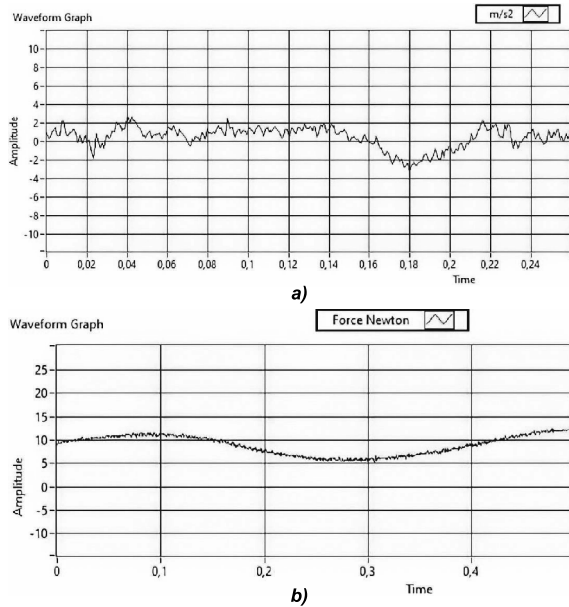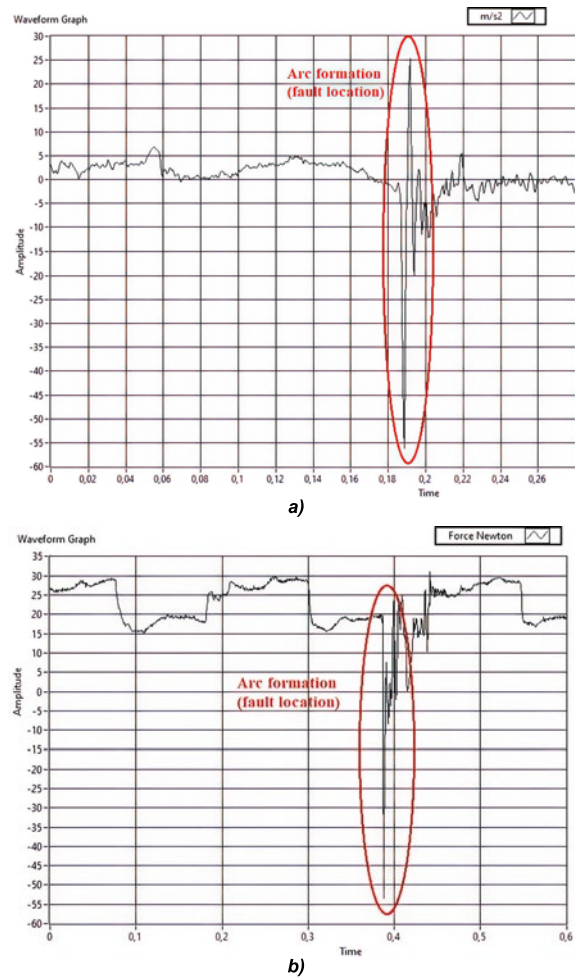
Fig. 4. Electric train in motion (*no fault*), signals from the accelerometer (*a*) and signals from the force sensor (*b*)

measurements conducted physically in the test environment, the signals received from the electric train are shown in Figs. 3–5.

In Fig. 3, when the electric train is stationary, signals from the accelerometer and signals from the force sensor are shown. In Fig. 4, the electric train is in motion (no malfunction), signals from the accelerometer and signals from the force sensor are shown. In Fig. 5, the electric train is in motion (at the time of failure), signals from the accelerometer and signals from the force sensor are shown.

The moment when the visual conditions are the most important for the camera is the breakdown moment in Fig. 5. During the malfunction, the sensors detect vibration because they measure physically. That is, sensors detect the malfunction, but if the vision conditions are not good, the camera cannot detect the malfunction. The accelerometer and force sensors detected this malfunction. Therefore, vision conditions need to be improved. If the camera recording the fault clearly detects it, the fault

Fig. 5. Electric train in motion (*at the time of failure*), signals from the accelerometer (*a*) and signals from the force sensor (*b*)

can be detected. If the lighting conditions are not suitable, some faults are not visible. However, the sensors that make physical measurements verify the fault information. Therefore, the lighting criteria cannot be neglected.

3. AREA LIGHTING DESIGN

Point lighting calculation method was used in area lighting calculation. In this method, the area
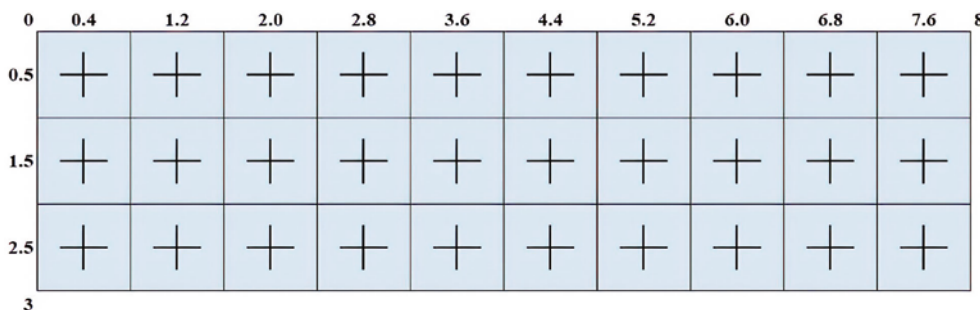
Fig. 6. Divided account areas of the surface to be illuminated

Table 1. The Area and Lighting Parameters

Number of lanes	1	Lighting class	*M*2
Strip width (m)	3	Console angle (degree)	0
Total width (m)	3	Luminaire angle (degree)	15
Road surface class	*R*1	Lamp type	LED
Q_o	0.10	Luminaire power (W)	18
Distance to illumination	0	Luminous flux (lm)	1825
Illumination height from ground (m)	5	Maintenance factor (once a year)	0.88

to be calculated for lighting is selected. According to the observer, who is positioned to stand in the middle of the area, point calculation has been made. Fig. 6 shows the entire illuminated field of the pantograph with the calculated areas of the illuminated surface separated. The LED luminaire mounted in the wagon illuminates the pantograph at a right angle. Calculations were made according to the total illuminance levels and total luminance values coming from all luminaires [7–10, 50–52].

3.1. Features of The Area Lighting

The road surface class is *R*1. Additionally, Q_o=0.10, and the distance of the luminaire is 5 m. The maintenance factor of the luminaire is 0.91, and all calculated luminance values are corrected. The ratio of the lowest luminance value to mean luminance value is greater than 0.4 in the calculations for area lighting, ensuring that the rate of the lowest luminance value to the highest at the latitude coordinate of the observer is greater than 0.7. The illuminance levels, luminance value, and uniformities of the area are in accordance with relevant standards. Luminaires were established in single from

Table 2. Optimal Parameters of The Illuminated Surface for The Camera

Observer location (m)	1.50
$L_{average}$	1.51
U_o	0.77
U_l	0.82
TI%	3.00
$E_{average}$	29.06
E_{min}	20.92
E_{max}	35.84
U_{oa}	0.72
U_{la}	0.58

to the axis of the area and at a distance of 5 m. This study simulation was performed accordingly with LED luminaires [48, 49, 53–55]. Table 1 shows the area and lighting parameters.

3.2. Simulation Study

The main purpose of the new studies is to reach the most economical results that provide adequate visibility conditions. In the new study on area (zonal) lighting, classifications are taken into consideration in the various scenarios' conditions. The most correct reference to area lighting is international standards. For this reason, simulation is adapted to CIE standards. According to CIE140, the luminance values, average luminance level, average and longitudinal uniformity values of all points were calculated for the observers.

Luminaries used in area lighting should be selected taking into account the glare level, the luminance level of the area, uniformity, and economy, and they should be determined in consequence of computer calculations according to the luminance method.

It is a simulation program written with *Visual Basic*. Various options are available for area parameters in the simulation program. For the lighting parameters are selected such characteristics as distance to the luminaire, height of the luminaire, distance of the luminaire from the road, console angle, IP protection class, pollution rate, cleaning period, and maintenance factor for the pole or suspended lighting installation. For the luminaire parameters (the name, angle of the luminaire (angle relative to the road), power of the lamp used, lifetime, luminous flux, ballast power, and new lamps) can be added into this simulation under the database process at any time. It is possible to add any type of lamp into the simulation [48, 49, 53–61]. The result of this simulation is a simple and correct calculation.

Table 3. The Illuminance Levels for The Camera

E_{min}=20.92 lx E_{max}=35.84 lx $E_{average}$=29.06 lx U_{oa}=0.72 U_{la}=0.58									
m/m	**0.35**	**1.05**	**1.75**	**2.45**	**3.15**	**3.85**	**4.55**	**5.25**	**5.95**	**6.65**
0.50	25.38	20.91	27.30	24.88	25.84	25.84	24.88	27.30	20.91	25.38
1.50	30.29	30.71	34.56	35.83	34.42	34.43	35.83	34.56	30.71	30.30
2.50	27.68	27065	28.54	32.03	29.74	29.74	32.03	28.54	27.66	27.69

Table 4. The Luminance Values for The Camera

Observer: $L_{average}$= 1.51 cd/m^2, U_o= 0.77, U_i= 0.82, TI= 3.0 %									
m/m	**0.35**	**1.05**	**1.75**	**2.45**	**3.15**	**3.85**	**4.55**	**5.25**	**5.95**	**6.65**
0.50	1.28	1.15	1.33	1.30	1.41	1.44	1.36	1,39	1.17	1.29
1.50	1.61	1.65	1.78	1.91	1.97	1.93	1.96	1,81	1.66	1.62
2.50	1.29	1.29	1.34	1.50	1.50	1.50	1.57	1,38	1.33	1.32

4. LIGHTING APPLICATION

In this study, a 1-lane area that is suitable for CIE140–2000 and 2019 (2nd edition) area lighting calculations has been investigated in the simulated environment. Calculations were made at an angle of 15° for 18 W LED luminaire. While $L_{average}$ =1.50 cd/m^2, this corresponds to CIE140–2000 and 2019 (2nd edition) road lighting calculations for M2. If $L_{average}$ =1.50 cd/m^2 is less, then the lighting is not suitable for CIE140–2000 and 2019 (2nd edition). To increase the camera vision, 18 W LED luminaire was used in the lighting. This LED light was able to meet the normalized parameters according to CIE140–2019. As for the illuminance level and luminance values, the 18 W LED luminaire increased visibility. The optimal parameters of the illuminated surface for the camera are shown in Table 2.

In this study, measurement and calculation were made using simulation at 30 points selected in horizontal and vertical positions. Table 3 shows the illuminance levels for the camera, and Table 4 shows the luminance values for the camera.

6. RESULTS

Proper design of the lighting installation is of great importance for both driving and safety. The main purpose of new studies investigating the pantograph catenary interaction in electric rail systems is the detection of malfunctions.

The main subject of this study is to increase the visibility of cameras used in railway systems. Supplying optimal lighting is to refine fault detection.

For this purpose, a camera and a LED luminaire 18 W were installed on a wagon, which is one of the electric railway system elements. This allows you to see more clearly the failures that occur during the movement of the electric train.

There is 5 m between the LED luminaire and the pantograph catenary contact point. The measurements were made while the wagon was moving. For lighting criteria, it was treated as a road vehicle moving under normal road conditions. The simulation used was adapted to CIE140–2019 (2nd edition) standards. According to CIE140, the luminance values, average illuminance level, average and longitudinal uniformity values of all points were calculated for the observers. The data of the luminaire used has been entered into the simulation database. The results were analysed for the good vision of the camera recording on the moving wagon.

Lighting conditions are very important in such experimental studies. Because the visual ability of the camera on the wagon affects the success of the applied mathematical methods. For example, in a mathematical method that detects 85 % malfunction, fault detection can be 99 % if the camera records more clearly. In this respect, the lighting of the test environment is one of the most parameters affecting the failure detection success. As in this study, special solutions should be analysed in simulated lighting environments.

ACKNOWLEDGEMENT

AG: Electrical Electronics Engineering Research Group).

REFERENCES:

1. Yaman O., Pantograf-Katener Sistemlerinde Görüntü İşleme Tabanli Temassız İzleme Yöntemlerinin Geliştirilmesi, Yüksek Lisans Tezi, Firat Üniversitesi, Fen Bilimleri Enstitüsü, 2014, p. 122.

2. Karaköse E., Rayli Sistemlerde Pantograf-Katener Sisteminin Modellenmesi, Simülasyonu ve Ariza Teşhis Yöntemlerinin Geliştirilmesi, Yüksek Lisans Tezi, Firat Üniversitesi, Fen Bilimleri Enstitüsü, 2014, p. 190.

3. Aydın I., Karaköse E., Karaköse M., Gençoğlu M.T., Akın E. A new computer vision approach for active pantograph control, 2013 International Conference on Innovations in Intelligent Systems and Applications, 2013, pp. 1–5.

4. Karakose E., Gençoğlu M.T., Karakose M., Yaman O., Aydin, I., Akin E. (2018) A new arc detection method based on fuzzy logic using S-transform for pantograph–catenary systems, Journal of Intelligent Manufacturing, 2018. V29, #4, pp. 839–856.

5. Parlakyıldız S., Gençoğlu M.T., Cengiz M.S. 2018. Development of Rail Systems from Past to Present. International Conference on Multidisciplinary, Science, Engineering and Technology (2018 Dubai, BAE)

6. Cengiz Ç., Yapıcı, İ., Cengiz M.S. 2018. Fourier Analysis in Rail Systems. International Conference on Multidisciplinary, Science, Engineering and Technology (2018 Dubai, BAE).

7. Cengiz M.S., The Relationship Between Maintenance Factor and Lighting Level in Tunnel Lighting, Light & Engineering, 2019. V27, #3, pp. 75–84.

8. Cengiz M.S., Cengiz, Ç., Numerical Analysis of Tunnel LED Lighting Maintenance Factor, IIUM Engineering Journal. 2018. V19, #2, pp. 154–163.

9. Efe S.B., Varhan D. Interior Lighting of A Historical Building By Using LED Illumınators: A Case Study Of Fatih Paşa Mosque, Light & Engineering, 2020. V28, #4, pp. 77–83.

10. Cengiz M.S., A Simulation and Design Study for Interior Zone Luminance in Tunnel Lighting, Light & Engineering, 2019. V27, #2, pp. 42–51.

11. Sabato, A. and Niezrecki, C. Feasibility of Digital Image Correlation for railroad tie inspection and ballast support assessment. Measurement, 2017. V103, pp. 93–105.

12. Manikandan, R., Balasubramanian, M. and Palanivel, S. Machine Vision Based Missing Fastener Detection In Rail Track Images Using Svm Classifier. International Journal on Smart Sensing and Intelligent Systems, 2017. V10, #4, pp. 574–589.

13. Biswas R., Khan R.A., Islam S. and Uddin J. A Novel Approach to Detect and Classify the Defective of Missing Rail Anchors in Real-time. International Journal of Emerging Technology and Advanced Engineering, 2016. V6, #12, pp. 270–276.

14. Liu J., Li B., Xiong Y., He B., and Li L., 2015. Integrating the symmetry image and improved sparse representation for railway fastener classification and defect recognition. Mathematical Problems in Engineering, 2015.

15. Gibert X., Patel V.M. and Chellappa R. Robust fastener detection for autonomous visual railway track inspection. IEEE Winter Conference on Applications of Computer Vision (WACV), 2015. pp. 694–701.

16. Gibert X., Patel V.M., and Chellappa R. Deep multitask learning for railway track inspection. IEEE Transactions on Intelligent Transportation Systems, 2017. V18, #1, pp. 153–164.

17. Fan H., Cosman P.C., Hou Y. and Li B. High-Speed Railway Fastener Detection Based on a Line Local Binary Pattern. IEEE Signal Processing Letters, 2018. V25, #6, pp. 788–792.

18. Yuan X., Liu B. and Chen H. Algorithm and program design for fastener locating and detection using wavelet transformation and template matching. IEEE17th International Conference on Communication Technology (ICCT), 2017. pp. 1116–1121.

19. Liu J. and Li B. Railway fastener defects recognition algorithm based on computer vision. International Conference on Electronic Science and Automation Control (ESAC2015), 2015. pp. 285–288.

20. Trinh H., Haas N., Ying Li., Otto C., Pankanti S. Enhanced rail component detection and consolidation for rail track inspection, IEEE Workshop on Applications of Computer Vision (WACV), 2012. pp. 289–295.

21. Feng H., Jiang Z., Xie F., Yang P., Shi J., Chen L. Automatic fastener classification and defect detection in vision-based railway inspection systems. IEEE Transactions on Instrumentation and Measurement, 2014. V63, #4, pp. 877–888.

22. Babenko P. Visual inspection of railroad tracks, Doctoral dissertation, University of Central Florida Orlando, Florida, 2009.

23. Ying L., Trinh T., Haas N., Otto C., Pankanti S. Rail Component Detection, Optimization, and Assessment for Automatic Rail Track Inspection, IEEE Transactions on Intelligent Transportation Systems, 2014. V15, pp. 760–770.

24. Sawadısavı S.V. Development of Machine-Vision Technology for Inspectıon of Railroad Track, Graduate

College of the University of Illinois at Urbana-Champaign, 2010.

25. Mao Q., Cui H., Hu Q. and Ren X. A rigorous fastener inspection approach for high-speed railway from structured light sensors. ISPRS Journal of Photogrammetry and Remote Sensing, 2017.

26. Aytekin Ç., Rezaeitabar Y., Dogru S. and Ulusoy I. Railway fastener inspection by real-time machine vision. IEEE Transactions on Systems, Man, and Cybernetics: Systems, 2015. V45, #7, pp. 1101–1107.

27. Santur Y., Karaköse M. and Akin, E. A new rail inspection method based on deep learning using laser cameras. International Artificial Intelligence and Data Processing Symposium (IDAP), 2017. pp. 1–6.

28. Santur Y., Karaköse M. and Akin E. Big data framework for rail inspection. International Artificial Intelligence and Data Processing Symposium (IDAP), 2017. pp. 1–4.

29. Wang C., Li Y., Ma Z., Zeng J., Jin T. and Liu H. Distortion Rectifying for Dynamically Measuring Rail Profile Based on Self-Calibration of Multiline Structured Light. IEEE Transactions on Instrumentation and Measurement, 2018.

30. Xiong Z., Li Q., Mao Q. and Zou Q.. A 3D laser profiling system for rail surface defect detection. Sensors, 2017. V17, #8, p. 1791.

31. Yunjie Z., Xiaorong G., Lin L., Yongdong P. and Chunrong Q. Simulation of Laser Ultrasonics for Detection of Surface-Connected Rail Defects. Journal of Nondestructive Evaluation, 2017. V36, #4, p. 70.

32. Wohlfeil J. Vision based rail track and switch recognition for self-localization of trains in a rail network. In Intelligent Vehicles Symposium (IV), 2011. pp. 1025–1030.

33. Johansson A., Pålsson B., Ekh M., Nielsen J.C., Ander M.K., Brouzoulis J. and Kassa E. Simulation of wheel–rail contact and damage in switches & crossings. Wear, 2011. V271, #1, pp. 472–481.

34. Palsson B. Optimisation of railway switches and crossings, Chalmers University of Technology, 2014.

35. Singh A. K., Swarup A., Agarwal A. and Singh D. Vision based rail track extraction and monitoring through drone imagery. ICT Express, 2017.

36. Li Q., Shi Z., Zhang H., Tan Y., Ren S., Dai P. and Li W. A cyberenabled visual inspection system for rail corrugation. Future Generation Computer Systems, 2018. V79, pp. 374–382.

37. Zhuang L., Wang L., Zhang Z. and Tsui K.L. Automated vision inspection of rail surface cracks: A double-layer data-driven framework. Transportation Research Part C: Emerging Technologies, 2018. V92, pp. 258–277.

38. Min Y., Xiao B., Dang J., Yue B. and Cheng T. Real time detection system for rail surface defects based on machine vision. EURASIP Journal on Image and Video Processing, 2018. V1, p. 3.

39. Biao Y. U. E. and MIN Y.Z. An Adaptive Background Adjusting Algorithm for Rail Surface Defect Image Segmentation. DEStech Transactions on Computer Science and Engineering, 2017.

40. Gan J., Li Q., Wang J. and Yu H. A Hierarchical Extractor-Based Visual Rail Surface Inspection System. IEEE Sensors Journal, 2017. V17, #23, pp. 7935–7944.

41. Shang L., Yang Q., Wang J., Li S. and Lei W. Detection of rail surface defects based on CNN image recognition and classification. 20th International Conference on Advanced Communication Technology (ICACT), 2018. pp. 45–51.

42. Faghih-Roohi S., Hajizadeh S., Núñez A., Babuska R. and De Schutter B. Deep convolutional neural networks for detection of rail surface defects. International Joint Conference Neural Networks (IJCNN), 2016. pp. 2584–2589.

43. Liu Z., Wang W., Zhang X. and Jia W. Inspection of rail surface defects based on image processing. International Asia Conference on Automation and Robotics Informatics in Control, 2nd, 2010. V1, pp. 472–475.

44. Dubey A., and Jaffery Z. Maximally Stable Extremal Region Marking (MSERM) based Railway Track Surface Defect Sensing, IEEE Sensors Journal, 2016.

45. Steenbergen M. and Dollevoet R. On the mechanism of squat formation on train rails–Part I: Origination, International Journal of Fatigue, 2013. V47, pp. 361–372.

46. Tastimur C., Yetis H., Karaköse M. and Akın E., Rail Defect Detection and Classification with Real Time Image Processing Technique. International Journal of Computer Science and Software Engineering (IJCSSE), V5,#12, pp. 283–290.

47. Zheng S. Chai X. An X., Li L. Railway Track Gauge Inspection Method Based on Computer Vision, International Conference on Mechatronics and Automation (ICMA), 2012. pp. 1292–1296.

48. CIE140:2000 – Road Lighting Calculations. CIE140, International Commission on Illumination, Road Lighting Calculations, Vienna-Austria, 33 (2000).

49. CIE140:2019 Road Lighting Calculations. CIE140, International Commission on Illumination, 2nd Edition ISBN:978–3–902842–56–5.

50. Cengiz Ç., Kaynaklı M., Gencer G., Eren M., Yapici İ., Yildirim S., Cengiz M.S., Selection Criteria and Economic Analysis of LEDs, Book of Abstracts, Imeset Int. Conf. Mult. Sci. Eng. Tech., October 27–29, 2017, Bitlis, Turkey.

51. Gencer G., Eren M., Yildirim S., Kaynaklı M., Palta O., Cengiz M.S., Cengiz Ç., Numerical Approach to City Road Lighting Standards, Book of Abstracts, Imeset Int. Conf. Mult. Sci. Eng. Tech., October 27–29, 2017, Bitlis, Turkey.

52. Yıldırım S., Yapıcı İ., Atiç S., Eren M., Palta O., Cengiz Ç., Cengiz M.S., Yurci Y., Numerical Analysis of Productivity and Redemption Periods in LED Illimunation. Imeset Book of Abstracts, Int. Conf. Mult. Sci. Eng. Tech., 12–14 July 2017, Baku.

53. Onaygil S., TEDAŞ Genel Müdürlüğü Meslek İçi Eğitim Semineri, TEDAŞ Basımevi, Ankara, 2005, pp. 1–70.

54. Onaygil S., 2007. TEDAŞ Genel Müdürlüğü Meslek İçi Eğitim Semineri-Gölbaşı Eğitim Tesisleri, Yol aydnlatma Semineri 23–24 Ocak 2007.

55. Güler Ö. & Onaygil S., The effect of luminance uniformity on visibility level in road lighting, Lighting Research Technology, 2002. V35, pp. 199–215.

56. Çıbuk M., Cengiz M.S. Determination of Energy Consumption According to Wireless Network Topologies in Grid-Free Lighting Systems. Light & Engineering, 2020. V28, #2, pp. 67–76.

57. Çıbuk M., Reducing Energy Consumption in Single-Hop and Multi-Hop Topologies of Road Lighting Communication Network, 2020. V28, #4 pp. 91–102.

58. Efe S. B., UPFC Based Real-Time Optimization of Power Systems for Dynamic Voltage Regulation. Computer Modeling in Engineering & Sciences, 2018. V116, #3, pp. 391–406.

59. Efe S. B., Cebeci M. Power Flow Analysis by Artificial Neural Network. International Journal of Energy and Power Engineering, 2013. V2, #6, pp. 204–208.

60. Cengiz, M.S. Simulation and Design Study for Interior Zone Luminance In unnel Lighting. Light & Engineering, 2019. V27, #2, pp. 42–51.

61. Cengiz M.S. Effects of Luminaire Angle and Illumination Topology on Illumination Parameters in Road Lighting. Light & Engineering, 2020. V28, #4 pp. 47–56.

Sakir Parlakyıldız,
M. Sc. He is a Ph.D. student in Firat University, faculty of engineering, department of electrical and electronics engineering. He currently works as a lecturer at Bitlis Eren University, Vocational school of technical sciences, department of biomedical device technologies

Muhsin Tunay Gencoglu
was an associate professor in 2011 and a professor in 2017 at Fırat University, Department of Electrical and Electronics Engineering. His area of interest is electrical facilities and power supply systems

Mehmet Sait Cengiz,
Ph.D. He had got his Master Degree in 2011 and Ph.D. in 2016. His specialization area is electrical-electronics engineering (light). He still works in the field of applied lighting

REMEMBRANCE LIGHT AT MEMORIAL SITES

Nikoiay I. Shchepetkov and Tatyana N. Zavgorodskaya

Moscow Institute of Architecture (State Academy), Moscow
E-mail: n_shchepetkov@inbox.ru

ABSTRACT

Everyone in Russia has been preparing to the 75th anniversary of the victory in World War Two despite the fact that the state-level commemoration events are being impeded by the global disaster which may be compared to a world war: the COVID-19 pandemic. Like a war, it will eventually end but the memory about the anniversary must and will live on. Therefore, the subject of the article is topical: commemoration light and memory in light of an eternal flame and artistic and sacral illumination (Tribute in Light, like it was in New York in 2001). Numerous issues of architectural lighting of memorial sites and monuments in different Russian cities are under consideration. Positive and negative examples of light design solutions are described. It is also noted that information on contemporary state of this area is extremely insufficient.

Keywords: light design, memorial sites and monuments, war, memory, light

The memory of the most disastrous war in the Russian history, the World War Two, is kept not only in people's minds and literature, fine arts, music, theatre, cinema and TV series, but also in sculptural and architectural memorial sites and monuments which have been increasing in numbers over the years. For some time now, in terms of visuals and emotions, these sites have been starting living not one, mainly daytime, life but two lives, i.e. also a man-made night time life under artificial illumination. And sometimes the visions of this second life are even more impressive, then of the first one since a site becomes a gigantic theatrical stage with dramatic effects of light. At least, this is the main goal of light-design solutions which, unfortunately, are still not implemented at all sites or the effect of their implementation has not reached the lofty objective due to poor design quality or inadequate maintenance of lighting installations.

Fig. 1. Daytime and night time images of the Broken Ring monument in memory of the Siege of Leningrad

Fig. 2. The Tomb of the Unknown Soldier in Alexander garden

In the daytime, the idea to express the dramatic nature of a memorial site not only by means of conventional sculptural and spatial composition is negated by the overwhelming light from the sky and the Sun incident indifferently on all elements. It is good if the authors, a sculptor and an architect, have thought about orientation of dominant objects, axes of composition and design and main directions of perception as related to the Sun (let us remember the monument of to A.S. Pushkin in Moscow, which has lost part of poetic dramatics designed by Alexander Opekushin after it was moved to another place and rotated by 180 degrees). However, in the night time, a spectator's attention is controlled and original lighting images are created by means of electric light and it is possible to predict and calculate its parameters and, therefore, emotional reactions of visitors based on the designed script. Look at the daytime and night time photos of the Broken Ring monument commemorating the Siege of Len-

ingrad: as compared to the latter, the former looks emotionless while the latter is filled with emotions, light deliberately and confidently directs a spectator's attention to the elements of the composition, the surroundings do not deflect attention and dramatise the situation persuasively and appropriately (Fig. 1). With invention and development of LED lighting installations (LI) and programmable control systems, the kinetic adjustment of all lighting parameters has been becoming much easier. However, these features are still used only sometimes as part of temporary, one-time holiday shows. A century ago, the symbolic expression of an idea or a spirit of a memorial site was ingeniously found in the form of an eternal flame: like the flaming heart of Maxim Gorky's Danko, living flame lights the road of memory for us. The first eternal flame was lighted up in 1923 on the Tomb of the Unknown Soldier of the World War One under the Triumphal Arch at the Place de l'Étoile (now known as Place Charles de Gaulle) in Paris. The first eternal flame in the USSR was lighted up in 1957 at the Field of Mars in Leningrad near the Monument to the Fighters of the Revolution and then in 1967 at the Tomb of the Unknown Soldier near the Kremlin wall in Alexander garden, Moscow. From then on, in hundreds of large cities and small towns of Russia and former republics of the USSR, eternal flame as a small in size but the key, reverent non-material compositional and substantive dominant shines day and night at the bottom of single monuments and in focus of great memorial ensembles, at communal cemeteries and graves, in places of memorable events and heroic exploits. An eternal flame always provides any monument with a clear, obvious and sacral meaning. In these cases, the role of a material dominant is played by sculptural objects such as obelisks,

Fig. 3. Memorial to heroes of the Battle of Stalingrad on the Mamayev Kurgan in Volgograd

Fig. 4. The Brest fortress

figures, steles, arcs, pyramids, etc. To keep their dominant role in an ensemble during night time, they shall be illuminated properly. This obvious function still fights for its legit aesthetic right for implementation.

The tradition of intent symbolic and artistic illumination of memorial sites has appeared in the case of the first Tomb of the Unknown Soldier in the USSR in the Alexander garden (designed by architects D.P. Burdin, V.A. Klimov, Yu.B. Rabaev, and sculptor N.V. Tomsky). Architect V.G. Makarevich (MARKhI) has designed architectural illumination of this minimalistic (according to our today's understanding) landscape composition substantiated by historical context the main light element of which, apart from the eternal flame, was the temperate memorial lighting of the Kremlin wall with backlighted somber blue spruces. Above it all, the floodlighted (based on the VNISI design) Arsenal building "floated" cheerfully (Fig. 2).

At the same time, the similar idea had been elaborated for the largest memorial site in the USSR to the heroes of the Stalingrad battle on the Mamayev Kurgan in Volgograd commissioned in 1967. Since 1965, the architectural lighting laboratory of VNISI (N.V. Gorbachyov, P.S. Evdokishkin, V.M. Tsarkov) had designed the lighting project finally implemented in 1976 [1]. Using the models of main sculptures and lens covered spotlights and reflector lamps, the workshop of the head of the design team E.V. Vuchetich designed the techniques of their lighting in order to select correct direction of floodlighting for the most spectacular presentation during night time, to clarify locations of lighting devices (LD) in the area and to experimentally define the levels of illuminance for the dominant sculpture The Motherland Calls on the top of Mamayev Kurgan overlooking the city so that it

could be seen at night time at 10 km from the city stretched along the Volga river for tens of kilometres as well as from the surrounding plains (the total height of the monument and the hill above the level of Volga is about 190 m). It is worth noting that this method of light modelling is the second best after field simulation method as compared to others, including computer-aided methods which were still unknown at that time.

Apart from the dominant, the compositional and planning structure of the memorial includes also a hierarchised system of thematic sculptural compositions and architectural objects arranged in space and terrain along the path of visitors. As compared to today's level of equipment, the authors disposed very limited lighting capabilities: just spotlights with incandescent lamps (IL) with power of up to 3,000 W. Therefore installed capacity of the main monument only equalled to 240 kW while the total capacity was equal to 480 kW!

High power consumption, short service life, operation expenses, progress in production of more ef-

Fig. 5. The Motherland monument in Kiev

Fig. 6. Kartlis Deda (The Mother of Georgia) monument in Tbilisi

ficient discharge light sources (LS) and new social and aesthetic preferences have given rise to periodic modernisations of LIs of the memorial with corresponding redesign of technical and artistic characteristics of lighting. In the 1980's, the IL-based spotlights S-60, PFS, PZS, PKN were replaced with PGC spotlights based on metal halide lamps (MHL). In the course of preparation to the 60th anniversary of the Battle of Stalingrad, Prosvet LLC designed another modernisation of LIs as a result of which the number of LDs and spotlight batteries had been reduced and light of MHL and high-pressure sodium lamps (HPSL) of different spectra was used, which created an emotional (although it was stationery) effect of fire flashes on the sculptures rather appropriate in this area. The capacity of LIs of the dominant sculpture has reduced by more than 10 times, down to 18.8 kW, while total capacity reduced down to 26.7 kW [2] (Fig. 3).

In 2017, major reconstruction of the main sculpture The Motherland Calls with further modernisation of LI's for the 75th anniversary of the victory has started. Despite this fact, the grand nighttime show Light of the Great Victory has been conducted on Mamayev Kurgan for thousands of spectators on each 8th and 9th of May since 2016. The anni-

Fig. 7. The Victory Park at the Poklonnaya Hill in Moscow

Fig. 8. The monument to heroic defenders of Leningrad

Fig. 9. The monument to Panfilov's Twenty-Eight Guardsmen

versary-related improvements will be implemented before publication of this issue of the journal, and we plan to inspect them in field (if the COVID pandemic does not prevent it) and then describe our explorations. By the way, information on light design in this important artistic and ideological sphere of art and culture is extremely insufficient. The last special issue of the journal on this subject [1] was published 35 years ago and publications have been nearly absent since then. Why don't specialists share their ideas and results? Aren't memorial sites illuminated? Is light design just a method to make profit confidentially? How do previously installed LIs operate? It is difficult to find information, even in the Internet. For instance, the new large memorial is being constructed near Rzhev and its authors, architect K. Fomin and sculptor A. Korobtsov claim that they do not know who has designed its lighting arrangement presented in the Internet! How is it possible without their approval? (Fig. 12).

The Brest Fortress innovatively illuminated in the 1980's [1] does not demonstrate its tragic images during nighttime excursions nowadays due to lack of funding. It is not known whether the Red Army Glory Hill near Minsk [1] and Khatyn [2], the memorial to Panfilov's Twenty-Eight Guardsmen in Almaty and memorial to the Red Army liberated Riga from fascist invaders [4], the Motherland memorial in Kiev and Kartlis Deda in Tbilisi, etc. (although they are abroad nowadays) are illuminated today (Fig. 4–6).

Designing of memorial sites with different degree of monumentality had been initiated by Soviet architects and sculptors even before the war was over, expressing the strong faith in victory and gratitude to liberators. Tens of rather large and expressive ensembles have been created over 75 years and many of them were state-recognised: the Victory

Park on the Poklonnaya Hill, Dubosekovo station and the Glory Belt in Moscow region, memorials in Novorossiysk and Sevastopol, Magnitogorsk and Leningrad [5], Murmansk and Saratov, the Prokhorovka field [6], etc. All of them are illuminated individually with different degrees of artistic perfection (Fig. 7–11).

The decisions of the state authorities of the USSR and the Russian Federation to award honorary titles of Hero City or City of Military Glory to cities distinctive for wide-spread heroism and bravery of their defenders were more socially important for perpetuation of memory of multi-million victims of the war than local thematic monuments: in 1965–1985, by decrees of the Presidium of the Supreme Council of the USSR, the Brest Fortress and 12 cities of the USSR became hero cities, and in 2006–2009, by decrees of the President of the Russian Federation, 45 cities and towns of Russia accepted the new title of a city of military glory. Probably this list is still not completed while

Fig. 10. The monument to defenders of Soviet Arctic (the Alyosha monument) in Murmansk

Fig. 11. The Rear-front Memorial in Magnitogorsk

memories of few veterans and war workers who are still alive as well as of generations of grateful descendants about the immortal heroism and numerous victims in every family live of, while historians keep exploring the archives and enthusiasts, veterans associations and other people interested in this somber and unforgettable subject keep searching for remains of the fallen. As part of this work, we still need to find adequate ways to reflect historical events and facts appropriately.

Each monument is based on a specific event, the fate of some person or many people which affected the course of battles or reflected their terrors.

Monuments are mostly created by sculptors in cooperation with architects who embed sculptural and architectural forms into actual spatial context. However, authors rarely remember about architectural lighting at the stage of creative search and timely invite a light designer. After approval of massing usually designed under daylight and the cost estimate, light designers' hands are often tied: the authors want their monument (especially if it is a portrait) to be illuminated from above (like during the daytime), the elements of LI's to be non-visible (despite the fact that it is already impossible to embed LDs into structures) and not blinding spectators during night time, the lighting system to be nearly free, and sometimes they even cannot clearly explain what the want from the light designers. Many of these requests cannot be realised. To create, a light designer shall not only get familiarised with an object (models, presentation images) but also shall know the authors' "mythology" usually reflected in the form of some script, i.e. prediction of spectator's reaction when moving through space and time (explanatory note, presentation of the project and underlying ideas, conversations with authors, etc.).

Like an individual creator (although it will be necessary to approve a light design with the project authors), a light designer shall not only compose his/her own illumination script taking the authors' requests into account to some extent, but also,

Fig. 12. The memorial to Soviet soldiers near Rzhev

which is more important, to suggest an original visual interpretation of the authors' ideas based both on the properties of a material and spatial arrangement of an object and on aspects of visitors' adaptation to darkness while moving and perception of a monument during night time. Capacities of modern lighting equipment provide a light designer with capabilities to create a lighting composition with required distribution of luminance and chromaticity over the objects, their gradients, selection luminance and colour contrasts, multi-mode kinetics of lighting, large-scale and rhythmic light modulation of space, etc. Unfortunately, not every designer is competent enough to solve these problems which are based on selection of the most appropriate and efficient means and techniques of lighting.

Analysing the available night time photos of some memorial sites (although we cannot believe them completely due to reasons familiar to specialists but, unfortunately, we have to because we do not possess our own photo information and observations), we can define the common features of light composition:

• The most difficult to find visual dialogue between light environment and light forms is formed randomly because theory and practice usually pay attention to artistic interpretation of light forms and the light environment is created based on primitive standards of utility lighting. Scale and rhythmic modulation of nighttime environment providing perception of its depth and human scale is insufficient.

Street LDs taken from catalogues and forming the light environment are neutral relative to a memorial site architecture in the ideal case, despite the fact that there are examples of their personal, single-piece, specific design in the world.

• Although there are standards of architectural lighting (although they are not perfect) [8], no one knows actual values of object luminance individually and as part of hierarchy (dominant, accents, background objects) as well as luminance contrasts and gradients which affect major visual (artistic) evaluations. Some values rarely published [1] are either exceptions to the rules or calculated values not substantiated by field measurements. It is especially relevant to definition of the value of luminance adaptation in different observation points.

• There is even less hope about scientific data on radiation chromaticity, colour contrasts, gradients and adaptation since no one is interested in it.

• Like during the daytime, images of a memorial site on clear and overcast days, in winter and summer, during night time change not only due to different weather conditions but also due to quality of operation of LIs. They usually lose their integrity and expression over time. Proper imagination could make weather changes an element of programmable lighting kinetics.

Nevertheless, sometimes existing light-composition solutions include original techniques providing a light image of the entire memorial site or of its important element with a creative feature. In the large light ensemble of the Poklonnaya Hill, it is definitely reached by 1418 red fountain jets in five basins along the central valley, corresponding to the number of bloody days and year of the war [7], Fig. 7. In the monument to heroic defenders of Leningrad [5], the original technique of "creeping" light was used: concentrated beams of spotlights creeping radially along the pavement of the oval circus towards the central obelisk create a halo around it in the form of light "lashes". Unfortunately, they do not focus into light along the height of the dominant obelisk as its luminance is obviously insufficient (Fig. 8). The figures of soldiers of the Dubosekovo monument to Panfilov's Twenty-Eight Guardsmen (Fig. 9) are illuminated too primitively: a bright strip of light illuminates the belts of all figures while their heads sink in deep contrast shadows. The monument to defenders of the Soviet Arctic ("Alyosha") in Murmansk flooded with light of HPSL-based LD's is rather ornamentally perceived in winter against the background of cold northern landscape (Fig. 10). The moderately illuminated figures of a worker and a soldier (The Rear-Front Monument) monumentally dominate in the light silhouette of the city (Fig. 11).

In the end, we would like to share two dreams: officials of the Ministry of Culture shall pay attention (funding is desirable too) to social and aesthetic relevance of the subject and the creators (sculptors, architects, light designers) shall share their ideas and results in professional journals.

REFERENCES

1. Special issue of the Svetotekhnika journal to the 40th anniversary of the victory: 1985, issue 5:

a) Lysov, F.M. Lighting of the Memorial Site to the Heroes of the Battle of Stalingrad [Osveshcheniye me-

morialnogo kompleksa – pamyatnika Geroyam Stalingradskoy Bitvy]. Svetotekhnika, 1985, Vol. 5, pp. 8–10.

b) Obolensky, N.V., Shchepetkov, N.I., Yaremchuk, Yu.R. Architectural Lighting of Ensembles of the Monuments to Heroes of the Great Patriotic War [Arkhitekturnoye osveshcheniye ansambley – monumentov geroyam Velikoy Otechestvennoy Voiny]. Svetotekhnika, 1985, Vol. 5, pp. 2–5.

c) Epstein, S.N. Lighting of the Soviet Army Glory Hill [Osveshcheniye Kurgana slavy Sovetskoy Armii]. Svetotekhnika, 1985, Vol. 5, pp. 7–8.

d) Topuz, V.G. On Architectural and Artistic Lighting of the Alley of Glory Memorial and the Monument to Unknown Sailor in Odessa [Ob arkhitekturno-khudozhestvennom osveshchenii memoriala Alleya Slavy – pamyatnika Neizvestnomu matrosu v Odesse]. Svetotekhnika, 1985, # 5, pp. 11–12.

e) Lesman, E.A. Lighting of the Monuments to Partizan Glory and Pilots Defending the Sky of Leningrad [Osveshcheniye pamyatnikov Partizanskoy slavy i lyotchikam-zashchitnikam Leningradskogo neba]. Svetotekhnika, 1985, # 5, pp. 12–14.

2. Alexandrova, E.M., Nechaev, V.V., Stepanov, V.N., Tsarkov, V.M. Modernisation of Lighting of the Mamayev Kurgan Memorial Site [Rekonstruktsiya osveshcheniya memorialnogo kompleksa Mamayev Kurgan]. Svetotekhnika, 2003, # 4, pp. 23–26.

3. Basalyga, N.N., Epstein, S.N. Lighting of the Victory Monument in Minsk and the Khatyn Memorial Site [Osveshcheniye monumenta Pobedy v Minske i memorialnogo kompleksa Khatyn]. Svetotekhnika, 1985, # 4, pp. 4–5.

4. Shchepetkov, N.I. Lighting Design of a City [Svetovoy dizain goroda]. Moscow: Arkhitektura-S, 2006, pp. 66, 73 and 277.

5. Lesman, E.A. Lighting of the Monument to Heroic Defenders of Leningrad [Osveshcheniye pamyatnika geroicheskim zashchitnikam Leningrada]. Svetotekhnika, 1985, #1, pp. 2–4.

6. Bartsev, A.A., Burtseva, N.B., Chernyak, A. Sh. Lighting of the Prokhorovka Field Victory Monument [Osveshcheniye Monumenta Pobedy na Prokhorovskom pole]. Svetotekhnika, 1996, #7, pp. 26–27.

7. Gorbachyova, Z.K., Dudkina, G.D. Lighting of the Fountains of the Ensamble of the Poklonnaya Hill Victory Monument [Osveshcheniye fontanov ansamblya pamyatnika Pobedy na Poklonnoy gore]. Svetotekhnika, 1996, # 9, pp. 2–3.

8. SP 52.13330.2016. Daylighting and artificial lighting. Moscow: 2016.

Nikolay I. Shchepetkov,
Dr. of Architecture, Professor. At present he is a head of the Architectural Physics Department of Moscow Architecture Institute, laureate of the State Prize of the Russian Federation (for architectural lighting of Moscow), editorial board member of the Light & Engineering Journal

Tatyana N. Zavgorodskaya,
postgraduate student of the Department of Architectural Physics of Moscow Architectural Institute (scientific supervisor Shchepetkov N.I.), Master of Landscape Architecture; graduated from the Moscow Architectural Institute (Faculty of Landscape Architecture) and with honors the magistracy at the Bauman Moscow State Technical University in the specialty "Landscape Architecture" (topic: "Study of compositional techniques of artistic lighting."). At present, she is the Chief Landscape Architect at ZA_Garden & Light, teacher in landscape design and vertical planning in several universities. Her research interests: architectural and landscape lighting, artistic techniques of artificial lighting in parks and memorial complexes

CONTENTS

VOLUME 28   **NUMBER 1**   **2020**

LIGHT & ENGINEERING

CONTENTS

VOLUME 28   **NUMBER 2**   **2020**

LIGHT & ENGINEERING

CONTENTS

VOLUME 28   **NUMBER 3**   **2020**

LIGHT & ENGINEERING

CONTENTS

VOLUME 28   **NUMBER 4**   **2020**

LIGHT & ENGINEERING

CONTENTS

VOLUME 28   **NUMBER 5**   **2020**

LIGHT & ENGINEERING